# Atom Probe Tomography and in-situ micro-compression coupling for understanding the mechanisms involved in hardening of neutron irradiated ferritic model alloys

Maria Vrellou

Normandie Université

UNIVERSITÉ DE ROUEN NORMANDIE

# THÈSE

**Pour obtenir le diplôme de doctorat**

**Spécialité PHYSIQUE**

**Préparée au sein de l'Université de Rouen Normandie**

# Atom Probe Tomography and in-situ micro-compression coupling for understanding the mechanisms involved in hardening of neutron irradiated ferritic model alloys


**Présentée et soutenue par**
**MARIA VRELLOU**


| Thèse soutenue le 30/03/2023 devant le jury composé de | | |
|---|---|---|
| M. MICHAEL MOODY | PROFESSEUR DES UNIVERSITES, Université d'Oxford (ROYAUME-UNI) | Rapporteur du jury |
| MME MARTA SERRANO | , Centre Rech. Energétique, Environ. Tech. | Rapporteur du jury |
| M. AKIYOSHI NOMOTO | , | Membre du jury |
| M. BERTRAND RADIGUET | MAITRE DE CONFERENCES, Université de Rouen Normandie | Membre du jury |
| M. NAOKI SONEDA | , | Membre du jury |
| MME CRISTELLE PAREIGE | PROFESSEUR DES UNIVERSITES, Université de Rouen Normandie | Président du jury |
| M. PHILIPPE PAREIGE | PROFESSEUR DES UNIVERSITES, Université de Rouen Normandie | Directeur de thèse |

**Thèse dirigée par PHILIPPE PAREIGE (GROUPE DE PHYSIQUE DES MATERIAUX)**

ED 591 PSIME

GPM Groupe de Physique des Matériaux

Normandie Université

# THÈSE

**Pour obtenir le diplôme de doctorat**

**Spécialité PHYSIQUE - SCIENCE DES MATERIAUX**

**Préparée au sein de l'Université de Rouen Normandie**

# Atom Probe Tomography and in-situ micro-compression coupling for understanding the mechanisms involved in hardening of neutron irradiated ferritic model alloys


**Présentée et soutenue par**

**Maria VRELLOU**


**Thèse soutenue publiquement le 30/03/2023**
**devant le jury composé de**

| | | |
|---|---|---|
| Pr. MARTA SERRANO GARCIA | CIEMAT | Rapporteur du jury |
| Pr. MICHAEL MOODY | University of Oxford | Rapporteur du jury |
| Dr. NAOKI SONEDA | CRIEPI | Membre du jury |
| Dr. AKIYOSHI NOMOTO | CRIEPI | Co-encadrant de these |
| Pr. CRISTELLE PAREIGE | Université de Rouen | Présidente du jury |
| Dr. BERTRAND RADIGUET | Université de Rouen | Co-encadrant de these |
| Pr. PHILIPPE PAREIGE | Université de Rouen | Directeur de thèse |

**Thèse dirigée par Pr. Philippe PAREIGE, Groupe de Physique des Materiaux (UMR CNRS 6634 - Universite de Rouen Normandie)**

UNIVERSITÉ DE ROUEN NORMANDIE

GPM Groupe de Physique des Matériaux

CRIEPI Central Research Institute of Electric Power Industry

ED 591 PSIME

GENESIS

cnrs

# Abstract

*Keywords: Atom Probe Tomography, Micro-compression, Irradiation hardening, Post-Irradiation Annealing, Mn-Ni-Si clusters, RPV, Model alloys*

Irradiation is well known to alter the Reactor Pressure Vessel's (RPV) microstructure, inducing embrittlement, and thus threatening the integrity and safety of the Nuclear Power Plants. In spite of the many research studies carried out on the correlation of the microstructure with irradiation hardening of the RPV steel, the underlying mechanisms driving this process are still unclear, mainly because irradiation evolution of microstructure is very sensitive to many parameters concerning the irradiation conditions (as temperature, flux, fluence) and also the material (chemical composition, its fabrication conditions and even its thermomechanical history).

In this work, the way that the typical RPV alloying elements Mn and Ni are involved in the formation and evolution of the irradiation induced microstructure and its consequential effects on the mechanical properties, in the absence of the well-studied impurity Cu, was studied using two ferritic binary model alloys (Fe-Ni and Fe-Mn) and a ternary (Fe-Mn-Ni).

APT microstructural study of the alloys revealed the formation of nano-sized clusters under neutron irradiation. The clusters formed in the Fe-Mn alloy outnumbered those of the other two alloys, producing the highest number density, almost an order of magnitude higher that the density of the other binary alloy (Fe-Ni), the clusters of which were more solute enriched. Therefore, it appears that there is a synergistic effect between Mn and Ni. The Mn contributes by producing solute clusters in high number density and while Ni increases their solute enrichment, which combined together led to the significant increased volume fraction of the clusters developed in the Fe-Mn-Ni alloy.

The mechanical properties of the three alloys before and after irradiation were assessed by in-situ SEM micro-compression of FIB fabricated single crystal micro-pillars, inside grains having favorable crystal orientation. The irradiation hardening was calculated higher in the ternary alloy, followed by the Fe-Ni and the Fe-Mn.

The ability of the irradiation induced clusters to hinder the motion of the dislocations, was evaluated using the obstacle strength, provided from two theoretical models. The obtained specific resistance and obstacle strength values, suggest that the presence of Ni in the solute clusters leads to an enhanced resistance to dislocation motion, while the Mn produces clusters, that cannot effectively hinder the dislocations which pass through them relatively easily and hence the Mn-enriched clusters, mainly contribute to irradiation hardening due to their highly increased number density.

The study of the energy dissipated by the dislocations for overcoming the solute clusters during the plastic deformation of the micropillars is in good agreement between the strength of the clusters as suggested by the theoretical models.

To study the effect of the deformation on the microstructure, APT tips and TEM lamellas were fabricated from lifted-out pillars. The TEM calculated dislocation density of a non-compressed pillar of the non-irradiated Fe-Mn-Ni model alloy, verified the literature suggested value.

APT analysis of the compressed neutron irradiated Fe-Mn pillars, indicated that the characteristics of the clusters were similar with those of the bulk ones, with the exception that an increased number density of 'large' clusters was detected. These 'large' clusters were assumed to be partially sheared from the dislocations that passed through them and, to our knowledge, their presence is reported for the first time.

# Résumé

*<u>Mots-clés</u> : Sonde atomique tomographique, Micro-compression, Durcissement par irradiation, Recuit post-irradiation, Amas Mn-Ni-Si, Cuve de réacteur nucléaire, Alliages modèles*

L'irradiation est bien connue pour altérer la microstructure de la cuve des réacteurs nucléaires (RPV), induisant une fragilisation, et menaçant ainsi l'intégrité et la sécurité des centrales nucléaires. Malgré les nombreuses recherches menées sur la corrélation entre la microstructure et le durcissement par irradiation de l'acier de cuve, les mécanismes sous-jacents de ce processus ne sont toujours pas clairs, principalement parce que l'évolution de la microstructure par irradiation est très sensible à de nombreux paramètres concernant les conditions d'irradiation (comme la température, le flux, la fluence) et aussi le matériau (composition chimique, ses conditions de fabrication et même son histoire thermomécanique).

Dans ce travail, la manière dont Mn et Ni sont impliqués dans la formation et l'évolution de la microstructure induite par l'irradiation et ses effets conséquents sur les propriétés mécaniques, en l'absence de l'impureté Cu bien étudiée, a été étudiée en utilisant deux alliages modèles binaires ferritiques (Fe-Ni et Fe-Mn) et un ternaire (Fe-Mn-Ni).

L'étude microstructurale par sonde atomique a révélé la formation de amas de taille nanométrique sous irradiation neutronique. Les amas formés dans l'alliage Fe-Mn étaient plus nombreux que ceux des deux autres alliages, produisant la densité numérique la plus élevée, presque un ordre de grandeur plus élevé que la densité de l'autre alliage binaire (Fe-Ni), dont les amas étaient plus enrichis en soluté. Par conséquent, il semble qu'il y ait un effet synergique entre le Mn et le Ni. Le Mn contribue en produisant des amas de soluté en haute densité numérique et tandis que le Ni augmente leur enrichissement en soluté, ce qui, combiné, a conduit à l'augmentation significative de la fraction volumique des amas développés dans l'alliage Fe-Mn-Ni.

Les propriétés mécaniques des trois alliages avant et après irradiation ont été évaluées par micro-compression MEB in-situ de micro-piliers monocristallins fabriqués par FIB, à l'intérieur de grains ayant une orientation cristalline favorable. Le durcissement par irradiation a été calculé comme étant plus élevé dans l'alliage ternaire, suivi par le Fe-Ni et le Fe-Mn.

La capacité des amas induits par irradiation à entraver le mouvement des dislocations, a été évaluée en utilisant la force d'obstacle, fournie par deux modèles théoriques. Les valeurs de résistance spécifique et de force d'obstacle obtenues suggèrent que la présence de Ni dans les amas de soluté conduit à une résistance accrue au mouvement des dislocations, tandis que le Mn produit des amas qui ne peuvent pas entraver efficacement le mouvement des dislocations qui les traversent relativement facilement.

L'étude de l'énergie dissipée par les dislocations pour surmonter les amas de soluté pendant la déformation plastique des micropiliers est en bon accord avec la force des amas suggéré par les modèles théoriques.

Pour étudier l'effet de la déformation sur la microstructure, des échantillons de SAT et MET ont été fabriquées à partir des piliers. La mesure de MET de la densité de dislocations d'un pilier non comprimé de l'alliage Fe-Mn-Ni non irradié, a vérifié la valeur suggérée par la littérature.

L'analyse en sonde des piliers comprimés de l'alliage Fe-Mn irradié, a indiqué que les caractéristiques des amas étaient similaires à celles des amas dans le bulk, à l'exception d'une densité élevée de "grands" amas. Ces "grands" amas ont été supposés être partiellement cisaillés par les dislocations qui les ont traversés et, à notre connaissance, leur présence est signalée pour la première fois.

# Acknowledgements

This work was carried out within the Materials Physics Group (Groupe de Physique des Matériaux UMR CNRS 6634) of the University of Rouen Normandie, directed successively by Pr. Philippe Pareige and Dr. Xavier Sauvage. This research was co-funded from the Central Research Institute of Electric Power Industry (CRIEPI, Japan), represented by Dr. Akiyoshi Nomoto as our scientific partner. I would like to thank them all, for allowing me to work in these institutions during these years

First and foremost, I owe my deepest gratitude to my PhD director, Pr. Philippe Pareige and to my PhD supervisor, Dr. Bertrand Radiguet for giving me the opportunity to work on such a challenging and interesting project. Their guidance, support and encouragement have been invaluable throughout my research journey. I am grateful for the countless hours they have spent mentoring and advising me. I am forever indebted to them.

Effective collaboration is necessary and extremely valuable in research and I am grateful for having the opportunity to work together with scientists from CRIEPI. Specifically, I am very grateful to our scientific partner, Dr. Akiyoshi Nomoto for his extremely valuable advice which has greatly enriched my research. I would also like to extend my thanks to Tomohiro Kobayashi and Kenji Nishida for participating in our GPM - CRIEPI meetings, and for their ideas and all their implication on my PhD work.

I would like to express my deepest appreciation to Pr. Cristelle Pareige, who guided me with her expertise in atom probe and her experience with ex-situ micro-compression.

I wish to extend my heartfelt gratitude to my thesis reviewers, Pr. Marta Serrano and Pr. Michael Moody, who kindly accepted to review my PhD manuscript in a very short period of time, offering their valuable feedback and suggestions. I am sincerely grateful to the dissertation committee members, Dr. Naoki Soneda and Pr. Cristelle Pareige, for the fruitful discussion during my defense. Their comments and suggestions have been invaluable in shaping the final version of my thesis.

I want to extend my sincere thanks to the engineers of the GPM laboratory and of the GENESIS platform for their invaluable contributions to my research. Specifically, I would like to acknowledge Auriane Etienne for her valuable help and comprehensive training and valuable assistance, Ronan Henry for his guidance in micro-compression experiments, Fabien Cuvilly for his support in FIB techniques, Emmanuel Cadel and Simona Moldovan for their continuous assistance, Ivan Blum for his invaluable help in APT training, and Gerald Dacosta for his explanations of the GPM software and atom probe data treatment.

Additionally, I thank Yuichi Miyahara and Masaya Kozuka from CRIEPI for their exceptional work with TEM.

I also deeply appreciate the GPM's administration and IT team, including Linda Widerowski, Christine Vurpillot, Caroline Jorry, Romain Vincent, Germain Martigny, and Marie-Ange Derue.

I express my deep gratitude to Constantios Hatzoglou, my former internship supervisor, for his invaluable guidance in atom probe tomography, which greatly contributed to the success of my research. I am honored to have had the opportunity to learn from him and I do acknowledge his significant impact on my academic and professional development.

I would like to extend my thanks to the past and present PhD students and post-docs; Loic Rousseau, Elie Paccou, Sonia Guehairia, Josephine Rezkallah, Louis Dubocquet, Jeoffrey Renaud, Arnaud Duplessi, Alexandre Rakotomizao, Alireza Dashti, Pierre Andre Goujon, Deepak Sharma, Frederic Habiyaremye and Amelie Taieb, thank you for your valuable advice and friendly discussions.

Special thanks to the coffee-fueled group consisting of Aidar Zakirov, Olha Nakonechna, Mykola Lavrsky, Felix Schwab, Gilles Demange, Solene Rouland, Ivan Blum, Ben Jenkins, Begona Gomez-Ferrer, Andrei Medvedev, and Yuri Borges Lima. Thank you all for making this journey a memorable one.

Finally, I would like to thank my friends and especially my family for their constant support. I am deeply grateful to my parents, without whom none of this would have been possible and who despite the distance, have always been present.

# Table of Contents

# List of abbreviations

| | |
|---|---|
| 3D | Three-dimensional |
| ALARA | As Low As Reasonably Achievable |
| amu | Atomic Mass Unit |
| APT | Atom Probe Tomography |
| BCC | Body Centred Cubic |
| BF | Bright Field |
| BKS | Bacon-Kock-Scattergood |
| BR2 | Belgian Reactor 2 |
| BWR | Boiling Water Reactor |
| CCC | Chemical Composition Correction Model |
| CEC | Cu-enriched Cluster |
| CI | Confidence Index |
| CRIEPI | Central Research Institute of Electric Power Industry |
| CRP | Cu-rich Precipitate |
| CRSS | Critical Resolved Shear Stress |
| CS | Core Solutes Element |
| DBTT | Ductile-to-brittle Transition Temperature |
| DD | Dislocation Dynamics |
| DF | Dark Field |
| DLD | Delay Line Detector |
| dpa | Displacement per Atom |
| DR | Detection Rate of APT |
| DS | Dislocation Starvation |
| EBSD | Electron Backscatter Diffraction |
| EDX (or EDS) | Energy-dispersive X-ray Spectroscopy |
| EONY | Eason, Odette, Nanstad, Yamamoto |
| FCC | Face Centered Cubic Lattice |
| FIB | Focused Ion Beam |
| FIM | Field Ion Microscope |
| FS | Fundamental Stereographic Sector |
| GB | Grain Boundary |
| GENESIS | Groupe d'Etudes et de Nanoanalyses des Effets d'Irradiations |
| GIS | Gas Injection System |
| GPM | Groupe de Physique des Matériaux |
| HCP | Hexagonal Close-Packed Lattice |
| ICF | Image Compression Factor |
| IPF | Inverse Pole Figure |
| IPM | Iso-position Method |
| LE | Local Electrode |
| LEAP | Local Electrode Atom Probe |
| LWR | Light Water Reactor |
| MC | Monte Carlo |
| MCP | Micro-channel Plate |
| MD | Matrix Damage |
| MD | Molecular Dynamics |
| MNSP | Mn-Ni-Si Precipitate |
| MR | Mass Resolution of APT |

| | |
|---|---|
| MRSSP | Maximum Resolved Shear Stress Plane |
| MSM | Maximum Separation Method |
| MTR | Material-test Reactor |
| NDT | Nil-Ductility Temperature |
| NPP | Nuclear Power Plant |
| OKMC | Object Kinetic Monte Carlo |
| PAS | Positron-annihilation Spectroscopy |
| PD | Point Defect |
| PKA | Primary Knock-on Atom |
| PWR | Pressurised Water Reactor |
| RED | Radiation Enhanced Diffusion |
| REP | Radiation Enhanced Precipitation |
| RIP | Radiation-induced Precipitation |
| RIS | Radiation-induced Segregation |
| ROI | Region of Interest |
| RPV | Reactor Pressure Vessel |
| SANS | Small Angle Neutron Scattering |
| SAS | Single Arm Source Regieme |
| SCK CEN | Belgian Nuclear Research Centre |
| SEM | Scanning Electron Microscopy |
| SF | Schmid Factor |
| SIA | Self-interstitial Atom |
| STEM | Scanning Transmission Electron Microscopy |
| SST | Standard Stereographic Triangle |
| TEM | Transmission Electron Microscopy |
| TOF | Time of flight |
| TTS | Transition Temperature Shift |
| V | Vacancy |
| WBDF | Weak Beam Dark Field |
| WWER | Water-water Energetic Reactor |
| UMD (or UMF) | Unstable Matrix Defect (or Unstable Matrix Feature) |
| USE | Upper Shelf Energy |
| UTS | Ultimate Tensile Strength |

# General introduction

The growing energy demand and environmental constraints require new forms of sustainable electrical energy production. Indeed, it is estimated that by 2050, the global population will increase from 8 to 10 billion [1]. Consequently, the energy consumption should double or even triple depending on the scenarios [2]. Therefore, more energy resources should be available to be exploited for the on-demand production of energy in large quantities, and in such a way that it has the most limited consequences on the environment.

Fossil fuels or intermittent renewable energy sources cannot fulfill entirely these requirements. Conversely, nuclear energy can respond and contribute to successfully addressing the environmental, social and economic impacts.

Nuclear fission reactors can produce energy, responding dynamically to changes in demand and emitting far less greenhouse gases than sources such as fossil fuels. Some countries reprocess used nuclear fuel, recycling fissile materials and thus extracting 25 to 30 % [2], [3] more energy and at the same time reducing the volume of the disposed radioactive waste. Nonetheless, improvements should be made to reduce the risks and the effects of a possible accident, but also to minimize dependence on uranium.

The majority of the currently operating nuclear power plants (NPPs) had an original lifetime of 40 years. As the fusion reactors and the safer new generations of fission reactors are under development, there is a pressing need for extending the lifetime of the operating nuclear plants. Japan opts for an extension of maximum 20 years [4] with very strict conditions, while France has unlimited operational license [5], [6] of its NPPs which undergo continuous assessments to ensure that they fulfill all the regulatory requirements.

An essential and defining factor for the extension of the NPPs' life is the degree of the possible embrittlement of the reactor pressure vessels (RPVs) due to neutron irradiation. RPVs are massive and irreplaceable vessels housing the reactor core, also offering a significant protection level by confining the radioactive material, and hence being a barrier against its release into the environment.

Neutrons produced in the nuclear reactions that take place inside the core, cause changes in the microstructure of the reactor pressure vessel, generating nanosized defects such as interstitial loops, nano-voids, and different types of solute clusters. Although their nanometric size, the solute clusters can effectively hinder the movement of dislocations in the RPV material, harden and embrittle it, by deteriorating the ductility of the metallic structural materials. This may challenge RPVs' extended operation and in the extreme case may lead to reactor shutdown to avoid any possible catastrophic failure of the vessel.

For this reason, it is crucial to thoroughly study the irradiation damage manifested as the hardening and embrittlement of the RPVs steels. The underlying mechanisms driving this process are still unclear, mainly because the evolution of the irradiated microstructure is very sensitive to many parameters that depend on both the irradiation conditions and the nature and thermomechanical history of the material.

Valuable help to acquire knowledge regarding the physical insights involved, is obtained through theoretical models predicting the mechanical response based on the microstructural data. Thus, the experimental study of both microstructure and mechanical properties can help

to understand and corelate the mechanisms involved in hardening and to improve irradiation damage predictability.

In this work three ferritic model alloys, two binary Fe-Mn and Fe-Ni alloys and a ternary Fe-Mn-Ni one have been studied to investigate the role of the Mn and Ni in the clustering process due to neutron irradiation. The impact of the clustering on the mechanical properties was measured using in-situ micro-compression experiments performed on single crystal micropillars. The obstacle strength of the developed clusters was estimated, corelating the Atom Probe Tomography (APT) detected microstructure with the measured irradiation hardening. Additionally, in this work the stability of the clusters generated after irradiation of the ternary alloy, was evaluated to provide insights into the mechanism leading to their formation. Further the microstructure within the micropillars, was investigated for possible changes due to the imposed deformation.

The first chapter of this dissertation reviews the literature, presenting in brief the background information needed for the interpretation of the following chapters. At first, are presented the fundamentals of crystal structures, especially of the BCC crystal structure, and the crystal lattice defects, with emphasis on the dislocations. The fundamentals of the plastic deformation are reviewed, particularly for the BCC single crystals, discussing the origin of their deviation from the predictions of the Schmid's law. Next, follows a brief description of the strengthening mechanisms modifying the mechanical properties of materials at macroscopic scale, along with the proposed mechanisms acting at small (micron or sub-micron) scale. The next topic is a concise overview of the interactions between neutron irradiation and the structural components of the NPPs and the resulting irradiation damage, focusing on the mechanisms involved in solute clusters and precipitates formation.

The second chapter reports the studied model alloys, their irradiation conditions along with the instrumentation and the experimental methods and techniques applied in this study, namely: the Atom Probe Tomography (APT) for microstructural characterization at near atomic resolution , the Transmission Electron Microscopy (TEM) for measuring the dislocation density, the Electron Backscatter Diffraction (EBSD) for locating and selecting the grains with the suitable crystal orientation, the Focused Ion Beam (FIB) for fabrication of single-crystal micropillars, APT tips and TEM lamellas. Also, the experimental setup for the in-situ scanning electron microscopy (SEM) micropillar compression tests, is outlined as well as the performed post compression trace analysis for evaluating the activated slip systems.

In the third chapter are described the results of the APT experiments carried out to investigate the microstructure of the three model alloys. The solutes' distribution and the microstructure before and after irradiation was studied by APT and the size, number density, volume fraction along with the chemical composition of the identified nanometric size clusters were calculated. Whether the formed clusters after irradiation of the ternary Fe-Mn-Ni model alloy are stable intermetallic phases or irradiation induced solute clusters, is evaluated by studying their stability after isochronal Post Irradiation Annealing (PIA) at 400$^{o}$C, 500$^{o}$C and 600$^{o}$C and discussed in this chapter.

The fourth chapter deals with the in-situ micro-compression experiments performed to investigate, the mechanical properties of the model alloys, before and after neutron irradiation, and to determine the irradiation hardening. The effect of applying the Sneddon's correction on the stress-strain data, acquired by the picoindenter, the shape of the obtained curves and the presence of sample size effect are investigated and discussed.

The final fifth chapter is devoted to the correlation of the measured irradiation hardening with the observed microstructure, calculating the obstacle strength of the clusters developed after irradiation. Additionally in this chapter, the microstructure within the pillars of the model alloys, before and after deformation, is investigated for changes due to the imposed compression, analyzing APT tips and TEM lamellas fabricated from lifted out non-compressed and compressed pillars.

A summary and perspectives are closing this work.

# Bibliography


[1] "World Population Clock: 8 Billion People (LIVE, 2023) - Worldometer." https://www.worldometers.info/world-population/ (accessed Feb. 18, 2023).

[2] "Processing of Used Nuclear Fuel - World Nuclear Association." https://world-nuclear.org/information-library/nuclear-fuel-cycle/fuel-recycling/processing-of-used-nuclear-fuel.aspx (accessed Feb. 11, 2023).

[3] Center for Sustainable Systems, University of Michigan. 2022., "Nuclear Energy Factsheet, Pub. No. CSS11-15."

[4] R. Krivanek, "Factors limiting lifetime of nuclear power plants with pressurized-water reactors," *Nucl. Eng. Des.*, vol. 370, p. 110872, Dec. 2020, doi: 10.1016/j.nucengdes.2020.110872.

[5] "Factors limiting lifetime of nuclear power plants with pressurized-water reactors | Elsevier Enhanced Reader." https://reader.elsevier.com/reader/sd/pii/S002954932030366?token=5A7629D1E7AA76ABB9996F3F84D15A84B5749263FC2029BDE36895FA27BFB456D7AC9C1C54E27B32C4393E50A15DE3F8&originRegion=eu-west-1&originCreation=20230211132328 (accessed Feb. 11, 2023).

[6] "The Economics of Long-term Operation of Nuclear Power Plants," *Nuclear Energy Agency (NEA)*. https://www.oecd-nea.org/jcms/pl_14752/the-economics-of-long-term-operation-of-nuclear-power-plants?details=true (accessed Feb. 11, 2023).

# Chapter 1: Literature review

## I. Characteristics of Reactor Pressure Vessel (RPV) steels

Nowadays 10% [1] of world's electricity comes from nuclear energy. More than 30 countries use nuclear reactors that produce 2553 TWh of electricity [2]. France has at the moment 56 reactors that produce more than the 70% of the country's electricity [1], [3] whereas in Japan 33 reactors operate and yield 5.1% [1], [4] of the country's electricity. The majority of the world's operating nuclear power plants are Generation II reactors and more precisely, Pressurized Water Reactors (PWR) and Boiling Water Reactors (BWR). These are Light-Water Reactors (LWR) meaning the use of normal water as both coolant and neutron moderator. Their main difference is that in PWR there are 2 coolant circuits whereas in BWR there is only one (Figure 1).

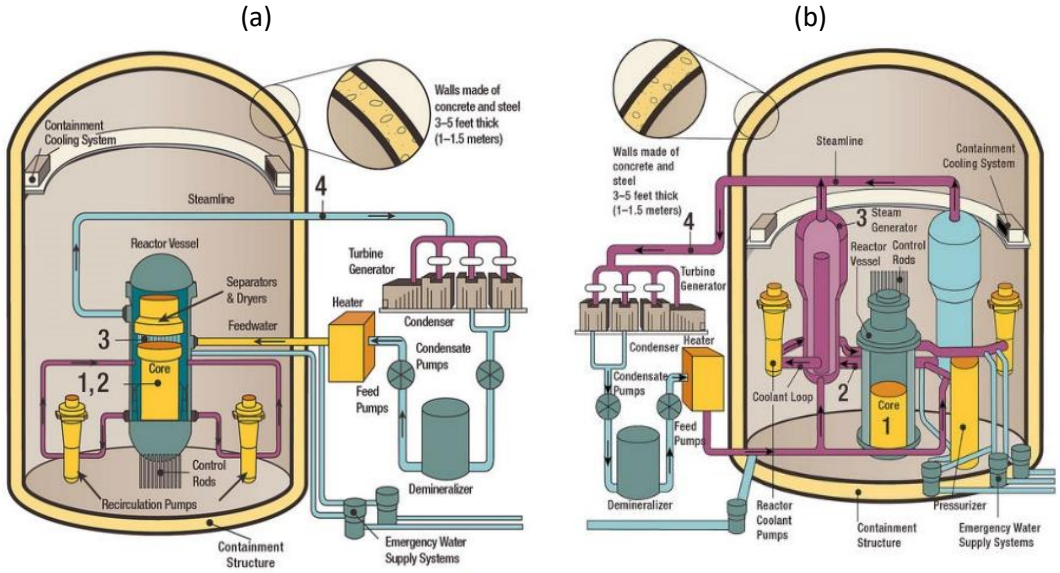


*Figure 1: Circuits of a (a) BWR reactor [5] and (b) PWR reactor [6].*

The most important and irreplaceable component for LWR safety is the reactor pressure vessel (RPV) as its main function is to house the reactor core. Indeed, RPV acts not only as the first radiation barrier but also as a pressure barrier between the exterior and the fuel, with a wall thickness in the core region of about 200-250 mm [7]. BWR usually operate at 6.9 MPa and 272 °C [8] whereas PWR at 15.5 MPa, and temperatures around 288 °C [8].Typical dimensions for BWR RPVs are 22 m in height with a nominal inside diameter of 6.4 m [8] and for PWR RPVs are 13.5 m in height, with an inside diameter of 4.4 m , as for the Westinghouse-design PWRs [9]. This difference in size is due to the larger core in the BWR and the steam drying equipment installed at the top portion of the BWR RPV [8]. In both cases, it is understandable that their large sizes make the RPVs irreplaceable. Thus, the lifetime of the RPV determines the lifetime of the nuclear power plant (NPP).

The fabrication of Western-type LWRs can be achieved with 2 different ways (Figure 2). Historically, the first way of fabricating LWRs is by the use of rolled and welded plates to form separate shell courses and then welding them in both longitudinal (axial) and circumferential (girth) directions. All BWR and most of the PWR RPVs were fabricated by this method.


*Figure 2: (a) A pressure vessel of the Shippingport reactor (1956) (b) 50 years after, a nozzle support shell ring of the pressure vessel of the EPR for the Olkiluoto Finnish plant [7].*

The most recent fabrication method is by using large ring forgings (Figure 2 (b)). This way the number of welds is decreased, increasing the reactor's reliability. PWR RPVs can be entirely constructed from forged rings due to their smaller size (avoiding longitudinal welds). Development in forging technology allowed further increase in the dimensions of components like ring forgings for core region, shells, flanges etc. This enabled the construction of advanced boiling water reactor (ABWR) plants using forged components.

After this, the vessels are tempered and thermally annealed at 620±15°C [10] for about 30 h in order to alleviate stresses. This way, an as-fabricated yield stress of about 475±50 MPa [5] is achieved.

The materials used for the construction of the Western RPVs are low-alloy steels that typically contain 0.05 – 0.2% of C, 0.7 – 1.6% of Mn, 0.4 – 0.6% of Mo, 0.2 – 1.4% of Ni, 0.2 – 0.6% of Si, and 0.05 – 0.5% of Cr [10] along with impurities such as Cu and P [8]. They also typically have a stainless-steel inner lining to prevent corrosion from the coolant water.

More precisely, base metals used are typically low-alloyed NiMnMo ferritic steels with Body Centered Cubic (BCC) structure.

- For plates, SA 302 Grade B was used for earlier vessels and SA 533 Grade B Class 1 for later vessels [8].
- For forgings, SA 508 Class 2 (corresponding to German standard 22NiMoCr37 ) and SA 508 Class 3 (corresponding to French 16MND5 , German 20MnMoNi55 & Japanese standard JIS G 3204 SFVQ1A) were used [8].

The composition of these materials is given in Table 1.

*Table 1: Typical compositions of modern LWR pressure vessels [11].*

| Material specification | Country of origin | Number of analyses | C | Mn | Ni | Mo | Si | Cr | P | S | Cu | Al |
|---|---|---|---|---|---|---|---|---|---|---|---|---|
| S533B Cl 1 | Japan[a] | 175 | 0.201 | 1.371 | 0.616 | 0.520 | 0.243 | 0.136 | 0.007 | 0.006 | 0.049 | 0.025 |
| S533B Cl 1 | United States | 13 | 0.218 | 1.367 | 0.547 | 0.547 | 0.236 | 0.074 | 0.009 | 0.014 | 0.117 | |
| SA508 Cl 3 20MnMoNi 55 forging grade | Japan[a] | 166 | 0.200 | 1.398 | 0.753 | 0.505 | 0.243 | 0.097 | 0.007 | 0.007 | 0.054 | 0.028 |
| SA508 Cl 3 (etc.) | France[b] | 125 | 0.161 | 1.338 | 0.722 | 0.503 | 0.235 | 0.295 | 0.010 | 0.010 | 0.065 | |
| SA508 Cl2 | Japan[a] | 64 | 0.206 | 0.803 | 0.844 | 0.585 | 0.231 | 0.374 | 0.006 | 0.006 | 0.048 | 0.029 |
| SA508 Cl 2 | United States | 5 | 0.238 | 0.682 | 0.600 | 0.595 | 0.284 | 0.374 | 0.006 | 0.011 | 0.040 | |

a Additional analyses of Japanese steels shows that As 0.007–0.009, Sn 0.008, Sb 0.002, Co 0.009–0.010 wt%.

b Analyses of French SA508 Cl 3 showed As 0.016, Sn 0.011, Co 0.017 wt%.

Weld compositions differ from the base metal and may vary significantly even within the same weld. Prior to 1972, Cu was used as a coating for weld wire to reduce corrosion during storage and to increase electrical conductivity during the welding process. Submerged Arc Welding (SAW) produces welds that have the higher copper content while Manual Metallic Arc (MMA) welds present the lowest Cu content [12]. The detrimental effect of the residual Cu and P with regards to the RPV's embrittlement, arose in the late 1960s and early 1970s [11]. Consequently, the coating for welds in the RPV beltline region (which is located adjacent to the reactor core and experiencing the highest neutron fluence) was removed [4]. Nowadays impurities levels of RPVs are lower and well-controlled.

Currently (Figure 3) Gen-III and Gen-III+ reactors are in construction and their operation is expected to last until about 2080 [7], [13]. These reactors are considered as advanced LWR reactors with optimized design, reinforced structure, longer operating life – typically 60 years and more efficient fuel consumption [14]. But the greatest difference from the in-operation Gen-II reactors is that they incorporate many passive safety features, which rely on gravity, natural convection or resistance to high temperatures and thus they don't require active intervention in the event of malfunction.

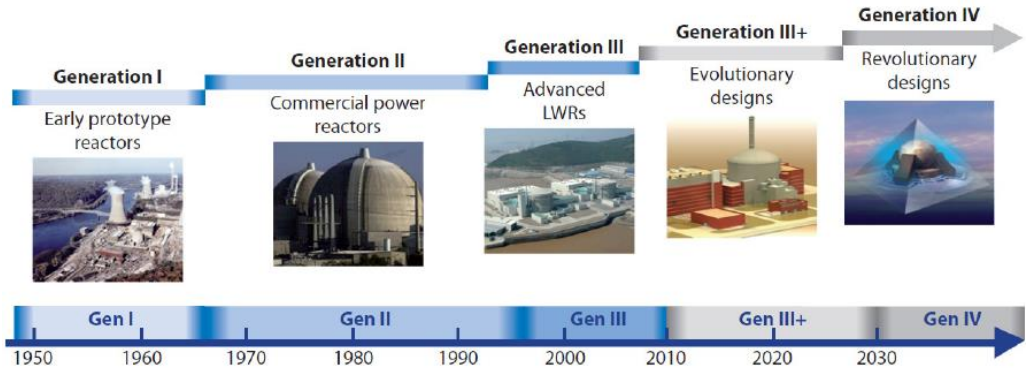


*Figure 3: Timeline of different generations of nuclear power plants' deployment [15].*

In the meantime, current LWRs will probably continue to have a prominent role in the world electricity production. Although Gen-II reactors were initially aimed for 40-year operation, research and engineering has established that it is possible to extend the operating RPV end of life to at least 60 years. So, Gen-II can be in service until 2030-2040, provided that operational reliability is maintained with RPV safety analyses supporting it.

## II. Plasticity in ferritic alloys

The most demanding part of the nuclear power plants (NPPs), the reactor pressure vessels (RPVs) are made using low-alloy steels ferritic steels. At beginning of life, these steels, have mechanical properties that ensure that they are adequately strong for the hard in-service conditions. Irradiation damage can significantly alter the extent that they can plastically deform, degrading their resistance to fracture and hence raising serious safety issues about a potential catastrophic failure. Thus, a quick review of the fundamentals of the mechanisms of the plastic deformation is required.

### 1. Ferritic crystal structures

A solid material can be characterized as crystalline when its atoms are arranged in a pattern which repeats itself in the three dimensions, exhibiting a long-range order. When this regular repetition does not occur, the material is characterized as amorphous. The smallest identical repeating pattern is called unit cell. In a crystalline solid, the unit cell is regularly repeated in a three-dimensional arrangement, thus constituting a lattice.

In 1848, Auguste Bravais showed that only 14 distinct lattices exist and can be categorized in 7 crystal systems: cubic, tetragonal, orthorhombic, trigonal, hexagonal, monoclinic, and triclinic [16].

Most of the metals adopt one of the three densely packed crystal structures:

- Body-centered cubic (BCC)
- Face-centered cubic (FCC) or cubic close-packed (CCP) structure
- Hexagonal close-packed (HCP)

Examples of BCC structures are Fe, Cr, Mn, Mo, Nb, Ta, W and V, examples of FCC structures are Al, Cu, Au, Pb, Ni, Pt and Ag, whereas Be, Mg, Ti, Co, Zn are HCP. Figure 4 represents the periodic table of elements with respect to their crystal structure.

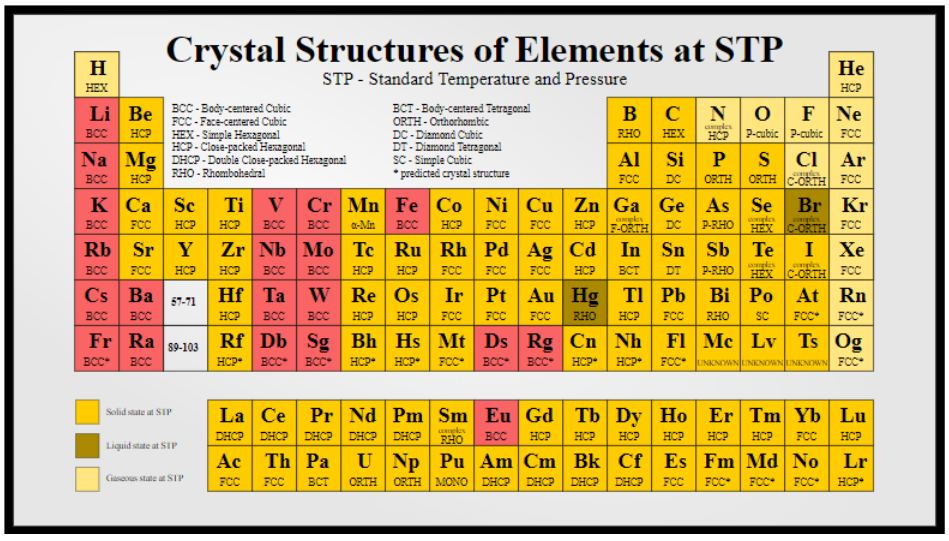


*Figure 4: Crystal structure of elements. BCC metals are highlighted with red color [17].*

Some metals exist in more than one crystalline form depending on the temperature and/or the pressure. Those crystals are "allotropic" and Fe is such a crystal. At room temperature,

pure iron has a BCC structure and is named ferrite or α-iron (α-Fe). Ferrite has a lattice parameter of 0.286 nm. Between 910◦C and 1400◦C the stable crystal structure of iron is FCC, and this phase of iron is known as the γ-iron or austenite. The lattice parameter of austenite is 0.355 nm. Between 1400◦C and 1538 ◦C, the crystal structure becomes again BCC but with bigger lattice parameter of 0.292 nm and this phase of iron is termed as δ-iron.

As already said, RPV steels have a BCC structure. There are 2 atoms in total in the BCC structure (Figure 6); they are located at the eight vertices and a single atom at the cube center. These atoms are filling 68 % of the unit cell volume. The coordination number for the BCC is 8 and the atoms "touch" each other along cube (body) diagonals.

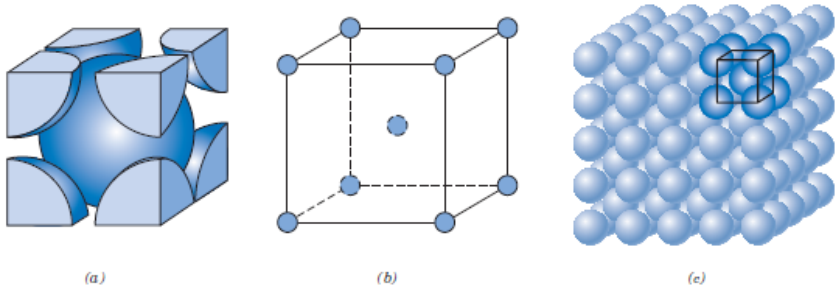


*Figure 5: Body-Centered Cubic (BCC) crystal structure, unit cell representations [18].*

## 2. Crystal Defects

In reality, the crystal lattice of all metals is not perfect. The regular repetition of the atoms is disturbed by local imperfections called crystal defects. These defects are classified as point, line, surface, and volume defects or according to their dimensionality as 0-D, 1-D, 2-D, 3-D defects respectively.

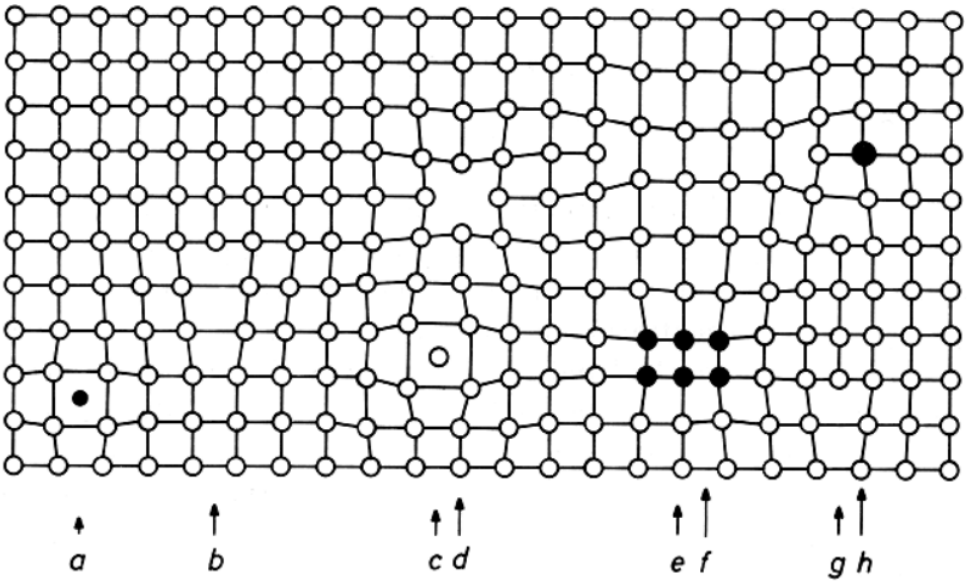


*Figure 6: Examples of crystal defects; (a) Interstitial impurity atom, (b) Edge dislocation, (c) Self-interstitial atom, (d) Vacancy, (e) Precipitate of impurity atoms, (f) Vacancy type dislocation loop, (g) Interstitial type dislocation loop and (h) Substitutional impurity atom [19].*

**0-D: point defects (PD)**

These are small defects that occupy a single lattice site and are mainly vacancies, (self) interstitial and substitutional atoms (Figure 6). Vacancies and self-interstitials are the two types of point defects (PD) that can be found in pure crystals [20].

Thermal vacancies are always present inside metals and are created when inner atoms diffuse to the free surface of a crystal leaving vacant lattice sites (Schottky mechanism - Figure 7) and their equilibrium concentration increases exponentially with increasing temperature.

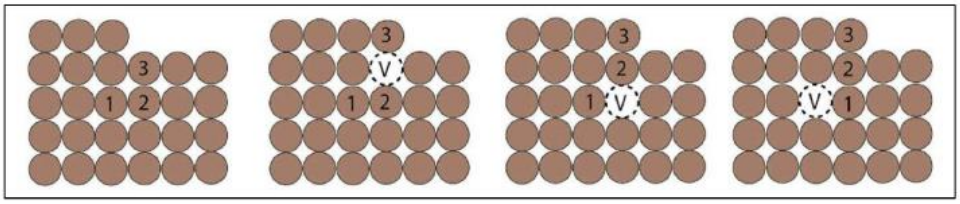


*Figure 7: Schottky mechanism for vacancy formation [21]*

Self-Interstitial atom is an atom in excess compared to the number of lattice sites. Since it has the same size than other atoms, it cannot occupy tetrahedral or octahedral interstitial sites, resulting in different configurations (crowdion, dumbbell) depending of the metal. Due to their high formation energy, their equilibrium concentration is neglectable at all temperatures.

Vacancies and self-interstitials can be produced in materials by high-energy particle irradiation. In addition, impurity atoms are always present in the metal and can play an important role in modifying the physical and mechanical properties of the materials. The impurity atom can either replace an atom in the original lattice site (substitutional atom) or can be placed as an extra atom between the atoms occupying the crystal lattice sites (interstitial atom).

**1-D: Line defects or Dislocations**

One-dimension defects are lines through the crystal along which there is disruption of the atoms' arrangement in the crystal lattice (Figure 6). They occur in high densities and strongly influence the mechanical properties of material, playing fundamental role in plastic deformation. More details about dislocations are given in the next section.

**2-D: Planar or surface defects**

Planar defects are distortions of the perfect crystal structure across a plane (surface). The most common surface defects are of course the actual external surface of the material (free surface), the grain boundaries, the interfaces between phases, stacking faults and twin boundaries.

Metals are usually polycrystalline materials. In their volume there are regions (called grains) having different specific crystalline orientations. Atoms at the grain boundaries are not in perfect crystalline arrangement forming a locally distorted lattice.

Stacking faults are planar defects in which the normal stacking sequence of planes is changed in a specific region. Stacking faults are common in FCC metals but unstable in BCC metals.

A twin boundary is a boundary that separates two domains of a crystal so that crystal structures on either side are mirror images of each other (Figure 8). Commonly, twinning occurs during plastic deformation of materials with low stacking fault energies, often at low temperatures and when the strain rate is too high for the mobility of the dislocations to handle the strain.

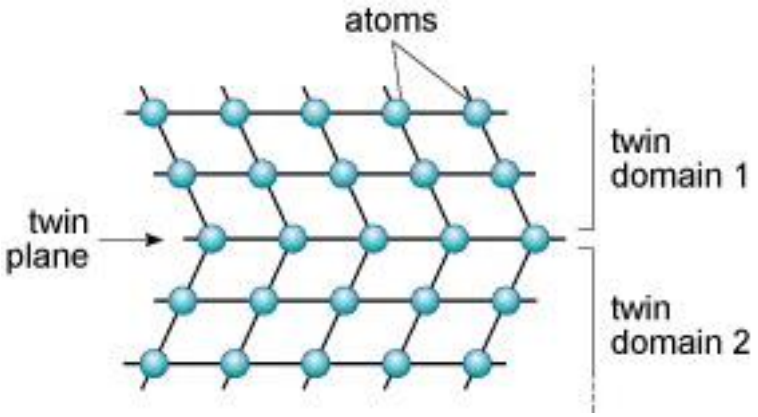


*Figure 8: Illustration of crystal twinning: the twin domains are crystal regions that are mirror images of each other, separated by the twin plane [22].*

**3-D: Volume defects**

There are three-dimensional imperfections inside the crystals. They can be aggregates of solutes and/or impurities atoms (precipitates), inclusions of foreign particles or clusters of vacancies (voids). Under irradiation, the transmutation of certain elements may produce insoluble gases that fill the voids and thus 'bubbles' are generated [23].

## 3. Dislocation characteristics and motion

In the early part of the 20$^{th}$ century, it was thought that plastic deformation of crystalline materials must take place by sliding of whole atomic planes past each other. The shear stress required for this process, in a perfect dislocation-free crystal, was first calculated by Frenkel in 1926. He estimated the maximum value of the applied shear stress that a single crystal can sustain before exhibiting permanent deformation ($\tau_{th}$) as:

$$\tau_{th} = \frac{b}{a}\frac{G}{2\pi} \tag{1.1}$$

where $\tau_{th}$ is the applied shear stress, G is the shear modulus, b the spacing between atoms in the direction of the shear stress, α the spacing of the rows of atoms.

This theoretical value is many orders of magnitude larger than the observed experimental values measured in real crystals [20], [23]. This substantial difference was explained, independently by each other, from Orowan, Polanyi and Taylor in 1934. They suggested that the (edge) dislocations inside the real crystals act as stress concentrations facilitating plastic flow. Instead of a whole plane slipping over another, slip occurs in localized regions (dislocations) and these regions move progressively across the plane. In 1939, Burgers

introduced the screw dislocation and in 1950, Frank and Read [24] proposed a way of how the dislocations can form and multiply.

### *3-A. Types of dislocation*

There are thus two main types of dislocation (edge and screw). For their description, a simplified model using cubic primitive structure is presented. Real lattices are more complicated, and the exact nature of the bonding determines the fine detail of the arrangement of the atoms around the dislocation.

1. <u>The edge dislocation</u>

The edge dislocation appears as an extra half-plane of atoms inserted in the lattice. This is illustrated by the surface ABCD in Figure 9. The lattice is significantly disturbed only along the dislocation line DC which is described by the dislocation line vector (s).

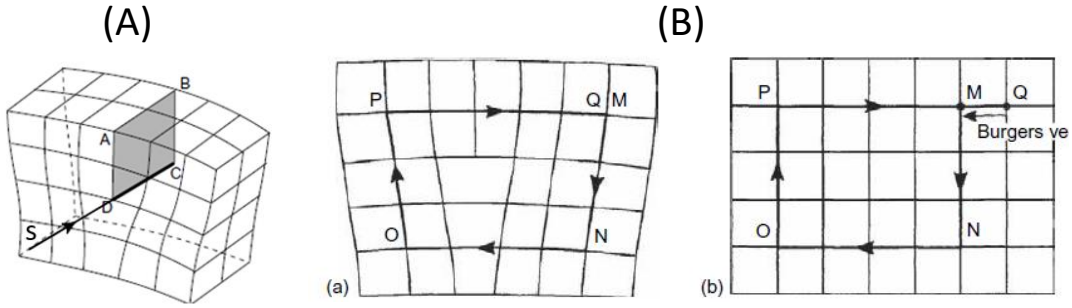


*Figure 9: (A) Illustration of edge dislocation (B) Burgers vector definition: (B-a) Burgers circuit constructed around an edge dislocation (B-b) The same circuit on a perfect crystal, the Burgers vector is defined by the closure failure. [20].*

Another important property of a dislocation is the Burgers vector, which represents the magnitude and the direction of the lattice distortion caused by the presence of a dislocation. In order to define the Burgers vector, two Burgers circuits need to be made. First, we define the positive direction, s, along the dislocation line (e.g., into the paper). Looking along this direction, an atom-to-atom clockwise close loop is formed including the dislocation (Figure 9 (B)-a). Then, the same atom-to-atom sequence is followed in a dislocation free area of the crystal and the circuit will not close (Figure 9 (B)-b). The vector needed for closing the circuit in the dislocation free crystal is by definition the Burgers vector (b). For an edge dislocation, the Burgers vector (b) is normal to the dislocation line vector (s).

Since the dislocation line sense is arbitrary defined, if the opposite direction along the dislocation line (e.g., out of the paper) was selected (Figure 10 - a, b), then making the clockwise closed loop would produce an opposite sense Burgers vector, but the relationship between s and b is the same and the dislocation illustrated in Figure 10 - a is identical to the one in Figure 10 - b, while an opposite sign dislocation is in Figure 10 - c.

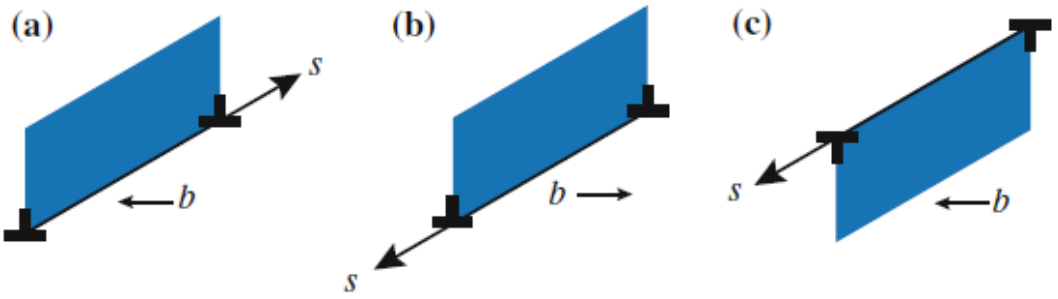


*Figure 10: Edge dislocations (a) and (b) are identical (having the same relationship between s and b) but (c) has opposite sign [25]*

2. <u>The screw dislocation</u>

A screw dislocation can be illustrated by displacing the crystal on one side of ABCD relative to the other side in the direction DC (Figure 11). The shape obtained is a helicoid surface, rather looking like a spiral staircase.

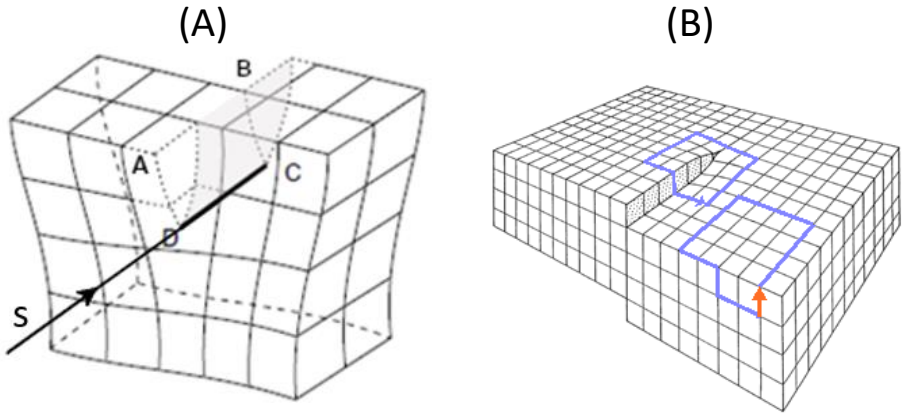


*Figure 11: (A) Screw dislocation (after [20]) (B) Burger vector definition for screw dislocation: By construction of burger circuit around a screw dislocation and transfer it at a region where the lattice is perfect [19].*

By convention, looking along the dislocation line the screw dislocation is characterized as a right-handed screw dislocation, if the helix advances one plane when a clockwise circuit is made round it and if the reverse is true, it is left-handed. For a screw dislocation, the Burgers vector (b) is parallel to the dislocation line vector (s).

3. The mixed dislocation

The most common type of dislocations in crystalline materials are the mixed dislocations which are neither pure edge nor pure screw dislocations but exhibit components of both types.

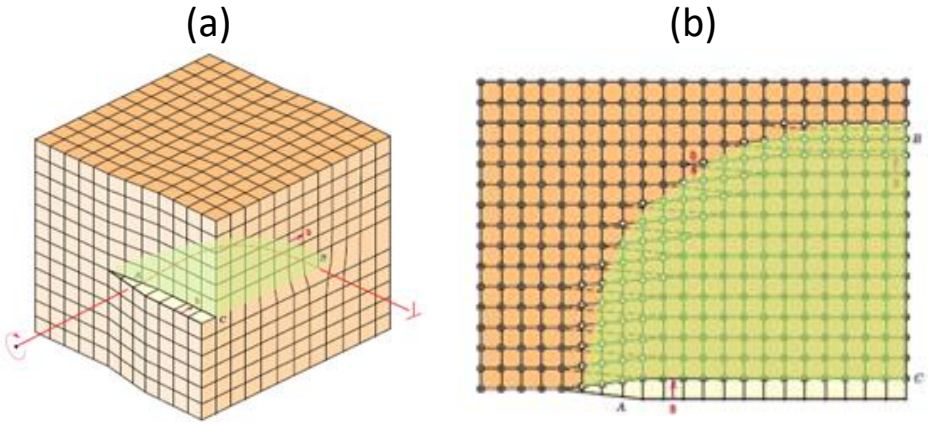


*Figure 12: The Mixed dislocation: at A pure screw character, at B pure edge and mixed character in the intermediate regions [modified from [18]].*

The Burgers vector of a mixed dislocation lies at an arbitrary angle to the dislocation line which does not need to be straight. In the case of Figure 12, the dislocation has screw character at A and an edge character at B, while the intermediate regions have both edge and screw components, the magnitudes of which, depend on the angle between b and s.

*3-B. Dislocation movement*

Plastic deformation of metals commonly takes place as dislocations move progressively across a plane. At a distance from the dislocation line, atoms are almost at their perfect crystal position, but the atoms near the line are displaced. As illustrated in Figure 13 (a), (b), a small relative change in position of atom 1 is needed for the extra half plane to move from x to y. By repeating this process dislocation glides.

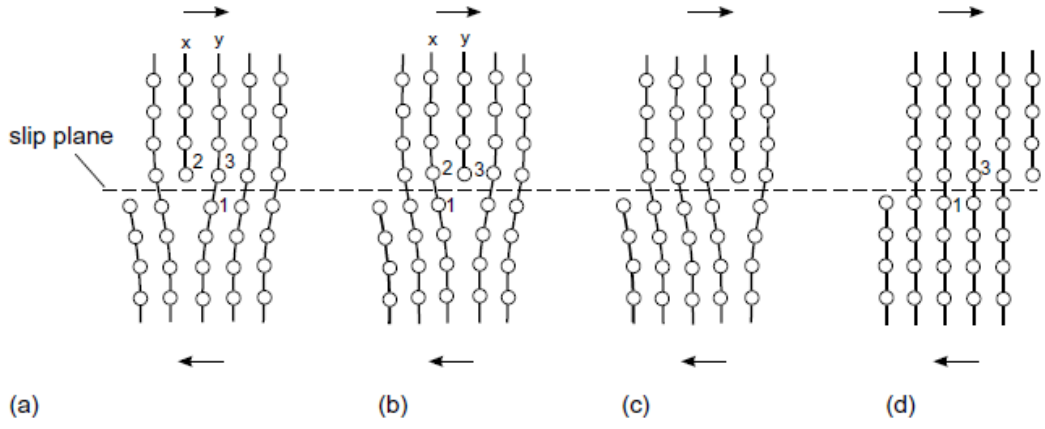


*Figure 13: Dislocation glide, an energy efficient mechanism. The arrows indicate the applied shear stress [20].*

The applied shear stress to overcome the lattice resistance and set dislocation in motion is called the Peierls - Nabarro stress and expressed in equation (1.2) [20].

$$\tau_P = \frac{2G}{(1-\nu)} \exp\left(\frac{-2\pi w}{b}\right) \tag{1.2}$$

where $w = \frac{d_{hkl}}{(1-\nu)}$ for an edge dislocation and $w = d_{hkl}$ for screw dislocation, $d_{hkl}$ the interplanar spacing, G is the shear modulus and ν is the Poisson's ratio.

The described mechanism is an energy efficient one, since the Peierls - Nabarro stress is considerably less than the theoretical critical shear stress (equation 1.1). Dislocation glide is a conservative type of movement as the dislocation moves within a surface, called slip plane, containing both the dislocation line and its Burgers vector.

Typically, slip planes are the most closely packed and most widely spaced crystallographic planes [20]. The slip direction is a direction in the slip plane with highest linear density and the shortest lattice vector (Burgers vector). The slip plane together with the slip direction establishes the slip system.

In polycrystal metals, dislocation glide is the most common mechanism by which plastic deformation occurs. Additional mechanisms as twining and grain boundary sliding also contribute to yielding [20]. However, single crystals deform only by slip and/or twining (Figure 14).

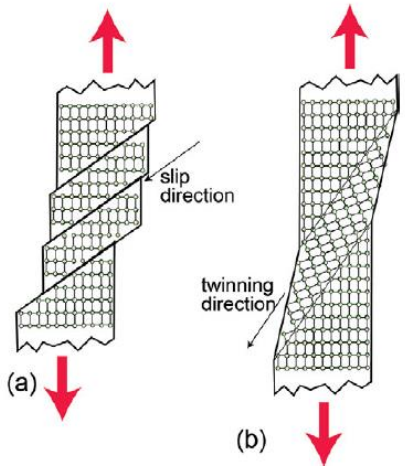


*Figure 14: Plastic deformation in mono crystals by either (a) slip or (b) twinning [26].*

## 4. Slip in Body Centered Cubic (BCC) metals

In BCC crystals the closest packed directions are the ones along the cube diagonals and correspond to the <111> crystallographic directions. Thus, the shortest lattice vector (Burgers vector) is $\vec{b} = \frac{1}{2} < 111 >$ and its magnitude is $b = \left|\vec{b}\right| = a\frac{\sqrt{3}}{2}$ , with a the lattice parameter of the cubic unit cell.

There are no true closed packed planes in BCC metals and in the literature, dislocation slip is reported on {110}, {112} and {123} plane families. These planes in combination with the <111> directions define a total of 48 possible slip systems (Figure 15).

- 6 {110} planes having each 2 <111> directions combine to 12 slip systems
- 12 {112} planes each one with a <111> slip direction result in 12 slip systems
- 24 {123} slip planes each one with a <111> slip direction establish the remaining 24 slip systems

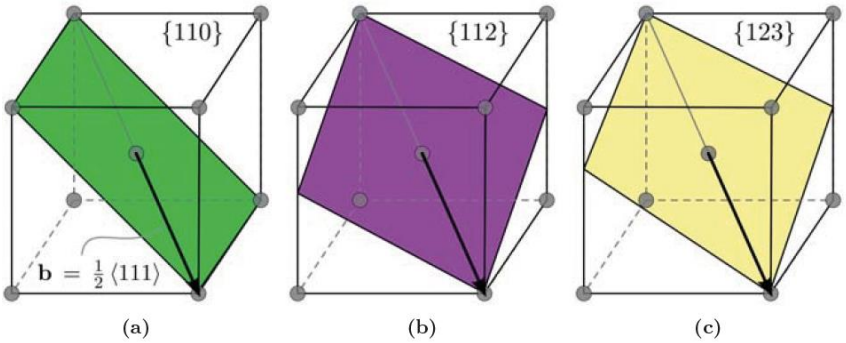


*Figure 15: The three slip plane families in the BCC crystal [27].*

It is generally considered that temperature determines the activation of slip planes [28–30]. The {110} and {112} are activated at lower temperatures, while {123} planes need higher temperatures. For $\alpha$-Fe, slip on {123} planes at ambient temperature are not commonly reported [31], [32], since there is not sufficient thermal energy to activate dislocation slip.

### *4-i. The Schmid's law*

During a tensile or compressive test of a single crystal, the applied load (F) causes a normal stress (σ). The resolved shear stress (RSS), is the shear component of the externally applied stress, acting on a crystallographic slip plane and along its slip direction (Figure 16).

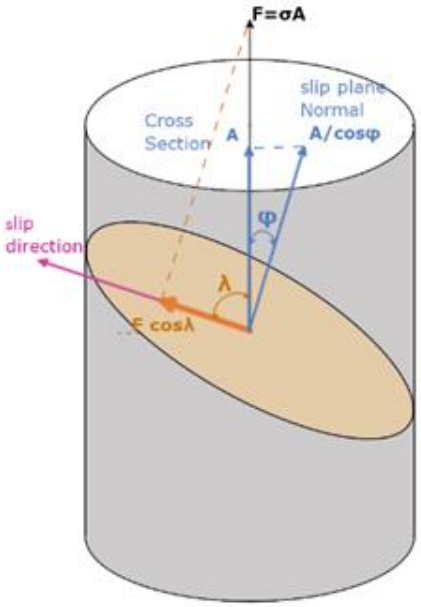


*Figure 16: Illustration of the relations between slip direction, slip plane and loading at tensile testing.*

The resolved shear stress (τ) is expressed by the equation (1.3), where φ is the angle between the loading direction and the normal of the slip plane and λ is the angle between the loading direction and the slip direction

$$\tau = \frac{F\cos\lambda}{\frac{A}{\cos\varphi}} = \frac{F}{A}\cos\varphi\cos\lambda \tag{1.3}$$

The product $cos\,\varphi\,cos\,\lambda$ is known as the Schmid factor and its maximum value is 0.5 ,when both $\varphi$ and λ angles are equal to 45 degrees [33].

When the resolved shear stress becomes large enough, the crystal starts yielding as the dislocations begin to move on the slip plane. The minimum shear stress required to initiate dislocations' gliding is the critical resolved shear stress ($\tau_{CRSS}$). The stress that corresponds to the onset of yielding is the yield stress ($\sigma_Y$). The Schmid's law is expressed by the equation:

$$\tau_{CRSS} = \sigma_Y \cos\varphi\cos\lambda \tag{1.4}$$

From the Schmid's law it is obvious that between the available slip systems, the one that reaches first the critical resolved shear stress and hence is activated first, is the system with the most favorable orientation and consequently with the greatest value of Schmid factor.

This system is the primary slip system. Eventually, as the load increases, more slip systems will reach the $\tau_{CRSS}$ and then they will start operating as well.

*4-ii. The apparent slip plane and the maximum resolved shear stress plane (MRSSP)*

The structure of the BCC lattice ensures that there are 12 possible slip planes intersecting along the same <111> direction (three {110}, three {112} and six {123}) increasing the chances of the screw dislocation to cross slip. Cross slip is observed as wavy and ill-defined slip steps on the polished sample surface [20] (as in Figure 17 and Figure 18) and the apparent slip plane usually is non-crystallographic, meaning that the wavy slip traces do not correspond to a low-index plane. Actually, this is the result of the composite slip between the slip planes where dislocations glide by elementary steps [34], [35].

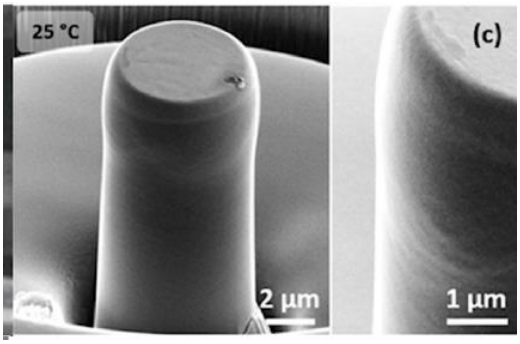


*Figure 17: Deformation with delocalized wavy slip lines suggesting cross slipping of dislocations [29]*

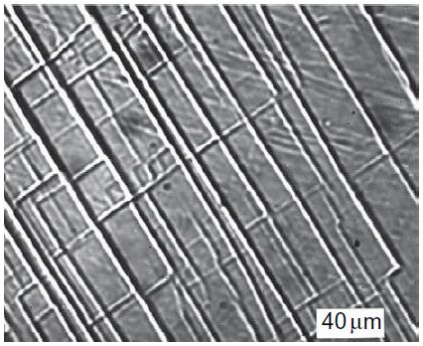


*Figure 18: Cross slip apparent on the surface of a single crystal silicon-iron [18]*

The plane for which the resolved component of the stress acting parallel to the Burgers vector (pure shear stress) maximizes, is the maximum resolved shear stress plane (MRSSP). Atomistic calculations of the glide of the screw dislocations have been performed [36–40] for defining the critical resolved shear stress (CRSS) for various orientations of the MRSSP.

The MRSSP can be calculated using equation (1.5) [28], where $m^{\alpha}$ is the slip direction, $n^{\alpha}$ the normal of the slip plane (n), l is the direction of the applied stress, φ is the angle between the loading direction and the normal of the slip plane and λ is the angle between the loading direction and the slip direction.

$$\cos\varphi\cos\lambda = \frac{l.n^{\alpha}}{\|l\|.\|n^{\alpha}\|}.\frac{l.m^{\alpha}}{\|l\|.\|m^{\alpha}\|} \tag{1.5}$$

The MRSSP orientation is characterized by the angle that it makes with the $(\bar{1}01)$ plane (Figure 19). This angle (denoted χ) is defined as positive, when the MRSSP is between $(\bar{1}01)$ and $(\bar{1}10)$, and negative when it is between $(\bar{1}01)$ and $(0\bar{1}1)$. Due to crystal symmetry, it is only necessary to consider -30 ≤χ ≤ 30°, having in mind that orientations corresponding to positive and negative angles χ are not equivalent.

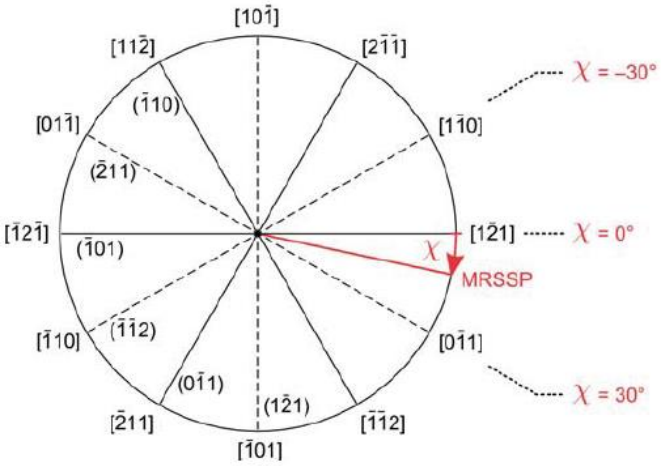


*Figure 19: Orientation of the {110} and {112} planes and the MRSSP of the [111] zone. Owing to the crystal symmetry, $(\bar{1}\bar{1}2)$ & $(\bar{2}11)$ define the boundaries [27].*

At the boundaries of this range lie the $(\bar{1}\bar{1}2)$ & $(\bar{2}11)$ planes, which are the twinning planes for the BCC crystal.

It is important to note that when χ<0 the nearest {112} plane to the MRSS is the $(\bar{2}11)$ plane and shearing occurs in the twining sense, while for χ>0 the $(\bar{1}\bar{1}2)$ is the nearest plane and shearing occurs in the anti-twining sense, even if the actual slip plane is not of the {112} family [20].

It must be clarified that dislocation movement in twining or anti-twinning sense is irrelevant to the twining deformation [27] that can occur either at high strain rates or at low temperature.

### *4-iii. Deviation of the BCC metals from the Schmid's law*

The Schmid's law is based on two main assumptions. The first is that the $\tau_{CRSS}$ is independent of the slip system and the sense of slip. The second is that only the shear stress resolved on the activated slip system causes the plastic deformation while all other components of the stress tensor have no influence.

For FCC and HCP metals, Schmid's law is confirmed to be valid. However as early as in 1928, the distinctive behavior of BCC metals was reported by Taylor while investigating α-Iron and β-Brass [41].

BCC metals exhibit a strong dependence of the yield and flow stress on the temperature and strain rate [20], [29], [42] and also BCC single crystals deviate from the Schmid's law, since $\tau_{CRSS}$ depends on both crystal orientation (reflected by the twinning/anti-twinning asymmetry) and also on the loading direction (resulting in the tension/ compression asymmetry).

### 4-iii.A. Twinning / anti-twinning asymmetry

The twinning / anti-twinning asymmetry is an intrinsic property of the BCC lattice and crystal symmetry must be reflected on the core structure of the screw dislocation [43], [44].

As first perceived by Hirsch in 1960 [36], [44], [45], the screw dislocation lies along a three-fold symmetry axis of the BCC structure. Hence, its nonplanar and three-dimensional core is spreading into non-parallel planes of the <111> zone.

In the BCC lattice, the <111> directions impose a three-fold rotation symmetry, so the slip planes along the same [111] direction are non-mirror symmetric (with the exception of the {110} planes where the <101> 2-fold (diad) axis assures this symmetry).

The symmetry – asymmetry of the {110} and {112} planes is illustrated in Figure 20 where planes normal to [111] are represented. This asymmetry, related to the sense of shearing, makes dislocations easier to move on the twinning direction than in the anti-twinning direction of {112} planes.

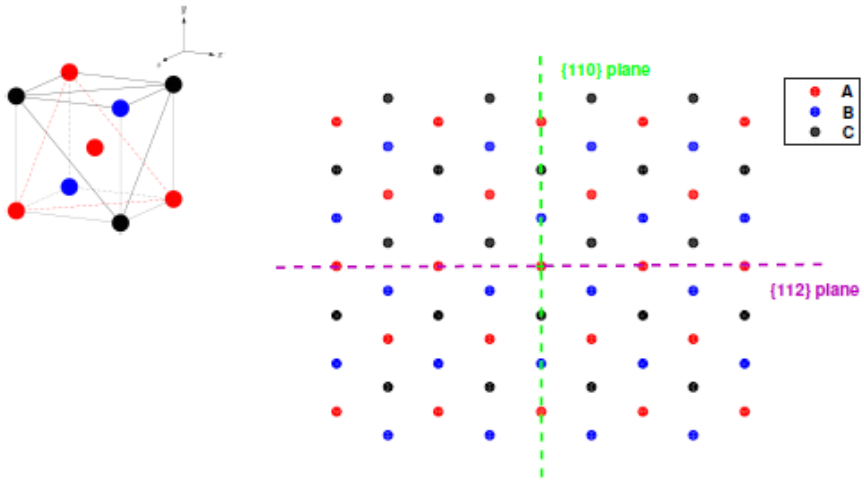


*Figure 20: Arrangement of atoms for a BCC lattice in planes A, B and C, normal to [111]. The stacking sequence has mirror symmetry with respect to (110) planes but not for the (112) ones [28].*

In Figure 21 - a, a detailed view of the stacking sequence ABCDEF of the {112} planes for a two-unit cell, is illustrated. On a (110) projection, the traces of the {112} planes with the associated atoms reveal their stacking sequence (Figure 21 – b). If e.g., an E layer is displaced by 1/6 $\left[\bar{1}11\right]$ it becomes a C layer and repetition of this translation on the successive plane leads to the ABCDCBA sequence, the stacking sequence of a twinned crystal. Clearly, displacement at the opposite sense, 1/6 $\left[1\bar{1}\bar{1}\right]$, moves E to D and eventually creates the anti-twinned, high energy, structure.
Therefore, 1/6 <111> translations are asymmetric for the twinning and anti-twinning sense, on {112} planes of the BCC crystals [20].

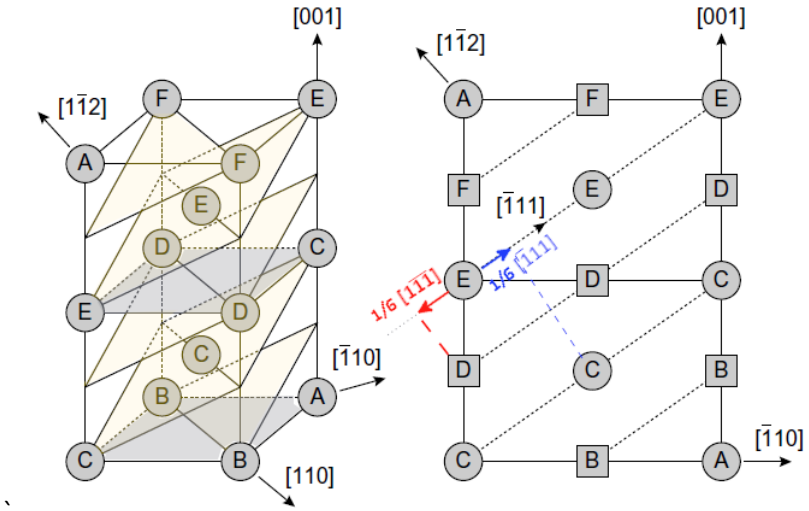


*Figure 21: Stacking sequence ABCDEF of the {112} planes for a two-unit cell [after 20].*

Simulation data for α-iron [42] (Figure 22) clearly demonstrate that $\tau_{CRSS}$ varies with the orientation of the MRSSP (black dots). Note that only pure shear stress was applied, so that stress tensor had only the components acting parallel to the slip direction.

$$\sum_{\sigma} = \begin{bmatrix} 0 & 0 & 0 \\ 0 & 0 & \sigma \\ 0 & \sigma & 0 \end{bmatrix} \tag{1.6}$$

According to Schmid law, dislocation glide is activated when the shear stress resolved in the glide plane reaches the Peierls stress in this plane. The yielding on the maximum resolved shear stress plane (MRSSP), measured as a function of the angle χ, should comply with the relation:

$$\tau_p(\chi) = \frac{\tau_p^0}{\cos(\chi)} \tag{1.7}$$

Where $\tau_p^0$ ,is a material constant, expressing the Peierls stress on the reference $(\bar{1}10)$ slip plane (where the angle χ is 0) [46], [47].

Thus, the resolved shear stress, calculated according to Schmid law should vary as $\cos^{-1}\chi$ (dashed line in Figure 22) [36]. The necessary pure shear stress, $\tau_{CRSS}$ ,parallel to the slip direction in the MRSSP (circles), does not coincide with the predicted by Schmid law, being lower that the predicted at χ<0 which corresponds to the twinning region and higher at χ >0 at the antitwinning region.

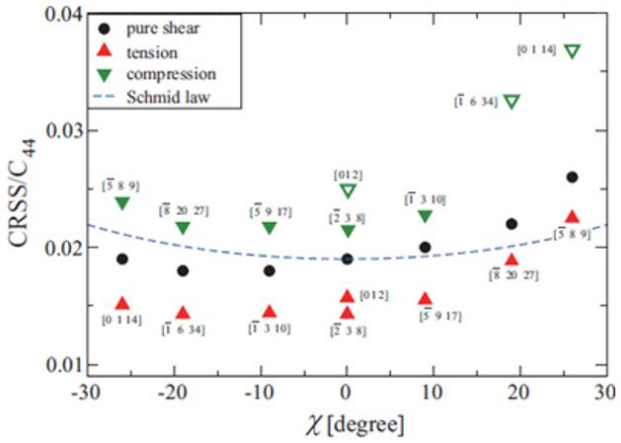


*Figure 22: Dependence of the CRSS on the orientation of the MRSSP (χ) for loading by pure shear stress parallel to the slip direction in the MRSSP (circles), in tension (up-triangles) and compression (down-triangles for α-Iron [42].*

This dependence of the $\tau_{CRSS}$ on χ, points out the breakdown of the Schmid law. As Ito and Vitek state [36], the reason for the non-Schmid behavior is that prior to the dislocation motion the nonplanar core is modified by the applied stress (Figure 23) and these modifications are dependent on the orientation of the MRSSP.

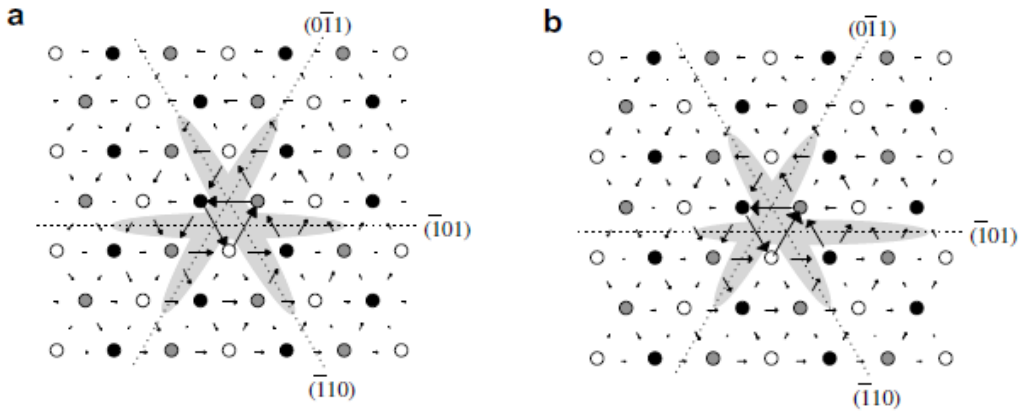


*Figure 23: Differential displacement map illustrating the structure of the 1/2[111] screw dislocation core in molybdenum (a) Relaxed (b) After the application of shear stress in the $(\bar{1}01)$ plane (χ = 0). The circles (black, gray, white) correspond to the positions of atoms in the three adjacent (111) planes (as in fig 19). The lengths of the arrows connecting atoms represent the relative displacements of two neighboring atoms parallel to the Burgers vector [48].*

## 4-iii.B. Tension/compression asymmetry

The second asymmetry of slip is an extrinsic effect related to non-glide stresses that are always present at mechanical testing of material carried out using uniaxial loading.

Only the pure shear stress parallel to the slip direction can move the dislocations while the other components of the stress tensor affect the shape of the screw dislocation core. Gröger [39] states that these changes of the dislocation core are solely caused only by shear stress acting perpendicular to the slip direction <111>.

Thus, adding the non-glide stress perpendicular to the slip direction in the MRSSP (denoted as τ), the stress tensor changes:

$$\sum_{\sigma} = \begin{bmatrix} -\tau & 0 & 0 \\ 0 & \tau & \sigma \\ 0 & \sigma & 0 \end{bmatrix} \tag{1.8}$$

In tension $\tau_{CRSS}$ is lower (up triangles, see Figure 22) than in pure shear stress (black dots) since the positive (τ) non-glide stress perpendicular to slip direction modifies the shape of the core (Figure 24(a)) making easier the glide on $(\bar{1}01)$). But in compression, the negative non-glide stress (τ) alters the shape of the core (Figure 24 (b)) so that it extents to the other {110} planes making harder to glide (down triangles in Figure 22) and for large enough compression load the glide can change from $(\bar{1}01)$ to one of these planes. Note that τ is always positive for tension and negative for compression [37].

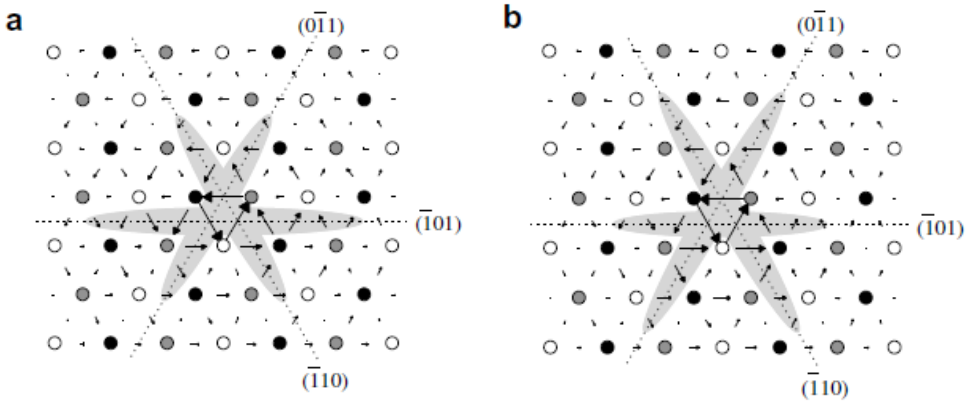


*Figure 24: Differential displacement map illustrating the structure of the 1/2[111] screw dislocation core in molybdenum when applying of shear stress perpendicular to the slip direction for a) positive stress (tension) and b) negative (compression). The circles (black, gray, white) correspond to the positions of atoms in the three adjacent (111) planes (as in fig 19). The lengths of the arrows connecting atoms represent the relative displacements of two neighboring atoms parallel to the Burgers vector [48].*

Edge dislocations have planar core structure, on either {110} or {112} planes [20], [44], [49]. They glide at much lower stress having low lattice friction and high mobilities. Unlike the screw dislocations, they are insensitive to non-shear stresses.

## 5. Dislocation multiplication

The most common mechanism of dislocation multiplication is the Frank-Read mechanism (Figure 25). On a dislocation segment pinned at both its ends on obstacles, (e.g., as precipitates, dislocation junctions, etc.) the resolved shear stress imposes a force τb per unit length that makes the dislocation to bow out. If the resolved shear stress is higher that Gb/2R, it cannot be balanced by the force due to the curvature of the dislocation line (where 2R is equal to the distance L between the pining obstacles) (Figure 25 - B). Then the dislocation exceeds the critical configuration of a semicircle, becomes unstable and continues to expand (Figure 25 – C, D). The two segments (Figure 25 - E) eventually will contact and annihilate, thus

creating an outer loop that keeps expanding and also, a regenerated straight dislocation segment between the obstacles, that restarts the dislocation multiplication process (Figure 25 - F).

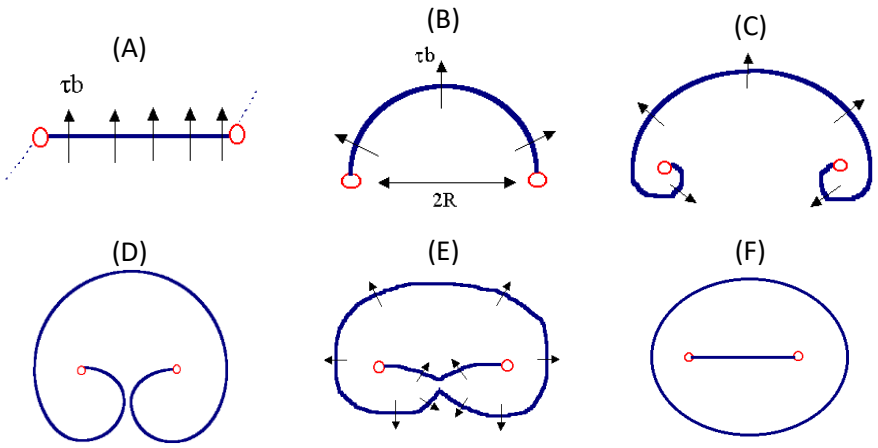


*Figure 25: Frank - Read source mechanism: (A) The resolved shear stress acts on a pinned dislocation segment (B)-(E) evolution of dislocation bowing until its opposite segments touch each other & annihilate [19].*

So, for the initiation of their motion, dislocations must break free from the Frank-Read sources under the "unpinning" stress $\tau_{FR}$=Gb/L. Frank-Read sources with larger pinning distance (larger L) operate at lower stress and that is the reason why they are the first that generate dislocations. To overcome the lattice resistance and start propagating on their slip planes, dislocations require a shear stress to be applied. This stress, due to the periodic structure of the crystal lattice, is the Peierls-Nabarro stress (lattice friction stress) in a pure metal.

## III. Strengthening mechanisms in metals

As a dislocation moves, it might encounter various defects (short range interactions) and will also be affected by the stress field due to defects and other dislocations, located at longer distances (long range interactions). As a result, the stress needed for the dislocation to continue its movement increases, resulting in elevating the material's hardness.

### 1. Work or forest hardening

Dislocations interact with each other even when they are not in contact, through the stress fields they create in the crystal lattice. Consequently, the stress needed for dislocations to start yielding or to maintain plastic flow is affected by the presence of other remote dislocations (forest dislocations). In 1934, Taylor [50], [51] introduced the model of work-hardening (Equation (1.10)), proving forest hardening to be proportional to the square root of the dislocation density.

In fact, there are different types of interactions between the dislocations on different slip systems. Figure 26 illustrates the dislocation interactions for BCC metals; they can be classified in four types.

- Junction interaction: both slip plane and slip direction of two slip systems are not the same. Most dislocation interactions are of this type.
- Collinear interaction: the interaction between dislocations sharing the same slip direction but gliding on two slip planes.
- Self-interaction: this interaction occurs between dislocations on same slip system.
- Dipolar interaction: the dislocations are on the same slip plane but glide at different slip directions. In the case of BCC metals, this can only occur in {110} <111> slip systems that are the only having two slip directions on a single {110} slip plane.

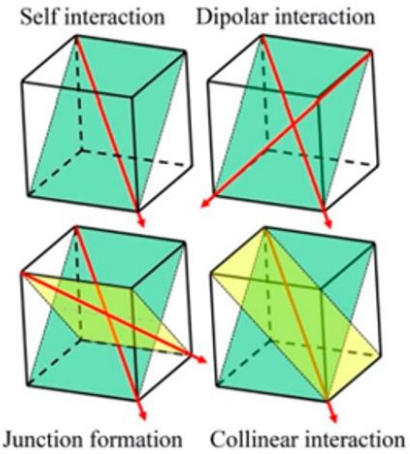


*Figure 26: Four types of interactions between slip systems in a BCC unit cell [32].*

Their contributions to the critical stress are assumed to be quadric [20], [52] and can be combined in the form:

$$\tau_{forest}^{i} = Gb\sqrt{\sum_{j} a^{ij}\rho^{i}} \tag{1.9}$$

where $\tau^i$ is the stress for slip system i, $\rho^j$ the dislocation density in slip system j and $a^{ij}$ coefficient of interaction between systems i and j.

Equation (1.9) can be simplified in the form of the well-known Taylor equation:

$$\tau = \alpha_{forest} Gb\sqrt{\rho_d} \tag{1.10}$$

where $\alpha_{forest}$ is the Taylor coefficient (the average interaction coefficient) and $\rho_d$ the total dislocation density.

## 2. Solid solution strengthening

In general, metals contain additional elements such as impurities and alloying elements.

The solubility limit is the maximum concentration up to which the atoms of the additional element(s) remain in solid solution in the metallic crystal. For concentrations lower than the solubility limit, solid solution hardening is observed. This is the strengthening effect due to the resistance to the motion of the dislocations caused by the additional elements' atoms, which are dispersed randomly inside the metallic lattice.

When a solute atom resides as a substitutional atom on a lattice site, it causes relatively small and non-shearing (purely hydrostatic) misfit strain and is thus interacting with only edge dislocations (or the edge components of mixed dislocations).

On the other hand, the presence of interstitial atoms (such as carbon and nitrogen atoms in steels) creates higher stresses with dilatational and even deviatoric (shape changing) effect in the lattice, interacting with all kinds of dislocations. As a result, higher solid solution hardening is observed.

Interstitial atoms have elevated mobility and at a temperature just high enough, they migrate towards the core regions of the dislocations and form dense atmospheres of solute atoms (Cottrell atmospheres - Figure 27), even at very low solute concentration. At too high temperature, dissolution of these atmospheres occurs.

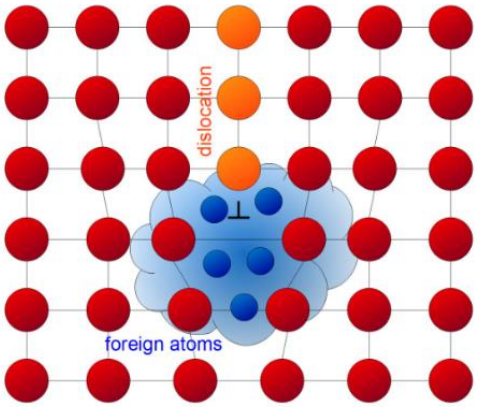


*Figure 27: Cottrell atmosphere: Impurity atoms (in blue) in the vicinity of an edge dislocation (in orange) [53].*

In the presence of Cottrell atmospheres, an elevated stress, the upper yield point of the stress-strain curve, is needed for dislocations to overcome their resistances. Then, dislocations are no longer pinned and move at lower stress (lower yield point) causing a specific strain (Luder's Strain) before stress must be increased again. This is observed in irradiated FCC and in both unirradiated and irradiated BCC metals (Figure 28).

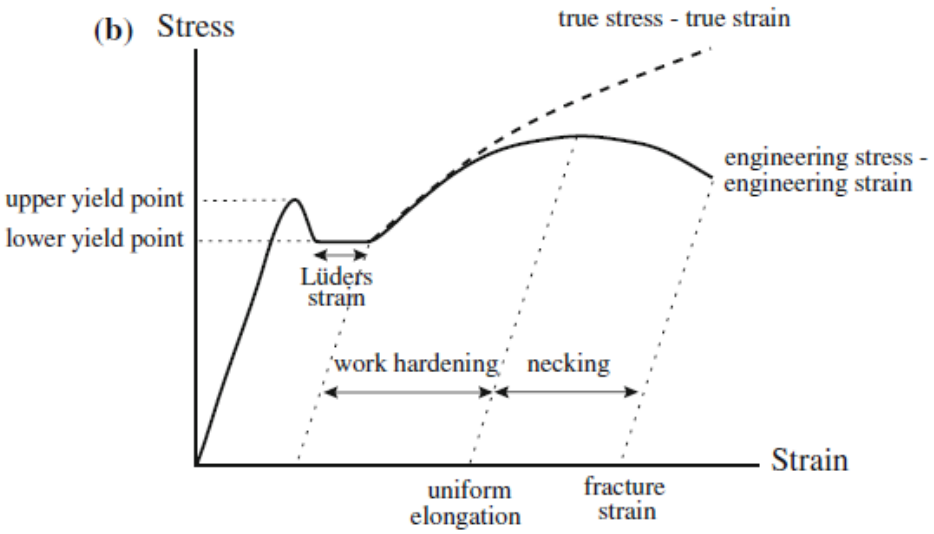


*Figure 28: Stress-strain curves of a uniaxial tensile test of a BCC metal [23].*

At a special temperature range, in which the rate of dislocations' propagation matches the interstitials' mobility velocity, the escaping dislocations from the Cottrell atmospheres are captured again by the post diffusion accumulations of the interstitials, reactively leading to the serrated shape of the stress-strain curve (Figure 29). This phenomenon is termed the Portevin – Le Chatelier effect.

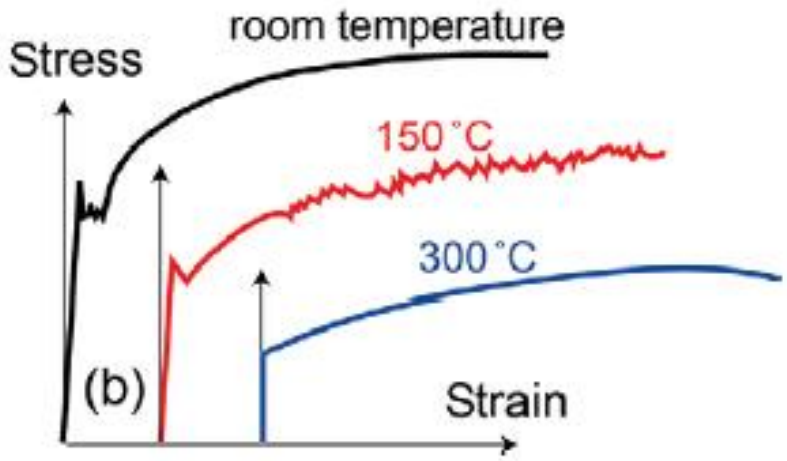


*Figure 29: At elevated temperature the Portevin – Le Chatelier effect can be observed at Stress strain curves (red curve) [26].*

## 3. Precipitation hardening

One of the oldest metallurgical methods to elevate an alloy's yield strength is precipitation hardening, also called age hardening.

This is a heat treatment which typically consists of three stages [26], [54], [55]. First, the formation of a homogenous single-phase solution, followed by rapid cooling or quenching of the alloy to the ambient temperature. This leads to a supersaturated solid solution in the host metal. Then the aging stage takes place, which is the most time-consuming stage, allowing diffusion to form an array of solute-rich clusters. This process is driven by thermodynamics since the alloying elements' concentration is above their equilibrium solubility limit.

As the precipitation process proceeds, the precipitates go through a series of stages, with changes in the size, form, density and composition. At first, the nucleated nanometric precipitates are in the under-aged state, coherent with the host lattice and dislocations can shear them. The precipitation hardening (Figure 30) increases with the annealing time obtaining a maximum value, caused by still coherent but larger precipitates that have reached the peak-aged state and that might be either still shearable or dislocations bypass them by looping, if they have become big enough. The final state is the over-aged state, the size of the precipitates increases but their number density and the precipitation hardening they cause, both decreases. The precipitates are now impenetrable by the dislocations (Orowan precipitates).

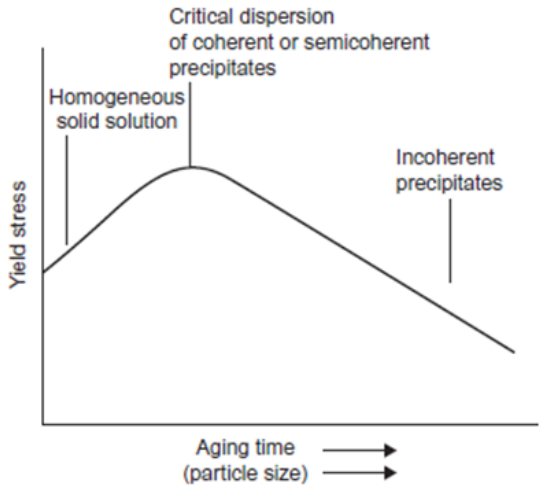


*Figure 30: Age hardening of aluminum alloy: yield stress vs aging time [56].*

Another similar hardening method, involving particles, is the dispersion hardening. We refer to dispersion hardening, when particles stable at high temperature (usually oxide particles) are introduced in the metallic lattice, e.g., oxide dispersion strengthened (ODS) steels manufactured with thermomechanical treatment of pre-alloyed oxide powders.

Depending on the way dislocations interact with precipitates, precipitates are classified in two main types.

1. Unshearable precipitates

Dislocations are unable to pass through unshearable precipitates (Figure 31). In this case, a dislocation bypasses the precipitate by forming a loop around it (Orowan looping). The loop formation starts when the dislocation lines become parallel, having the same Burgers vector and opposite line senses and so they are attracted to each other. This happens when the angle between the dislocation lines is at 0-degree, since they are parallel, and the force acted from the precipitate is the maximum. As the dislocation lines eventually come together, they annihilate at the meeting point, forming a loop around the precipitate.

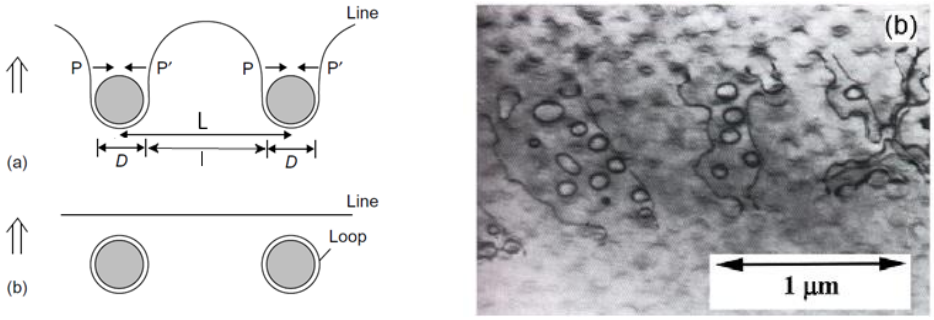


*Figure 31: (Left) (a) Dislocation interacting with Orowan precipitates of diameter D , having a distance L between them (b) The dislocation bypasses the precipitates and leaved a loop around them (modified from [20]) (Right) a TEM micrograph showing dislocation loops in a Ni-based superalloy [26].*

Following pinch-off, the dislocation is free to continue along its glide plane until it encounters the next precipitate, and the process repeats itself. The precipitates are left with a dislocation loop surrounding them, which presents a stronger obstacle to the next dislocation that comes along.

Classically, using the dislocation line tension and assuming randomly distributed impenetrable precipitates, the precipitation hardening is:

$$\tau_{orowan} = Gb\sqrt{N_D D} \tag{1.11}$$

where $N_D$ the number density and D the size of the precipitates

In 1973 Bacon, Kocks and Scattergood (BKS), considered that "*In reality a dislocation is not an elastic string with a well-defined line tension because it will interact with itself due to its own stress field*" [57]. They introduced self-stress interactions between different sections of the dislocation and considered the size of the obstacle. The modified precipitation hardening equation becomes:

$$\tau_{BKS} = \left( \frac{\ln(2\bar{D}/b)}{\ln(l/b)} \right)^{3/2} \frac{\ln(l/b)}{2\pi} Gb\sqrt{N_D D} \tag{1.12}$$

where l is the free distance between the precipitates (l=L-D with L the center-to-center precipitates distance) and $\bar{D}$ is the harmonic mean of the obstacle size and spacing $\bar{D} = lD / (L + D)$ .

2. Shearable precipitates

Unlike the Orowan unshearable precipitates, a dislocation breaks through the shearable objects. The finite precipitates strength is accounted by its relative strength $a_{obs}$ to the unshearable precipitates ,making the precipitation hardening (often termed dispersed barrier hardening) [23] :

$$\tau_{obs} = a_{obs} Gb\sqrt{N_D D} \tag{1.13}$$

Classically, the relative strength is reflected to the bowing angle θ, just before dislocation cuts through the precipitate

$$a_{obs} = \cos(\theta) \tag{1.14}$$

Equation (1.15) formulates the precipitation hardening according to Friedel's geometric considerations, about the random distribution of the precipitates.

$$\tau_{obs} = \alpha_{obs}^{3/2} Gb\sqrt{N_D D} \tag{1.15}$$

Russell and Brown (1972) [58] studying Cu precipitates in Fe, proposed an explanation of the obstacle strength of such shearable 'soft' precipitates, attributing it, rather arbitrarily, to the difference of the shear modulus between precipitates and matrix.

Recently, Monnet et al. (2019) [52], [59] presented their multiscale model of crystal plasticity, which uses the concept of obstacle shear resistance. The specific resistance stress $\Omega_{obs}$ is acting as a friction stress only inside the precipitate. Dislocations need an effective shear stress more than $\Omega_{obs}$ to propagate inside the precipitate. Precipitates having specific resistance stress $\Omega_{obs}$ , that exceeds the maximum threshold value of 4.5GPa ( $\Omega_{\infty}$ ) are unshearable and dislocations bypass it with the Orowan mechanism. For the shearable precipitates the ratio $\Omega_{obs}/\Omega_{\infty}$ corresponds to the relative obstacle strength. According to this model, the precipitation hardening is given by:

$$\tau_{obs} = \left( \frac{\Omega_{obs}}{\Omega_{\infty}} \frac{\ln(2\bar{D}/b)}{\ln(l/b)} \right)^{3/2} \frac{\ln(l/b)}{2\pi} Gb\sqrt{N_D D} \tag{1.16}$$

## 4. Strengthening due to the material's size

The mechanical properties of polycrystalline materials are well known to be affected by the size of the grains that consist of them. The yield strength ($\sigma_y$) increases inversely proportional to the square root of the grain size. This is formulated in the well-known Hall-Petch equation:

$$\sigma_y = \sigma_i + k_y d^{-1/2} \tag{1.17}$$

where $\sigma_i$ is the friction stress opposing dislocation motion in the slip plane, k is a constant and d is the grain size.

In single crystals, mechanical testing at the at micro and nano scale, has revealed that the yield strength increases as the size of the test specimen is reduced [60–70]. This "smaller is stronger" phenomenon is attributed to dimensional constrains as the sample size decreases that alter the underlying deformation mechanisms involved in dislocations generation and motion.

***Regimes of deformation***

Current theories for deformation of single crystals can be associated to three dimensional regimes [60], [70], [71], as schematically illustrated in Figure 32. The boundaries of these regimes are not yet exactly established in literature, since they are highly dependent not only on the smaller dimension of the sample but also on the initial dislocation density of the material. Only as an indication, we can consider that the dislocation starvation regime is for the very small dimensions up to about 300 nm, while the bulk-like regime typically extents from a few microns and above.

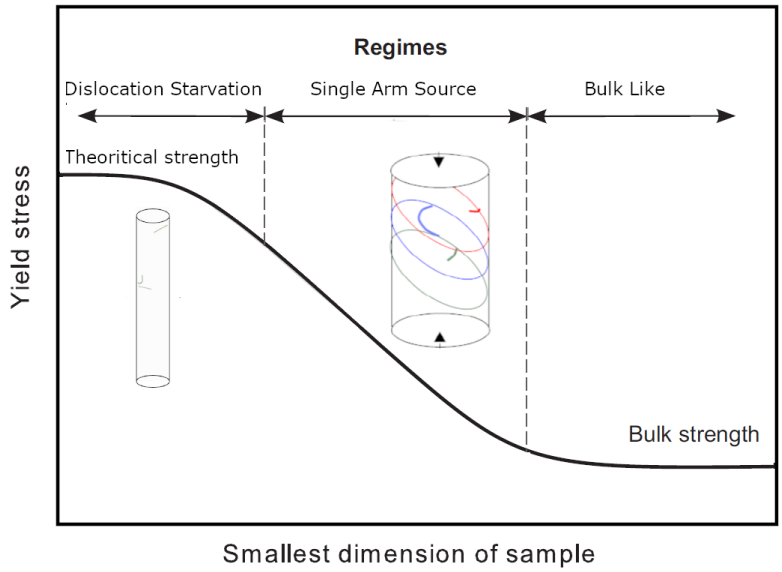


*Figure 32: Schematic indicating the regimes of the plastic deformation mechanisms as a function of the sample smallest dimension.*

1) The dislocation starvation (DS) regime

Ordinary, plastic flow in bulk materials is sustained by the multiplication of moving dislocations from sources, as typically the Frank–Read source. Gliding dislocations interact with each other, and eventually further dislocation multiplication occurs also by double cross-slip.

If the sample dimensions are small enough and the dislocation density is low ($<10^{12}$ $m^{-2}$), then the moving dislocations reach and annihilate at the nearby sample surface before having the chance to multiply. This leaves the crystal in a dislocation starved condition where the mobile dislocations are not enough to accommodate the strain imposed by the externally applied load. Then very high stress is needed to produce new dislocations via a different mechanism as for example the dislocation nucleation from the surface of the sample. This "dislocation starvation" concept has been developed by Nix and Greer [61].

While experiments on FCC samples confirm this mechanism, BCC crystals of the same dimensions need less stress to deform [62], [63], [66] .This is attributed to the difference in dislocation behavior between the two types of crystals, as suggested by DD simulations (Figure 33).

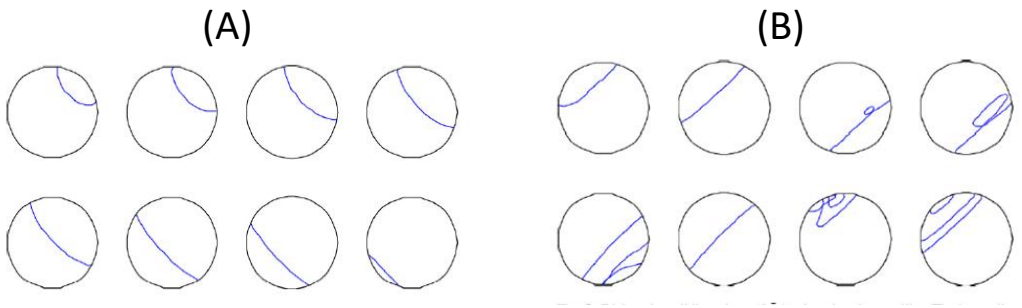


*Figure 33: Dislocation dynamics simulation of a dislocation gliding (A) in an FCC crystal and annihilates when reaching the surface leaving the pillar in dislocation starved condition (B) in a BCC crystal it emits additional dislocations creating strain hardening conditions [62].*

Weinberg [67] described a self-multiplication mechanism for screw dislocations which makes dislocation starvation unlike to occur in small dimensions BCC single crystals. Using, Molecular Dynamics (MD) and Dislocation Dynamics (DD) simulations [62], [67] the motion of a screw dislocation was studied. A mixed dislocation was introduced (Figure 34 - A) in the simulation BCC pillar on the (0 1 $\bar{1}$) glide plane. Soon, the much faster edge components escaped, leaving the screw dislocation gliding (Figure 34 - B). As it approaches the other side of the pillar, a cusp is formed from kinks nucleated on two different planes, meaning that the dislocation line at the two sides of the cusp is not precisely positioned on the same plane (Figure 34 - C). The cusp becomes a loop (Figure 34 - D) and (Figure 34 – E and F, arrows indicate the direction of dislocation motion) eventually the initial dislocation transforms into three dislocations, one of which is traveling in the opposite direction. The same mechanism re-appears when this dislocation reaches the surface.

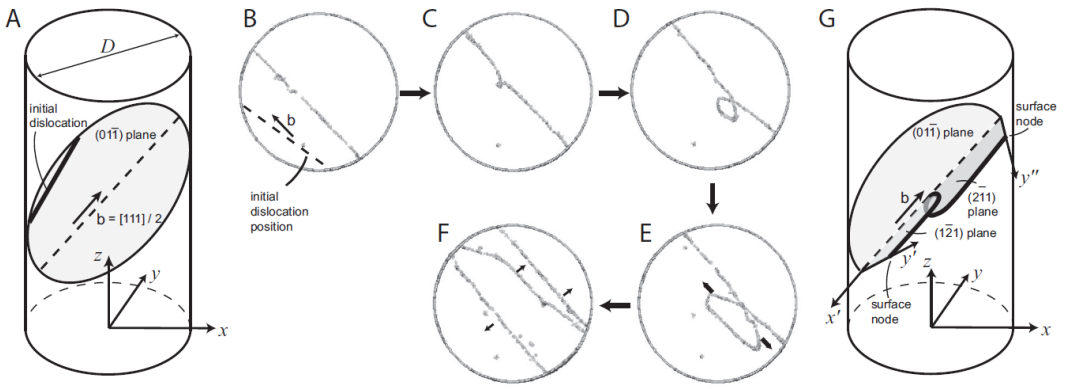


*Figure 34: BCC dislocation multiplication mechanism, for single crystal pillars at very small scales by molecular dynamics simulation [67].*

According to Greer et al. [62] , the entanglement of the dislocation segments inside the BCC pillar can operate in a similar manner to the forest hardening model of the bulk crystals.

Moreover, the authors experimentally confirmed that starvation mechanism is valid for FCC pillars having diameters at 300 - 800 nm, while does not apply for BCC pillars of the same diameters. The same conclusion reached Brinckmann et al. [61] testing 241 nm FCC (Au) and 240 nm BCC (Mo) pillars.

2) The single arm source (SAS) regime

When the dislocations source lengths and the smallest dimension of the sample are of the same order of magnitude, as the produced dislocations grow, their segments that reach the sample's surface annihilate. So, the sources appear as being single ended having a dislocation arm, which has its start at each source pin location and its end at the sample surface (Figure 35 - a). Since sources are randomly distributed, the length of the truncated single arms is also random. The weakest single arm source defines the critical stress needed to start plastic deformation. This source is the one with longest arm, due to the reverse relationship between the stress and the source length. This mechanism was proposed by Parthasarathy at al. [68] , who also quantified the stress needed for single arm source operation (Equation (1.18)).

$$\tau = \alpha \frac{Gb}{\bar{\lambda}_{max}} \tag{1.18}$$

where $\tau$ is shear stress, α is a geometrical constant, G is shear modulus, b is the Burgers vector modulus and $\lambda_{max}$ is the mean value of the length of the weakest single arm source, which is a function of the sample size.

Using the previous equation, the critical resolved shear stress ($\tau_{CRSS}$) in pure metal is expressed as in:

$$\tau_{CRSS} = \alpha \frac{Gb}{\bar{\lambda}_{max}} + \tau_0 + 0.5Gb\sqrt{\rho_{tot}} \tag{1.19}$$

where $\tau_0$ the friction stress and $\rho_{tot}$ the total dislocation number density.

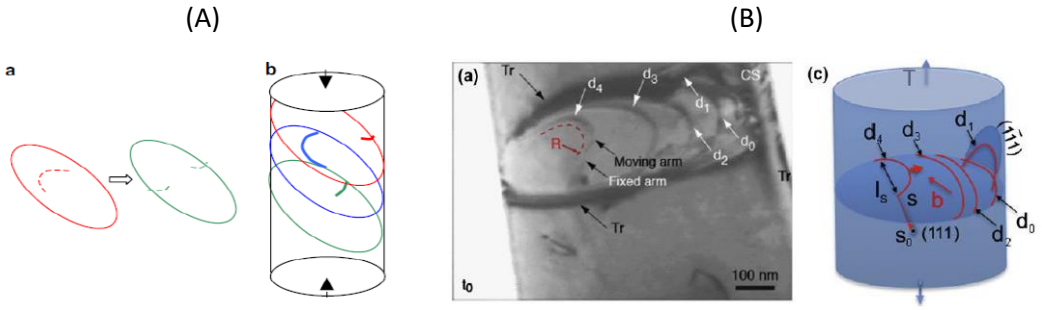


*Figure 35: (A) Schematic of single ended sources [68] (B) In situ TEM micrograph of an operating single arm source [69].*

3) The bulk-like regime

As sample dimensions increase, typically a few microns or larger, plastic flow is expressed by the well-established mechanisms of dislocation multiplication and interaction forming dislocation network structures (forest hardening mechanism). However, at the lower

boundary of this regime, the limited volume constrains dislocations' function, resulting in a strengthening effect [60].

## 5. Strain-Rate dependency in BCC metals

It is well established [72] in literature that the flow stress of BCC metals is sensitive to the imposed strain rate while loading. Unlike the FCC metals in which both edge and screw dislocations have planar cores, due to the geometry of BCC lattice the core of the screw dislocations has multi-plane structure. The glide of the BCC screw dislocations is believed to proceed by nucleation and propagation of kink-pairs, mechanism [20], [73], [74] responsible for the strong temperature and strain rate dependence of the flow stress.

Huang et al. [75], conducted in situ micro-compression test on α-Fe pillars with diameter from 200-1000 nm. They reported important size effect and also strain rate sensitivity that reduced with pillar size reduction as in Figure 36. The larger (1000 nm in diameter) pillars exhibit elevated strain rate dependence while the 200 nm were nearly insensitive to the strain rate. Additionally, both Wei [76] and Cheng [77], reported that for materials with ultrafine grains (UFG) or nanocrystalline (NC) microstructure, the BCC strain rate sensitivity was observed to decrease with decreasing grain size.

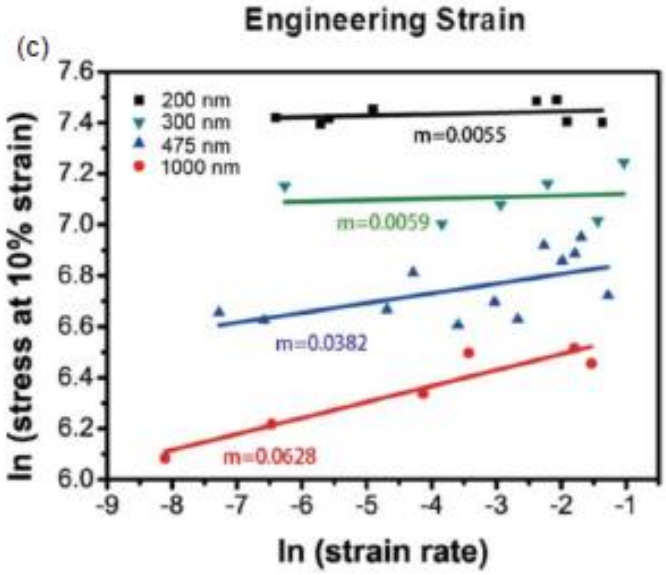


*Figure 36: Size dependence of the strain-rate sensitivity (quantified by the slope, m) of iron pillars [75]*

In this PhD study, taking into account the previously described mechanisms that affect the plastic deformation of the BCC crystals, we fabricated 3μm single crystal pillars for micromechanical testing (in-situ micro-compression).

We considered that this size is fairly big enough to avoid significant size dependent effects on the plastic deformation, that might possibly alter the measurement of their mechanical properties.

Irradiation is well known to modify the mechanical properties and alter the microstructure of the RPV alloys. In the next section are briefly reviewed both the mechanisms, acting under irradiation, resulting in altering the alloys microstructure and also the mechanical properties that are typically measured to evaluate the effect of the irradiation.

# IV. Irradiation effects in ferritic (RPV) alloys

## 1. Irradiation effects on chemistry and microstructure

Inside the core of the nuclear reactor, nuclear fission reactions occur when a thermal neutron (E≈0.25 eV) is captured by a fissile atom ($^{235}$U), as described by the following equation.

$$^{235}_{92}U + ^{1}_{0}n \rightarrow ^{236}_{92}U^{*} \rightarrow ^{A'}_{Z'}X + ^{A''}_{Z''}Y + 2.43\,^{1}_{0}n \qquad (1.20)$$

Note that 2 different elements are produced, one having a heavier mass than the other. On average, fission of $^{235}$U by thermal neutrons releases 2.43 neutrons and 200 MeV of energy. Each of these neutrons has energy about 2 MeV (fast neutrons) and must be slowed down by the moderator (which is water in the case of LWRs) in order to make a chain reaction easier to attain, generating fission events.

Only a few of these fast neutrons manage to reach the vessel steel of the plant. These neutrons are either captured by some atomic nucleus leading to activation or transmutation of the atom, or they collide with some atoms and displace them causing structural damage to the lattice of the material.

The extend of this damage is a function of crystallography of the steel, neutron fluence and flux, irradiation temperature and chemical composition [78].

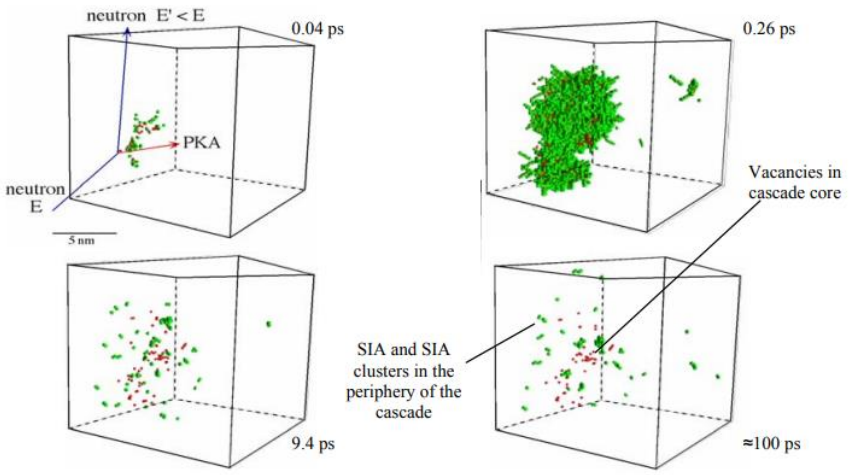


*Figure 37: Molecular dynamic snapshots of a displacement cascade in Fe created by high-energy neutrons. Time sequence starts from the initial collisions (upper left) illustrating the existing defects until after ≈ 100 ps when the thermal energy has dissipated from the cascade (lower right). SIA are represented as green dots and vacancies as red dots; lattice Fe atoms are not shown [79].*

During a collision between an incident neutron and a lattice atom (mostly iron), a part of the neutron's kinetic energy is transferred to the target atom (Figure 37-upper left). Typically, a 1 MeV neutron transfers up to about 70 keV [80] to the iron atom when colliding with it (frontal choc). In any case, if the transferred energy (T) is greater than the displacement threshold energy ($E_d$) of an Fe atom of the lattice (~ 40 eV) then the atom (called Primary Knocked Atom - PKA) is ejected from its crystalline site, thus generating there a vacancy (V). Further, as it is

displaced inside the crystal lattice it becomes at first a projectile that ends up as a self-interstitial atom (SIA) [81]. This vacancy and SIA pair is known as Frenkel pair. For sufficiently high transferred energy, the target atom that becomes a projectile, generates a branching, tree-like, distribution of displaced atoms termed displacement cascade (Figure 37 upper right)). This mechanism ends when the n-th recoil atom possesses an energy lower than $E_d$. These events take place within a time frame of only 10 ps, making their observation possible only via molecular dynamics simulations.

Most of the Frenkel defects will annihilate by recombination within some tens of ps. The remaining point defects that avoided the recombination, are mobile and they diffuse through the ferrite matrix at RPV operating temperatures, being the basic sources of the irradiation damage [79].

The SIA's will quickly cluster to form small mobile dislocation loops prior to their rapid long-range migration towards the sinks (unless they are strongly trapped by other defects or solutes). Vacancies, although less mobile than the SIAs, eventually diffuse too or combine in small, three-dimensional clusters (Figure 37 lower part).

Irradiation creates the elevated concentration of the point defects, well above the expected at thermal equilibrium, imposing a considerably increased diffusion rate. The accelerated diffusion of the point defects (and defect clusters) is known as Radiation Enhanced Diffusion (RED).

RPV steels can be considered as super-saturated solid solutions of solutes having very low solubility limit in iron, like Cu. Even the low Cu steels (less than 0.1% at Cu) are supersaturated since the Cu solubility limit is less than 100 appm at 290°C [79]. Thus, Cu precipitation is thermodynamically favored. Under irradiation conditions, as during RPV operation, the radiation-enhanced diffusion (RED) accelerates the thermodynamically possible precipitation and radiation-enhanced precipitation (REP) occurs.

But RPV steels, generally, contain elements as Mn, Ni, Si, P and Cr in concentrations lower than the solubility limit of the corresponding binary phase diagrams, and thus, they are undersaturated in terms of their bulk compositions. In this case, precipitation is not thermodynamically possible. Therefore, the formation of nanosized solute clusters under irradiation, is a result of a different mechanism, namely, the irradiation-induced segregation (RIS).

Under irradiation, the PDs are present at elevated concentrations and are migrating towards the defect sinks where they annihilate. Consequently, point defect flux is created towards the sinks.

Movements of the atoms inside a crystal lattice are mediated by the PDs. An alloying or impurity element may preferentially associate with one of the PDs. In that case, this association may lead to either enrichment or depletion of the solute elements at sinks.

For example, in the simple case of a binary system composed of 50 % A atoms and 50 % B atoms, a vacancy flux $J_V$ towards a sink is created, as result of the PD's concentration gradient. The vacancy flux is counterbalanced by an opposite flux of the A and B atoms so that $J_V=-(J_A+J_B)$. $J_A$ and $J_B$ are proportional to the vacancy diffusion coefficients of A and B. If $J_A > J_B$ as in Figure 38 (A), more A atoms are migrating away of the sink than B.

The concentration profile at the sink boundary (Figure 38 (B)) reveals that the boundary is enriched of B atoms and depleted of A. This vacancy-solute flux coupling is known as Inverse Kirkendall effect.

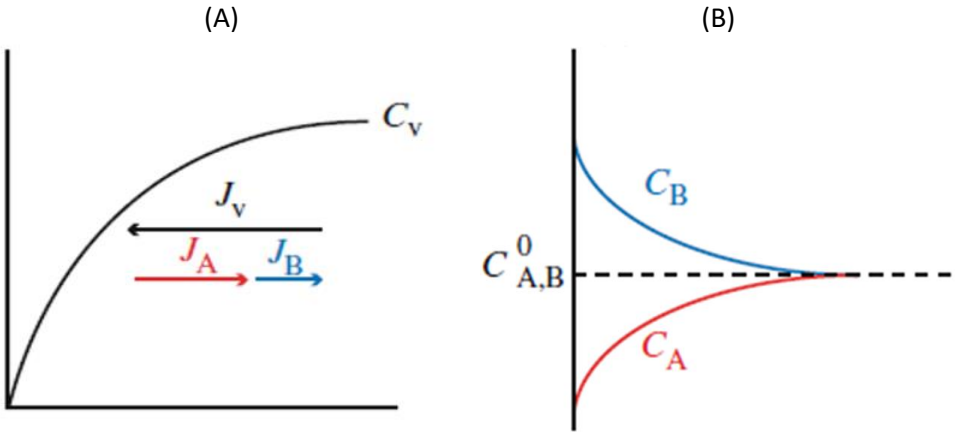


*Figure 38: (A) vacancy-solute flux coupling. Flux of vacancies is counterbalanced by the sum of solute fluxes (B) concentration profiles for A and B elements, indicating sink enrichment for B and depletion for A [25]*

On the other hand, since interstitials are actually A and B atoms, the flux $J_I$ is equal and in the same sense as the $J_A$ and $J_B$, ($J_I = J_A + J_B$). If the interstitial diffusivity of B element is greater than of the A, as in Figure 39, then the sink boundaries get enriched in B atoms and depleted of A.

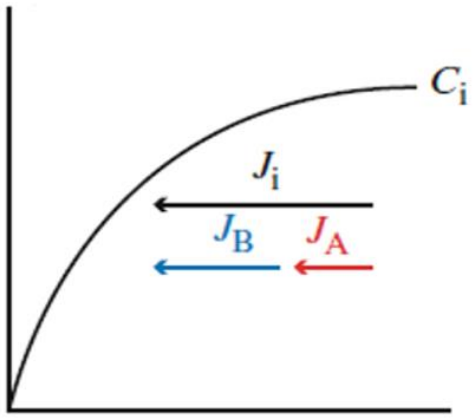


*Figure 39: Fluxes of interstitials migrating to a sink [25].*

In ferritic alloys, the small impurity atoms (as carbon, oxygen, nitrogen) are interstitials. Self-interstitials are only produced by irradiation and usually they exist in “dumbbell” configuration, that is two atoms sharing one lattice site. The <110> dumbbell is the most stable dumbbell configuration in BCC iron represented in (Figure 40).


*Figure 40: (A) Illustration of interstitials in the BCC lattice at <110> dumbbell configuration [25] (B) Solid sphere representation of BCC crystal unit cell (left) and the arrangement with a self-interstitial (right) [82].*

Big substitutional solute atoms may either combine with SIAs, forming 'mixed dumbbells' and then migrate with them by the interstitial drag effect or they can migrate by using the vacancy mechanism.

When stable enough solute-vacancy complexes are formed, then the solute atoms are transported in the same direction as the vacancies (Figure 41 - a), resulting in solute enrichment at the sinks. This mechanism of solutes transportation is referred as vacancy dragging.

For the binary A-B system, (Figure 41 - b) both vacancy and solute B flux lead to the sink direction, so in order to preserve lattice integrity, the flux of solute A is in the opposite direction, ($J_V + J_B = -J_A$).

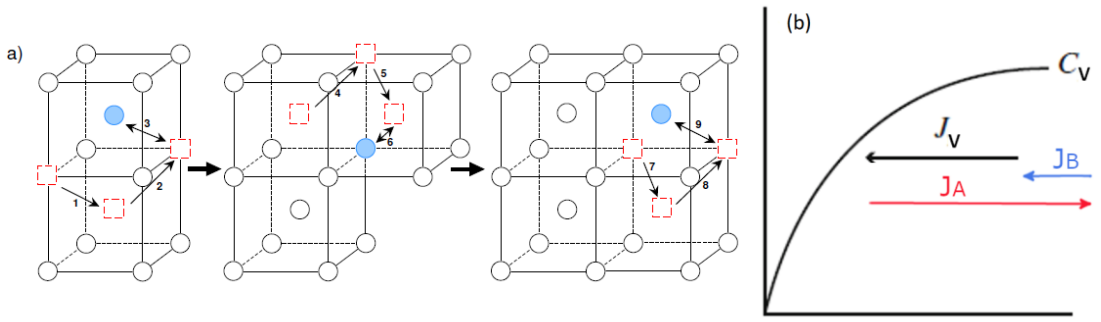


*Figure 41: (a) Correlated vacancy-solute migration producing "solute -vacancy drag" [81] (b) Element B forms stable enough solute-vacancy complexes and thus is "dragged" by vacancies' flux resulting in B enrichment at the sink.*

Unlike the binary alloy, RPV steels contain a variety of solute elements as Mn, Ni, Si, P and Cr that can form stable enough point defect-solute complexes, that is complexes that their dissociation energy is greater than the migration energy [73].

The ability of vacancies and self-interstitials to carry solute atoms to PDs sinks that may act as nucleation sites for solute cluster formation is currently under research, using various, modeling methods as ab initio calculations and object kinetic Monte Carlo simulations [83], [84]. Messina et al. [85] suggest that P, Mn, and Cr diffuse preferentially by mixed dumbbells with P being the fastest diffuser, while Cu diffuses exclusively by vacancies. Atoms of Ni and Si use both mechanisms in competition, with the dominant mechanism to depend on the relative concentration of the vacancies and interstitials ($C_V/C_I$) (Figure 42).

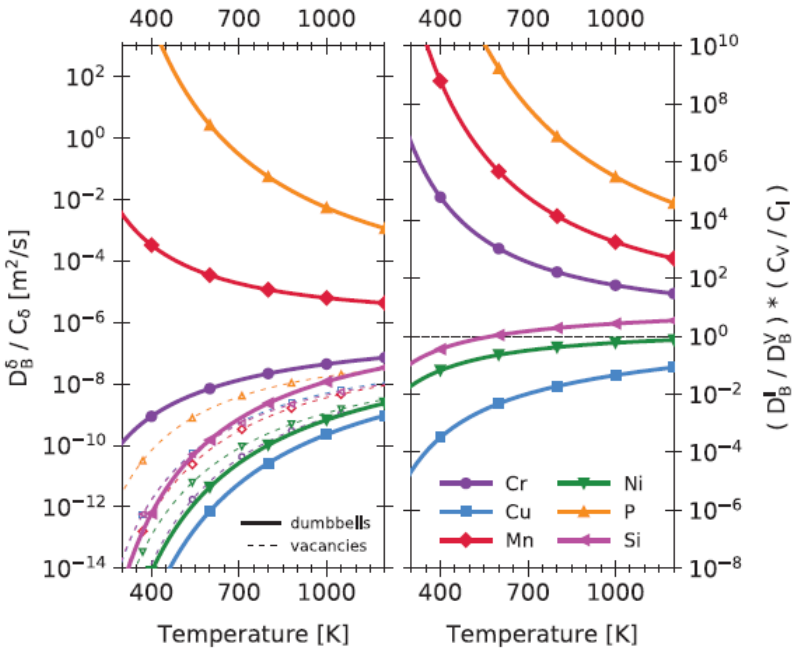


*Figure 42: (left) Solute tracer diffusion coefficients for the dumbbell mechanism (continuous lines) and the vacancy mechanism (dashed lines), divided by the corresponding defect concentration. (right) Ratio between the diffusion coefficients of the two mechanisms, showing that P, Mn, Cr are transported preferentially by dumbbells, and Cu by vacancies [85].*

So, the kinetic coupling between the fluxes of the PDs and solutes may cause radiation-induced segregation (RIS), resulting in migration of the solutes either towards or away of discrete defect sinks, through mechanisms that include the inverse Kirkendall effect, vacancy-solute and self-interstitial-solute complexes drag [85–89]. In turn, RIS can modify the microstructure of an initially homogenous undersaturated alloy causing the nucleation and growth of solute clusters at these sites, resulting to precipitate formation if the local solute concentration is elevated above the solubility limit, named radiation induced precipitation (RIP) or precipitate dissolution if the local concentration drops below it.

At the same time an opposite solute concentration gradient is developed inducing back diffusion of the segregating elements that balances the RIS and eventually a quasi-steady state [25] is reached.

## 2. Irradiation damage & Embrittlement of RPVs

Irradiation, at the microscopic scale, provokes the formation of nanofeatures that in turn alter the mechanical properties of the materials and is detrimental to RPV integrity [8], [11], [90]. The irradiation damage is classified in 3 broad categories [8], [12], [91–93].

- Solute segregation at grain boundaries.
- Matrix Damage (MD)
- Small Solute Clusters (CRPs/MNPs)

Macroscopically, irradiation damage is manifested either as hardening embrittlement, through matrix damage and solute clusters that harden the material and increase the yield

strength, or as non-hardening embrittlement through solute segregation on grain boundaries that can decrease the fracture strength.

*2-i. Microscopical manifestation of irradiation damage*

## 2-i.A. Non-hardening embrittlement

Segregation to grain boundaries (GBs) of embrittling impurities elements capable of causing non-hardening embrittlement, has been proved and quantified by several reliable techniques (Auger-Electron-Spectroscopy (AES), Field Emission Gun Scanning Transmission Electron Microscopy (FEGSTEM), and Atom Probe Tomography (APT)) [11], [90] (Figure 43).

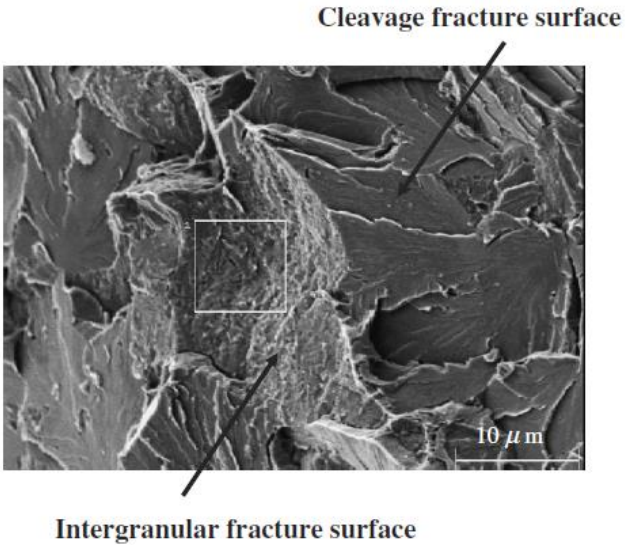


*Figure 43: SEM micrograph of fractured surface on steel with high phosphorus content ( 0.011 wt%) aged at 450°C for 3,000 h [96].*

Phosphorus (P) segregation to grain boundaries (GBs) can occur in the absence of irradiation under thermal ageing conditions, as during post-weld heat treatment of the fabrication process. During in service operation, irradiation damage severely enhances grain boundaries' segregation of P, which is believed to reduce grain boundary cohesion. [86]. Losch [97] proposed that phosphorus atoms at grain boundaries of steels reduce the boundary cohesion by attracting electrons from the surrounding iron atoms. Suzuki et al. [98] verified Losch's hypothesis in the case of α-Fe by studying the X-ray photoelectron spectroscopy of phosphorus segregated at grain boundaries and the Mössbauer isomer shift in an iron-phosphorus solid solution. This isomer shift primary depends on the number of outer electrons of the solute atom.

Phosphorus migrates to grain boundaries by flux coupling with irradiation-induced defects and thus it's dragged [10], [17]– [11], [95], [99], [100] to the sinks. According to Messina [81], P is the fastest solute diffuser for both vacancies & interstitial mechanisms and its dominant diffusion mechanism is the high mobile P-interstitial dumbbell (Figure 42). High-level segregation of P to grain boundaries can lead to intergranular fracture causing non-hardening embrittlement (illustrated in Figure 43). In this case transition temperature shift is proportional to the P segregation level, and takes place only when the P concentration at GBs exceeds a threshold value [96].

Practically, phosphorus [101] is the main impurity that threatens the integrity of eastern WWER-440/V-230 type RPVs while has negligible consequences for the low P containing western PWR vessels.

Sulfur has a similar behavior when segregated to grain boundaries. It embrittles iron more severely than phosphorus [98], [102] and thus being a liability for the high sulfur RPV steels (of the older plants) [103–107].

Segregation of C to grain boundaries [98], [102] displays a different behavior. Unlike P, GBs cohesion is enhanced by C. Since P and C are competitive segregants in steels, an increase in P coverage is expected to cause a decrease in C coverage. Presence of strong carbide-forming elements [108] such as Mo, Ti, V and the less strong Cr, Mn affects the availability of C for segregation.

## 2-i.B. Hardening embrittlement

Plasticity is expressed via the movement of dislocations. When dislocations are pinned, more stress is needed to endorse their movement, resulting in hardening of the material. Defects produced by irradiation impede dislocation movement ('pinning'), reduce the material's plasticity, harden it and embrittle it, threatening the RPV's integrity.

Odette, Lucas and co-workers developed the conventional two-feature model attributing embrittlement to two mechanisms, matrix damage and solute clusters formation [8], [56], [109].

### Matrix Damage

Knott and English [12] define matrix damage (MD) as "a generic term used to define a range of near atomic scale defect clusters introduced into the crystalline lattice during irradiation". According to Soneda and Nomoto [110] "*matrix damage is primarily related to the point defect clusters generated by neutron irradiation*".

Matrix Damage is classified into two subcategories. The Stable Matrix Damage or Features (SMD or SMF) which are thermally stable matrix defects that their contribution to hardening increases roughly proportionally with the square root of fluence $\left(\Delta\sigma_Y\sqrt{\phi t}\right)$ [25], and the Unstable Matrix Damage or Features (UMD or UMF) that are thermally unstable causing significant hardening only in high flux and low temperature irradiation conditions [56], [111].Their effect can be quantified by low temperature annealing recovery measurement (Figure 44).

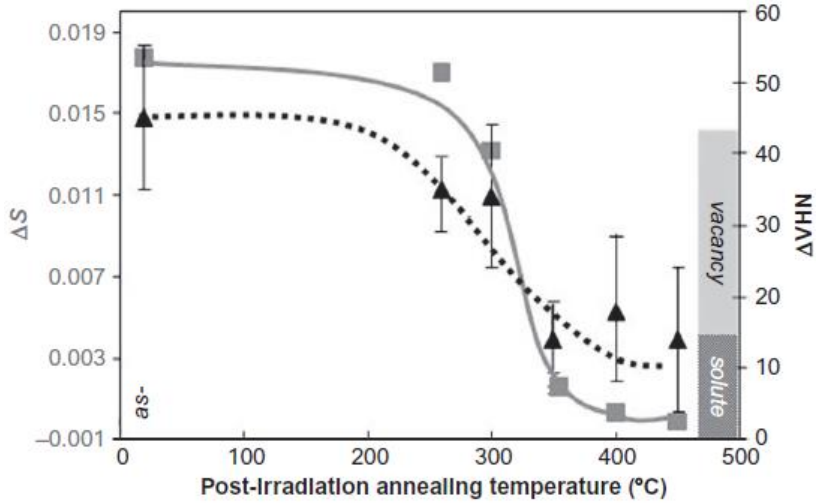


*Figure 44: 5-hour annealing of high Ni steel 124S285 (between 250°C and 350°C) reduces the Positron Annihilation Lineshape Analysis (PALA) ΔS signal, which is attributed to UMDs, since it is associated with vacancies. Although hardness (triangles) is also reduced, a significant amount remains which can be attributed to solute atom hardening* [56].

## Formation of Solute Clusters

During irradiation, two different small nanometric cluster families have been observed to form in the RPV steels and welds, depending on their nominal composition: Cu-rich clusters and Mn-Ni-Si clusters (MNSPs). Although there is not a strictly defined compositional limit separating them, meaning that the Cu clusters can contain small amounts of Ni, Mn and Si and vice versa, the difference in composition suggests different formation mechanism.

### *Cu-rich clusters*

Cu is an impurity element introduced in RPV steels from the scrap added to the melt or from the coating on weld wire [8]. Depending on the content of Cu, they are defined as “low-Cu” and “high-Cu” however their definition, in literature, is not precise and can vary. Usually [93], [99], [112–114] the limit at 0.1 % wt. Cu is chosen. In addition, when Cu content is less than 0.03-0.04 % wt. it is classified as “very low-Cu” [8].

As soon as the late 1960s [11], Cu was recognized as the primary factor threatening RPV safe operation. More than a decade later, Odette [115] considering the supersaturation of Cu in BCC Fe and the high vacancy concentration produced by irradiation, attributed the formation of Cu-rich clusters to RED. The correlation of high Cu content with elevated embrittlement and in turn to the formation of Cu-rich clusters under irradiation, had as result the fabrication of RPV steels and welds with low Cu content.

At first, the Cu-rich clusters were referred as Copper Rich Precipitates (CRPs) since it was thought that Cu precipitated and formed copper pure precipitates. This is observed in thermally aged RPV steels [12] that might contain larger precipitates (about 6nm in diameter) with crystal structure 9R which if grow to a diameter about 15 nm they transform to FCC [12], [116].

At in-service conditions, in commercial steels, small sized (typically about 2nm and up to 4nm) coherent clusters, soon appear during irradiation and their number density and volume fraction saturates at a maximum value, since the matrix gets depleted of Cu (Figure 45).

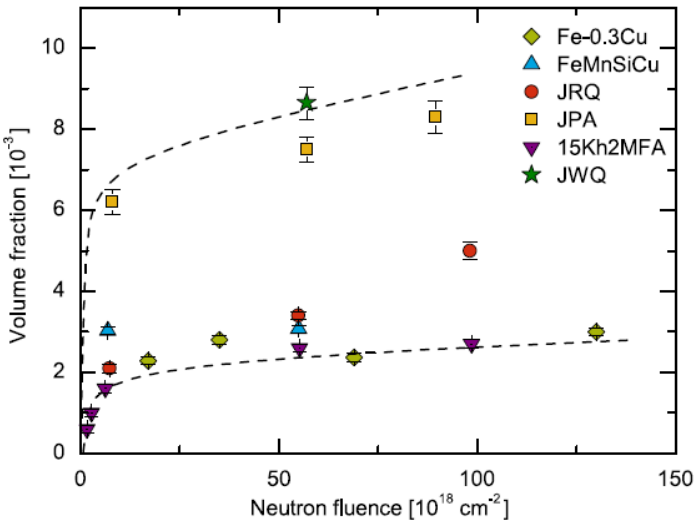


*Figure 45: For the high Cu (0.15-0.42 % wt.) model alloys, precipitates volume fraction corresponds to their bulk Cu nominal content. Typically, at low fluences the volume fraction increases very rapidly but afterwards it increases only slightly. The materials' content in Cu in % wt. is: 0.42 for the FeMnSiCu, 0.15 for JRQ, 0.22 for JPA, 0.22 for 15Kh2MFA and 0.26 for JWQ. The dashed lines indicate the authors' visual estimation of the upper and lower bounds [114].*

Many works [90], [109], [117–122] report that these clusters have reduced Cu concentration and important Fe content. These enriched with Cu clusters are referred in literature as Cu-enriched clusters (CECs). They are believed to be small enough to be crystallographically indistinct from the matrix [123], meaning that they are coherent solute clusters in the BCC solid solution.

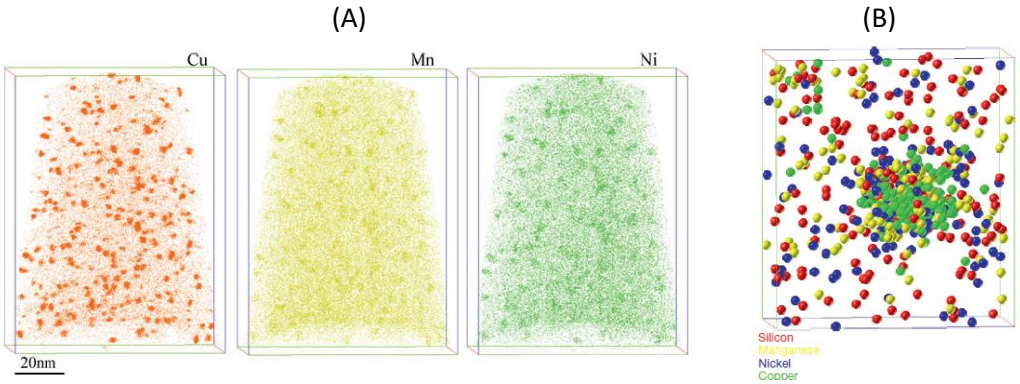


*Figure 46: (A) Typical atom maps in the irradiated FeCu0.8NiMn alloy [124] (B) Typical Irradiation-induced 3nm sized cluster [11]*

CRPs/CECs are enriched with Mn, Ni and Si, typically with a core-shell structure [11], [89], [125] (Figure 46). Cu, even in very low amounts, appears to catalyze the MNSPs formation [126–129] inducing co-segregation (or co-precipitation) and thus bypassing the barrier of the nucleation step. At low to medium fluencies [126], Cu has the dominant role on clusters' formation and the corresponding hardening. But at very high fluencies ($\phi t \approx 2.1 \times 10^{20}$ n/cm$^2$),

corresponding to more than twice the fluence acting on the RPV at 80 years operation, Cu has well before depleted from $\alpha$-Fe matrix so MNSPs have the dominant effect on clusters that have grown as an appendage (Figure 47) to the initial Cu-rich clusters [126].

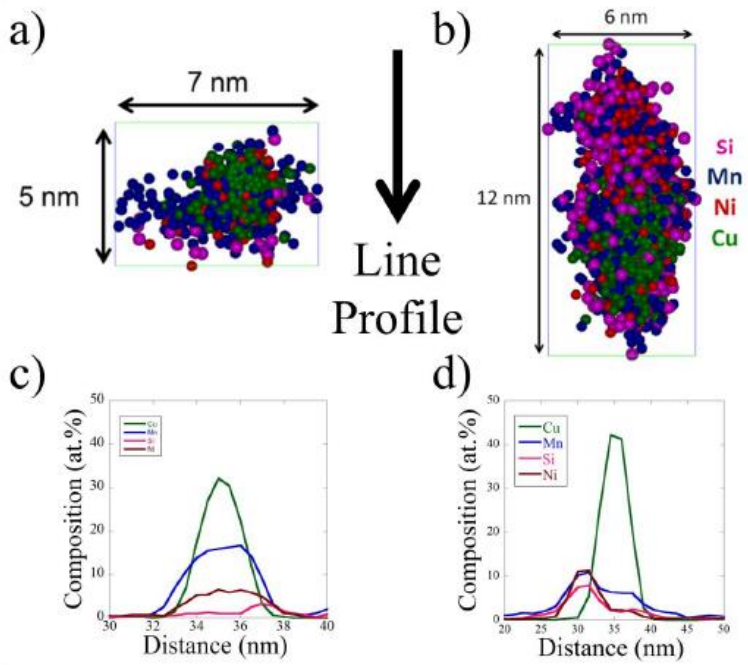


*Figure 47: APT maps and composition profiles of a smaller cluster (a & c) and a bigger cluster (b & d) with a Mn-Ni-Si appendage in high Cu-low Ni (0.18%) steel irradiated at very high fluence [126]*

*Mn-Ni rich clusters (MNSP or MNS or MNP)*

Odette in 1995 [93], [124] predicted the formation of Mn-Ni-Si precipitate (MNSPs) phases even in very low Cu steels that would nucleate but exhibit a delayed growth at high fluences (>>$10^{19}$ n/cm$^2$) and thus named them "Late Blooming Phases" (LBPs). Odette suggested that LBPs would contribute significantly to the embrittlement limiting the lifetime of RPVs [126]. Since then, an extensive research effort has been dedicated to investigate LBPs' safety considerations especially at high fluence typical of the extended RPVs' life conditions

Mn and Ni are important alloying elements added to strengthen the ferrite and to provide adequate mechanical properties to the RPV's steel [8]. Specifically, Ni is added to increase hardenability and toughness [56], but also increases irradiation sensitivity, enhancing hardening and embrittlement [90]. While addition of Mn increases hardenability and reduces the adverse effect of sulfur and P (by forming phosphides) but Mn in interaction with Ni increases the irradiation sensitivity.

Hence, RPV steels contain these elements in much larger quantities compared to the Cu impurity, which at the later or extended stages of reactors' lifetime are available to form MNSPs at very large number densities that in turn can cause significant hardening and embrittlement.

Contrary to Cu clusters, MNSPs clusters haven't been observed to form in thermally aged RPV steels at temperatures relevant to LWR operation. However, Lindgren [130] reported MNSPs to form on dislocations at the Ringhals, Swedish nuclear reactor's pressurizer, after 28 years of operation at 345$^{o}$C on a low Cu weld. At higher than LWRs operation temperatures and after very long-time thermal aging, Styman et al. [108], [131] reported thermally produced MNSPs located at grain boundaries in model RPV weld and recently, Jenkins et al. [129] observed MNSPs form in model RPV steels in the absence of other precipitates.

However, MNSPs are commonly observed by APT and Small Angle Neutron Scattering (SANS), following irradiation, in both very low Cu steels and Cu-depleted steels but also in Cu-free model alloys [126], [132]. At neutron irradiation elevated fluences between $10^{23}$ and $10^{24}$ n.m$^{-2}$ (E > 1 MeV), they are reported as small diameter (about 3 nm) clusters [90], [114], [128], [133], [134] with number densities at the range $10^{23}$-$10^{24}$ m$^{-3}$ typically increasing with fluence. Object kinetic Monte Carlo (OKMC) [83], [135], [136] simulations suggest that probably small immobilized interstitial loops are likely to be the precursors to MNSPs solute clusters formation, acting as their nucleation sites.

There is still a strong debate concerning whether MNSPs are thermodynamically stable precipitates, that is intermetallic phases like the G and Γ2 phase, formed as predicted by thermodynamic models [132] or they are irradiation induced and would not form and grow without the coupling of the PDs and solutes fluxes [81], [83], [85], [136]

### *2-ii. Macroscopical manifestation of irradiation damage*

RPV embrittlement is commonly studied by performing Charpy V-notch tests to define the energy needed to cause fracture of the specimens and therefore evaluating their toughness.

Materials such as the ferritic steels, have high toughness at high temperatures but they become brittle at low temperatures, presenting a Charpy curve shape like the green one in Figure 48(a).

On the Charpy curve, upper shelf is the part that corresponds to the temperature range at which the specimen breaks at higher energy. It defines the upper shelf energy (USE). At the upper shelf domain, ductile rupture (with plastic deformation) takes place while fragile rupture (without plastic deformation) occurs at the lower shelf part and at a lower energy (Lower Shelf Energy - LSE) .The temperature at the transition between those two shelfs is called the ductile to brittle transition temperature (DBTT) or the nil-ductility temperature (NDT) [25].

The interpretation of the Charpy test curve is difficult because its shape at the region of the ductile to brittle transition does not produce a distinct point corresponding to a specific value of absorbed energy (Figure 48 - a). So, the temperature shift at which a Charpy specimen breaks by (the conventionally defined) 41 J amount of energy is widely used as the transition temperature noted as $\Delta T_{41J}$ or $\Delta T_{30}$ (referring to 30 ft-lb) in US literature.

The curve of the irradiated specimen is shifted at higher temperatures and exhibits a drop in the upper shelf energy (USE) [25], [86] and a reduction in the slope of the curve. Was [25], [137] suggests that in irradiated ferritic steels, flow localization because of dislocation channeling is a probable contributing factor for the observed reduced ductility and USE.

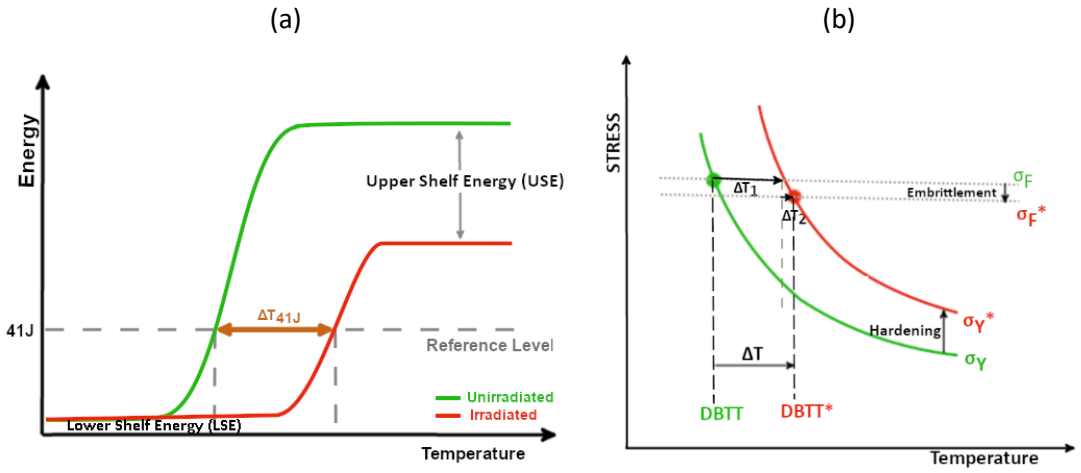


*Figure 48: (a) Charpy curve for an unirradiated and an irradiated material. (b) Modified Davidenkov diagram. DBTT defined by the intersection ($\sigma_y = \sigma_F$) between the yield stress curve and the fracture stress curve $\sigma_F$. Under irradiation the yield stress is increased causing a DBTT shift ($\Delta T_1$) and in the presents of non-hardening embrittling elements as P, an additional DBTT increase ($\Delta T_2$).*

In Figure 48 (b) the contributions to the transition temperature shift and the irradiation-induced stress increase are plotted as a function of the temperature. It can be seen that irradiation causes changes of the DBTT. In that representation, DBTT is defined by the intersection ($\sigma_Y = \sigma_F$) between the yield stress curve and the fracture stress curve $\sigma_F$. After irradiation, the yield stress curve $\sigma_Y$* is shifted upwards (high temperature), denoting the irradiation hardening and resulting in an increase in DBTT ($\Delta T_1$). Although, fracture stress ($\sigma_F$) is almost unaffected by irradiation [56], RIS segregation of embrittling elements as P at grains boundaries can decrease $\sigma_F$ to $\sigma_F$*creating an additional DBTT increase ($\Delta T_2$). So, when both mechanisms occur at the same time, a total combined shift of DBTT to higher temperature takes place ($\Delta T$).

Usually, Vickers microhardness tests are used instead of tensile/compression test because of being simple and need much smaller volumes of irradiated materials. A correlation (Figure 49) has been established to determine yield stress variation ($\Delta\sigma_Y$) from a change in microhardness ($\Delta H_V$) for ferritic steels:

$$\Delta\sigma_Y = 3.06\Delta H_V \tag{1.21}$$

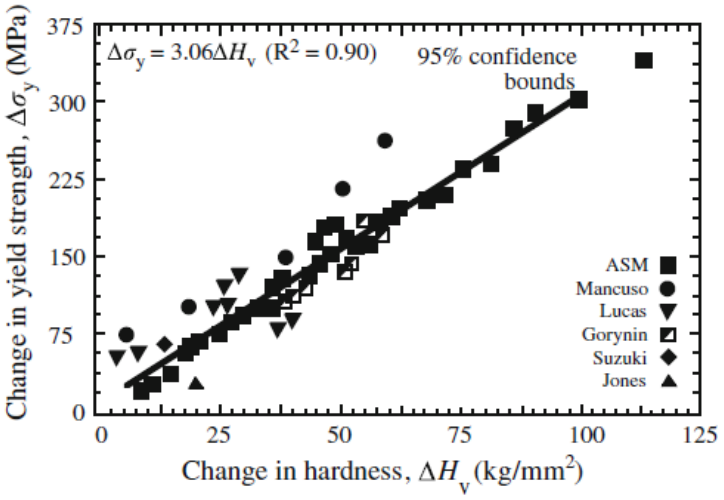


*Figure 49: The hardness-yield stress correlation derived from experimental data for ferritic steels [25].*

By monitoring the mechanical properties of the RPV steels under irradiation, it becomes clear that yield stress ($\sigma_y$) increases (hardening) with the increase of fluence (Figure 50), being higher for the high Cu steels at least up to the typical RPVs' end-of-life dose ( 1 – 3 x $10^{19}$ n $cm^{-2}$ for the US reactors [80]).

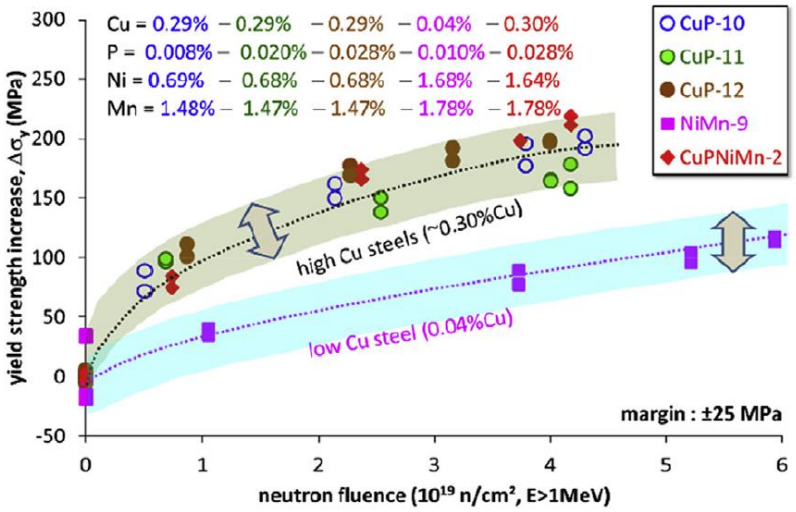


*Figure 50: Irradiation Hardening manifesting as yield strength increase in response to the neutron fluence applied to high Cu and low Cu alloys [138].*

The use of semi-mechanistic models [139–141], permitted to evaluate the contribution of each irradiation damage mechanism in hardening and embrittlement, as illustrated in Figure 51.

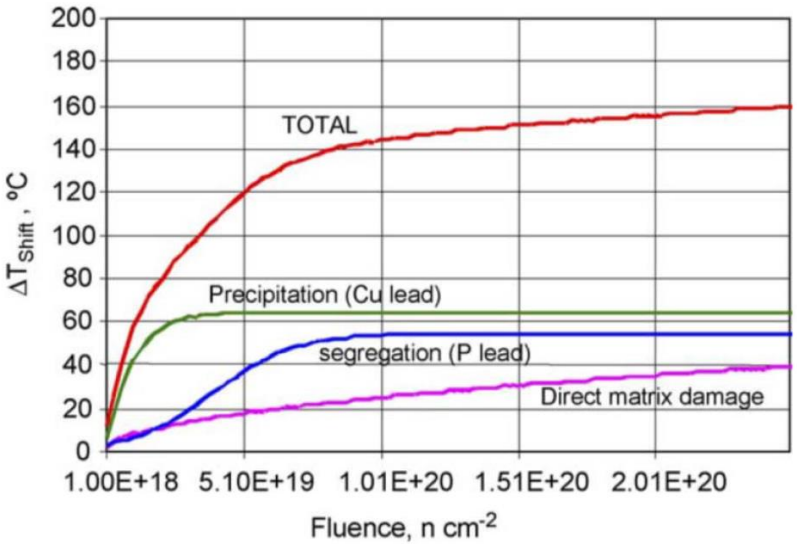


*Figure 51: Relative contribution of the irradiation damage mechanisms as determined by a semi-mechanistic analytical model [139].*

The Cu-precipitation contribution to the irradiation hardening increases rapidly with the increase of the neutron fluence and soon saturates at a plateau value since Cu is depleted from the matrix. The value of this saturation plateau is proportional to the nominal Cu content (Figure 52 - a), while the yield strength increase is inversely proportional to the irradiation temperature (Figure 52 - b).

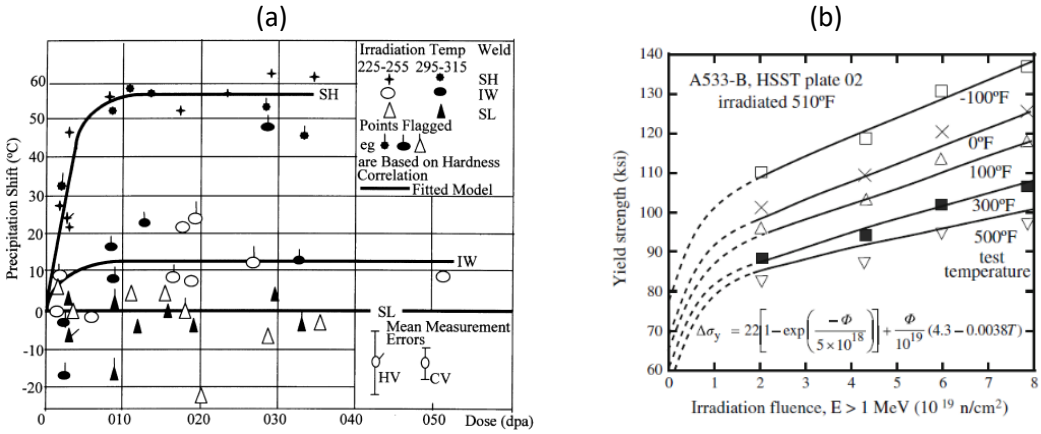


*Figure 52: (a) DBTT shift caused by Cu-precipitation as a function of fluence for low Ni PWR SAW welds deduced by subtracting fitted model predictions for the matrix shift from the total measured shift [12] (b) Influence of irradiation fluence on the yield strength of a A533-B steel for varying test Temperatures [25].*

## Summary

In this literature review chapter, at first, we presented some important information about the fundamentals of crystal structures, especially the BCC crystal structure. Crystal lattice imperfections as point, line, surface and volume defects have been briefly discussed, with emphasis on the dislocations, their motion and multiplication.

Since we aim to study the mechanical properties of the ferritic iron, we also reviewed the fundamentals of the plastic deformation of the BCC metals which is more complex compared to that of the FCC metals. The bcc metals have in total 48 possible slip systems and exhibit a strong dependence of the yield and flow stress on the temperature and the strain rate.

In addition, we have explained that during micromechanical testing (tensile or compressive tests) of BCC single crystals, the critical resolved shear stress deviates from the predicted from the Schmid's law, since bcc metals exhibit twinning / anti-twinning and tension/compression asymmetry, due to modification of the nonplanar three-dimensional core of the screw dislocation by the applied stress.

In the following part, we focused on the strengthening mechanisms that increase the necessary stress needed for the dislocation to continue its movement as it might encounter various defects (short range interactions) or be affected by the stress field due to other dislocations or defects, located at longer distances (long range interactions). Thus, we reviewed the forest hardening, the solid solution strengthening and the precipitation hardening. Additionally, we have reviewed the possible mechanisms, acting at small scale (micron or sub-micron scale) and affecting the mechanical behavior of BCC materials. These strengthening mechanisms include the dislocation starvation and the single arm source (SAS) hardening.

The next topic reviewed, is the irradiation effects on the microstructure in ferritic RPV alloys. Irradiation creates point defects (PDs) at increased concentrations that migrate towards sinks at accelerated diffusion rates known as Radiation Enhanced Diffusion (RED) which can accelerate the thermodynamically possible precipitation and thus radiation-enhanced precipitation (REP) occurs. On the other hand, coupling of solute elements and PDs fluxes might generate nanosized solute clusters even if it is not thermodynamically favorable. This mechanism is called radiation-induced segregation (RIS). If the local solute concentration becomes elevated above the solubility limit, precipitate formation might occur, named radiation-induced precipitation (RIP).

Irradiation damage is manifested at a microscopical scale either by the non-hardening embrittlement due to segregation to grain boundaries of embrittling impurity elements, or by the hardening embrittlement caused by the matrix damage and the solute clusters, acting as obstacles for dislocations motion. The formation of solute clusters in the RPV steels during irradiation was discussed, specifically the formation of clusters containing Cu and Mn-Ni. At the macroscopical scale, irradiation modifies the mechanical properties of the RPV steels which are typically evaluated by the degree of the increase either of ductile to brittle transition temperature or of the yield stress.

In the next chapter, we present the materials and review the techniques used in this research to detect, analyze, and quantify the irradiation induced microstructure and also to evaluate the impact of the irradiation damage on their mechanical properties.

# Bibliography


[1] “Nuclear Power Today | Nuclear Energy - World Nuclear Association.” https://world-nuclear.org/information-library/current-and-future-generation/nuclear-power-in-the-world-today.aspx (accessed Jul. 04, 2022).

[2] “Plans for New Nuclear Reactors Worldwide - World Nuclear Association.” https://world-nuclear.org/information-library/current-and-future-generation/plans-for-new-reactors-worldwide.aspx (accessed Jul. 04, 2022).

[3] “Nuclear Power in France | French Nuclear Energy - World Nuclear Association.” https://world-nuclear.org/information-library/country-profiles/countries-a-f/france.aspx (accessed Jul. 04, 2022).

[4] “Nuclear Power in Japan | Japanese Nuclear Energy - World Nuclear Association.” https://www.world-nuclear.org/information-library/country-profiles/countries-g-n/japan-nuclear-power.aspx (accessed Jul. 04, 2022).

[5] “Differences Between BWRs and PWRs.” http://large.stanford.edu/courses/2018/ph241/owusu2/ (accessed Oct. 22, 2019).

[6] “Modern Pressurized Water Reactor Safety Systems.” http://large.stanford.edu/courses/2017/ph241/kraus1/ (accessed Oct. 22, 2019).

[7] J. C. van Duysen and G. Meric de Bellefon, “60th Anniversary of electricity production from light water reactors: Historical review of the contribution of materials science to the safety of the pressure vessel,” *J. Nucl. Mater.*, vol. 484, pp. 209–227, Feb. 2017, doi: 10.1016/j.jnucmat.2016.11.013.

[8] N. Soneda, *Irradiation Embrittlement of Reactor Pressure Vessels (RPVs) in Nuclear Power Plants*. Elsevier, 2015. doi: 10.1016/C2013-0-17428-4.

[9] “Westinghouse Technology Systems Manual - Section 3.1 -Reactor Vessel and Internals.”

[10] G. R. Odette and G. E. Lucas, “Embrittlement of nuclear reactor pressure vessels,” *JOM*, vol. 53, no. 7, pp. 18–22, Jul. 2001, doi: 10.1007/s11837-001-0081-0.

[11] C. English and J. Hyde, “4.05 - Radiation Damage of Reactor Pressure Vessel Steels,” in *Comprehensive Nuclear Materials*, R. J. M. Konings, Ed. Oxford: Elsevier, 2012, pp. 151–180. doi: 10.1016/B978-0-08-056033-5.00087-2.

[12] J. F. Knott and C. A. English, “Views of TAGSI on the principles underlying the assessment of the mechanical properties of irradiated ferritic steel Reactor Pressure Vessels,” *Int. J. Press. Vessels Pip.*, vol. 76, no. 13, pp. 891–908, Nov. 1999, doi: 10.1016/S0308-0161(99)00068-X.

[13] “Advanced Nuclear Power Reactors | Generation III+ Nuclear Reactors - World Nuclear Association.” https://world-nuclear.org/information-library/nuclear-fuel-cycle/nuclear-power-reactors/advanced-nuclear-power-reactors.aspx (accessed Jul. 04, 2022).

[14] OECD and Nuclear Energy Agency, *Nuclear Power Plant Life Management and Longer-term Operation*. OECD, 2006. doi: 10.1787/9789264029255-en.

[15] GENIV International Forum, “Technology Roadmap Update for Generation IV Nuclear Energy Systems.”

[16] H. K. D. H. Bhadeshia, *Geometry of Crystals, Polycrystals, and Phase Transformations*, 1st ed. CRC Press, 2017. doi: 10.1201/9781315114910.

[17] Brandon, “Body-Centered Cubic (BCC) Unit Cell,” *Materials Science & Engineering Student*. https://msestudent.com/body-centered-cubic-bcc-unit-cell/ (accessed Jul. 03, 2022).

[18] W. D. J. Callister and D. G. Rethwisch, *Materials Science and Engineering*.

[19] Helmut Föll, “Defects in Crystals.” https://www.tf.uni-kiel.de/matwis/amat/def_en/

[20] D. Hull and D. J. Bacon, *Introduction to dislocations*, 5. ed. Amsterdam Heidelberg: Butterworth Heinemann, Elsevier, 2011.

[21] A. Paul and S. V. Divinski, Eds., *Handbook of solid state diffusion*. Amsterdam, Netherlands: Elsevier, 2017.

[22] “Minerals and the crystalline state,” *Minerals and the crystalline state*. https://www.open.edu/openlearn/science-maths-technology/minerals-and-the-crystalline-state/science-maths-technology/minerals-and-the-crystalline-state (accessed Jul. 03, 2022).

[23] G. S. Was, *Fundamentals of radiation materials science: metals and alloys*. Berlin ; New York: Springer, 2007.

[24] W. T. Read, *Dislocations in crystals*. McGraw - Hill Book Company Inc, 1953.

[25] G. Was, *Fundamentals of Radiation Materials Science, Metals and Alloys*, 2nd ed. Springer, 2017.

[26] T. W. Clyne and J. E. Campbell, *Testing of the Plastic Deformation of Metals*, 1st ed. Cambridge University Press, 2021. doi: 10.1017/9781108943369.

[27] B. R. S. Rogne, “Nanomechanical Testing of Iron and Steel.”

[28] D. C. Señas, “Multiscale modeling of the plastic behaviour in single crystal tungsten: from atomistic to crystal plasticity simulations.”

[29] H. Yilmaz, “Mechanical Properties of BCC Nanopillars,” University of Manchester, 2018.

[30] A. Seeger, “Experimental evidence for the {110} ↔ {112} transformation of the screw-dislocation cores in body-centred cubic metals,” *physica status solidi*, 2004.

[31] C. Du, F. Maresca, M. G. D. Geers, and J. P. M. Hoefnagels, “Ferrite slip system activation investigated by uniaxial micro-tensile tests and simulations,” *Acta Mater.*, vol. 146, pp. 314–327, Mar. 2018, doi: 10.1016/j.actamat.2017.12.054.

[32] D. Xie, B. Wei, W. Wu, and J. Wang, “Crystallographic Orientation Dependence of Mechanical Responses of FeCrAl Micropillars,” *Crystals*, vol. 10, no. 10, p. 943, Oct. 2020, doi: 10.3390/cryst10100943.

[33] E. Schmid and W. Boas, *Plasticity of crystals*. 1950.

[34] W. A. Spitzig and S. Keh, “THE EFFECT OF ORIENTATION AND TEMPERATURE ON THE PLASTIC FLOW PROPERTIES OF IRON SINGLE CRYSTALS”.

[35] J. Chaussidon, M. Fivel, and D. Rodney, “The glide of screw dislocations in bcc Fe: Atomistic static and dynamic simulations☆,” *Acta Mater.*, vol. 54, no. 13, pp. 3407–3416, Aug. 2006, doi: 10.1016/j.actamat.2006.03.044.

[36] K. I. Vitek V., “Atomistic study of non-Schmid effects in the plastic yielding of bcc metals,” *Philos. Mag. A*, vol. 81, no. 5, pp. 1387–1407, May 2001, doi: 10.1080/01418610110033885.

[37] R. Gröger, A. G. Bailey, and V. Vitek, “Multiscale modeling of plastic deformation of molybdenum and tungsten- I. Atomistic st,” *Mater. Sci. Forum*, vol. 482.

[38] V. Vitek, “Computer Simulation of the Screw Dislocation Motion in b.c.c. Metals under the Effect of the External Shear and Uniaxial Stresses,” 1976, doi: https://doi.org/10.1098/rspa.1976.0166.

[39] R. Gröger, V. Racherla, J. L. Bassani, and V. Vitek, “Multiscale modeling of plastic deformation of molybdenum and tungsten: II. Yield criterion for single crystals based on atomistic studies of glide of 1/2〈111〉 screw dislocations,” *Acta Mater.*, vol. 56, no. 19, Art. no. 19, Nov. 2008, doi: 10.1016/j.actamat.2008.07.037.

[40] R. Gröger and V. Vitek, “Multiscale modeling of plastic deformation of molybdenum and tungsten. III. Effects of temperature”.

[41] G. I. Taylor, “The Deformation of Crystals of β-Brass,” *Proc. R. Soc. Lond. Ser. Contain. Pap. Math. Phys. Character*, vol. 118, no. 779, pp. 1–24, 1928.

[42] Z. Chen, “Modelling the plastic deformation of iron.”

[43] M. S. Duesbery and V. Vitek, “PLASTIC ANISOTROPY IN B.C.C. TRANSITION METALS,” no. 128, p. 12.

[44] J. W. Christian, “Some surprising features of the plastic deformation of body-centered cubic metals and alloys,” *Metall. Trans. A*, vol. 14, no. 7, pp. 1237–1256, Jul. 1983, doi: 10.1007/BF02664806.

[45] M. S. Duesbery, V. Vitek, and D. K. Bowen, “The effect of shear stress on the screw dislocation core structure in body-centred cubic lattices,” *Proc. R. Soc. Lond. Math. Phys. Sci.*, vol. 332, no. 1588, pp. 85–111, Feb. 1973, doi: 10.1098/rspa.1973.0014.

[46] A. Patra, T. Zhu, and D. L. McDowell, “Constitutive equations for modeling non-Schmid effects in single crystal bcc-Fe at low and ambient temperatures,” *Int. J. Plast.*, vol. 59, pp. 1–14, Aug. 2014, doi: 10.1016/j.ijplas.2014.03.016.

[47] E. Clouet, B. Bienvenu, L. Dezerald, and D. Rodney, “Screw dislocations in BCC transition metals: from ab initio modeling to yield criterion,” *Comptes Rendus Phys.*, vol. 22, no. S3, pp. 83–116, Dec. 2021, doi: 10.5802/crphys.75.

[48] R. Groger, “DEVELOPMENT OF PHYSICALLY BASED PLASTIC FLOW RULES FOR BODY-CENTERED CUBIC METALS WITH TEMPERATURE AND STRAIN RATE DEPENDENCIES.”

[49] C. R. Weinberger, B. L. Boyce, and C. C. Battaile, “Slip planes in bcc transition metals,” *Int. Mater. Rev.*, vol. 58, no. 5, Art. no. 5, Jun. 2013, doi: 10.1179/1743280412Y.0000000015.

[50] G. I. Taylor, “The Mechanism of Plastic Deformation of Crystals. Part I. Theoretical,” 1934.

[51] G. I. Taylor, “The mechanism of plastic deformation of crystals. Part II.—Comparison with observations,” *Proc. R. Soc. Lond. Ser. Contain. Pap. Math. Phys. Character*, vol. 145, no. 855, pp. 388–404, Jul. 1934, doi: 10.1098/rspa.1934.0107.

[52] G. Monnet, “Multiscale modeling of irradiation hardening: Application to important nuclear materials,” *J. Nucl. Mater.*, vol. 508, pp. 609–627, Sep. 2018, doi: 10.1016/j.jnucmat.2018.06.020.

[53] tec-science, “Tensile test,” *tec-science*, Jul. 13, 2018. https://www.tec-science.com/material-science/material-testing/tensile-test/ (accessed Jul. 03, 2022).

[54] “Precipitation Hardening | Precipitation Hardening Stainless Steel.” https://www.sst.net/precipitation-hardening/ (accessed Jul. 03, 2022).

[55] “Precipitation Strengthening,” *Industrial Metallurgists*, Jun. 29, 2014. https://www.imetllc.com/precipitation-strengthening/ (accessed Jul. 03, 2022).

[56] T. Williams and R. Nanstad, “Low-alloy steels,” in *Structural Alloys for Nuclear Energy Applications*, Elsevier, 2019, pp. i–ii. doi: 10.1016/B978-0-12-397046-6.09991-3.

[57] D. J. Bacon, U. F. Kocks, and R. O. Scattergood, “The effect of dislocation self-interaction on the orowan stress,” *Philos. Mag.*, vol. 28, no. 6, pp. 1241–1263, Dec. 1973, doi: 10.1080/14786437308227997.

[58] K. C. Russell and L. M. Brown, “A dispersion strengthening model based on differing elastic moduli applied to the iron-copper system,” *Acta Metall.*, vol. 20, no. 7, pp. 969–974, Jul. 1972, doi: 10.1016/0001-6160(72)90091-0.

[59] G. Monnet, L. Vincent, and L. Gélébart, “Multiscale modeling of crystal plasticity in Reactor Pressure Vessel steels: Prediction of irradiation hardening,” *J. Nucl. Mater.*, vol. 514, pp. 128–138, Feb. 2019, doi: 10.1016/j.jnucmat.2018.11.028.

[60] O. Kraft, P. A. Gruber, R. Mönig, and D. Weygand, “Plasticity in Confined Dimensions,” *Annu. Rev. Mater. Res.*, vol. 40, no. 1, pp. 293–317, Jun. 2010, doi: 10.1146/annurev-matsci-082908-145409.

[61] J. R. Greer, W. C. Oliver, and W. D. Nix, “Size dependence of mechanical properties of gold at the micron scale in the absence of strain gradients,” *Acta Mater.*, vol. 53, no. 6, pp. 1821–1830, Apr. 2005, doi: 10.1016/j.actamat.2004.12.031.

[62] J. R. Greer, C. R. Weinberger, and W. Cai, “Comparing the strength of f.c.c. and b.c.c. sub-micrometer pillars: Compression experiments and dislocation dynamics simulations,” *Mater. Sci. Eng. A*, vol. 493, no. 1–2, pp. 21–25, Oct. 2008, doi: 10.1016/j.msea.2007.08.093.

[63] J. R. Greer and W. D. Nix, “Nanoscale gold pillars strengthened through dislocation starvation,” *Phys. Rev. B*, vol. 73, no. 24, p. 245410, Jun. 2006, doi: 10.1103/PhysRevB.73.245410.

[64] M. D. Uchic and D. M. Dimiduk, “A methodology to investigate size scale effects in crystalline plasticity using uniaxial compression testing,” *Mater. Sci. Eng. A*, vol. 400–401, pp. 268–278, Jul. 2005, doi: 10.1016/j.msea.2005.03.082.

[65] E. Lilleodden and W. Nix, “Microstructural length-scale effects in the nanoindentation behavior of thin gold films,” *Acta Mater.*, vol. 54, no. 6, pp. 1583–1593, Apr. 2006, doi: 10.1016/j.actamat.2005.11.025.

[66] S. Brinckmann, J.-Y. Kim, and J. R. Greer, “Fundamental Differences in Mechanical Behavior between Two Types of Crystals at the Nanoscale,” Apr. 2008, Accessed: Jul. 03, 2022. [Online]. Available: https://link.aps.org/doi/10.1103/PhysRevLett.100.155502

[67] C. R. Weinberger and W. Cai, “Surface-controlled dislocation multiplication in metal micropillars,” *Proc. Natl. Acad. Sci.*, vol. 105, no. 38, pp. 14304–14307, Sep. 2008, doi: 10.1073/pnas.0806118105.

[68] T. A. Parthasarathy, S. I. Rao, D. M. Dimiduk, M. D. Uchic, and D. R. Trinkle, “Contribution to size effect of yield strength from the stochastics of dislocation source lengths in finite samples,” *Scr. Mater.*, vol. 56, no. 4, pp. 313–316, Feb. 2007, doi: 10.1016/j.scriptamat.2006.09.016.

[69] F. Mompiou, M. Legros, A. Sedlmayr, D. S. Gianola, D. Caillard, and O. Kraft, “Source-based strengthening of sub-micrometer Al fibers,” *Acta Mater.*, vol. 60, no. 3, pp. 977–983, Feb. 2012, doi: 10.1016/j.actamat.2011.11.005.

[70] B. R. S. Rogne and C. Thaulow, “Strengthening mechanisms of iron micropillars,” *Philos. Mag.*, vol. 95, no. 16–18, pp. 1814–1828, 2014, doi: 10.1080/14786435.2014.984004.

[71] B. R. S. Rogne and C. Thaulow, “Effect of crystal orientation on the strengthening of iron micro pillars,” *Mater. Sci. Eng. A*, vol. 621, pp. 133–142, Jan. 2015, doi: 10.1016/j.msea.2014.10.067.

[72] W. F. Hosford, *Mechanical Behavior of Materials*, 1st ed. Cambridge University Press, 2005. doi: 10.1017/CBO9780511810930.

[73] W. Cai, V. V. Bulatov, J. Chang, J. Li, and S. Yip, “Dislocation Core Effects on Mobility,” in *Dislocations in Solids*, vol. 12, Elsevier, 2004, pp. 1–80. doi: 10.1016/S1572-4859(05)80003-8.

[74] F. Maresca, D. Dragoni, G. Csányi, N. Marzari, and W. A. Curtin, “Screw dislocation structure and mobility in body centered cubic Fe predicted by a Gaussian Approximation Potential,” *Npj Comput. Mater.*, vol. 4, no. 1, p. 69, Dec. 2018, doi: 10.1038/s41524-018-0125-4.

[75] R. Huang *et al.*, “Flow Stress in Submicron BCC Iron Single Crystals: Sample-size-dependent Strain-rate Sensitivity and Rate-dependent Size Strengthening,” *Mater. Res. Lett.*, vol. 3, no. 3, pp. 121–127, Jul. 2015, doi: 10.1080/21663831.2014.999953.

[76] Q. Wei, S. Cheng, K. T. Ramesh, and E. Ma, “Effect of nanocrystalline and ultrafine grain sizes on the strain rate sensitivity and activation volume: fcc versus bcc metals,” *Mater. Sci. Eng. A*, vol. 381, no. 1–2, pp. 71–79, Sep. 2004, doi: 10.1016/j.msea.2004.03.064.

[77] G. M. Cheng, W. W. Jian, W. Z. Xu, H. Yuan, P. C. Millett, and Y. T. Zhu, “Grain Size Effect on Deformation Mechanisms of Nanocrystalline bcc Metals,” *Mater. Res. Lett.*, vol. 1, no. 1, pp. 26–31, Mar. 2013, doi: 10.1080/21663831.2012.739580.

[78] I. M. Deprez, “Effect of Post-Irradiation Annealing on Defects in Irradiated Model Alloys by Means of Positron Annihilation Coincidence Doppler Broadening Spectroscopy.”

[79] E. D. Eason, G. R. Odette, R. K. Nanstad, and T. Yamamoto, “A physically-based correlation of irradiation-induced transition temperature shifts for RPV steels,” *J. Nucl. Mater.*, vol. 433, no. 1–3, Art. no. 1–3, Feb. 2013, doi: 10.1016/j.jnucmat.2012.09.012.

[80] G. R. Odette and G. E. Lucas, “Embrittlement of nuclear reactor pressure vessels,” *JOM*, vol. 53, no. 7, pp. 18–22, Jul. 2001, doi: 10.1007/s11837-001-0081-0.

[81] L. Messina, “Multiscale modeling of atomic transport phenomena in ferritic steels,” Unpublished, 2015. Accessed: Jul. 02, 2022. [Online]. Available: http://rgdoi.net/10.13140/RG.2.1.3464.4880

[82] R. J. M. Konnings, T. R. Allen, and R. E. Stoller, *Comprehensive Nuclear Materials, vol.1_ Basic aspects of radiation effects in solids*-. Elsevier, 2012.

[83] N. Castin *et al.*, “The dominant mechanisms for the formation of solute-rich clusters in low-Cu steels under irradiation,” *Mater. Today Energy*, vol. 17, p. 100472, Sep. 2020, doi: 10.1016/j.mtener.2020.100472.

[84] “Exact ab initio transport coefficients in bccFe–X(X=Cr,Cu,Mn,Ni,P,Si) dilute alloys,” 2014.

[85] L. Messina, T. Schuler, M. Nastar, M.-C. Marinica, and P. Olsson, “Solute diffusion by self-interstitial defects and radiation-induced segregation in ferritic Fe–X (X=Cr, Cu, Mn, Ni, P, Si) dilute alloys,” *Acta Mater.*, vol. 191, pp. 166–185, Jun. 2020, doi: 10.1016/j.actamat.2020.03.038.

[86] G. S. Was and P. L. Andresen, “Radiation damage to structural alloys in nuclear power plants: mechanisms and remediation,” in *Structural Alloys for Power Plants*, Elsevier, 2014, pp. 355–420. doi: 10.1533/9780857097552.2.355.

[87] M. Nastar and F. Soisson, “Radiation-Induced Segregation,” in *Comprehensive Nuclear Materials*, Elsevier, 2012, pp. 471–496. doi: 10.1016/B978-0-08-056033-5.00035-5.

[88] A. J. Ardell and P. Bellon, “Radiation-induced solute segregation in metallic alloys.,” 2015.

[89] G. R. Odette, N. Almirall, P. B. Wells, and T. Yamamoto, “Precipitation in reactor pressure vessel steels under ion and neutron irradiation: On the role of segregated network dislocations,” *Acta Mater.*, vol. 212, p. 116922, Jun. 2021, doi: 10.1016/j.actamat.2021.116922.

[90] K. Fukuya, “Current understanding of radiation-induced degradation in light water reactor structural materials,” *J. Nucl. Sci. Technol.*, vol. 50, no. 3, pp. 213–254, Mar. 2013, doi: 10.1080/00223131.2013.772448.

[91] W. L. Server and R. K. Nanstad, “Integrity and embrittlement management of reactor pressure vessels (RPVs) in light-water reactors,” in *Irradiation Embrittlement of Reactor*

*Pressure Vessels (RPVs) in Nuclear Power Plants*, Elsevier, 2015, pp. 132–155. doi: 10.1533/9780857096470.2.132.

[92] W. J. Phythian and C. A. English, "Microstructural evolution in reactor pressure vessel steels," *J. Nucl. Mater.*, vol. 205, pp. 162–177, Oct. 1993, doi: 10.1016/0022-3115(93)90079-E.

[93] G. R. Odette, "Radiation Induced Microstructural Evolution in Reactor Pressure Vessel Steels," *MRS Proc.*, vol. 373, p. 137, 1994, doi: 10.1557/PROC-373-137.

[94] Z. Lu, R. G. Faulkner, and P. E. J. Flewitt, "The role of irradiation-induced phosphorus segregation in the ductile-to-brittle transition temperature in ferritic steels," *Mater. Sci. Eng. A*, vol. 437, no. 2, pp. 306–312, Nov. 2006, doi: 10.1016/j.msea.2006.07.114.

[95] B. S. Bokshtein, A. N. Khodan, O. O. Zabusov, D. A. Mal'tsev, and B. A. Gurovich, "Kinetics of phosphorus segregation at grain boundaries of low-alloy low-carbon steel," *Phys. Met. Metallogr.*, vol. 115, no. 2, pp. 146–156, Feb. 2014, doi: 10.1134/S0031918X14020033.

[96] H. Nakata, K. Fujii, K. Fukuya, R. Kasada, and A. Kimura, "Grain Boundary Phosphorus Segregation in Thermally Aged Low Alloy Steels," *J. Nucl. Sci. Technol.*, vol. 43, no. 7, pp. 785–793, Jul. 2006, doi: 10.1080/18811248.2006.9711160.

[97] W. Losch, "A new model of grain boundary failure in temper embrittled steel," *Acta Metall.*, vol. 27, no. 12, pp. 1885–1892, Dec. 1979, doi: 10.1016/0001-6160(79)90079-8.

[98] S. Suzuki, S. Tanii, K. Abiko, and H. Kimura, "Site competition between sulfur and carbon at grain boundaries and their effects on the grain boundary cohesion in iron," p. 7.

[99] J. Kameda and A. J. Bevolo, "Neutron irradiation-induced intergranular solute segregation in iron base alloys," *Acta Metall.*, vol. 37, no. 12, pp. 3283–3296, Dec. 1989, doi: 10.1016/0001-6160(89)90201-0.

[100] A. V. Nikolaeva, Yu. A. Nikolaev, and A. M. Kryukov, "The contribution of grain boundary effects to low-alloy steel irradiation embrittlement," *J. Nucl. Mater.*, vol. 218, no. 1, pp. 85–93, Jan. 1995, doi: 10.1016/0022-3115(94)00361-0.

[101] M. Brumovsky, "Embrittlement of reactor pressure vessels (RPVs) in WWER-type reactors," in *Irradiation Embrittlement of Reactor Pressure Vessels (RPVs) in Nuclear Power Plants*, Elsevier, 2015, pp. 107–131. doi: 10.1533/9780857096470.2.107.

[102] G. Tauber and H. J. Grabke, "Grain Boundary Segregation of Sulfur, Nitrogen, and Carbon in α-Iron," *Berichte Bunsenges. Für Phys. Chem.*, vol. 82, no. 3, pp. 298–302, Mar. 1978, doi: 10.1002/bbpc.197800042.

[103] Z. Que *et al.*, "Environmental degradation of fracture resistance in high-temperature water environments of low-alloy reactor pressure vessel steels with high sulphur or phosphorus contents," *Corros. Sci.*, vol. 154, pp. 191–207, Jul. 2019, doi: 10.1016/j.corsci.2019.04.011.

[104] Z. Que, "High-Temperature Water Effects on the Fracture Behaviour of Low-Alloy Reactor Pressure Vessel Steels," p. 198.

[105] S. Ritter and H. P. Seifert, “Corrosion Fatigue Crack Growth Behaviour of Low-Alloy RPV Steels at Different Temperatures and Loading Frequencies under BWR/NWC Environment,” p. 11.

[106] H.-P. Seifert and S. Ritter, “Review and Assessment of SCC Experiments with RPV Steels in Oskarshamn 2 and 3 (ABB Report SBR 99-020),” p. 51.

[107] “Stress corrosion cracking in Alloy 182 – RPV Welds | LNM | Paul Scherrer Institut (PSI),” Jan. 21, 2020. https://www.psi.ch/en/lnm/scientific-highlights/stress-corrosion-cracking-in-alloy-182-rpv-welds (accessed Oct. 30, 2022).

[108] P. D. Styman, J. M. Hyde, K. Wilford, A. Morley, and G. D. W. Smith, “Precipitation in long term thermally aged high copper, high nickel model RPV steel welds,” *Prog. Nucl. Energy*, vol. 57, pp. 86–92, May 2012, doi: 10.1016/j.pnucene.2011.10.010.

[109] R. G. Carter, N. Soneda, K. Dohi, J. M. Hyde, C. A. English, and W. L. Server, “Microstructural characterization of irradiation-induced Cu-enriched clusters in reactor pressure vessel steels,” *J. Nucl. Mater.*, vol. 298, no. 3, Art. no. 3, Oct. 2001, doi: 10.1016/S0022-3115(01)00659-6.

[110] N. Soneda and A. Nomoto, “Characteristics of the New Embrittlement correlation method for the Japanese RPV,” 2010.

[111] R. Chaouadi and R. Gérard, “Neutron flux and annealing effects on irradiation hardening of RPV materials,” *J. Nucl. Mater.*, vol. 418, no. 1–3, Art. no. 1–3, Nov. 2011, doi: 10.1016/j.jnucmat.2011.06.012.

[112] V. Ghetta, D. Gorse, D. Mazière, and V. Pontikis, Eds., *Materials issues for generation IV systems: status, open questions and challenges ; [proceedings of the NATO Advanced Study Institute on Materials Issues for Generation IV Systems: Status, Open Questions and Challenges, Cargèse, Corsica, France, 24 September - 6 October 2007]*. Dordrecht: Springer, 2008.

[113] K. Fujii and K. Fukuya, “Characterization of defect clusters in ion-irradiated A533B steel,” *J. Nucl. Mater.*, vol. 336, no. 2–3, pp. 323–330, Feb. 2005, doi: 10.1016/j.jnucmat.2004.10.090.

[114] A. Wagner, A. Ulbricht, F. Bergner, and E. Altstadt, “Influence of the copper impurity level on the irradiation response of reactor pressure vessel steels investigated by SANS,” *Nucl. Instrum. Methods Phys. Res. Sect. B Beam Interact. Mater. At.*, vol. 280, pp. 98–102, Jun. 2012, doi: 10.1016/j.nimb.2012.03.008.

[115] G. R. Odette, “On the dominant mechanism of irradiation embrittlement of reactor pressure vessel steels,” *Scr. Metall.*, vol. 17, no. 10, pp. 1183–1188, Oct. 1983, doi: 10.1016/0036-9748(83)90280-6.

[116] P. J. Othen, M. L. Jenkins, and G. D. W. Smith, “High-resolution electron microscopy studies of the structure of Cu precipitates in α-Fe,” *Philos. Mag. A*, vol. 70, no. 1, pp. 1–24, Jul. 1994, doi: 10.1080/01418619408242533.

[117] P. Pareige, K. F. Russell, R. E. Stoller, and M. K. Miller, “Influence of long-term thermal aging on the microstructural evolution of nuclear reactor pressure vessel materials: an atom probe study,” p. 8, 1997.

[118] P. Pareige, B. Radiguet, and A. Barbu, “Heterogeneous irradiation-induced copper precipitation in ferritic iron–copper model alloys,” *J. Nucl. Mater.*, vol. 352, no. 1–3, pp. 75–79, Jun. 2006, doi: 10.1016/j.jnucmat.2006.02.073.

[119] B. Radiguet, P. Pareige, and A. Barbu, “Irradiation induced clustering in low copper or copper free ferritic model alloys,” *Nucl. Instrum. Methods Phys. Res. Sect. B Beam Interact. Mater. At.*, vol. 267, no. 8–9, pp. 1496–1499, May 2009, doi: 10.1016/j.nimb.2009.01.146.

[120] B. Radiguet, A. Barbu, and P. Pareige, “Understanding of copper precipitation under electron or ion irradiations in FeCu0.1wt% ferritic alloy by combination of experiments and modelling,” *J. Nucl. Mater.*, vol. 360, no. 2, pp. 104–117, Feb. 2007, doi: 10.1016/j.jnucmat.2006.09.007.

[121] E. Meslin, B. Radiguet, and M. Loyer-Prost, “Radiation-induced precipitation in a ferritic model alloy: An experimental and theoretical study,” *Acta Mater.*, vol. 61, no. 16, pp. 6246–6254, Sep. 2013, doi: 10.1016/j.actamat.2013.07.008.

[122] P. Auger, P. Pareige, M. Akamatsu, and D. Blavette, “APFIM investigation of clustering in neutron-irradiated FeCu alloys and pressure vessel steels,” *J. Nucl. Mater.*, vol. 225, pp. 225–230, Aug. 1995, doi: 10.1016/0022-3115(94)00522-2.

[123] Y. Matsukawa, “Crystallography of Precipitates in Metals and Alloys: (1) Analysis of Crystallography,” in *Crystallography*, T. Akitsu, Ed. IntechOpen, 2019. doi: 10.5772/intechopen.82693.

[124] C. L. Liu, G. R. Odette, B. D. Wirth, and G. E. Lucas, “A lattice Monte Carlo simulation of nanophase compositions and structures in irradiated pressure vessel Fe-Cu-Ni-Mn-Si steels,” *Mater. Sci. Eng. A*, vol. 238, no. 1, pp. 202–209, Oct. 1997, doi: 10.1016/S0921-5093(97)00450-4.

[125] G. R. Odette, T. Yamamoto, T. J. Williams, R. K. Nanstad, and C. A. English, “On the history and status of reactor pressure vessel steel ductile to brittle transition temperature shift prediction models,” *J. Nucl. Mater.*, vol. 526, p. 151863, Dec. 2019, doi: 10.1016/j.jnucmat.2019.151863.

[126] G. R. Odette, “High Fluency Low Flux Embrittlement Models of LWR Reactor Pressure Vessel Embrittlement and a Supporting Database from the UCSB ATR-2 Irradiation Experiment,” 11--3176, 1346148, Jan. 2017. doi: 10.2172/1346148.

[127] P. Pareige *et al.*, “Three-dimensional atom probe study of irradiated, annealed and re-irradiated VVER 440 weld metals,” *Surf. Interface Anal.*, vol. 36, no. 56, pp. 581–584, May 2004, doi: 10.1002/sia.1705.

[128] P. D. Edmondson, M. K. Miller, K. A. Powers, and R. K. Nanstad, “Atom probe tomography characterization of neutron irradiated surveillance samples from the R. E. Ginna reactor pressure vessel,” *J. Nucl. Mater.*, vol. 470, pp. 147–154, Mar. 2016, doi: 10.1016/j.jnucmat.2015.12.038.

[129] B. M. Jenkins *et al.*, “Observation of Mn-Ni-Si-rich features in thermally-aged model reactor pressure vessel steels,” *Scr. Mater.*, vol. 191, pp. 126–130, Jan. 2021, doi: 10.1016/j.scriptamat.2020.09.029.

[130] K. Lindgren, M. Boåsen, K. Stiller, P. Efsing, and M. Thuvander, “Cluster formation in in-service thermally aged pressurizer welds,” *J. Nucl. Mater.*, vol. 504, pp. 23–28, Jun. 2018, doi: 10.1016/j.jnucmat.2018.03.017.

[131] P. D. Styman, J. M. Hyde, A. Morley, K. Wilford, N. Riddle, and G. D. W. Smith, “The effect of Ni on the microstructural evolution of high Cu reactor pressure vessel steel welds after thermal ageing for up to 100,000 h,” *Mater. Sci. Eng. A*, vol. 736, pp. 111–119, Oct. 2018, doi: 10.1016/j.msea.2018.08.063.

[132] W. Xiong *et al.*, “Thermodynamic models of low-temperature Mn-Ni-Si precipitation in reactor pressure vessel steels,” *MRS Commun.*, vol. 4, no. 3, Art. no. 3, Sep. 2014, doi: 10.1557/mrc.2014.21.

[133] P. D. Styman *et al.*, “Post-irradiation annealing of Ni–Mn–Si-enriched clusters in a neutron-irradiated RPV steel weld using Atom Probe Tomography,” *J. Nucl. Mater.*, vol. 459, pp. 127–134, Apr. 2015, doi: 10.1016/j.jnucmat.2015.01.027.

[134] E. Meslin *et al.*, “Characterization of neutron-irradiated ferritic model alloys and a RPV steel from combined APT, SANS, TEM and PAS analyses,” *J. Nucl. Mater.*, vol. 406, no. 1, pp. 73–83, Nov. 2010, doi: 10.1016/j.jnucmat.2009.12.021.

[135] L. Messina, M. Chiapetto, P. Olsson, C. S. Becquart, and L. Malerba, “An object kinetic Monte Carlo model for the microstructure evolution of neutron-irradiated reactor pressure vessel steels: Microstructure evolution of neutron-irradiated reactor pressure vessel steels,” *Phys. Status Solidi A*, vol. 213, no. 11, pp. 2974–2980, Nov. 2016, doi: 10.1002/pssa.201600038.

[136] R. Ngayam-Happy, C. S. Becquart, C. Domain, and L. Malerba, “Formation and evolution of MnNi clusters in neutron irradiated dilute Fe alloys modelled by a first principle-based AKMC method,” *J. Nucl. Mater.*, vol. 426, no. 1–3, pp. 198–207, Jul. 2012, doi: 10.1016/j.jnucmat.2012.03.033.

[137] G. S. Was *et al.*, “Resolution of the carbon contamination problem in ion irradiation experiments,” *Nucl. Instrum. Methods Phys. Res. Sect. B Beam Interact. Mater. At.*, vol. 412, pp. 58–65, Dec. 2017, doi: 10.1016/j.nimb.2017.08.039.

[138] R. Chaouadi, R. Gérard, E. Stergar, and W. Van Renterghem, “Neutron irradiation hardening of chemically-tailored RPV steels with respect to Cu/P and Ni/Mn elements,” *J. Nucl. Mater.*, vol. 519, pp. 188–204, Jun. 2019, doi: 10.1016/j.jnucmat.2019.03.030.

[139] L. Debarberis, A. Kryukov, F. Gillemot, B. Acosta, and F. Sevini, “Semi-mechanistic analytical model for radiation embrittlement and re-embrittlement data analysis,” *Int. J. Press. Vessels Pip.*, vol. 82, no. 3, pp. 195–200, Mar. 2005, doi: 10.1016/j.ijpvp.2004.09.002.

[140] “NUGENIA position on RPV Irradiation Embrittlement issues based on the outcome of the EURATOM FP7 project LONGLIFE.”

[141] M. Brumovsky, “Irradiation hardening and materials embrittlement in light water reactor (LWR) environments,” in *Understanding and Mitigating Ageing in Nuclear Power Plants*, Elsevier, 2010, pp. 357–373. doi: 10.1533/9781845699956.2.357.

# Chapter 2: Materials and techniques

## I. Materials

Irradiation of the RPV material causes the formation of nanofeatures that can alter its mechanical properties, such as clusters mainly enriched in Mn, Ni and Si. This work is focused on the understanding of the formation of such clusters and their impact on mechanical properties.

Since commercial RPV steels' chemical composition varies in terms of percentage of the alloying elements and impurities that they contain, it complicates their systematic study.

To understand the way each element is involved in the formation and evolution of irradiation induced microstructure and its consequential effects on the mechanical properties, instead of RPV steels it is preferable to use model alloys, which have a well-controlled and simpler composition.

To study the effect of Mn, Ni as well as their synergistic effects, two binary (Fe-1Mn and Fe-1Ni) and a ternary alloy (Fe-1.1Mn-0.7Ni) were selected for this work. These alloys were studied in both non-irradiated and neutron irradiated states.

The neutron irradiation of the binary alloys took place in the experimental reactor iLVR-15 in UJV Rez in Czech Republic, whereas the ternary alloy was irradiated in the BR2 material test reactor (MTR) at SCK CEN in Belgium, as a part of the H2020 SOTERIA project. The irradiation conditions are detailed in Table 2, where flux and fluence are reported for high energy neutrons with E>1MeV.

The ternary alloy is irradiated up to 0.1dpa, corresponding to the dose rate that a PWR would accumulate at approximately 40 years of operation.

*Table 2: Irradiation conditions of the studied model alloys. Flux and fluence are given for neutrons with E>1MeV.*

| **Materials** | **Temperature** | **Flux (**$n.cm^{-2}.s^{-1}$**)** | **Fluence (**$n.cm^{-2}$**)** | **dpa** |
|---|---|---|---|---|
| Fe-1Mn & Fe-1Ni | 300°C | $1.35x10^{13}$ | $1.7x10^{19}$ | 0.022 |
| Fe-1.1Mn-0.7Ni | 300°C | $9.5x10^{13}$ | $6.9x10^{19}$ | 0.1 |

Furthermore, to better understand both the stability of the clusters and their impact on mechanical properties, the neutron irradiated ternary alloy was also studied after it was isochronally annealed at 400, 500 and 600 °C for 30 min., at SCK CEN.

## II. Method and experimental techniques

For the microstructural characterization of the alloys, atom probe tomography (APT) experiments were carried out. This technique was selected as the most appropriate to study and characterize the nanometric features that may exist in the alloys' microstructure after neutron irradiation or annealing treatments.

Irradiation hardening was experimentally measured from stress-strain curves obtained by in-situ micro-compression of Focused Ion Beam (FIB) fabricated single-crystal micropillars, on both the as received and the neutron irradiated samples. For these experiments polished samples were examined using Electron Backscatter Diffraction (EBSD) analysis for the selection of the appropriate oriented grains, inside which the pillars were milled.

To better correlate the measured hardening with the microstructure, compressed pillars were lifted out in order to fabricate samples for additional APT and Transmission Electron Microscopy (TEM) analyses.

The above-mentioned techniques were applied in the Genesis platform (abbreviation for Groupe d'Etudes et de Nanoanalyses des Effets d'Irradiations) (Appendix 1) which provides all the necessary equipment and was designed and constructed complying with all the safety regulations to handle radioactive samples.

The main principles of the techniques used, the equipment and the applied experimental conditions will be presented in the following.

### 1. Polishing

Prior to the microstructural or mechanical properties analysis, the materials need to be properly polished. Polishing is a crucial step for acquiring a valid signal for the EBSD analysis, needed for the selection of the appropriate oriented grains, inside which the pillars will be milled, but also to assure a flat surface needed to match the indenters' flat punch during the in-situ compression tests.

The samples were provided in the form of rods with dimensions about 10 x 0.4 x 0.8 mm. To study the samples' mechanical properties using micro-compression, the rods were cut in suitable dimensions to fit on the 6.5 mm diameter stub of the indenter.

In the case of the neutron irradiated samples, using an automatic polisher in the GENESIS platform is mandatory. For this, a holding device was designed to house the small sized samples, fixed on the indenter's stub using epoxy resin, and also to fit the specimen holders of the polisher (Figure 53). For detailed drawings of the custom-made holding device see Appendix 2.

Inside a homemade mold matching the stub's dimensions, the samples were cold mounted using the EpoxiCure™ 2 (20-3430-064) epoxy resin, mixed with the EpoxiCure 2 (20-3432) hardener, made by Buehler. The conductive filler (20-8500) was added to the mixture, to avoid electron accumulation on the sample's surface in both SEM/FIB manipulations and also in the in-situ micro-compression sessions. The mixture was allowed to cure for at least 6 hours according to the manufacturer's instructions and then the specimens were clamped in the designed holder.

Samples were polished using successively the 9, 3, 1, ¼ µm diamond suspensions utilizing a Struers Tegramin polisher. To achieve a smooth and strain free surface, a finishing dispersion of colloidal silica (OPU) was used for 20 min. Between the polishing steps, the specimens were thoroughly cleaned using first soapy water then ethanol and finally dried with air.

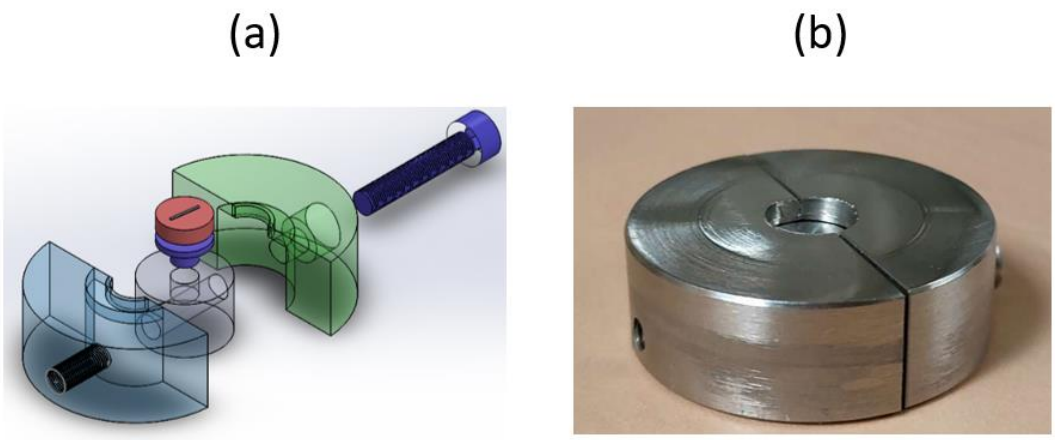


*Figure 53: (a) Transparent drawing of the custom-made specimen holding device: the indenter's stub (purple), sample mounted in the resin (red) (b) an image of the fabricated device.*

After this polishing procedure, the samples are ready to be studied using Electron Backscatter Diffraction (EBSD). This non-destructive microstructural analysis technique is capable of providing information such as phases identification, crystal lattice and grain orientations. This information is necessary for the selection of the grains inside which the micro-sized pillars will be fabricated to study their mechanical response under compression.

## 2. Atom Probe Tomography

Atom probe Tomography (APT) is a destructive 3D quantitative analytical technique with spatial resolution near the atomic scale, capable to measure chemical composition on the nanoscale.

The APT's operation principle is based on the field evaporation process of the specimen's atoms, while the chemical characterization of each atom relies on a time-of-flight mass spectrometer and the three-dimensional atomic-scale mapping of the analyzed sample relies on a position sensitive detector[1–4].

The aim of the APT experiments is to visualize and quantify the microstructure of the non-irradiated, neutron irradiated and annealed samples. At the same time to measure the chemical composition not only of the samples but mainly of the nanometer-sized clusters which are expected to develop under irradiation and are considered to alter the mechanical properties of the materials.

Consequently, tips suitable for APT analysis were fabricated from the non-irradiated and neutron irradiated bulk materials, along with from compressed pillars, to assess the microstructure involved in the measured mechanical properties.

*2 – i. Field Evaporation*

For an atom close to the surface, to evaporate, the difference between the potential energy of the ionic state and the neutral atomic state forms an energy barrier (Figure 54). In the absence of an electric field, this energy barrier ($Q_0$) for an n-fold-charged free ion is formulated by [1–3]:

$$Q_{0(n)} = \Lambda + \sum_n I_n - n\phi_e \tag{2.1}$$

where Λ is the sublimation energy, $I_n$ is the energy needed for the $n^{th}$ ionization and $\phi_e$ is the work function of the electrons.

When an electric field is applied the potential energy of the ionic state is affected and the height of the energy barrier ($Q_n$) lowers as the electric field increases (Figure 54). The electric field at which the barrier becomes zero at 0 K is called evaporation field and its value is characteristic for every element in its $n^{th}$ ionic state which is calculated using:

$$F_e = \frac{4\pi\varepsilon_0}{n^3 e^3}\left(\Lambda + \sum_n I_n - n\phi_e\right)^2 \tag{2.2}$$

with $\varepsilon_0$ the dielectric permittivity of the vacuum and e the elementary charge.

In the case of the pure Fe to evaporate as $Fe^{2+}$ the value for the evaporation field is 33 $V.nm^{-1}$ [4].

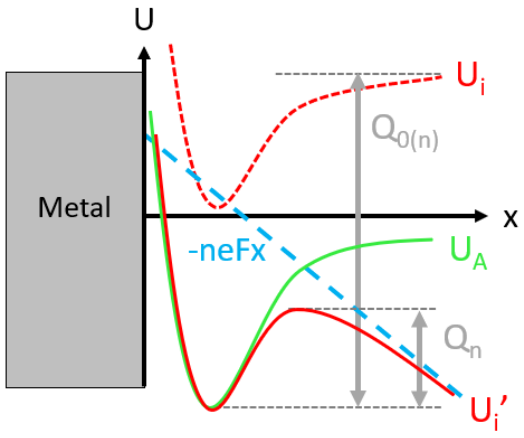


*Figure 54: Diagram of the atomic ($U_A$) and the ionic potential energy, ($U_i$) and ($U_i'$), without and with the presence of an electric field respectively. The evaporation energy barrier ($Q_{0(n)}$) drops to ($Q_n$) in the presence of the electric field.*

Since field evaporation is considered as a thermally assisted process, the rate constant $K_n$ for field evaporation of an n-charged ion is expressed by the Arrhenius equation:

$$K_n = v_0 \exp\left(-\frac{Q_n}{k_B T}\right) \tag{2.3}$$

where $Q_n$ the field evaporation activation energy, $v_0$ the vibration frequency of the surface atom, $k_B$ the Boltzmann constant and T the applied temperature.

To achieve the needed high electrostatic field at the surface of the sample, it must have the shape of a sharp needle with a radius around 50 nm. The tip is then placed inside a chamber

under ultra-high vacuum (below $10^{-8}$ MPa) and a high positive voltage (in the order of few kV) is applied to it [1], [3]. The electric field at the apex of the tip is estimated by:

$$F = \frac{V}{k_f R} \tag{2.4}$$

where F is the electric field, R the curvature radius of the tip and $k_f$ is the field factor, a constant (in the range 3 – 8, with a typical value of 5 [4]) that accounts for the tip shape and its electrostatic environment.

To control the evaporation, a continuous (DC) electric field, slightly less than the necessary field to evaporate any of the atoms, is applied. A counter-electrode (called "local electrode" in the case of LEAP atom probes) placed in front of the tip and connected to a high voltage pulser (HV), generates negative electrical impulses which last a few nanoseconds. The sum of the DC field and the field generated by the HV-pulses is sufficiently intense to evaporate the atoms of the tip at constant temperature (this is the so called "electric mode" configuration) (Figure 55). Alternatively, evaporation is controlled by increasing the temperature of the apex of the tip using laser pulses while the electric (DC) field is constant ("laser mode" configuration). This mode is essential for material with poor electrical conductivity [5].

In the electric mode, the ratio of the amplitude of the HV pulses to the standing voltage (DC) is called pulse fraction $\frac{V_P}{V_{DC}}$, where $V_P$ and $V_{DC}$ are respectively pulse and standing voltages. In the case of the laser mode, the effect of the laser pulses is described by the equivalent pulse fraction defined as $\frac{V_t - V_{DC}}{V_{DC}}$ where $V_t$ is the electric voltage necessary to evaporate surface atoms without any pulse.

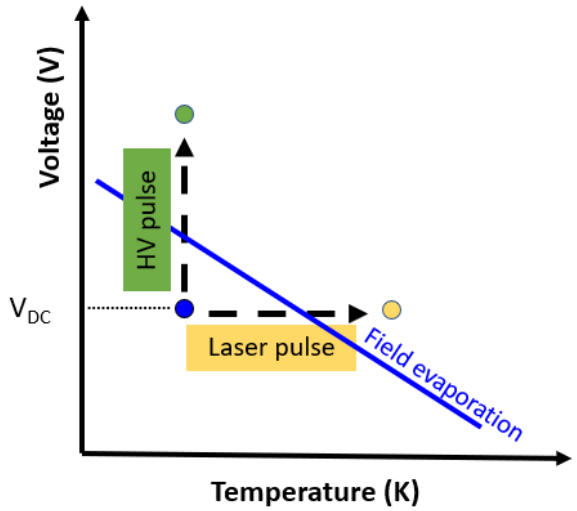


*Figure 55: A continuous (DC) voltage less than the necessary to field evaporate is applied. Either an HV pulse or a laser pulse is needed to overcome the threshold value for field evaporation to occur.*

*2 – ii. Time of flight mass spectroscopy*

Pulsing is fundamental to define the instant of departure of an ion from the apex of the sample, since it triggers the field evaporation and the measurement of the time-of-flight ($t_{flight}$), that is the time of arrival of the ion on the detection system, typically, in the range of about 1-5 µs [2].

As the evaporated ion is accelerated by the electrostatic field, assuming that when it leaves the surface it has no initial velocity, it has a potential energy given by:

$$E_p = neV \tag{2.5}$$

where *ne* is the ion charge and *V* is the evaporation voltage.

Since the acceleration length (a few nanometers) is negligible comparing to the flight length (L), that is 382 mm for the LEAP 4000 HR [3], the ion reaches its final speed (*v*) almost instantly:

$$v = \frac{L}{t_{flight}} \tag{2.6}$$

having kinetic energy:

$$E_k = \frac{1}{2}mv^2 \tag{2.7}$$

where *m* is the ion mass.

When the ion hits the detector, all its potential energy is being converted to kinetic energy. So, setting Eq (2.5) and Eq (2.7) equal and rearranging using Eq (2.6), we calculate the mass-to-charge ratio of the ion, expressed in atomic mass units (a.m.u.) or Daltons (Da).

$$\frac{m}{n} = 2eV\left(\frac{t_{flight}}{L}\right)^2 \tag{2.8}$$

The detection system used in APT consists of an assembly of two microchannel plates (MCP) coupled with a position sensitive Delay Line Detector (DLD) (Figure 56).

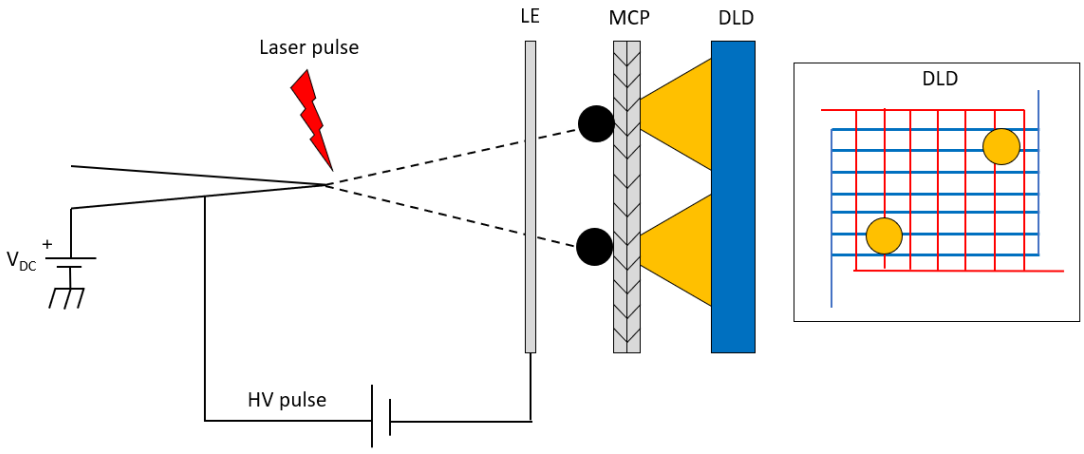


*Figure 56: When a field evaporated ion hits the microchannel plates (MCP), an electron cascade is formed that induces electrical signals on the windings of the delay line detector (DLD). Hit positioning information is deduced by the propagation delay of the signals.*

The microchannel plate consists of an array of microscopic channel electron multipliers oriented parallel to one another (Figure 57 – A). When an ion enters a microchannel and hits its inner wall, multiple electrons are emitted. These secondary electrons are accelerated by the applied potential and every time they hit the channel wall, they produce more secondary electrons (Figure 57 – B). In this way, the microchannel plate transforms an incoming ion into an electron cascade.

Not all the surface area of the MCP is channel area, so some of the incoming ions, independently of their chemical nature, may collide with the surface material of the MCP failing to enter a channel and to create an electron cascade (Figure 57 – C). Thus, they are not detected, limiting the detection efficiency (Q), that is the fraction of the actually detected ions to the ions hitting the detector, which varies depending on the APT's specifications between 35% and in the best case 80%. Since the ions are randomly missing, independently of their chemical nature, the calculation of the sample's chemical composition is not affected.

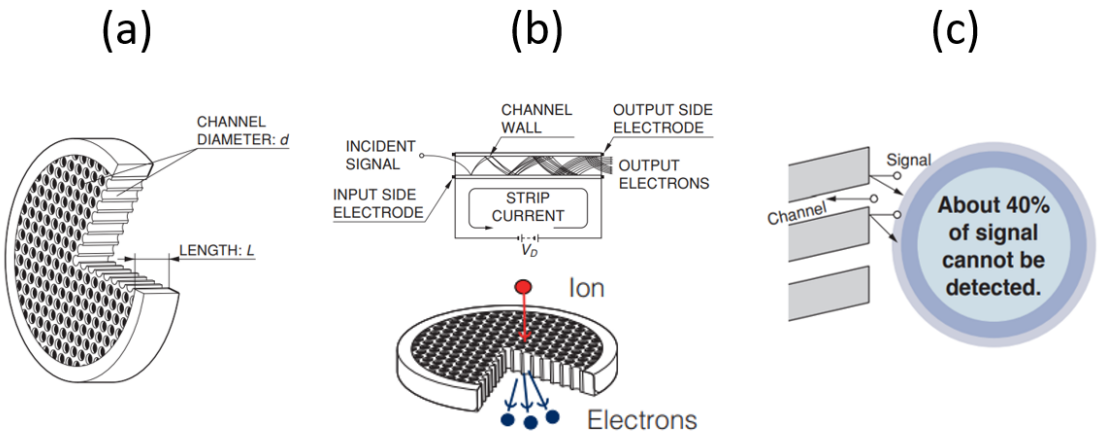


*Figure 57: (a) Schematic of a microchannel plate (MCP) consisting of microscopic channel electron multipliers of diameter d and length L, oriented parallel to one another (b) Representations of the electron multiplication mechanism (c) Some ions may collide with the surface material of the MCP failing to enter a microchannel, such collisions result in 40% of the signal not being detected (modified from [6]).*

The DLD consists of double layer of wire windings. The electrons cascade generated by incoming ions on the MCP induces electrical signals on the DLD that propagate along the wires towards their ends. The position of impact can be accurately deduced by measuring the propagation delay from one winding between the top and bottom, and the delay between the left and the right at the other winding of the detector. Multiple hit events (ions detected during the same pulse) are individually identified since their propagation delays on the DLD windings, are different. There is a limit for the detection system to discriminate signals too close in time (~1.5 ns) called dead time or Time Resolving Power (TRP), and a limit for signals too close in space (~1.5 mm) called dead zone or Spatial Resolving Power (SRP) [2]. Multiple hits happen when ions co-evaporate, that is, either neighboring atom of an element or atoms having the same m/n, evaporate within one pulse.

The first important acquired APT data is the number of the collected ions as a function of their mass-to-charge ratios. They are reported in a histogram, called mass spectrum (Figure 58).

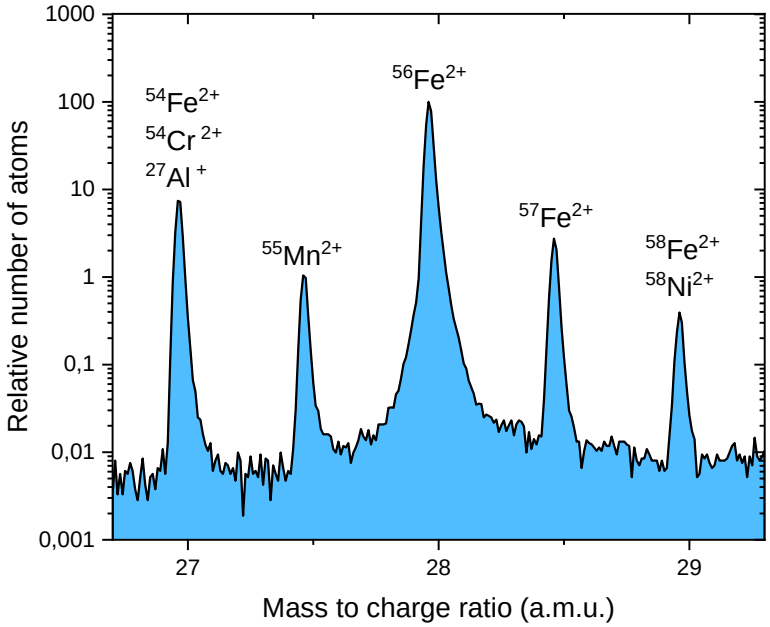


*Figure 58: Part of an APT mass spectrum of a ferritic alloy.*

In the mass spectrum, background noise is always present (the baseline is above zero). It is mainly caused by the residual gaseous atoms or molecules, despite the ultra-high vacuum in the analysis chamber, or by elements adsorbed at the specimen surface. A small part is due to electrons spontaneously generated by the detection system.

The identified peaks must be attributed to an isotope of an element, but this is not trivial. Some isotopes are overlapping, as at 29 a.m.u. where $^{58}Fe^{2+}$ and $^{58}Ni^{2+}$ can coexist or at 27 a.m.u. ($^{54}Fe^{2+}$ ,$^{27}Al^{+}$ and $^{54}Cr^{2+}$). Molecular ions can also be present as the $(^{56}Fe\ ^{16}O_2)^{2+}$ at 44 a.m.u.. In these cases, peak decomposition is performed using the expected natural abundances of the isotopes to quantify the contribution of each element.

An important indication of the "quality" of the mass spectrum is its mass resolution. Mass resolution $\left(M/\Delta M_{x\%}\right)$, is defined as the ratio of the mass-to-charge ratio (M=m/n) over the width of the peak at x% of the height of the peak (ΔMx%). For x%, usually are used the values at height 50% (full-width at half-maximum - FWHM)), at 10% (full-width at tenth-maximum (FWTM) or at 1% of the maximum of the peak (FW01M) (Figure 59). High values of mass resolution are an important factor to distinguish the peaks of elements with close m/n values.

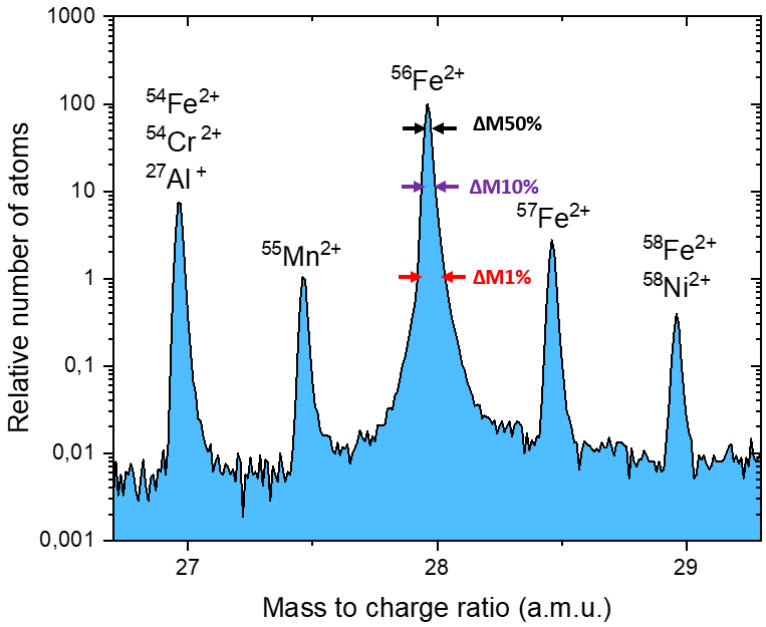


*Figure 59: Part of an APT mass spectrum of a ferritic alloy: the mass resolution at 50%, 10% and 1% is indicated in the major peak ($^{56}Fe^{2+}$).*

In the electrical mode, most of the ions are evaporated at the maximum value of the HV-pulse. The ones evaporated at a slightly different moment (but within the HV-pulse) acquire less energy resulting in peaks with a tail in the mass spectrum. To compensate this, high resolution APTs are equipped with a device called reflectron. Acting like an electrostatic mirror, the reflectron field reflects the trajectories of ions in a way that high energy ions travel longer inside the field, increasing the time of flight towards the detector and thus minimizing the time difference with the lower energy ions of the same m/n (Figure 60). This way the mass spectrum is optimized but at the cost of the detection efficiency (Q) since the electrostatic field of the reflectron is created using metal mesh electrodes, on which some of the incoming ions may collide and consequently, not be detected [4].

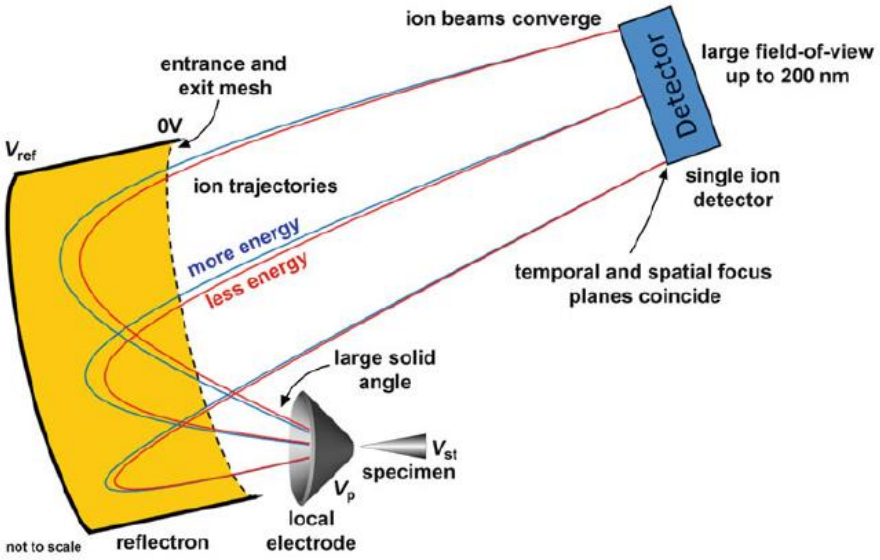


*Figure 60 Energy compensating reflectron deflecting the ions towards the detector [4]*

In the laser mode, light energy is transferred focused at the targeting area of the laser on the apex of the tip, creating thermal pulses that increase the sample temperature and trigger ion evaporation. Cooling occurs at a slower rate than heating depending on the material (thermal conductivity, tip shape and dimensions), so evaporation sustains for a few nanoseconds after the laser pulse, causing on the mass spectrum peaks having significant tails which can lead to peak overlapping and also to seriously degrade mass resolution.

The concentration of an element i, in atomic percent is calculated by:

$$C_i = \frac{N_i}{N_T} \tag{2.9}$$

where $N_i$ is the number of atoms attributed to the element i and $N_T$ is the total number of atoms of the analysis.

The uncertainty on the concentration ($\Delta C_i$), due only to counting statistics (Poisson statistics), is calculated using the standard deviation (σ), as:

$$\Delta C_i = 2\sigma = 2\sqrt{\frac{C_i(1-C_i)}{N_T}} \tag{2.10}$$

*2 – iii. Operation parameters*

- **Temperature**

The specimen is cooled down to cryogenic temperatures, between 20 and 80 K, to reduce surface atomic diffusion, which decreases the lateral resolution and the possibility of preferential evaporation to occur.

Values of the base temperature and pulse fraction must be suitably selected so that atoms of any of the specimen's elements, field evaporate owing to the addition of the HV-pulse to the standing voltage ($V_{DC}$) (Figure 61 - case 1).

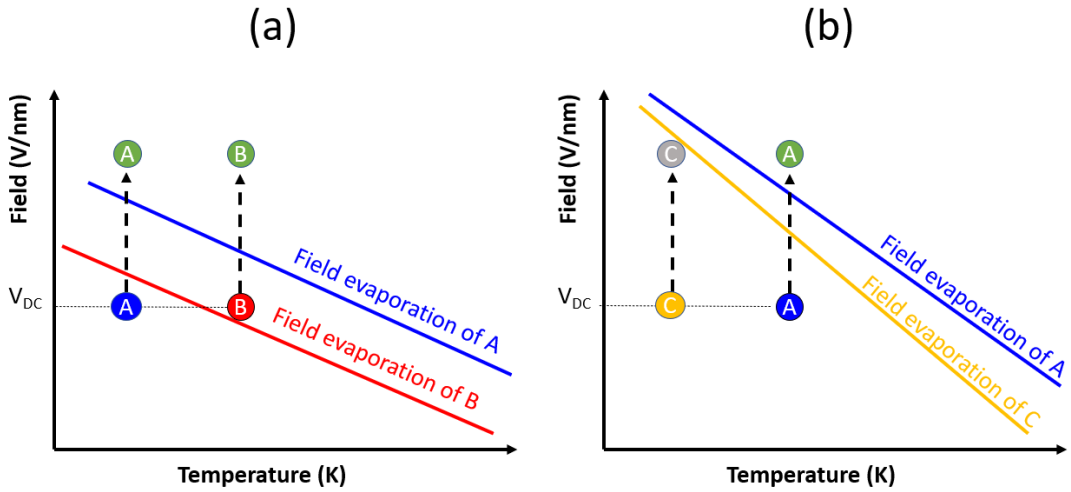


*Figure 61: $V_{DC}$ & $V_{HV}$ create an electric field (a) properly set for field evaporation of element A but causes preferential field evaporation of element B and (b) the electric field is inadequate for field evaporation of the element C causing its preferential retention.*

Preferential evaporation occurs when elements with the lower evaporation field, evaporate between pulses since the field created by the standing voltage alone, is strong enough to evaporate them. (Figure 61 - case 2). These ions are lost, either because they evaporated out of the detection window or are classified as background noise because of the incorrect time of flight that the detector assigned to them. Anyway, it results in measuring a biased composition. To counteract this effect, the base temperature is decreased, or the pulse fraction is increased. But by doing so, the probability of specimen fracture during analysis increases because of the cyclic electrostatic stress imposed by the field.

An example of an element causing important preferential evaporation, in the case of ferritic RPV steels, is Cu. Hyde [11] suggests that the optimum experimental conditions for the electrical mode to minimize the preferential evaporation of Cu are cryostat temperature of 50 K and pulse fraction of 20 % and in spite of this, 20% of the Cu atoms fail to be observed at this temperature. In 2020 Hatzoglou *et al*. [12] published an analytical model which quantifies the preferential evaporation and predicts the apparent chemical composition as a function of the experimental parameters (temperature , pulse fraction, and pulse rate). Therefore, this model can help defining the best analysis conditions, avoiding preferential evaporation to occur.

The opposite phenomenon (Figure 61 - case 3), that an element needs higher electric field to evaporate is called preferential retention. Elements having high evaporation field as the Boron (64 V $nm^{-1}$) are preferentially retained on the surface, increasing their surface concentration with time, until the field becomes high enough to field evaporate [13]. These elements might surface migrate towards high-electric field regions over the specimen surface, having significant impact on the chemical accuracy and also lowering the special resolution [14]. Since the surface migration effects are thermally activated, are more prominent when using laser pulsing mode.

- **Detection rate**

The detection rate is the average number of atoms detected per 100 pulses and typically is set to less than 0.5, to limit multiple hit events on the detector. Higher detection rate needs higher electric field which increases the probability of tip fracture and at the same time decreases the background noise.

As ions evaporate from the apex of the tip, its radius progressively increases (along with the field of view) and consequently the amplitude of the electrostatic field decreases. To counterbalance this effect, the voltage should increase accordingly, so to maintain the applied electrostatic field steady. At the same time, as the tip radius progressively increases, the detected ions evaporate and come from a wider region. In order to maintain constant the evaporation flux (ions. $s^{-1}$. $nm^{-2}$) during APT operation, the detection rate should be gradually increased.

- **Pulse rate**

Only a small fraction of pulses (considerably lower than 1%) produces events on the detector. In order to gather sufficient data at an acceptable time, high frequency of pulses is needed, typically in electric mode 200 kHz HV-pulse frequency is used. At the same time, the high frequency of the pulses minimizes the possibility of tip surface contamination from the residual gasses in the vacuum chamber.

In this study, APT experiments were carried out at 55K, with a pulse fraction of 20% and a pulse rate of 200kHz, using the CAMECA APTs LEAP 4000 X HR and LEAP 5000 XR (Figure 62) of the GENESIS platform, on electric mode. The detector efficiency of the LEAP 4000 X HR and LEAP 5000 XR is 0.36 and 0.52 respectively.

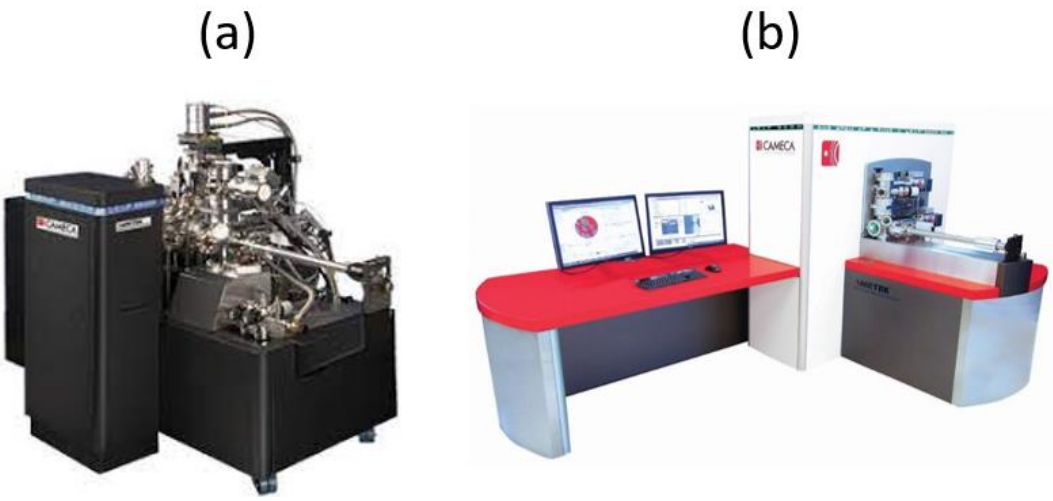


*Figure 62: The CAMECA LEAP (a) 4000 X HR and (b) 5000 X R of the GENESIS platform, GPM Rouen.*

### *2 – iv. 3D reconstruction*

In 1995, a model for the 3D reconstruction of the APT data was published by Bas et al [15]. This point-projection model assumes that all atoms have the same atomic volume and that the ions travel in perfectly straight trajectories, and estimates, by back-projection, the position (x, y) of the ions on the specimen surface at the evaporation moment, from the coordinates ($X_D$, $Y_D$) of the ion's impact position on the detector (Figure 63).

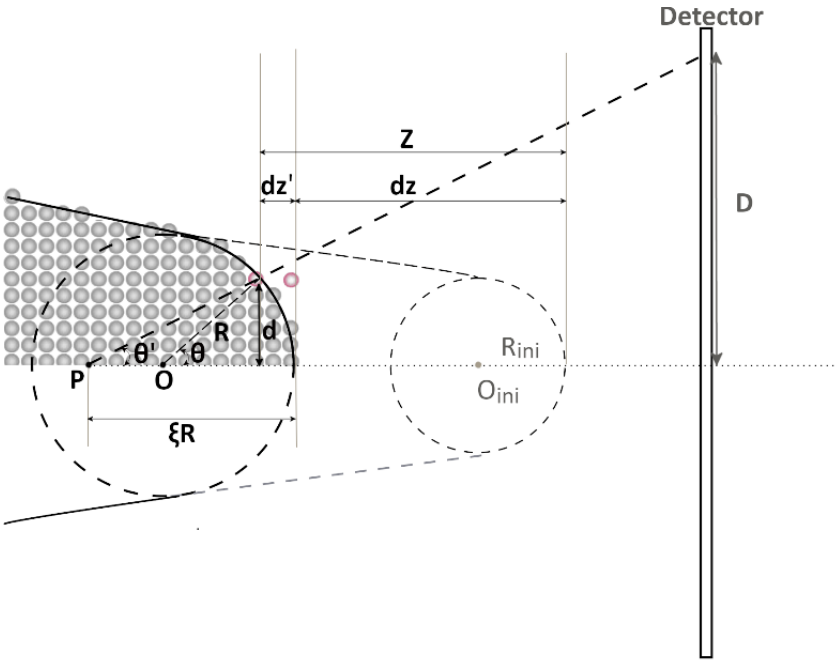


*Figure 63: Schematic drawing illustrating the basic geometrical reconstruction parameters. As the tip is field evaporated (dashed gray lines) its radius increases from $R_{ini}$ to R. modified from [1].*

As in the drawing (Figure 63), D is the distance from the ion impact point to the center of the detector and d is the distance between the specimen axis and the projection of the ion into the plane tangent to the specimen apex, then the Magnification (M) is defined as

$$M = \frac{D}{d} = \frac{L + \xi R}{\xi R} \approx \frac{L}{\xi R} \tag{2.11}$$

where ξ is the image compression factor and L is the flight path length (and since ξR is very small (in the order of a few nm) compared to L (in the order of about 40 cm -LEAP 4000), ξR+L can be approximated as L). Since angles θ and θ' are small, the image compression factor (ξ) is expressed as:

$$\xi = \frac{\tan\theta}{\tan\theta'} \approx \frac{\theta}{\theta'} \tag{2.12}$$

Using the ion's impact position ($X_D$, $Y_D$) on the detector and Equation (2.11), the coordinates (x,y) on the reconstructed specimen volume, correspond to:

$$x = \frac{X_D}{M} = \frac{X_D}{L}\xi R \quad \text{and} \quad y = \frac{Y_D}{M} = \frac{Y_D}{L}\xi R \tag{2.13}$$

The z dimension is obtained (in principle) by using the sequence of evaporated ions [15]. For the $i^{th}$ detected ion, considering the detection efficiency Q, the total field evaporated volume is $Vol_i = \frac{i}{Q} V_{at}$, where $V_{at}$ the average atomic volume.

The area of the detector, having diameter $d_D$, $S_D = \frac{\pi d_D^2}{4}$ corresponds to an area on the tip:

$$S = \frac{S_D}{M^2} = \frac{\pi d_D^2}{4M^2} \tag{2.14}$$

The field evaporated volume can be expressed also as:

$$Vol_i = i\frac{V_{at}}{Q} \approx S\, dz_i \tag{2.15}$$

and at that moment, the tip radius from (2.4) is $R_i = \frac{V_i}{k_f F}$, where $V_i$ the voltage when the $i^{th}$ ion evaporated.

The probed depth $\left(dz_i\right)$ is calculated by solving equation (2.15) and by inserting (2.14), (2.11) and (2.4):

$$dz_i = i\frac{V_{at}}{QS} = i\ \frac{V_{at}}{Q\frac{\pi d_D^2}{4M^2}} = i\ \frac{V_{at}}{Q\frac{\pi d_D^2}{4}}\left(\frac{L}{\xi R_i}\right)^2 = i\ \frac{V_{at}}{Q\frac{\pi d_D^2}{4}}\left(\frac{L\, k_f F}{\xi\, V_i}\right)^2 \tag{2.16}$$

A simple geometrical correction ($dz_i'$) is necessary to account for the curvature of the tip. Since $d_i$ is the distance of the $i^{th}$ reconstructed atom from the origin, it can be expressed by its cartesian coordinates as $d_i = \sqrt{x_i^2 + y_i^2}$ ,

and $$dz_i' = R\left(1-\sqrt{1-\frac{d_i^2}{R_i^2}}\right) = R\left(1-\sqrt{1-\frac{x_i^2+y_i^2}{R_i^2}}\right) = \frac{V_i}{k_f F}\left(1-\sqrt{1-\frac{x_i^2+y_i^2}{\left(\frac{V_i}{k_f F}\right)^2}}\right) \qquad (2.17)$$

So, the z-axis position of the $i^{th}$ detected ion ($z_i$) is the sequentially cumulating probed depth, $dz_i$, plus the corrective term $dz_i'$ for the $i^{th}$ ion:

$$z_i = \sum_1^i (dz_i) + dz_i' \qquad (2.18)$$

Inserting (2.16) and (2.17) into (2.18), it becomes:

$$z_i = \left(\sum_1^i \left(i\ \frac{V_{at}}{Q\frac{\pi d_D^2}{4}}\left(\frac{L}{\xi \mathbf{R}_i}\right)^2\right) + \mathbf{R}_i\left(1-\sqrt{1-\frac{x_i^2+y_i^2}{\left(\mathbf{R}_i\right)^2}}\right)\right) \qquad (2.19)$$

And by substituting with equation 1.4, it becomes:

$$z_i = \left(\sum_1^i \left(i\ \frac{V_{at}}{Q\frac{\pi d_D^2}{4}}\left(\frac{L k_f F}{\xi V_i}\right)^2\right) + \frac{V_i}{k_f F}\left(1-\sqrt{1-\frac{x_i^2+y_i^2}{\left(\frac{V_i}{k_f F}\right)^2}}\right)\right) \qquad (2.20)$$

Respectively, the x and y spatial coordinates of the $i^{th}$ reconstructed atom are:

$$x_i = \frac{\xi R_i}{L} X_D = \frac{\xi V_i}{L k_f F} X_D \quad \text{and} \quad y_i = \frac{\xi R_i}{L} Y_D = \frac{\xi V_i}{L k_f F} Y_D \qquad (2.21)$$

*2 – v. Reconstruction of an APT volume*

Most of the parameters needed for APT volume reconstruction are known, since they are either structural features of the instrument (L, Q, $d_D$) or measured during experiment ($X_D$, $Y_D$, $V_i$) and F is known as the evaporation field of the most abundant element of the specimen. Only $k_f$ and ξ remain to be defined (Eq (2.20)).

To define these parameters, crystallographic poles on the tip must be located and indexed based on the lattice symmetry. Poles due to the hemispherical shape of the tip, appear as structures of concentric atomic rings, namely the atomic terraces, where atomic planes (hkl) of specific orientation are parallel to the surface (Figure 64).

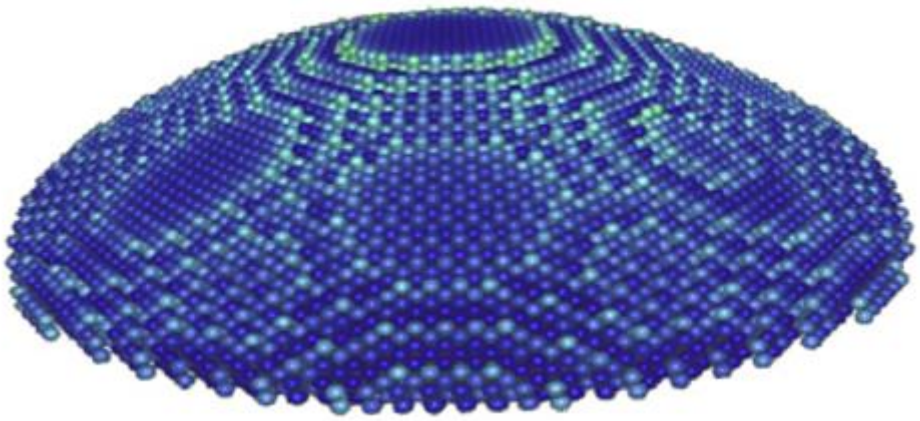

*Figure 64: Simulated representation of the atomic terraces at the apex of a tip [2].*

On a trial reconstruction made with the "usual" parameters for the alloy, i.e. $k_f$ =5.1 and ξ=1.60, the interplanar distance $d_{hkl}^{trial}$ is measured (Figure 65) ,which is proportional, Eq (2.16) to the square of the field factor used $k_f^{trial}$. Thus, using the real value for the interplanar distance $d_{hkl}$, known from crystallography, the value of $k_f$ can be adjusted as:

$$k_f = k_f^{trial}\sqrt{\frac{d_{hkl}}{d_{hkl}^{trial}}} \tag{2.22}$$

With more than one pole identified, the compression factor ξ can be approximated using Eq. (2.12) as:

$$\xi = \frac{L\theta}{D_p} \tag{2.23}$$

where $D_p$ the distance between the poles on the detector calculated using the reported X, Y coordinates.

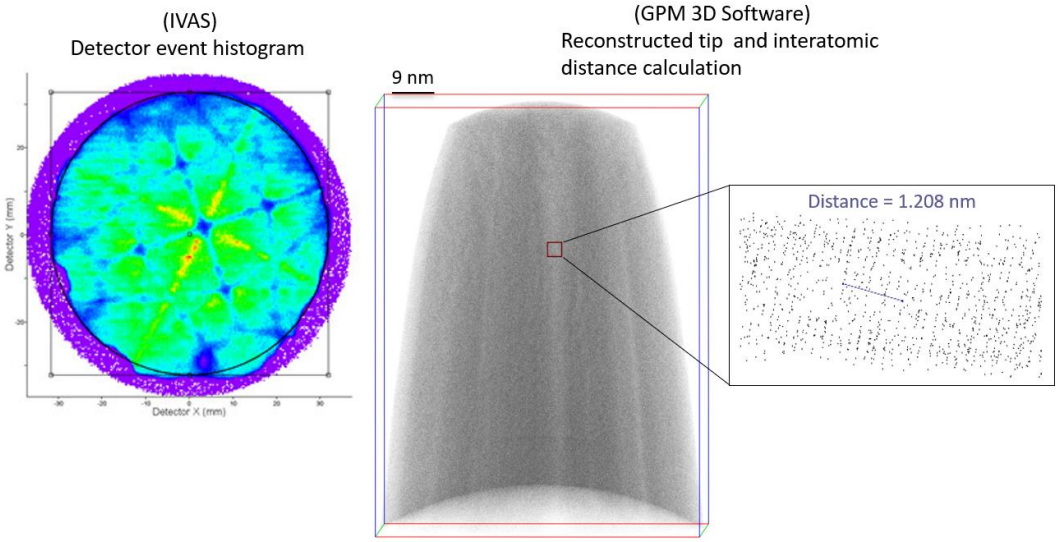


*Figure 65: To define the field factor $k_f$: (A) At the detector even histogram a crystallographic pole is identified based on the symmetry (b) At the reconstruction, the identified pole's interatomic distance is measured and used to correct the arbitrary $k_f$ value.*

The spatial resolution obtained using APT is highly anisotropic [16], [17]. The depth resolution, corresponding to the z-axis (direction of the analysis), is extremely good permitting individual atomic planes to be resolved directly. Commonly it is below 0.2 nm, which is significantly larger than a fraction of a picometer [2] that can be calculated using eq. (2.16), imposed by the uncertainty in the order of evaporation, due to the stochastic nature of the evaporation process.

Lateral x-y resolution is commonly about 1nm, affected by the physical mechanisms involved during the field evaporation. For example, despite the cryogenic temperatures, thermally activated processes, as surface diffusion and roll-up motion, can reallocate surface atoms to positions where evaporation is easier. Additionally, lateral resolution is significantly affected by diverging ion trajectories close to the tip surface [18].

Difference in the evaporation fields between the matrix ($F_M$) and the elements of a precipitate ($F_P$), provoke local variations of the curvature radius of the tip which in turn modifies the electrostatic field close to the specimen [19]. Since these field perturbations occur in the first steps of flight, they alter the ions trajectories and strongly magnify the deviations, resulting in discrepancies between the reconstructed atomic data and the original structure. This artifact, inherent to APT, is the so-called Local Magnification effect, which causes compression or expansion in the lateral X and Y directions on the tip reconstruction leaving unaffected the in-depth z-direction. Because of this, the spherical clusters of solute atoms can appear as ellipsoidal.

Specifically, in the case of high-field precipitates ($F_P > F_M$), the matrix atoms evaporate preferably before those of the precipitate, creating a locally increased curvature with a decreased radius, which generates a higher local field that repels the precipitate's ions. As a result, in the reconstruction the precipitate appears dilated with decreased atomic density.

However, in the case of the low-field precipitates ($F_P < F_M$), precipitate atoms evaporate first causing local flattening or even dimpling of the surface, which causes inwards deflection of

the trajectories, resulting in apparent compression of the precipitate with increased density (Figure 66).

Ion trajectory aberrations can bias the measured chemical composition of the particles. In the case of the low field particles, the trajectories of the matrix ions might cross the particles' and reach its core area, thus altering the measured chemical composition. (Figure 66 c). Only the core of the high field particles remains unaffected, since in this region there is no trajectory overlapping.

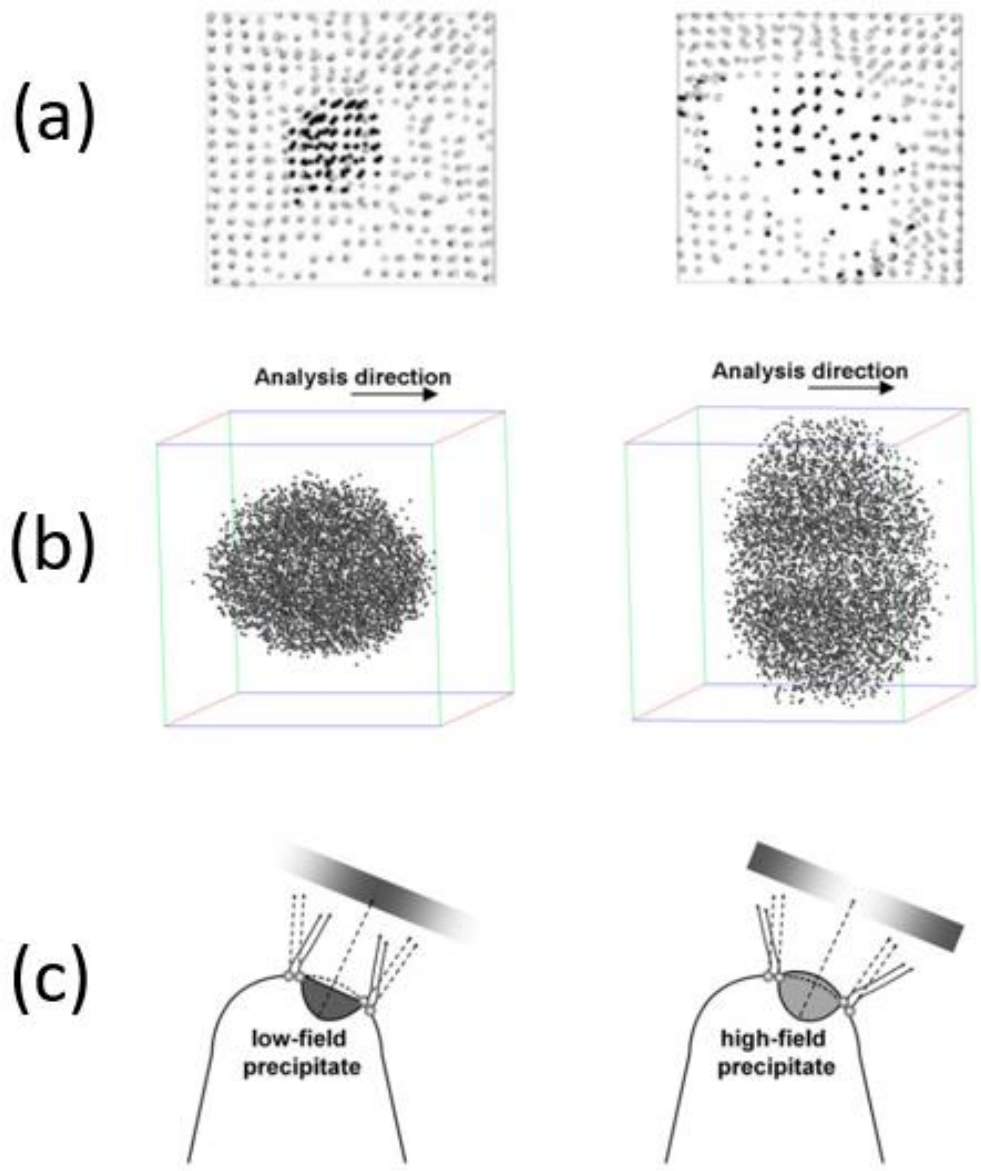


*Figure 66: For a binary alloy: (a) Cross sections of low field (left) and high field (right) reconstructed precipitates using simulation of ion trajectories [11] (b) Low field (left) precipitates are appearing elongated along the analysis direction which is indeed unaffected, while high field (right) appear compressed [20] (c) Illustration of the trajectory aberrations [2].*

*2 – vi. Cluster analysis*

## *Cluster Identification*

When in the reconstructed volume there are not obvious precipitates, it is very useful to determine if solute atoms are randomly distributed among matrix atoms or if there is an evidence of early stages of phase decomposition leading to nucleation of very small clusters [2]. For this an experimental frequency distribution of the element(s) in question is calculated and compared to a theoretical random distribution.

A variety of algorithms for clusters detection and their quantitative analysis are available. The most commonly used algorithm is the Maximum Separation Method (MSM) that calculates the distances to the $N^{th}$ Nearest Neighbor (NNN), usually the 1NN (first nearest neighbor) [2]. A maximum distance ($d_{max}$) is defined and solute atoms at a distance less than $d_{max}$ are grouped together to form a cluster. The so defined clusters contain only solute atoms. To select and include atoms of the other elements being in the vicinity of the cluster, the association and erosion method is used. In this step, at first, all atoms being at a selected distance L, around the atoms allocated to the cluster, are also included. Then the cluster is eroded from the solvent atoms that are within a distance $d_{ero}$ from any of the matrix atoms (Figure 67).

Finally, the clusters having less than a minimum number of atoms ($N_{min}$) are removed to eliminate artificially generated clusters due to concentration statistical fluctuations.

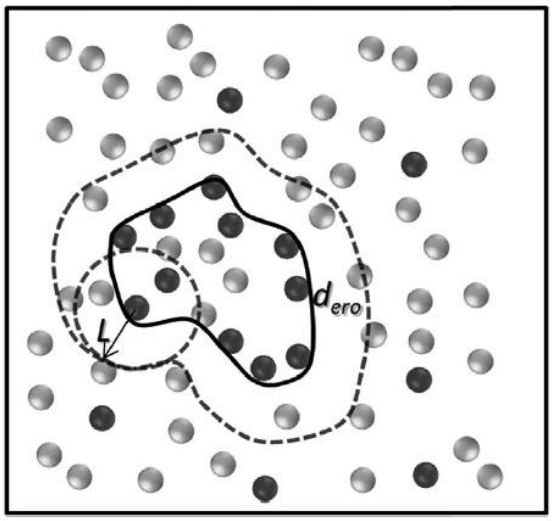


*Figure 67: Schematic illustration of the association and erosion method. Solvent atoms are represented with gray whereas solute atoms are represented with black [2].*

Using six simulated microstructures and consequently known clusters' data, Hyde *et al.* [21] compared the results produced by this method with those using another algorithm developed at GPM Normandie Rouen University, the Isoposition Method (IPM) [22]. They concluded that IPM was more efficient at detecting small clusters (less than 1 nm) than the MSM method and also using IPM, local magnification has no influence on the cluster detection.

In the present study, the Isoposition Method is used to identify the solute clusters and its working principles will be briefly explained.

The algorithm divides the sample volume into a grid of sub-volumes, corresponding to cubes of equal size (called voxels). A virtual 'core solutes element' (CS) is created by unifying all the main solute elements (i) considered to form the cluster, e.g., Ni, Mn, Si etc., so that:

$$X_{CS} = \bigcup_i X_i \tag{2.24}$$

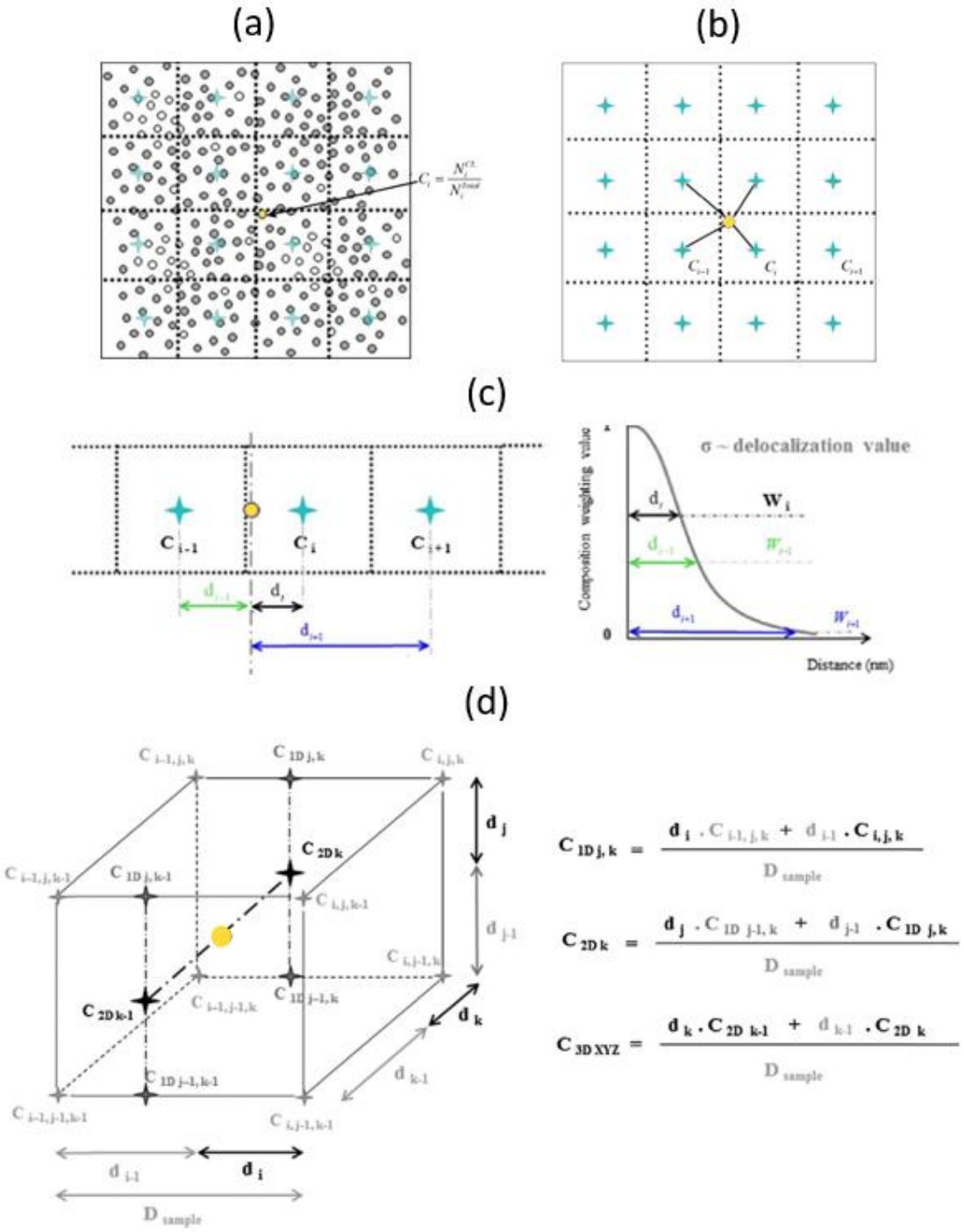


*Figure 68: The isoposition method: (A) The analysis volume is divided by a grid to voxels. To the center of each voxel a concentration value is assigned. (C) in the simplified 1-D grid the local concentration of each atom is calculated as a function of its distance to the neighboring grid volumes, weighted by a factor W. For 2D (B) & 3D grids (C), composition is calculated using interpolations, after [2].*

A concentration value is assigned to each sub-volume center, computed as the ratio of the number of core solutes atoms (CS) to the total number of atoms in the sub-volume, that is:

$$C_i = N_i^{CS} / N_i^{Total} \tag{2.25}$$

The local concentration associated to the position of each atom is calculated as a function of its distance to the center of neighboring grid volumes, weighted by a factor W. The value of the W depends on the distance between the atom and the center of the sampling box and is derived from the superimposed Gaussian function with a user defined standard deviation (σ), commonly equal to 0.5. As an example (Figure 68: - c), in the simplified 1-D grid case, the concentration at the atom position is:

$$C_i^{atom} = C_{i-1}W_{i-1} + C_iW_i + C_{i+1}W_{i+1} \tag{2.26}$$

In the example, the third term, $C_{i+1}W_{i+1}$, can be omitted since the weight values are negligible beyond 3σ.

For the 3D volume, the concentration $\left(C_{(x,y,z)}\right)$ associated on each atom positioned at the (x, y, z) coordinates, is calculated using tri-linear interpolations (Figure 68: - d).

Any atom is considered as a potential cluster atom, if its concentration is higher than a user defined value $C_{Thr}$. The envelope method is applied to define the clusters atoms, group them together and form the clusters (Figure 69). The user defines a new fine grid, having edge $d_{grid}$, to divide again the analysis volume into voxels. To the cluster are assigned all the atoms that belong to neighboring voxels that contain potential cluster atoms or any voxels that are surrounded by other cluster voxels.

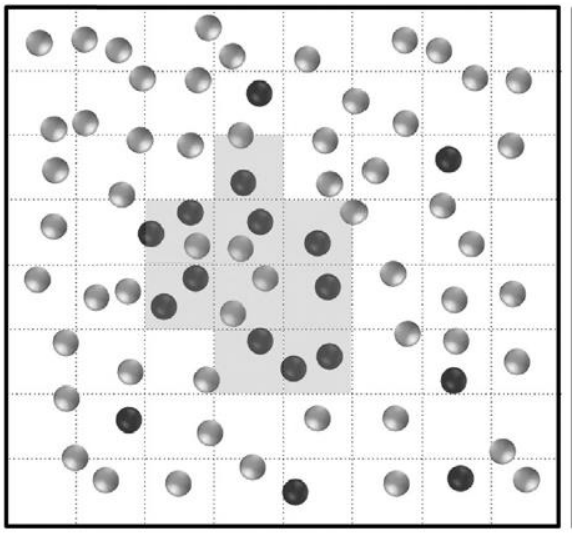

*Figure 69: Schematic illustration of the envelope method. The atoms of the neighboring voxels that contain potential cluster atoms, are grouped together and form a cluster [2]*

Alike the MSM method, to avoid clusters generated due to statistical concentration fluctuations, clusters having less than a minimum number of solute atoms ($N_{min}$) are considered as matrix.

When using the GPM Software, the value of the parameter $N_{min}$ is selected such as not to produce any cluster in a theoretical random volume.

## Erosion profiles

When the cluster identification is completed, the algorithm usually characterizes as cluster atoms, some of the matrix atoms that are located at the nearby surrounding area (cluster - matrix interface). In order to reassign these atoms to the matrix, the clusters are sorted into size ranges and for each size range, an erosion profile is plotted by the GPM software, as follows:

All cluster atoms, being at a certain distance from their nearest matrix atom, are summed up at a distance class, that by convention has negative sign. For all negative distance classes, the concentration profile is plotted. The same procedure is followed for the matrix atoms as well, but this time the distance is considered positive (Figure 70).

The zero distance indicates the position of the matrix-cluster interface, as identified by the clustering algorithm.

The boundaries of the clusters are moved back at a (negative) distance $d_{MH}$ corresponding at a concentration having the half-maximum value of the clusters' atoms and the atoms within this distance are reassigned as matrix atoms (Figure 70). The clusters have now acquired their final shape.

To minimize compositional biases, another erosion is performed at a distance $d_{PL}$ corresponding to the start of the area where the cluster atoms concentration is almost constant (forming a plateau). By doing so, the concentration is calculated only from a volume representing the core of the cluster which is the less affected by the APT artifacts due to trajectory aberrations or by an ill-defined matrix-cluster interface.

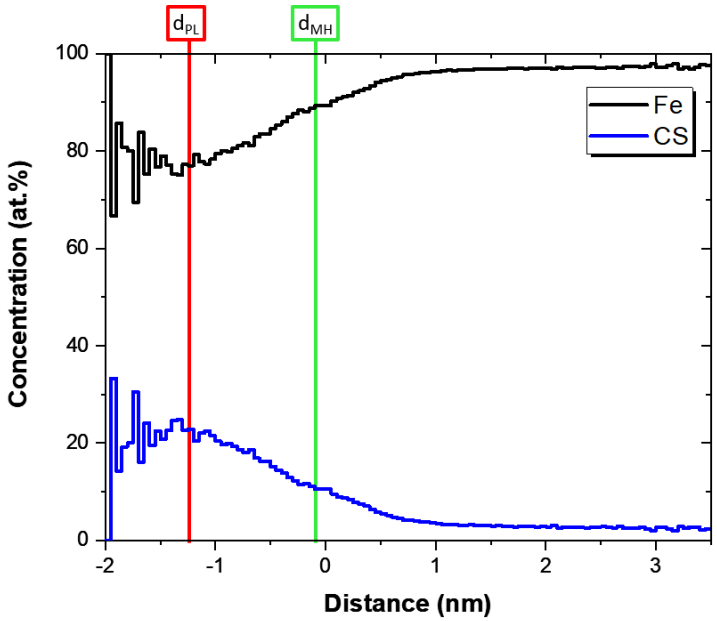


*Figure 70: Erosion profile of a ferritic alloy. Illustrating the concentration of the Fe and (CS) core solutes element. The clusters are eroded at the distance ($d_{MH}$) corresponding to a concentration having the half-maximum value and their core region is obtained by eroding at distance $d_{PL}$ corresponding to a rather constant maximum concentration of cluster atoms.*

## Cluster analysis

Having defined the clusters, now it is possible to visualize and to quantify them in terms of size, morphology, number density, volumes fraction and composition.

Cluster size can be characterized by the average radius:

$$< R >= \frac{1}{N_{CL}} \sum_{i=1}^{N_{CL}} R_i \qquad (2.27)$$

For cluster radius, the Guinier radius ($R_G$) is usually used. It is defined as:

$$R_G = \sqrt{\frac{5}{3}} R_g \qquad (2.28)$$

where $R_g$ is the *gyration radius* defined as the root mean square of mass-weighted distances of all sub-volumes in a particle from the center of mass and is calculated as:

$$R_g = \sqrt{\frac{1}{n} \sum_{i=1}^{n} (x_i - x_0)^2 + (y_i - y_0)^2 + (z_i - z_0)^2} \qquad (2.29)$$

where n the number of the atoms in the cluster, $(x_i, y_i, z_i)$ the coordinates of the $i^{th}$ atom of the cluster and $(x_0, y_0, z_0)$ the coordinates of the mass center of the cluster.

Alternatively, assuming that the clusters are almost spherical, cluster size can be estimated from the number of the atoms (n), in each cluster using:

$$R_{eq} = \sqrt[3]{\frac{3nV_{at}}{4\pi Q}} \quad (2.30)$$

where $V_{at}$ is the atomic volume and Q the APT's detector efficiency.

The Number Density (ND) of the clusters is the ratio of the number of the observed clusters to the analyzed volume ($V_{analysis}$):

$$ND = \frac{N_{clusters}}{V_{analysis}} = \frac{N_{clusters} Q}{N_{at}\, V_{at}} \quad (2.31)$$

Where $N_{at}$ is the number of the detected atoms of the analyzed volume

Regarding the volume fraction of clusters, 3 definitions are used:

1. As the ratio of the number of atoms contained in the clusters to the total number of the collected atoms:

$$fv = \frac{N_{at(CL)}}{N_{at}} \quad (2.32)$$

2. Using the number density (ND) and their average radius R (either $R_G$ or $R_{eq}$):

$$fv = \frac{4}{3}\pi < R^3 > ND \quad (2.33)$$

3. Using matter conservation as:

$$fv = \frac{X_{Global} - X_{Matrix}}{X_{Cluster} - X_{Matrix}} \quad (2.34)$$

where $X_{global}$, $X_{matrix}$ and $X_{cluster}$ are the global, matrix and cluster concentrations respectively.

In this work, the first method is reported in the results, since the number of the atoms are counted accurately (for the defined analysis parameters) while the other two methods involve the incertitude of the measurements. Moreover, for the number density calculation, clusters on the edge of the volume are counted as half and are ignored for the calculations of the average radius and composition, in order to avoid bias.

## Uncertainty Analysis

For each analyzed APT tip, the global, matrix and clusters composition, along with the clusters average Rg, Req, ND and fv were calculated as discussed. For every model alloy, multiple APT experiments were performed. Therefore, the ion weighted mean and standard deviation were calculated from the means of all the APT experiments, for a given alloy, by using the following formulas [7], [8]:

$$\bar{x}_w = \frac{\sum_{i=1}^{N} w_i x_i}{\sum_{i=1}^{N} w_i}, \quad sd_w = \sqrt{\frac{\sum_{i=1}^{N} w_i \left(x_i - \bar{x}_w\right)}{\frac{(N-1)}{N}\sum_{i=1}^{N} w_i}} \tag{2.35}$$

Where $\bar{x}_w$ is the weighted mean value for all the experiments of given alloy, $x_i$ is the calculated value for the $i^{th}$ experiment, $w_i$ is the weight (the number of atoms) for the $i^{th}$ experiment and N and the total number of APT experiments for given alloy.

To indicate the uncertainty around the estimated mean value of each alloy, we use the standard error of the mean, calculated as

$$SE = \frac{Sd_w}{\sqrt{N}} \tag{2.36}$$

The 95% confidence interval [9], [10]is obtained when a margin equal to two times the standard error of the mean is used above and below the weighted mean value ( $\bar{x}_w \pm 2\times SE$).

## Cluster Morphology

The identified clusters usually do not appear perfectly spherical (if they are). Their morphologies can be characterized using the cluster's aspect ratio and oblateness [23], derived from their smallest, middle and largest dimension of the best-fit ellipsoid of each cluster, provided by the GPM software.

$$\text{Aspect Ratio} = \frac{\text{Middle dimention of the cluster}}{\text{Largest dimention of the cluster}} \tag{2.37}$$

$$\text{Oblateness} = \frac{\text{Smallest dimention of the cluster}}{\text{Middle dimention of the cluster}} \tag{2.38}$$

Combining these two ratios, the cluster's morphology can be defined as sphere, rod, lath or disc (Figure 71).

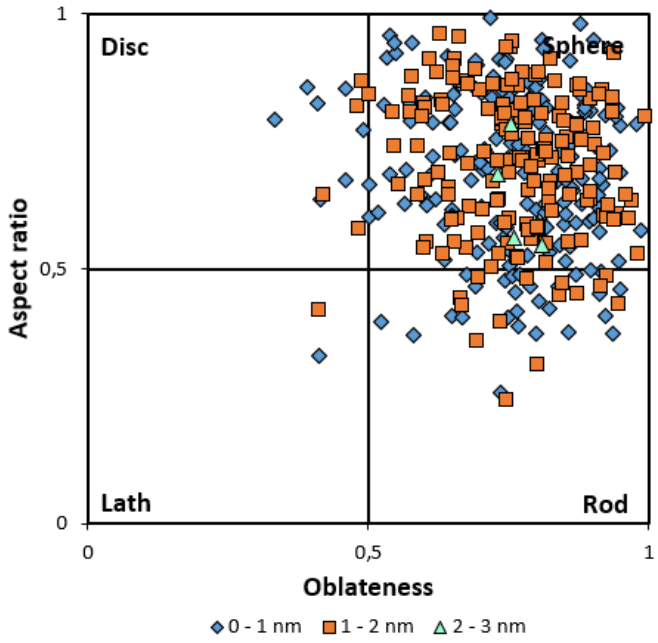


*Figure 71: Diagram of the aspect ratio vs oblateness of the identified clusters in a Fe-Mn neutron irradiated sample. Class sizes are identified by different colors to evaluate the evolution of the morphology of the clusters in respect to their size.*

## Chemical Composition Correction model

Trajectory aberrations of the evaporated ions due to the local magnification effect are caused by the lower evaporation field of the solutes-rich clusters. Specifically, trajectory focusing can result in altering the shape of the reconstructed particles, and if trajectory overlaps take place, then may result in the artificial introduction of matrix elements (Fe atoms mainly) inside the clusters, as well, biasing their chemical composition. This artifact is observed in APT atomic reconstructions as an unjustified much higher atomic density at the cluster's area compared to the density of the nearby matrix. The degree to which APT overestimates the Fe content of these clusters is still a topic of strong debate.

In order to calculate the real, free from APT biases, chemical composition of the nanoclusters, C. Hatzoglou and coworkers [16–18] published the Chemical Composition Correction model (CCC model). This model is applicable to cubic or spherical particles. The degree that the atomic density is altered by the ions' trajectory aberrations and the apparent shape, should be studied individually for each particle.

For this, concentration profiles are plotted through each particle along its three main directions (Figure 72). The Z profile is oriented along the evaporation direction, while X, Y are perpendicular to each other and also to Z. The cluster's shape factor (S) is defined by:

$$S = \frac{XY}{Z^2} \tag{2.39}$$

with X, Y, Z the cluster's dimensions measured by APT. For S = 1 morphology is not biased, and the shape of the cluster is perfectly spherical. If shape factor S < 1 it suggests a compression of the cluster perpendicular to the evaporation direction, while S > 1 indicates that the cluster is expanded.

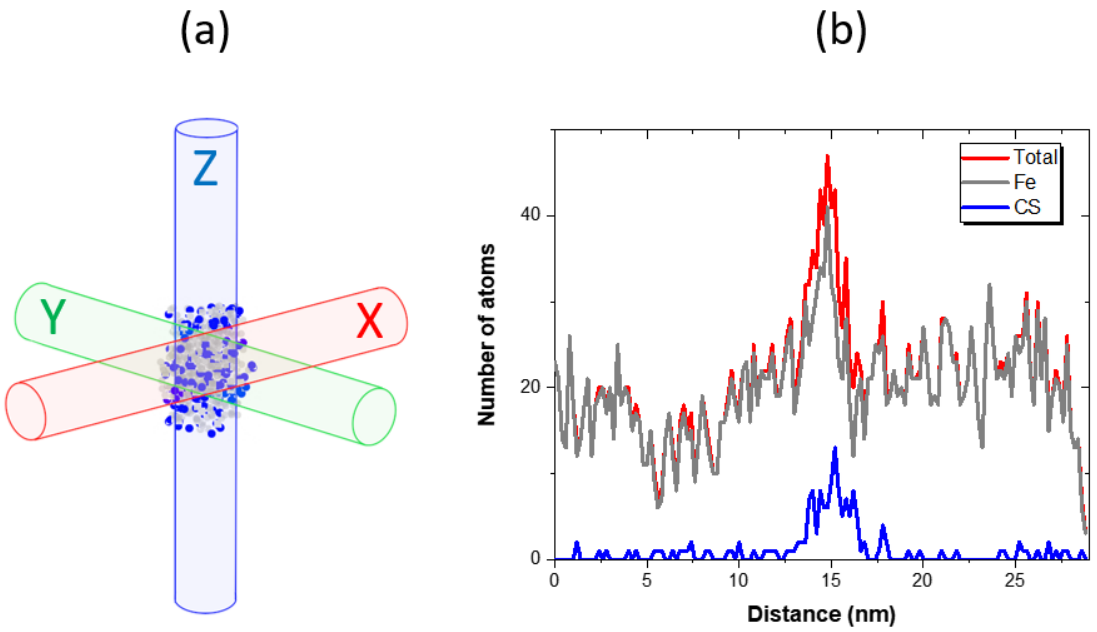


*Figure 72: (a) Cylindrical concentration profiles through a particle along its three characteristics directions. The Z (blue) profile is oriented along the evaporation direction (b) Diagram of the solutes (CS), solvent (Fe) and the total number of atoms along the Y axis profile derived from the concentration profile data, of a cluster in a Fe-Mn-Ni neutron irradiated sample.*

The presence of the APT artifact (local magnification effect) is evidenced by comparing the atomic density of a cluster with the atomic density of the surrounding matrix, namely by the reduced density ($\rho_r$) [27]. In the case of cylindrical concentration profiles, reduced density is calculated using the following relation:

$$\rho_r = \frac{V_{at}}{Q} \cdot \frac{N_B}{N.d_p.\pi R^2} \tag{2.40}$$

where R is the radius of the cross section of the cylindrical concentration profile, $V_{at}$ the atomic volume of a ferritic BCC structure ($1.17 \times 10^{-2}$ nm$^3$), Q the APT detector efficiency, N the number of elementary volumes that compose the profile, $d_p$ the depth of the elementary volume and $N_B$ the total number of atoms contained in the volume.

According to the CCC model the real chemical concentration of the i-element in a cluster is formulated by:

$$X_R^i = \left(X_{Mes}^i - X_{Mtx}^i\right)\frac{\rho_r S}{\gamma} + X_{Mtx}^i\left(1 - p_{NQ}\right) + p_{NQ}^i \tag{2.41}$$

where $X_R^i, X_{Mes}^i, X_{Mtx}^i$ the real, the APT measured and the matrix concentration of the i-element respectively, $p_{NQ} = N_{NQ} / N_R$, the proportion of the non-quantified atoms ($N_{NQ}$) due to APT artifacts such as preferential evaporation and $N_R$ the real number of particles' atoms

expected by APT and $p_{NQ}^{i}$ the proportion of the i-element's non-quantified atoms and $\gamma = \frac{V_{at}^{Mtx}}{V_{at}^{NP}}$.

In the present study, the APT analysis conditions have been suitably adjusted for our samples, in order to avoid preferential evaporation and thus the proportion of non-quantified atoms into the particles ( $p_{NQ}$ ) and ( $p_{NQ}^{i}$ ) to become negligible. So, for the real Fe concentration inside each cluster, assuming that $V_{at}^{Mtx} \approx V_{at}^{NP}$ , Eq(2.41) simplifies to:

$$X_{R}^{Fe} = \left( X_{Mes}^{Fe} - X_{Mtx}^{Fe} \right) \rho_r S + X_{Mtx}^{Fe} \tag{2.42}$$

A reasonable compromise was made, to use a radius of about 1nm for the cylindrical concentration profiles, since they are large enough for calculating the dilute solutes concentration and small enough to fit inside the bigger sized clusters detected at the APT analysis.

For each material and state, in average 6 clusters from every APT analysis, were studied with the CCC model to evaluate the existence of a possible chemical bias.

*2 – vii. Tip fabrication*

Most of the APT tips studied, were fabricated from lift outs from the surface of the samples using the ZEISS XB 540 SEM/FIB. For this, a protective 0.5 μm Pt layer is deposited on a selected polished region using the Gas Injection System (GIS). Trapezoid shapes are milled (Figure 73 – a) with a Ga ion beam of 30kV and 15 nA, followed by rectangle shapes near the protective layer region, milled with decreased current. The obtained 20 x 2 x 4 $\mu m^3$ chunk is Pt-welded on the Omni Probe 400 Oxford micromanipulator and lifted out of the material. It is then welded on one of the 36 flat-top microtips of a Si coupon (Figure 73 – b). From the chunk usually 5-6 tips can be made.

Successive annular milling steps using a ring shape mask (Figure 73 – c) are performed with Ga ion beam with accelerating voltage of 30kV and currents from 700pA to 20pA to obtain the thin needle-shape. During this procedure, the protective Pt layer is removed, and the tip is subjected to Ga ion implantation. Thus, a final cleaning step using low voltage Ga ions (2 kV and 90 pA), is needed to remove 100 – 250 nm from the surface, before the tip gets its final form (Figure 73 – d).

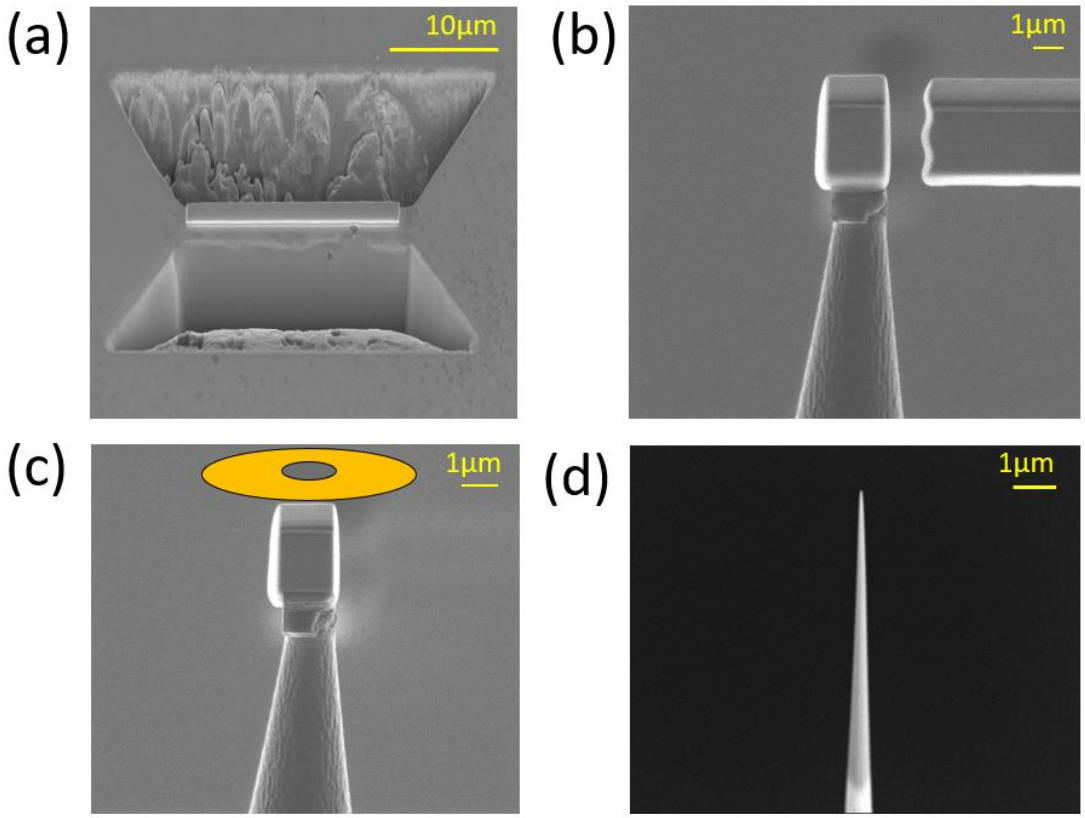


*Figure 73: FIB fabrication of an APT tip: (a) after Pt deposition, trapezoid shapes are milled to remove the maximum possible amount of material for lift-out. (b) Once the chunk is lifted out, it is welded on Si coupon pre-tips. (c) To achieve the needle-shape, a ring shape mask is applied for the annular milling procedure (d) a final cleaning step using low voltage is applied to minimize Ga ion contamination.*

In this study, the bulk samples' microstructure was investigated by APT but also, compressed pillars in the non-irradiated and neutron irradiated state were studied. These samples were prepared by depositing a protective Pt layer and then lifting out the pillar as in Figure 74 - a. The chunk was then welded on a one of the 36 flat-top microtips of a Si coupon, followed by the described annular and cleaning procedure so that the tip will take its final form (Figure 74 – b and c).

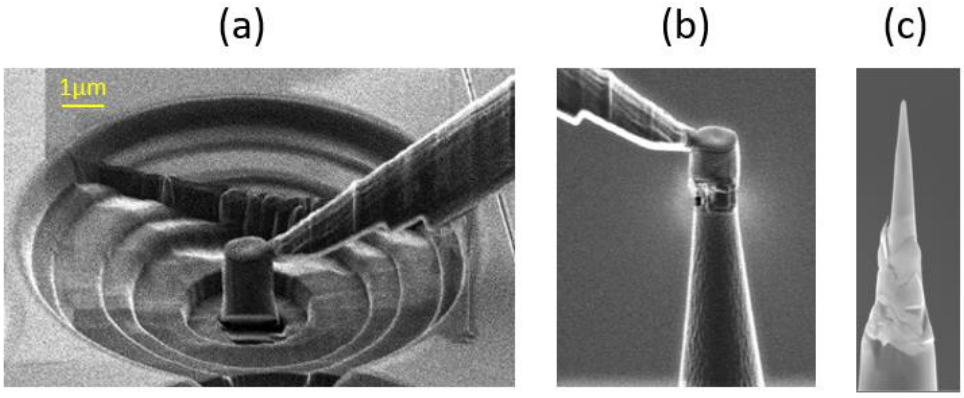


*Figure 74: FIB fabrication of an APT tip from a compressed pillar: (a) after Pt deposition the pillar is welded on a micro-manipulator and lifted-out (b) Once the chunk is lifted out, it is welded on Si coupon pre-tips (c) Annular milling and a final cleaning step using low voltage are applied, giving the tip's final shape.*

A more traditional way of fabricating APT tips is the chemical electropolishing. The material in the form of an about 20 x 0.3 x 0.3 $mm^3$ rod is repeatedly inserted through a metallic loop holding an electrolyte droplet (in this case, first, 25% perchloric acid in 75% acetic acid and next, 2% perchloric acid and 98% 2-butoxyethanol, but it depends on the nature of the sample) (Figure 75). Since the volume of electrolyte used is just a droplet, it must be renewed frequently to avoid electrolyte depletion. The loop is connected to the cathode of a continuous or pulsed DC voltage power supply and the specimen to the anode. After the sample has acquired the needle shape, it is removed and rinsed with alcohol.

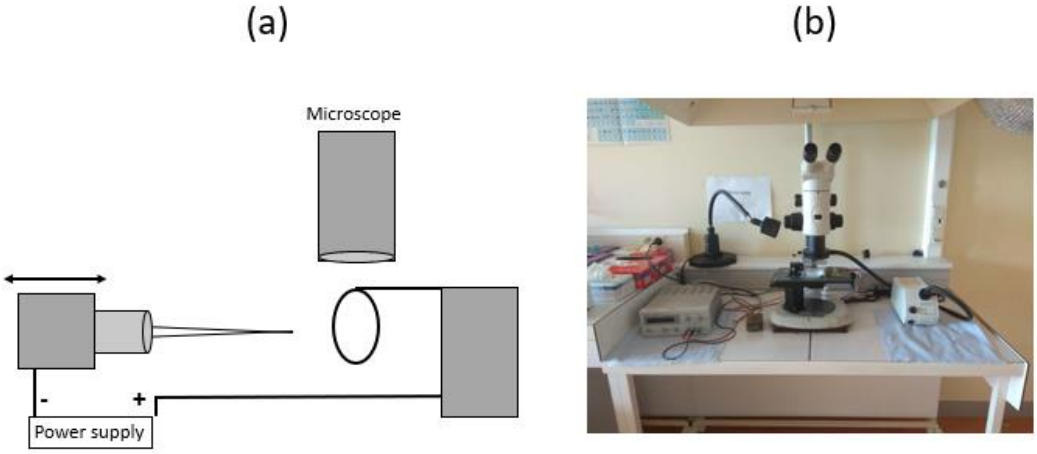


*Figure 75: (a) Schematic diagram and (b) the actual used micro-loop in the GPM laboratory.*

**Acknowledgement**

The tips of the neutron irradiated and annealed Fe-1.1Mn-0.7Ni samples were fabricated using electropolishing and analyzed by APT, at a prior time, by the supervisor of this PhD study, Dr. B. Radiguet, who handed me the acquired raw data, to study them using the IVAS and GPM 3D software.

## 3. Electron Backscatter Diffraction

After properly polishing, a grid was fabricated on the samples' surface using FIB, to facilitate locating the grains of interest while imaging the sample on the Scanning Electron Microscope. To select the appropriate grains inside which micropillars will be fabricated, knowledge of their crystallographic orientation is required.

Electron backscatter diffraction (EBSD) is a scanning electron microscope (SEM) based technique, characterizing the crystallography of a sample, providing information such as phases identification, the crystal lattice and grain orientations. EBSD analysis is a non-destructive but surface sensitive technique that needs well-polished and cleaned samples. The polished sample is placed in the SEM, tilted to approximately 70° relative to the horizontal, forming about 20° angle to the electron beam (Figure 76).

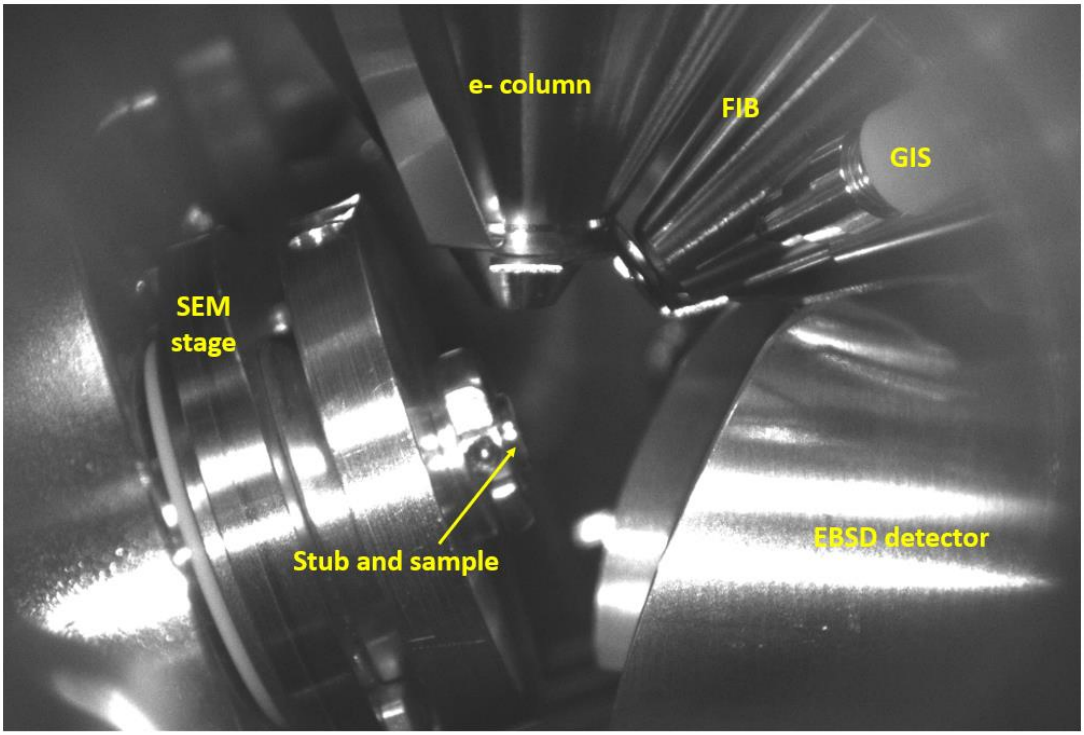


*Figure 76: SEM configuration for EBSD analysis: the ZEISS XB540's stage is tilted at 70º relative to the horizontal forming a 20º angle to the electron column and the EBSD detector is inserted. The FIB and GIS systems are also visible.*

Some of the beam's electrons are backscattered, that is, they interact with the atoms of the material and get scattered incoherently and quasi-elastically, suffering a small energy loss but an important change in their propagation direction, resulting in electrons traveling in all directions. The backscattered electrons appear as to emerge from a virtual point source, located below the surface of the crystalline material.

Using Monte-Carlo simulations of the backscattered electron trajectories, Zaefferer [28] calculated that in iron, the electrons originate from a maximum depth of 5.5 nm and experimentally measured for 15 kV electrons, a depth of 2 nm with lateral dimensions of 90 x 35 $nm^2$. Using these values, Mainprice [29] illustrated the interaction volume for the EBSD (Figure 77), which for the iron has a thin elliptical disc shape and is clearly very different from the well-known, for the X-Rays, pear shape volume.

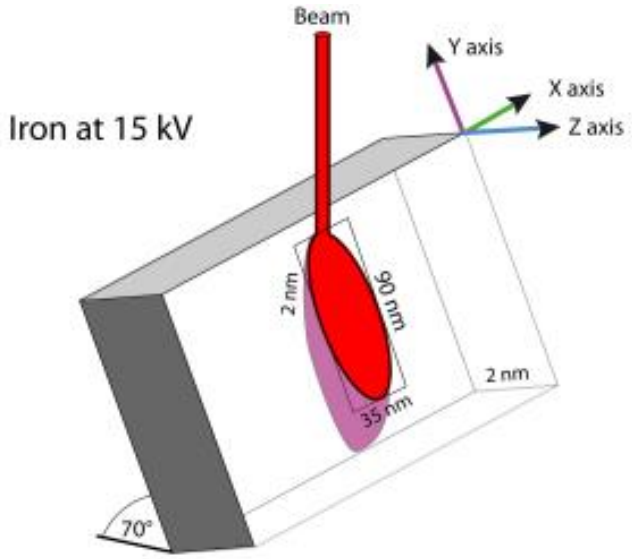


*Figure 77: As electrons of the primary beam with an accelerating voltage of 15kV hit the tilted specimen, electrons scatter quasi-elastically (backscatter). The interaction volume between the diffracting electrons and the sample makes a disc-like shape with thickness of 2nm for Fe [29].*

A fraction of these back scattered electrons is diffracted by the lattice planes, if their angle of incidence satisfies the Bragg condition:

$$n\lambda = 2d\ sin\theta \qquad (2.43)$$

where d is the spacing between planes, θ is the Bragg angle, λ the wavelength of the electron and n the order of diffraction.

Due to the cylindrical symmetry of the Bragg reflection condition with respect to the lattice plane normal [30], these electrons are diffracted forming pairs of diffraction cones (called "Kossel cones"). The intersection of the cones on the electron sensitive screen (a phosphor screen or a scintillator) produces the Kikuchi bands (Figure 78).

The imposed accelerating voltage (typically 10-20 kV) defines the wavelength of the electrons beam, which in turn determines that the typical Bragg angle is at the order of 1°. The very small Bragg angle explains why each diffraction cone is so flat, making Kikuchi lines to appear as almost straight lines.

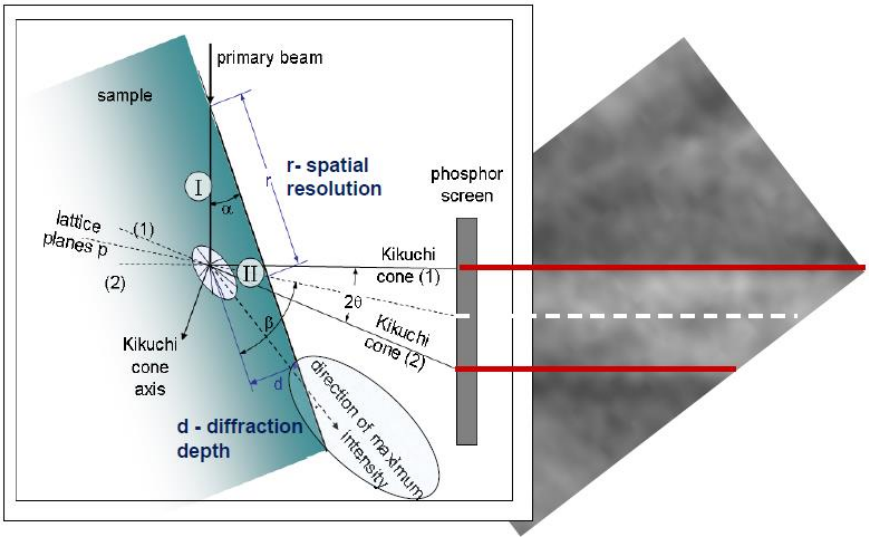


*Figure 78: A fraction of SEM column's electrons that hit the specimen, scatter quasi-elastically (I). These backscatter electrons create a virtual point source (II) from where electrons diffuse in all directions. Some of them satisfy the Bragg condition, diffract elastically and form a Kikuchi band which is recorded on the phosphor screen [31].*

The width of a Kikuchi band can be derived from the Bragg equation, using the small angle approximation, as:

$$w \approx \frac{l n \lambda}{d} \tag{2.44}$$

where w is the band's width and l the distance from the sample to the screen.

Each of the crystallographic planes that satisfy the Bragg condition produces a Kikuchi band and all together form the Kikuchi pattern. The Kikuchi pattern is bound to the crystal structure of the sample and changes with the crystal orientation (Figure 79).

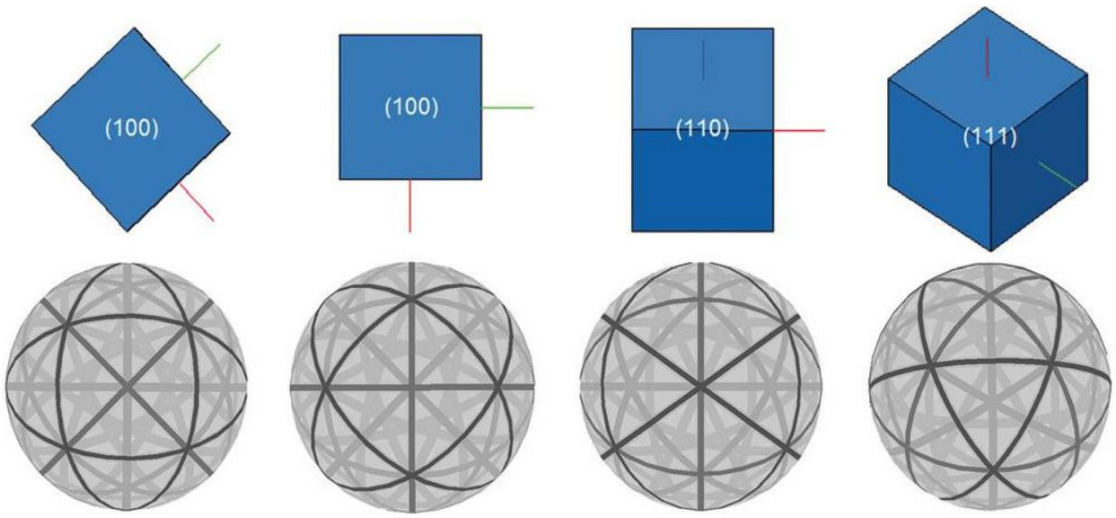


*Figure 79:Each orientation of a cubic structure generates a discrete spherical diffraction pattern [32]*

The angles between Kikuchi bands correspond to the interplanar angles and the star-like band crossings correspond to the zone axes of the crystal lattice. Thus, by digitizing and processing the geometry of the Kikuchi bands' pattern, the crystallographic phase and orientation can be defined.

Unlike humans, computers do not easily perceive lines, especially if they are fragmented. Hence to accurately detect Kikuchi bands, first a Hough transformation is needed [33–35] . In the image space, each line that passes through a defined pixel at the coordinates x, y can be described using the Hough parameters ρ and θ, as:

$$\rho = x\cos\theta + y\sin\theta \tag{2.45}$$

where ρ represents the perpendicular distance from the line to origin and θ the angle of its normal with the x-axis, as in Figure 80.

In this way, each pixel in image space transforms into a sinusoidal curve in Hough space and every point of the curve in Hough space represents a possible line, passing from one pixel in the image space. Thus, a line on the image transforms to a bright point in Hough space at the converging point of the sinusoidal curves (Figure 80).

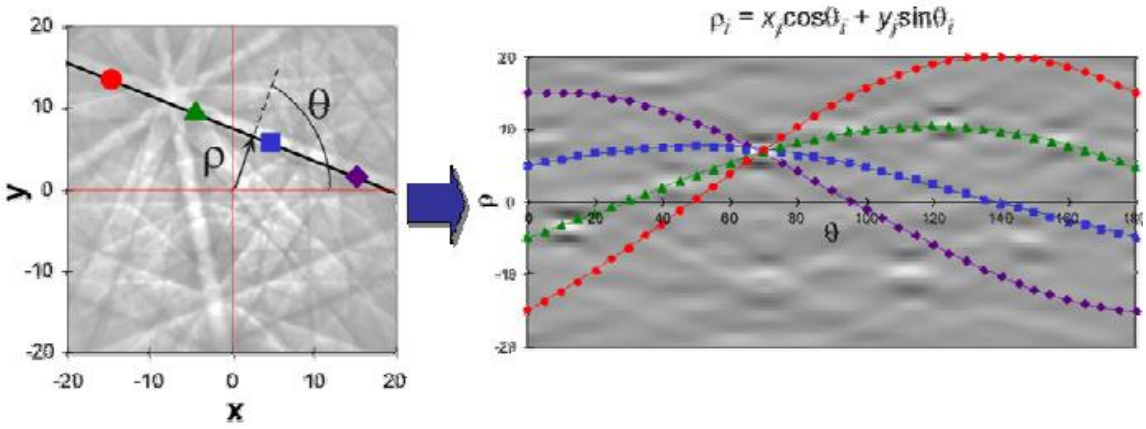


*Figure 80: On the Kikuchi pattern, each of the 4 pixels along a line is transformed, using the Hough parameters ρ and ϑ, to one of the 4 sinusoidal curves at the Hough space, their converging point (bright spot) represents the line ,on the image, that the pixels belon [36].*

When the Kikuchi band positions is defined, the angles between the detected bands are calculated in triplets. However, since the angles are distorted by the gnomonic projection of the pattern of the tilted sample on the flat phosphorus screen [37], [38], the accuracy of band detection is limited, and each triplet could possibly represent multiple orientations (Figure 81).

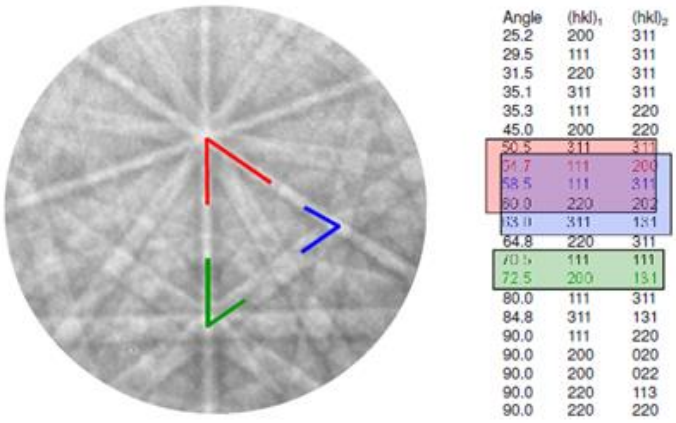

| Angle | $(hkl)_1$ | $(hkl)_2$ |
|---|---|---|
| 25.2 | 200 | 311 |
| 29.5 | 111 | 311 |
| 31.5 | 220 | 311 |
| 35.1 | 311 | 311 |
| 35.3 | 111 | 220 |
| 45.0 | 200 | 220 |
| 50.5 | 311 | 311 |
| 51.7 | 111 | 200 |
| 58.5 | 111 | 311 |
| 60.0 | 220 | 202 |
| 63.0 | 311 | 131 |
| 64.8 | 220 | 311 |
| 70.5 | 111 | 111 |
| 72.5 | 200 | 131 |
| 80.0 | 111 | 311 |
| 84.8 | 311 | 131 |
| 90.0 | 111 | 220 |
| 90.0 | 200 | 020 |
| 90.0 | 200 | 022 |
| 90.0 | 220 | 113 |
| 90.0 | 220 | 220 |

*Figure 81: Due to limited accuracy, each measured angle between the Kikuchi bands (red, blue, green). may match, within an angular tolerance, more than one angle between the crystallographic planes (indicated at the corresponding-colored rectangle) suggesting that each triplet could represent multiple orientations [36].*

For a reliable orientation determination, a triplet voting indexing algorithm [39] is used. The algorithm compares interplanar angles of all triplet combinations with a look-up table and establishes all possible indexing solutions. For each triplet, the potential orientations are identified, and each solution gets a vote. The solution with the highest number of votes is selected as the grain orientation (Figure 82).

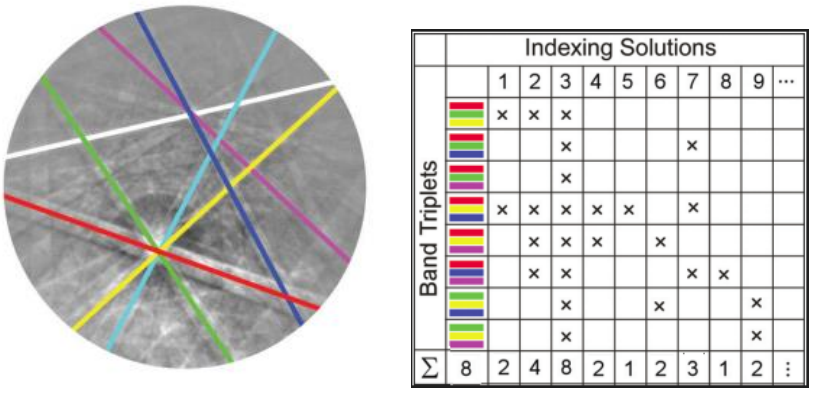


*Figure 82: The Voting Mechanism: Solution No 3 that gathers the highest number of votes is selected as the grain orientation (in this example, for simplicity, only 8 of the 35 triplets corresponding to the 7 colored bands are shown). Modified from [35].*

EBSD can generate maps, usually in gray scale, that are very useful to visualize the microstructure of polycrystalline materials. The Confidence Index (CI) (Figure 83) and commonly the Image Quality (IQ) map (Figure 84) are plotted in from the acquired EBSD data.

The Confidence Index (CI) is derived from the voting scheme , defined as [40] :

$$CI = \frac{V_1 - V_2}{V_{IDEAL}} \tag{2.46}$$

where $V_1$ and $V_2$ are the number of votes for the first and second in votes solutions and $V_{IDEAL}$ is the total possible number of votes from the detected bands.

CI is ranging between 0 and 1 and in the case presented in Figure 82, $V_1$=8, $V_2$=4 and $V_{IDEAL}$=8 making CI=(8-4)/8 =0.5 . A disadvantage of using the confidence index is that it, generally, produces higher values in the case that only few bands are identified.

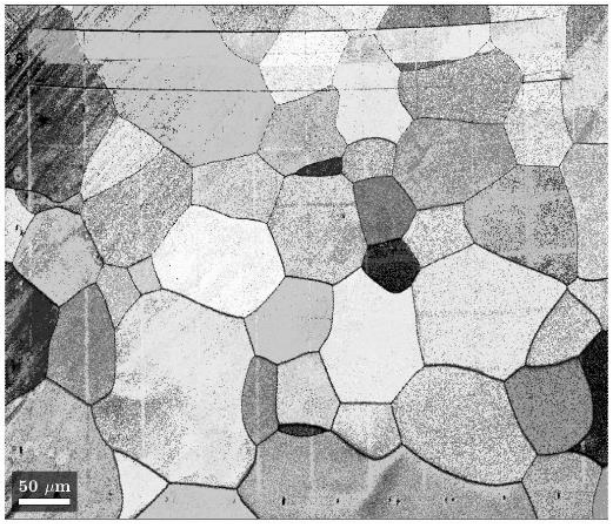


*Figure 83: Confidence Index map of a ferritic alloy. The grains are visible along with a Focused Ion Beam milled grid, to facilitate grain recognition when imaging the sample on the Scanning Electron Microscope.*

The IQ map describes the quality of the diffraction pattern by plotting the IQ value of each point acquired during scanning the sample. When performing the Hough transformation, the detected Kikuchi bands are transformed to intensity peaks. The value of the IQ is derived from the average amplitude of these peaks as [41]:

$$IQ = \frac{1}{N}\sum_{i=1}^{N} H(\rho_i, \theta_i) \tag{2.47}$$

where N is the number of peaks detected by the Hough transform, H ($\rho_i$, $\theta_i$) is the height of the $i^{th}$ peak.

Although the definition of IQ is almost arbitrary and the physical information it contains is not clear, in practice it has been proved to be very useful [42].

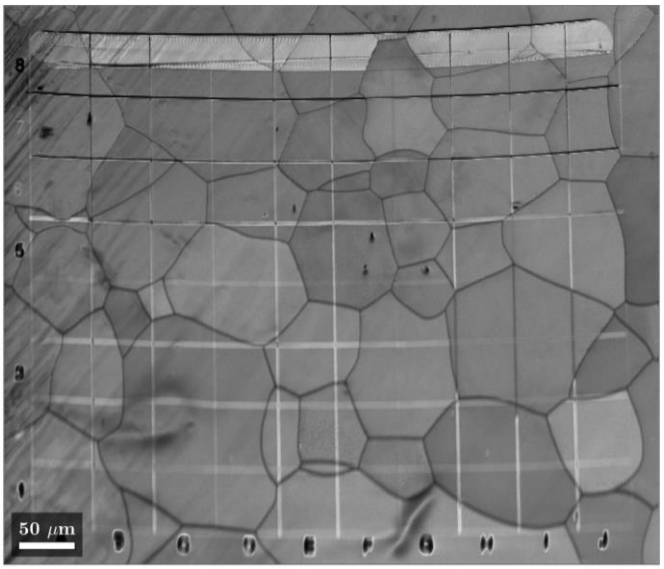


*Figure 84: Image quality map of a ferritic alloy. The grains, bearing some impurities, are visible along with a Focused Ion Beam milled grid, to facilitate grain recognition when imaging the sample on the Scanning Electron Microscope.*

For EBSD analysis, scanning the sample using a grid of hexagonal points (Figure 85– a), allows optimum measurement. An algorithm defines the grains by selecting neighboring and similarly oriented points, so that each grain has different crystallographic orientation from its surroundings but internally has little variation (Figure 85- b).

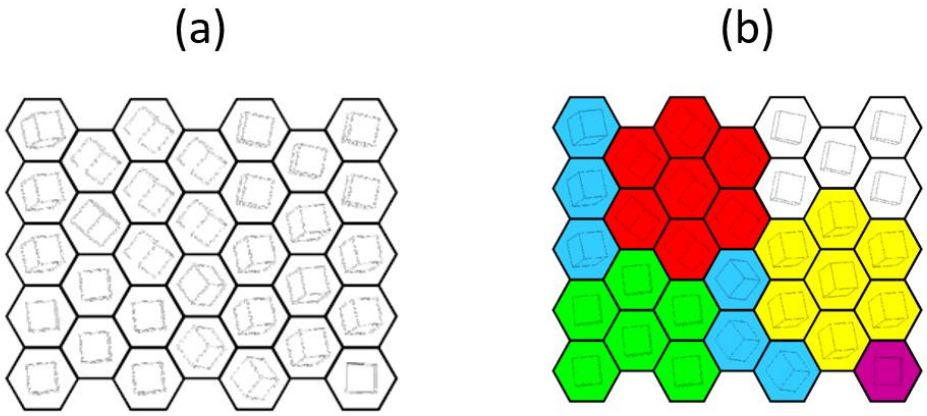


*Figure 85: A grid of hexagonal points is used to scan the sample (a) the neighboring and similarly oriented points constitute a grain (b) [43].*

Commonly, inverse pole figure (IPF) maps are used to represent, using a color-code, the crystal directions parallel to the sample normal (Figure 86 - a)

In this study, the EBSD analysis data were acquired using an EDAX detector and EDAX's TEAMS or APEX software. Data processing was performed using both the commercial OIM software

and MATLAB scripts developed using the MTEX toolbox [44]. The scripts were tested and confirmed to be in full agreement with OIM.

To properly select the grains with the most favorable crystal lattice orientation for the compression tests (the ones having a χ angle about zero (see chapter 1)), a set of EBSD maps and diagrams were plotted.

Amongst others, these include mean-orientation inverse pole figure (IPF) maps (Figure 86 - a), a projection of the mean-orientation of each grain on the standard stereographic triangle (Figure 86 - d), a map indicating the grains' Schmidt factors values (Figure 86 - b) . For each grain, the Iso-Schmidt contours are plotted for the {110} & {112} slip systems on the standard stereographic triangle where the grain's orientation is indicated (Figure 86 – e) .Using the later plot, the grains of interest are selected and then are indicated on an image quality (IQ) map (Figure 86 – c), essential at the pillar fabrication stage.

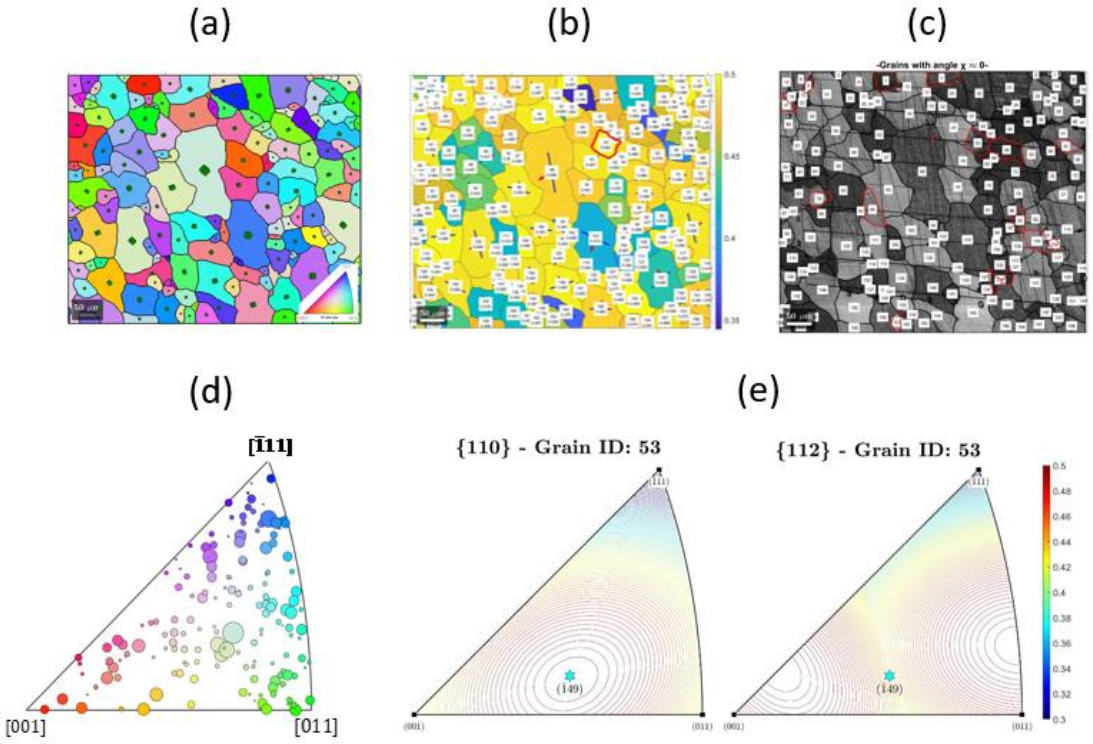


*Figure 86: Some of the maps used for EBSD analysis: (a) Mean orientation IPF map (b) Map indicating the grains' Schmidt factors values (c) IQ map indicating the grains of interest (d) Projection of the grains mean-orientation on the standard stereographic triangle and (e) Maps of the Iso-Schmidt contours for the {110} & {112} slip systems of these grains.*

To summarize, the preparation procedure used before the pillar fabrication consists of the following steps. First, the samples are properly polished using successively thinner diamond suspensions and finally a finishing dispersion of colloidal silica. The specimens are thoroughly cleaned using first soapy water then ethanol and finally dried with air. In the following step, a grid is fabricated on the samples' surface using FIB, to facilitate locating the proper grains and fabricate inside them the micropillars. The third step is the EBSD analysis of the sample. The orientation of the crystal lattice is studied using the acquired EBSD maps and the grains with

the most favorable orientation for pillar fabrication are selected. On the samples IQ map, where the milled grid is also apparent, the selected grains boundaries are marked, and this map is used at the micropillar fabrication stage.

## 4. Micro-compression

The mechanical properties of the studied samples were evaluated by in-situ micro-compression of FIB-fabricated single grain compressed pillars. After completed the described preparation procedure, micropillars are carefully milled to obtain the shape of straight columns surrounded with a wide enough crater.

The pillars are compressed in ambient temperature, using the Hysitron PI87R Picoindenter mounted on the ZEISS XB540's stage, at displacement control mode and with a constant stain rate. From the data acquired by the indenter the engineering stress-strain curves are calculated and studied.

For the assessment of the mechanical properties of the compressed pillars, it is crucial to identify the primary slip system activated during compression. For this, a post-compression slip trace analysis, using SEM, is necessary.

### *4 – i. Pillar fabrication*

After the grain selection, the pillar fabrication was performed using the ZEISS XB 540 SEM/FIB, using a Ga ion beam at a 30kV accelerating voltage.

Cylindrical micropillars were annular milled in a similar procedure as the two-step milling process described by Volkert and Lilleodden [45]. The first step consists of milling an annulus pattern with an outer diameter of 25 μm and an inner one of about 8 μm.

Although milling a wide surrounding crater is a time-consuming process, its purpose is not only to safely house the indenter's 5 μm diameter flat punch, avoiding any contact with other surfaces except with the pillar's top, but also lessens the probability that sputtered material will redeposit. Furthermore, it provides a better sight for micropillar- flat punch alignment during the in situ micro-compression. An initial current of 30 nA reduced to 3 nA, was used to prepare the crater with a depth close to the desired pillar height.

In the second step, the pillars were shaped using a sequence of thin ring milling patterns with decreasing diameter to about the target of the 3 μm (Figure 87), while reducing the milling current from 1 nA to 50 pA. The use of weak currents allows to fabricate pillars with less than $4^{o}$ tapering angle, minimizing the stress gradient during compression, developed due to the different cross sections across the pillar height.

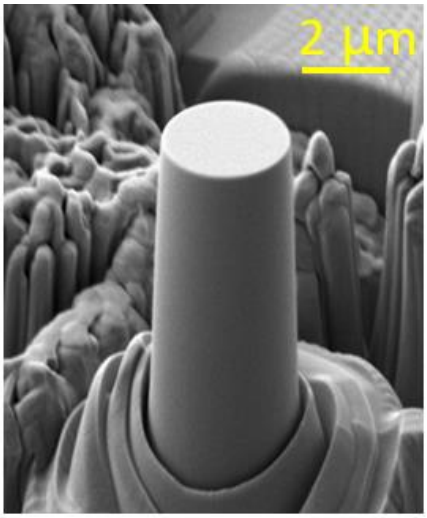


*Figure 87: SEM image of a FIB fabricated pillar.*

To avoid buckling during compression tests, pillars should have an aspect ratio (the ratio of the height over the diameter of the pillar) between 2 and 3, as Zhang suggests [46]. Keeping the aspect ratio in this range was a demanding part since continuous adjustment was needed, reducing the FIB beam current as the pillar diameter approached the target dimensions. But in these intermediate steps while pillar diameter was gradually reduced, at the same time the depth increased near the pillar. So, to obtain the desired pillar height, along with the current, also the dwell time required adjustment depending on both the sample material but also on the grain orientation even on the same sample, making pillar machining a process that needs a step-by-step customization.

Overall, the pillar fabrication process is a laborious time-intensive process. With the available milling currents, the mean time to machine the crater was about 40 mins and 25 mins more to fine tune the pillar dimensions and shape. However, the milling time significantly varies depending on the material of sample, and for the same material it varies a lot with grain orientation (Figure 88). In some orientations it was very difficult even to achieve a proper crater and pillar shape.

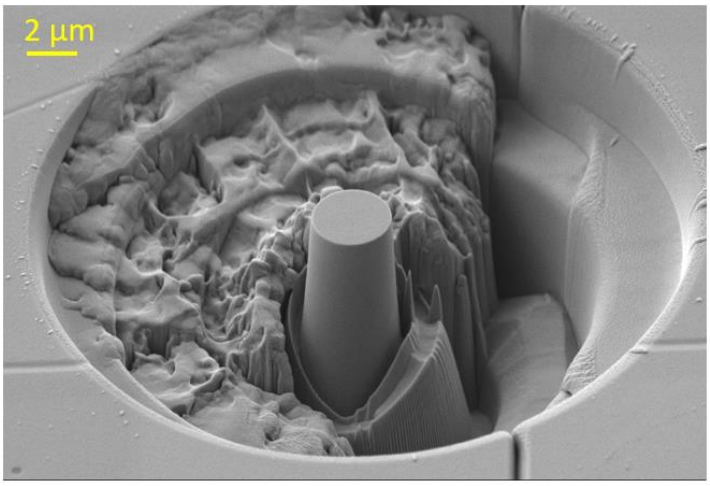


*Figure 88: Milling is greatly affected by grain orientation. The pillar crater extended at a nearby grain (at the right of the grid line) where milling was easy and smooth, in contrast milling at the left side was rough and time consuming (Fe-Mn-Ni sample).*

After pillar fabrication, the pillar top diameter and height as well as the taper angle were measured and recorded. Pillars with ratio greater than 3:1 or less than 2:1, were excluded from the experiments.

The above-described procedure produced pillars meeting the predefined dimensional criteria, having mean aspect ratio of 2.44 ± 0.46 and mean taper angle of 2.20 ± 0.80 degrees (the standard deviation describes the spread of data distribution).

No significant difference on the pillars characteristics was observed, between the different materials used (either irradiated or not), after applying this milling procedure.

To estimate the depth of Ga ion implantation inside the pillars, calculations made with SRIM on the Quick mode, for Gallium atoms of energy 30 keV and at an assumed 80° angle of incidence to the sides of the pillar, showed that they can penetrate at a depth of about 15 nm (Figure 89). So, Ga implantation happens only at the near surface, at a depth which is very small compared to the 3 μm pillars' diameter. Indeed, in literature Lee [12] suggests that FIB pillar preparation causes no significant change in yield stress, possibly affecting only the localization of the deformation.

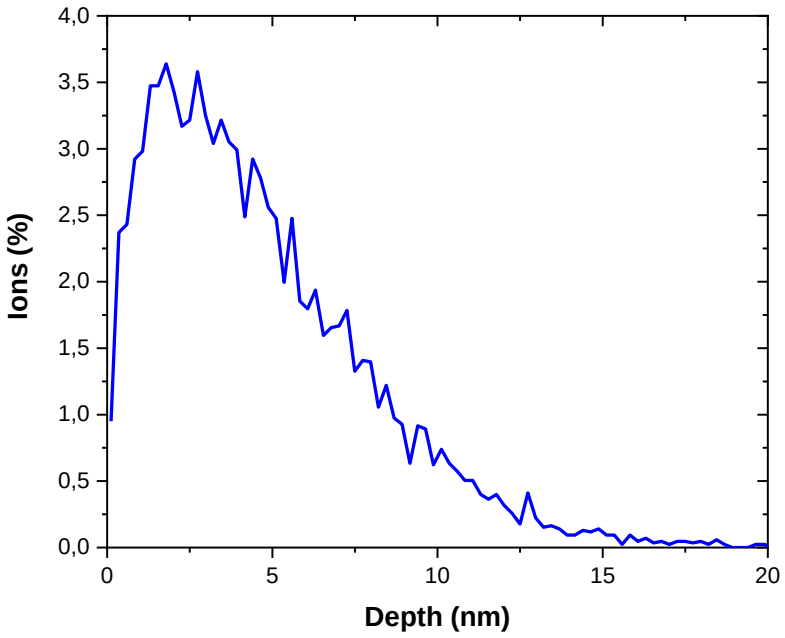


*Figure 89: Percentage of the implanted 30keV Ga ions in Fe, calculated using SRIM simulation (Quick mode) at 80° incident angle. The Ga ions are implanted up to a depth of 15 nm.*

### *4 – ii. Micro-compression*

The micro-compression experiments were performed using the Hysitron Picoindenter PI 87R equipped with a vacuum compatible load - displacement transducer and a 5 μm conical diamond flat punch, capable to exert a maximum loading force of 100 mN. The manufacturer provided a software package (TriboScan™ v.9) to perform setup testing, data analysis, sample positioning, and synchronization of mechanical data with SEM video.

For the in-situ micromechanical tests, the indenter was mounted on the specimen stage of the ZEISS XB540 SEM/FIB through a glove box (Figure 90 - a). In the SEM chamber, the stage

with picoindenter was tilted at 20° to optimize the monitoring of the punch tip while approaching and compressing the pillar (Figure 90 - b). Before compression, special care was taken to minimize any possible misalignment between the flat punch and the pillar axis, ensuring uniaxial loading.

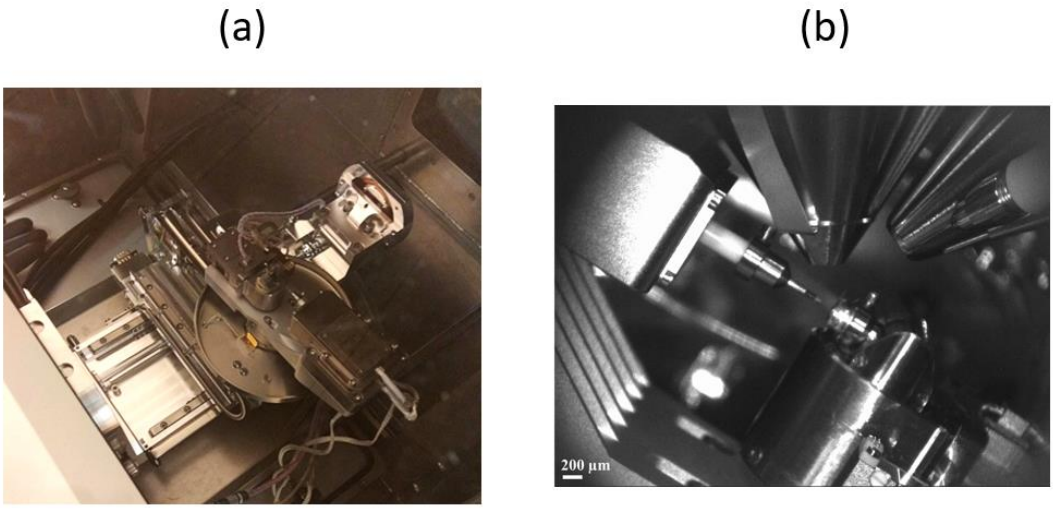


*Figure 90: (a) The Picoindenter PI87R is mounted on the ZEISSS XB540's stage through a glove box (b) The indenter is in the SEM chamber and tilted to a maximum possible angle, to allow maximum visibility during the compression test.*

All tests were carried out at room temperature. The loading was performed under displacement control mode to achieve a nominally steady strain rate and thus avoiding any possible strain rate effect. The suitable necessary parameters were inserted in the indenter's controlling software to produce the 0.001 $s^{-1}$ constant strain rate.

The in-situ compression tests were performed until a maximum strain less than 10%, trying to avoid the activation of many slip systems, which makes their identification very difficult. Ideally, only the primary slip system would be activated.

During pillar compression, the SEM screen along with the real time forming load – displacement diagram were recorded and used for post-compression detailed study of the pillar deformation.

To accurately estimate the pillar's strain during compression, as suggested by Sneddon [47], a correction, was applied to load–displacement data. From the measured displacement, the elastic deformation of both the indenter tip and the substrate bulk material below the base of the pillar were subtracted. This is formulated as:

$$\Delta L_{Pillar} = \Delta L_{Mes} - \frac{\left(1-v_{Sub}^2\right)}{E_{Sub}} . \frac{F_{mes}}{D_{Base}} - \frac{\left(1-v_{Tip}^2\right)}{E_{Tip}} . \frac{F_{mes}}{D} \qquad (2.48)$$

where $F_{mes}$ the measured force and $\Delta L_{Mes}$ the measured displacement by the instrument, $D$ and $D_{Base}$ the diameter of the pillar at top and at its base, respectively. $E_{Sub}$ , $v_{Sub}$ represent the Young's modulus and Poisson's ratio of model alloy assumed to be 200 GPa and 0.3

respectively [48–51]. Also, $E_{Tip}$ , $v_{Tip}$ represent the Young's modulus and Poisson's ratio of the diamond indenter tip, considered to be 1050 GPa and 0.1 respectively [36–38].

The diameter of the pillar at its base is geometrically estimated using the measured taper angle (ϕ) and its initial pillar length ($L_0$), as:

$$D_{Base} = D + 2 * L_0 * \tan(\varphi) \tag{2.49}$$

Then, using the load and the corrected displacement data, the engineering stress-strain curve was calculated. Engineering stress (σ) was calculated using the top diameter of the pillar since it is easily defined on the SEM images, minimizing the miscalculation error of the contact area,

$$\sigma = \frac{4F_{mes}}{\pi D^2} \tag{2.50}$$

And the strain (ε) as the ratio of the displacement (ΔL) over the initial pillar length ($L_0$):

$$\varepsilon = \frac{\Delta L}{L_0} \tag{2.51}$$

The deformation of most of the pillars was not in a homogeneous way. Discrete slip steps were observed on specific locations of their surface as in Figure 91 - b. Therefore, the geometry of the pillars was severely altered. For this, true strain and stress were not calculated.

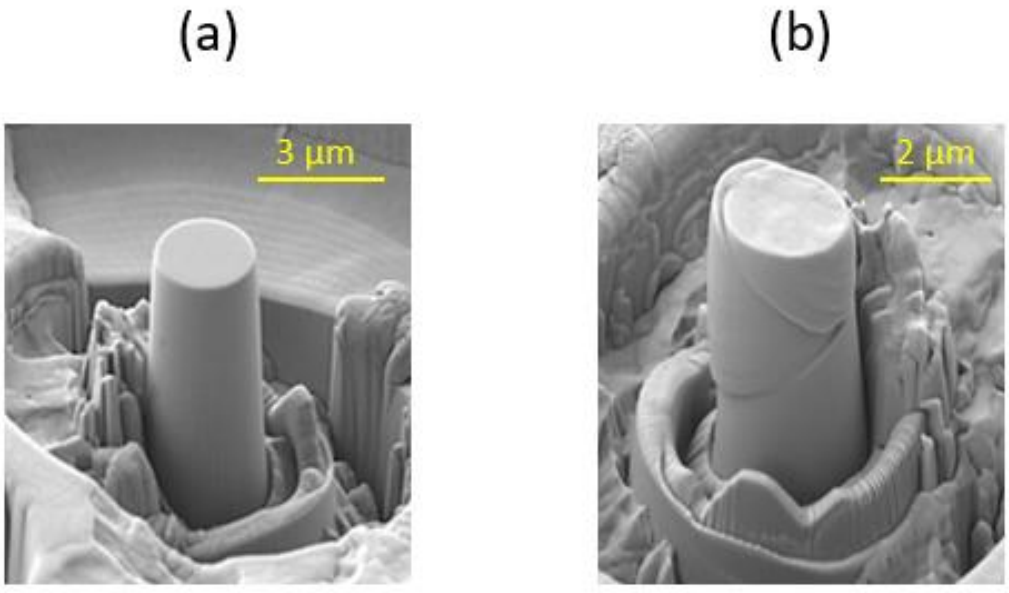


*Figure 91: Fe-1Ni pillar (a) before and (b) after in-situ compression. Discrete slip steps are observed after compression, altering the pillar's geometry.*

*4 – iii. Slip trace analysis*

After compressing the pillars, the activated slip system(s) need to be identified in order to use the Schmid factor and calculate the CRSS. For this, slip trace analysis was performed as follows:

Using SEM, the compressed pillars are observed. From the top view, we identify the direction of the slip, and the stage is rotated at an angle ω, so as to put the direction of slip horizontally (Figure 92 – a). At this position the stage is tilted so to observe the side view of the pillar. The angle (ϕ) between the apparent slip trace on the pillar surface and the top of the pillar, is measured (Figure 92 – b). For each grain, using the EBSD data, we have been calculated the possible slip systems and the angle between their slip plane and the grains surface plane and have sorted them in decreasing Schmidt factor. Comparing the measured angle (ϕ) with the angle of each slip plane to the pillar surface, we conclude about which slip system has been activated.

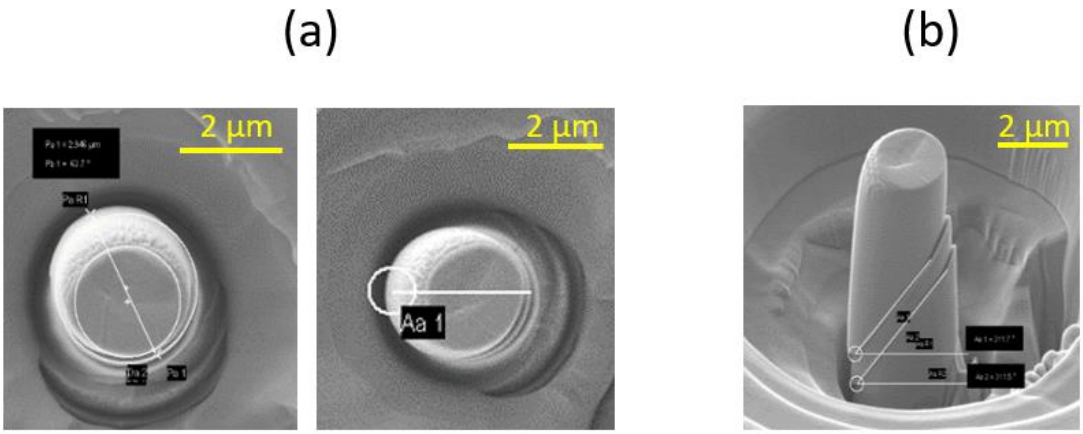


*Figure 92: Slip trace analysis: ( A) At the top view, the stage is rotated at an angle ω to put the direction of slip horizontally (B) At the side view, the angle (φ) between the apparent slip trace and the top surface of the pillar is measured and then is compared to the theoretically calculated angle between the pillar's surface plane and the slip plane of the primary and secondary slip systems.*

Additionally, to double check it, rotations with the same as the SEM measured angles are imposed to the EBSD data, corresponding to the pillar's location on the sample, in fact simulating a virtual rotation of the pillar. The axes around which the rotation of EBSD data is performed are defined in (Figure 93).

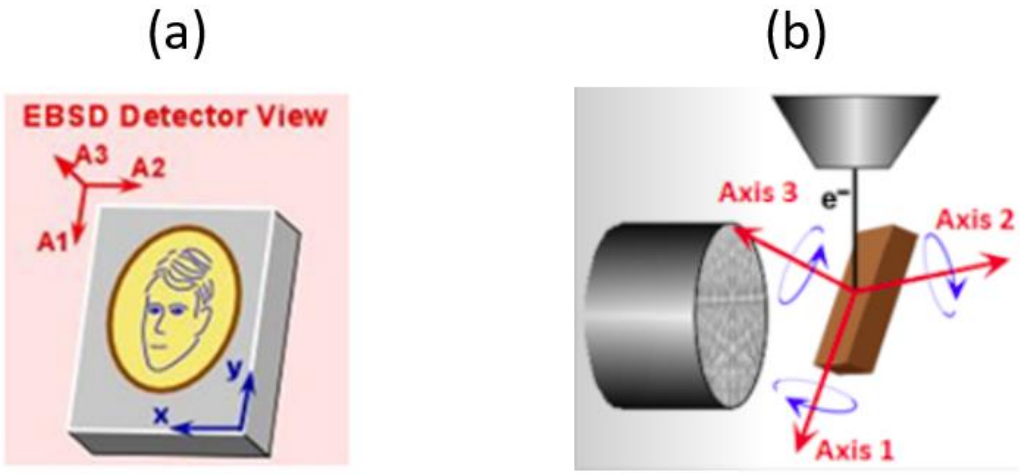


*Figure 93: (a) Axes of EBSD data as defined in the used EDAX setting and (b) representation of the A1, A2 and A3 axes on the sample in the Scanning Electron Microscope configuration.*

The first rotation (by ω around A3 axis) aims to obtain a 'profile' view of the pillar and the second (by ϕ around A2 axis) aims to align the slip plane with the surface of the sample (Figure 94). So, its pole should be at the center of the pole figure of its crystallographic plane family.

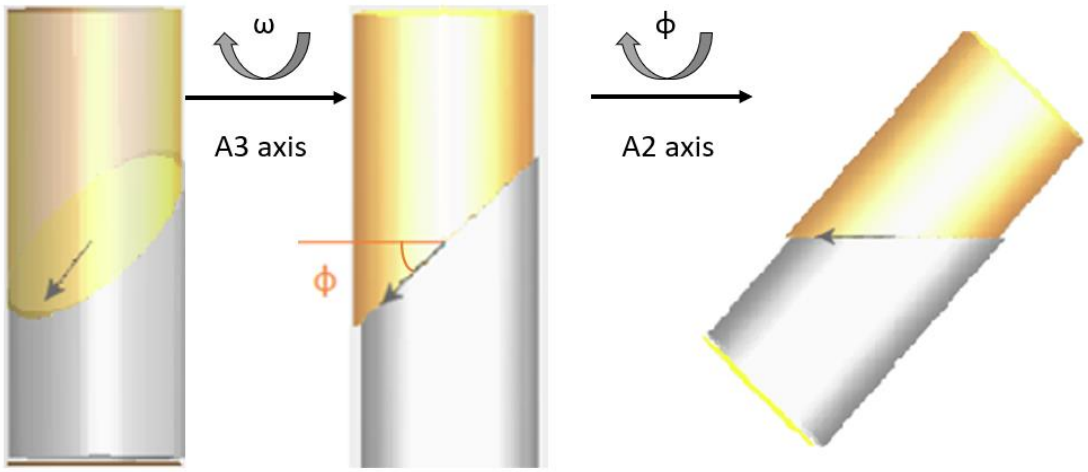


*Figure 94: Imposing rotations to the EBSD data corresponds to a 'virtual' rotation of the pillar. The pillar at it initial position (A) and after rotating by ω around A3 axis (B). The second rotation by φ around A2 axis should 'bring' the slip plane parallel to the sample surface (C), the arrow indicates the slip direction on the slip plane.*

For the ferritic alloys at ambient temperature, as mentioned in chapter 1, we expect activation of the {110} or/and {112} slip systems during the micro-compression. Plotting the pole figures of the crystallographic planes of the {110} and {112} families we verify whether the observed slip plane belongs to one of these families. For example, in Figure 95 the pole is at the center of the {110} pole figure, suggesting that the slip plane is one of the {110} planes.

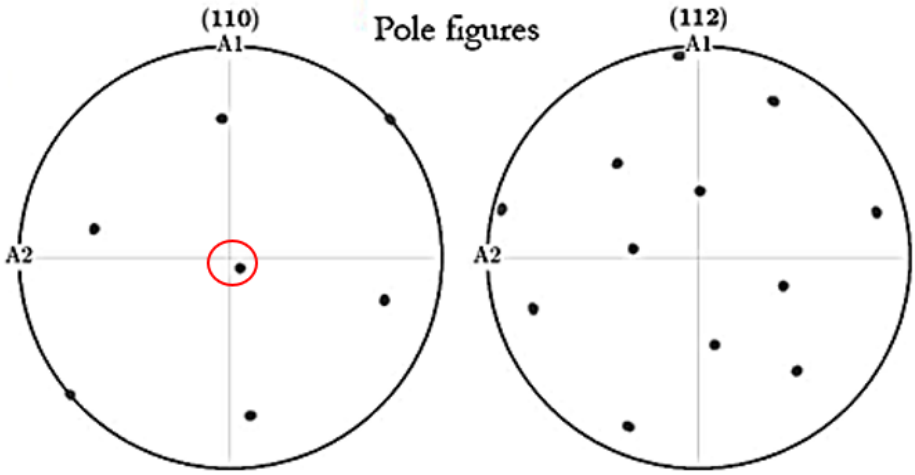


*Figure 95: After imposing the SEM measured angles to the EBSD data corresponding to the pillar area, the pole figures of the {110} & {112} family planes are examined. On the left, the pole figure of one (110) plane is almost at the center, indicating that the slip plane belongs to the {110} family.*

## 5. Scanning - Transmission Electron Microscopy

To further investigate the microstructure of the compressed pillars, affecting the mechanical properties of a material, namely the dislocation network, we used Transmission Electron Microscopy (TEM) and Scanning Transmission Electron Microscopy (STEM) to estimate the dislocation density. Compressed pillars from non-irradiated Fe-Mn-Ni alloy were lifted out and were send to CRIEPI for study. In parallel, in GPM, compressed pillars from the same alloy in the irradiated state, were lifted out and thinned into TEM lamellas using FIB and TEM/STEM images were acquired under the guidance and help of Dr. A. Etienne.

The principles of imaging the dislocations using TEM/STEM and counting their density using the 'line-intercept method', will be presented in brief, along with the procedure followed for TEM lamellae fabrication from the pillars' lift outs.

### *5 – i. Imaging crystal defects by diffraction in TEM*

TEM imaging with diffraction contrast is one of the most widely used methods for studying dislocations in a material. Usually, the weak beam dark field (WBDF) is suggested as the imaging technique of choice [55].

When observing defects in TEM either the direct beam or one of the diffracted beams is selected using an aperture. By convention, bright field (BF) image is formed when the incident direct beam passes through the aperture while if the scattered electrons of a diffracted beam are selected then they form a dark field (DF) image.

This is illustrated schematically on the diagrams showing the location of the aperture to realize BF imaging from the direct beam (Figure 96 - A) and DF using an off-axis diffracted beam in (Figure 96 - B). But the more off axis the beam is, the worse the image it forms because of the astigmatism and the aberrations. So, the beam must be tilted (Figure 96 - C) until the diffracted beam gets the on-axis position.

In a DF image, the sample will generally appear dark except the regions that scatter electrons, which are focused in the selected diffracted beam, that will appear white.

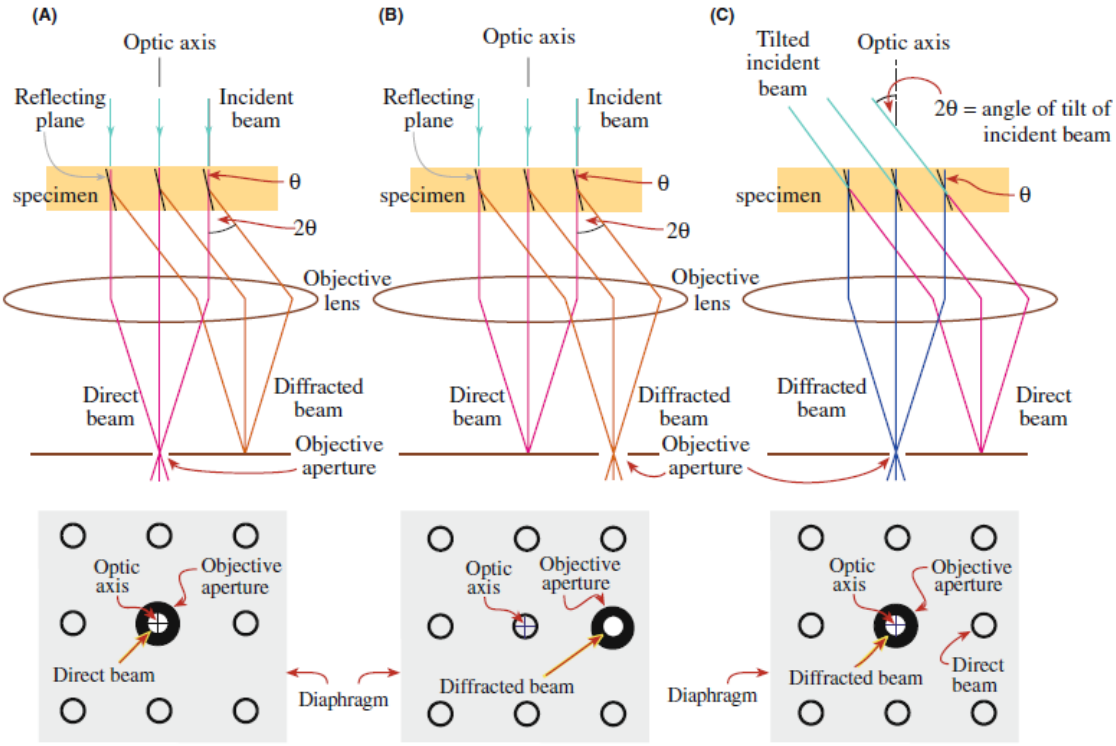


*Figure 96: Schematic representation of direct and diffracted beams indicating the corresponding position of the aperture to form (A) Bright Field image from the direct beam electrons (B) Dark Field image from a selected off-axis scattered beam and (C) Dark Field image from an on-axis scattered beam obtain by titling the electron beam [55].*

When Bragg condition are fulfilled, diffraction occurs at specific angles and strong diffraction contrast in both BF and DF images can occur in the two-beam condition.

The two-beam condition is obtained by tilting the crystal sample in the electron microscope, such that it has only one plane family at the perfect Bragg angle relative to the incident beam. This plane will strongly scatter, producing a bright diffraction spot in the electron diffraction pattern.

If we plot the Ewald sphere in the reciprocal lattice, (Figure 97 - a) the diffraction vector, g, which is always perpendicular to the Bragg scattering plane, will intersect the reciprocal lattice rod (rel-rod) at its center where the intensity distribution along this rel-rod maximizes. Note that the rel-rods represent the TEM specimen shape transformation in reciprocal lattice (Figure 97 - b).

Deviating, from the perfect Bragg condition by tilting the sample at a small angle Δθ, the Ewald sphere now intersects away from the center of the rel-rod. At this point, the intensity modulation is reduced, resulting in a significant decrease in the intensity of the diffracted beam. The vector $\vec{s}_g$, called the excitation or deviation vector, describes the deviation from

the perfect Bragg condition and its scalar quantity (s) is the excitation error (or the deviation parameter).

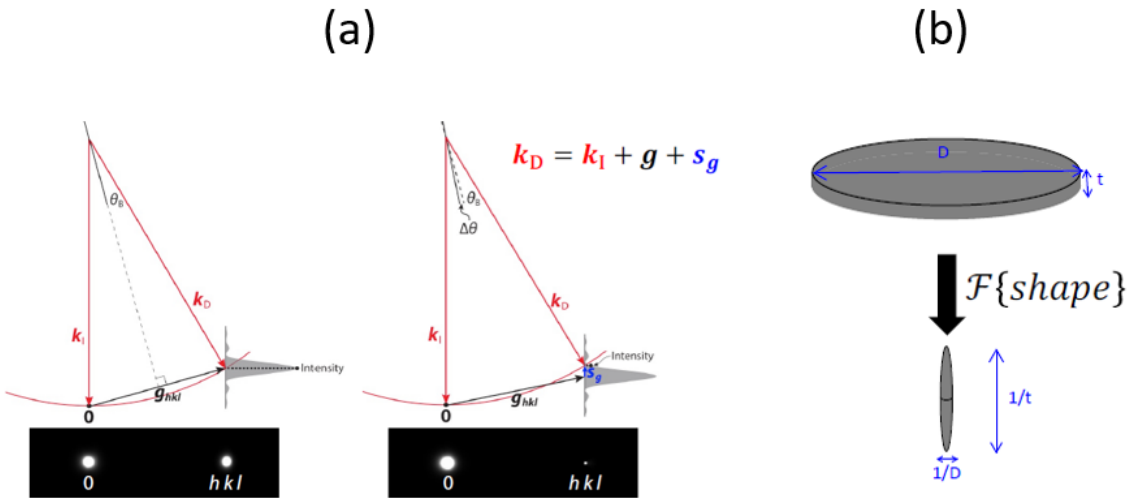


*Figure 97: (a) Representation of two-beam geometry in the reciprocal lattice. (Left) in the strong beam condition the diffracting plane is at the perfect Bragg condition (Right) the weak beam condition is obtained by titling the sample at a small angle Δθ. The Intensity distribution is plotted the along the rel-rods. (b) Illustration of the reciprocal relation of the specimen width and diameter with the rel-rod height and width respectively [56].*

For imaging defects as the dislocations, the WBDF is recommended. Setting the WBDF condition is best described in the reciprocal lattice.

First step is to tilt the sample, in the bright field, to obtain the two-beam condition 0(g) with a very small positive sg. This BF condition can be used to locate and focus on the imaging defects Figure 98 - a.
Next the incident beam is tilted until the g reflection gets the on-axis position (Figure 98 - b) becoming very weak, while the 3g reflection gets excited with $s_{3g}>0$, while no other reflections are strongly exited.

This WBDF condition, called 'g(3g)', is commonly used for studying the dislocations but any of the systematic row reflections can be used for the WBDF condition. The suitable reflection depends on the studied material, and in general (WBDF) imaging is performed in g(ng) conditions.

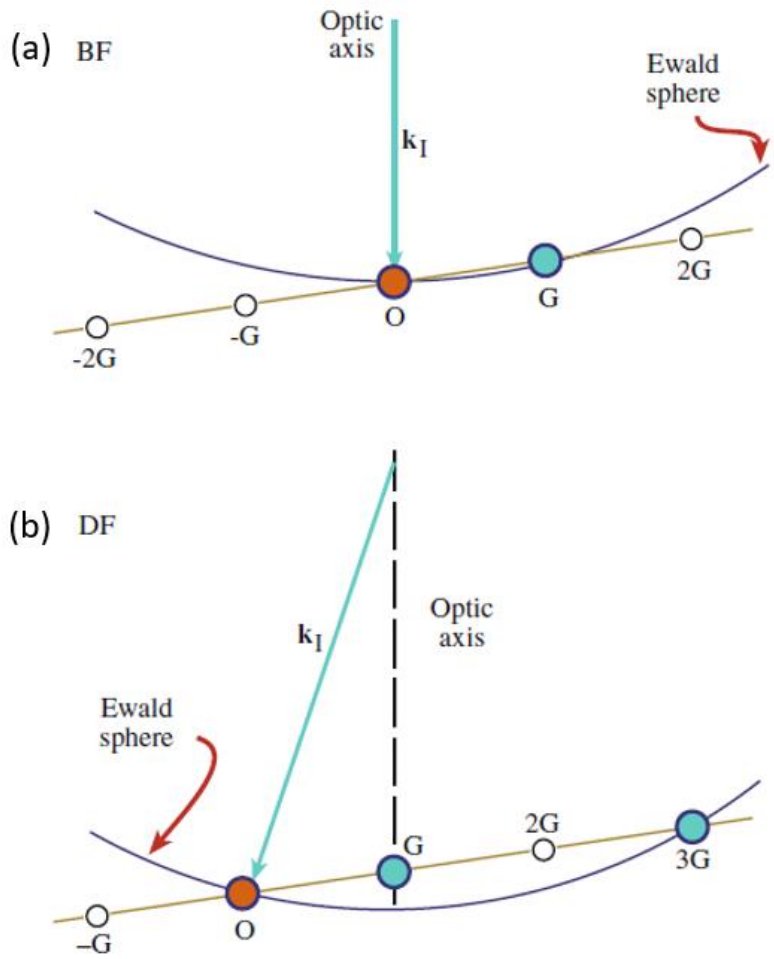


*Figure 98: Steps for obtaining the Weak-Beam Dark-Field condition (a) in the bright field, the sample is tilted to obtain the two-beam condition 0(g) (b) incident beam is tilted until the g reflection gets the on-axis position, while the 3g reflection gets excited while no other reflections are strongly exited [55].*

Dislocations distort the regular arrangement of the crystal planes, displacing them and inducing a stress filed, especially at the vicinity of their core. For the two-beam imaging, the specimen is tilted so that the diffracting crystal planes to be just off the Bragg condition. Only small regions near either side of the dislocation core are locally bent enough to resume the Bragg diffracting condition while the regions far from the core are not diffracting since they are well away the Bragg condition (Figure 99 - a). So, dislocations can be imaged due to the diffraction contrast they create.

In BF, dislocations appear wide, especially if $s_g$ is close to zero (Bragg condition) (Figure 99 – b – A) for this, as Williams and Carter recommend [55], setting $s_g$ = 0,2 $nm^{-1}$ can give in general a better image. In WBDF they appear much narrower (Figure 99 – b – B) and the diffracting lattice planes in most areas of the specimen are tilted so that $s_g$ is large and preferably positive. The increased $s_g$ value means that the diffracting planes must bend more to comply with the

Bragg condition which happens only near the dislocation core and thus only this narrow region produces the needed contrast for imaging.

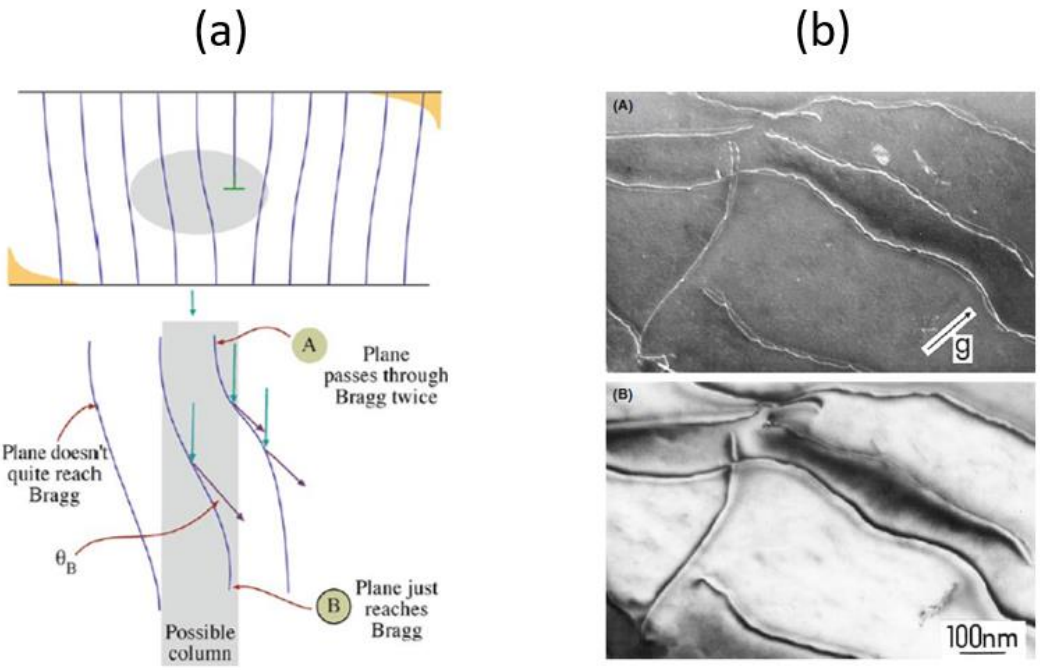


*Figure 99: (a) Edge dislocation illustration: (A) Only in the regions near the dislocation core, crystal planes are bend back into the Bragg diffracting condition. (B) core area magnified (b) Dislocation imaging under (A)weak beam and (B) strong beam conditions [55].*

Although in TEM thin foils of about 50 nm thickness normally are preferred, in the case of dislocation study thicker specimens (about 100 nm) are needed to avoid surface effects (as escaping of dislocation from the surface, foil bending, etc) [55].

*5 – ii. Scanning Transmission electron microscopy*

In Scanning Transmission Electron Microscopy (STEM) mode, the beam converges forming a probe and scans the specimen parallel to the optical axis at all times. An annular detector picks up the signal generated at the probing area of the specimen which is suitably modulated to form the corresponding part of the image on the recording screen [55]. That is, the image builds up point by point, making the imaging process much slower than in TEM. Also, since the recording screen dimensions are predefined, the image magnification depends only on the dimensions of the scanned area of the sample.

STEM uses annular concentric detectors (Figure 100). BF images are formed from the unscattered direct beam electrons either using the Bright-field (BF) detector or the Annular bright-field (ABF) detector. The latter gives better contrast to the BF image by using only the outer annulus of the bright-field disk [57], [58]. DF images are acquired either from the Bragg scattered electrons, using the Annular Dark-Field (ADF) detector or from electrons scattered

with a larger angle and thus minimizing the contribution of the Bragg scattered electrons, using the High-angle ADF (HAADF) detector.

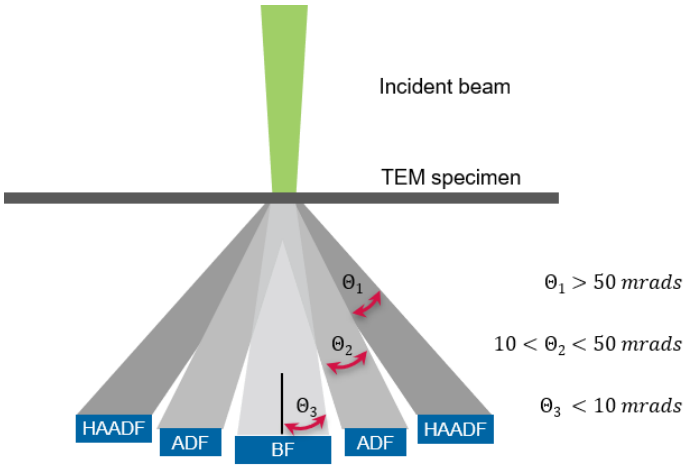


*Figure 100: Illustration of STEM detectors. The corresponding collection semi-angles are indicated for a system equipped with Gatan detectors [59].*

STEM offers clear imaging of dislocations due to the averaging of the intensities over the range of incident illumination angles [42, 43].

### *5 – iii. Dislocation density measurement*

The TEM and STEM images that were acquired, were compared to select the suitable ones for measuring the dislocation density.

Since automatic intersection counting (Figure 101) was not available, using a manually counting method was mandatory.

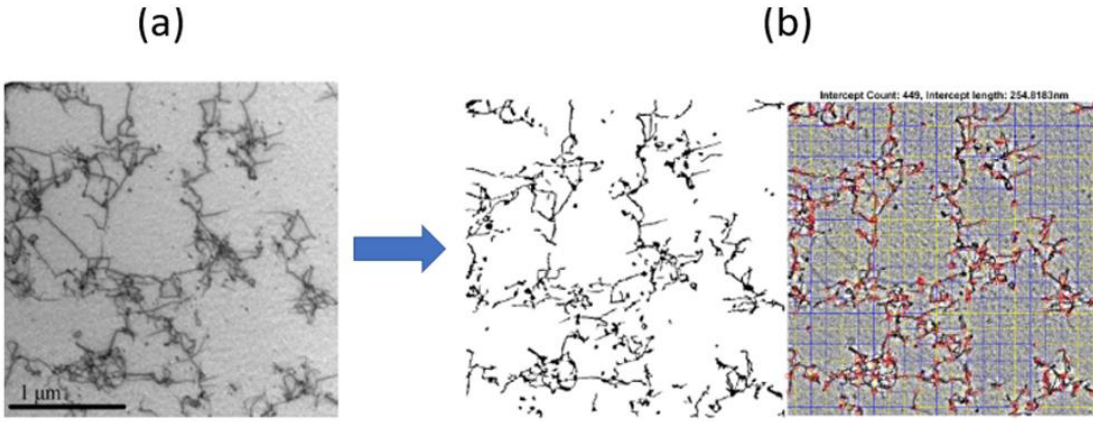


*Figure 101: (a) STEM images at zone axis [111] in BCC steel with 3.3% tensile deformation : ABF image (b) The automatic intersection counting applied on the STEM image: the black and white image and the contrast enhanced image with a 20 X 20 grid [61].*

We decide to use the 'line-intercept method' [62]. On the selected micrograph, five random lines are drawn and the number (N) of points that the dislocations intersect the lines are counted (Figure 102).

The dislocation density (ρ) is calculated as:

$$\rho = \frac{2N}{Lt} \tag{2.52}$$

where L is the total length of the lines and t is the thickness of the specimen.

The average dislocation density ( $\bar{\rho}$ ) is the mean value of densities of the measured areas and the standard deviation of the measurements represent the calculation error.

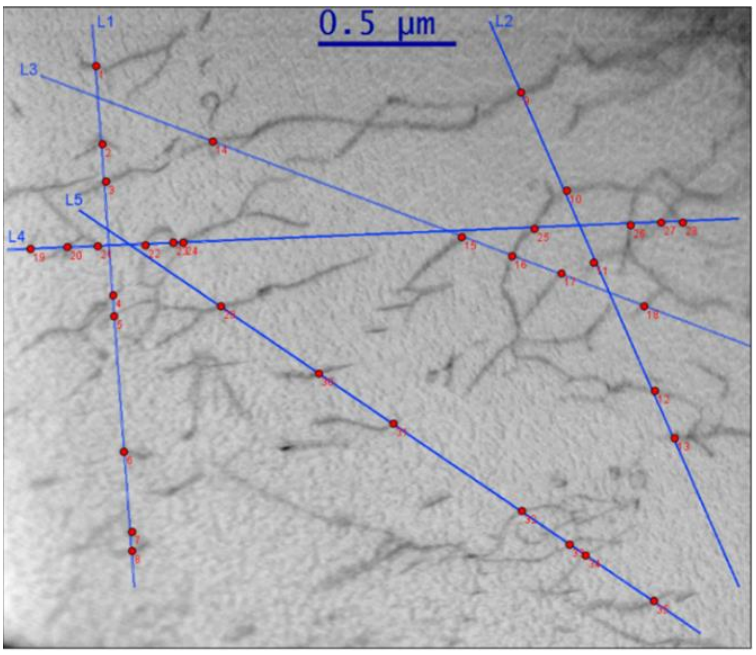


*Figure 102: Application of the 'line-intercept method' on STEM Bright Field image for dislocation density measurement.*

*5 – iv. Lamella preparation*

TEM lamellae were prepared from compressed irradiated and non-irradiated micro-pillars using the FIB.

At first using Gas Injection System (GIS), a protective 1 µm Pt layer was deposited on top surface of the pillar. The pillar was Pt-welded on the Omni Probe 400 Oxford micromanipulator and then, the whole pillar was lifted out of the bulk sample trying to retain as much of the pillar's height as possible.

The pillar was welded on a Cu TEM grid (Figure 103) and then it was thinned down using FIB, until a lamella width about 150 nm was fabricated. A final cleaning step, using a 2 kV Ga beam and 90 pA current, was applied to minimize the Ga ion contamination.

To further decontaminate from the Ga ions and at the same time, to additionally reduce the width of the lamella, Argon ion polishing was applied using the precision ion polishing system PIPS II (Gatan) at 0.5 kV for about 15 minutes.

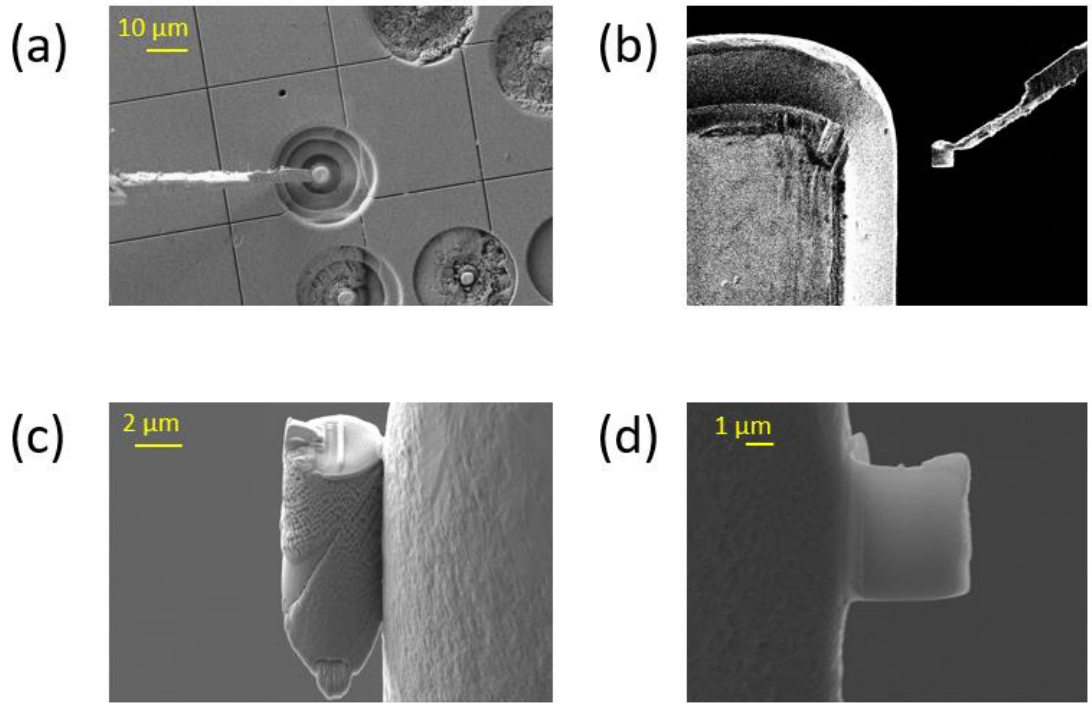


*Figure 103: (a)After Pt deposition on the top surface of the pillar, the micro-manipulator is welded. (b) The pillar is lifted out (FIB view) and (c)welded on the Cu TEM Grid (SEM view). (d)A TEM lamella is obtained with FIB thinning.*

To summarize, TEM lamellae of a thickness of about 100 nm, were fabricated from non-irradiated and neutron irradiated compressed pillars, in order to image the dislocation network for the estimation of the dislocation density. For this, TEM and STEM experiments were carried out and from the obtained micrographs the dislocation density was calculated using the line intercept method.

## Summary

Defects produced by irradiation impede dislocation movement, reduce the material's ductility, harden it, and eventually embrittle it. In this study, irradiation hardening was evaluated by comparing the mechanical properties of the ferritic model alloys, in the non-irradiated and neutron irradiated state, obtained by in-situ micro-compression of FIB fabricated monocrystal pillars. Milling the single crystal pillars is a laborious and time-consuming process that requires several steps. First the samples need to be mechanically polished to an EBSD finish. On the properly polished samples, a grid is milled using FIB and then the samples are studied using EBSD in order to define the crystal lattice orientation of their grains and select the appropriate ones inside which the pillars are fabricated.

The study of the microstructure, evolved under the irradiation of the samples, was mainly performed using APT. This technique is capable of visualizing and quantifying the nanometric sized defects and also to measure their chemical composition. TEM/STEM imaging is the method of choice to study the dislocation density that also affects the measured mechanical properties.

From non-irradiated and neutron irradiated Fe-Mn-Ni compressed pillars both, TEM lamellae and APT tips were fabricated and analyzed to obtain a coupled and completed estimation of the involved microstructure altering the mechanical properties of the materials under irradiation and evaluate the effect of the deformation on the pillars' microstructure.

# Bibliography


[1] B. Gault, *Atom Probe Microscopy*. Springer, 2012.

[2] W. Lefebvre-Ulrikson, Ed., *Atom probe tomography: put theory into practice*. London: Academic Press, 2016.

[3] D. J. Larson, T. J. Prosa, R. M. Ulfig, B. P. Geiser, and T. F. Kelly, *Local Electrode Atom Probe Tomography*. New York, NY: Springer New York, 2013. doi: 10.1007/978-1-4614-8721-0.

[4] M. K. Miller and R. G. Forbes, *Atom-Probe Tomography*. Boston, MA: Springer US, 2014. doi: 10.1007/978-1-4899-7430-3.

[5] "Atom Probe Tomography analysis of magnetostrictive multilayer materials." https://www.cameca.com/markets/advanced-materials/magnetostrictive-materials-apt (accessed Jul. 15, 2022).

[6] HAMAMATSU PHOTONICS K.K., "Microscopic channel electron multipliers oriented parallel to one another."

[7] DATAPLOT Reference Manual, "Weighted standard deviation." [Online]. Available: https://www.itl.nist.gov/div898/software/dataplot/refman2/ch2/weightsd.pdf

[8] DATAPLOT Reference Manual, "Weighted mean." [Online]. Available: https://www.itl.nist.gov/div898/software/dataplot/refman2/ch2/weigmean.pdf

[9] D. G. Altman and J. M. Bland, "Standard deviations and standard errors," *BMJ*, vol. 331, no. 7521, Art. no. 7521, Oct. 2005.

[10] School of Mathematics, Statistics & Physics Webserver, "Standard Errors and Confidence Intervals." [Online]. Available: http://www.mas.ncl.ac.uk/~njnsm/medfac/docs/se&ci.pdf

[11] J. M. Hyde *et al.*, "Atom probe tomography of reactor pressure vessel steels: An analysis of data integrity," *Ultramicroscopy*, vol. 111, no. 6, pp. 676–682, May 2011, doi: 10.1016/j.ultramic.2010.12.033.

[12] C. Hatzoglou *et al.*, "Preferential Evaporation in Atom Probe Tomography: An Analytical Approach," *Microsc. Microanal.*, vol. 26, no. 4, pp. 689–698, Aug. 2020, doi: 10.1017/S1431927620001749.

[13] F. Meisenkothen, E. B. Steel, T. J. Prosa, K. T. Henry, and R. Prakash Kolli, "Effects of detector dead-time on quantitative analyses involving boron and multi-hit detection events in atom probe tomography," *Ultramicroscopy*, vol. 159, pp. 101–111, Dec. 2015, doi: 10.1016/j.ultramic.2015.07.009.

[14] B. Gault, F. Danoix, K. Hoummada, D. Mangelinck, and H. Leitner, "Impact of directional walk on atom probe microanalysis," *Ultramicroscopy*, vol. 113, pp. 182–191, Feb. 2012, doi: 10.1016/j.ultramic.2011.06.005.

[15] P. Bas, A. Bostel, B. Deconihout, and D. Blavette, "A general protocol for the reconstruction of 3D atom probe data," *Appl. Surf. Sci.*, vol. 87–88, pp. 298–304, Mar. 1995, doi: 10.1016/0169-4332(94)00561-3.

[16] B. Gault, M. P. Moody, F. de Geuser, D. Haley, L. T. Stephenson, and S. P. Ringer, “Origin of the spatial resolution in atom probe microscopy,” *Appl. Phys. Lett.*, vol. 95, no. 3, p. 034103, Jul. 2009, doi: 10.1063/1.3182351.

[17] D. J. Larson, B. Gault, B. P. Geiser, F. De Geuser, and F. Vurpillot, “Atom probe tomography spatial reconstruction: Status and directions,” *Curr. Opin. Solid State Mater. Sci.*, vol. 17, no. 5, pp. 236–247, Oct. 2013, doi: 10.1016/j.cossms.2013.09.002.

[18] F. Vurpillot, A. Bostel, E. Cadel, and D. Blavette, “The spatial resolution of 3D atom probe in the investigation of single-phase materials,” *Ultramicroscopy*, vol. 84, no. 3–4, pp. 213–224, Aug. 2000, doi: 10.1016/S0304-3991(00)00035-8.

[19] F. Vurpillot, A. Bostel, and D. Blavette, “Trajectory overlaps and local magnification in three-dimensional atom probe,” *Appl. Phys. Lett.*, vol. 76, no. 21, pp. 3127–3129, May 2000, doi: 10.1063/1.126545.

[20] T. Philippe, M. Gruber, F. Vurpillot, and D. Blavette, “Clustering and Local Magnification Effects in Atom Probe Tomography: A Statistical Approach,” *Microsc. Microanal.*, vol. 16, no. 5, pp. 643–648, Oct. 2010, doi: 10.1017/S1431927610000449.

[21] J. M. Hyde *et al.*, “Analysis of Radiation Damage in Light Water Reactors: Comparison of Cluster Analysis Methods for the Analysis of Atom Probe Data,” *Microsc. Microanal.*, vol. 23, no. 2, pp. 366–375, Apr. 2017, doi: 10.1017/S1431927616012678.

[22] E. Meslin, B. Radiguet, and M. Loyer-Prost, “Radiation-induced precipitation in a ferritic model alloy: An experimental and theoretical study,” *Acta Mater.*, vol. 61, no. 16, pp. 6246–6254, Sep. 2013, doi: 10.1016/j.actamat.2013.07.008.

[23] R. K. W. Marceau, L. T. Stephenson, C. R. Hutchinson, and S. P. Ringer, “Quantitative atom probe analysis of nanostructure containing clusters and precipitates with multiple length scales,” *Ultramicroscopy*, vol. 111, no. 6, pp. 738–742, May 2011, doi: 10.1016/j.ultramic.2010.12.029.

[24] C. Hatzoglou, B. Radiguet, and P. Pareige, “Experimental artefacts occurring during atom probe tomography analysis of oxide nanoparticles in metallic matrix: Quantification and correction,” *J. Nucl. Mater.*, vol. 492, pp. 279–291, Aug. 2017, doi: 10.1016/j.jnucmat.2017.05.008.

[25] C. Hatzoglou, B. Radiguet, F. Vurpillot, and P. Pareige, “A chemical composition correction model for nanoclusters observed by APT - Application to ODS steel nanoparticles,” *J. Nucl. Mater.*, vol. 505, pp. 240–248, Jul. 2018, doi: 10.1016/j.jnucmat.2018.03.057.

[26] C. Hatzoglou, “Quantification et correction des biais inhérents à l’analyse par sonde atomique tomographique des nano-particules d’un acier ODS : Application à l’étude de leur formation et de leur comportement sous irradiation,” Université de Rouen, 2015.

[27] J.-L. Boutard *et al.*, “Oxide dispersion strengthened ferritic steels: a basic research joint program in France,” *J. Nucl. Mater.*, vol. 455, no. 1–3, Art. no. 1–3, Dec. 2014, doi: 10.1016/j.jnucmat.2014.08.059.

[28] S. Zaefferer, “On the formation mechanisms, spatial resolution and intensity of backscatter Kikuchi patterns,” *Ultramicroscopy*, vol. 107, no. 2–3, pp. 254–266, Feb. 2007, doi: 10.1016/j.ultramic.2006.08.007.

[29] D. Mainprice, “A personal and practical guide to the history, installation and future of the Electron Back--Scattered Diffraction (EBSD) system,” Dec. 2012.

[30] “Electron backscatter diffraction (EBSD).” https://ssd.phys.strath.ac.uk/techniques/scanning-electron-microscopy/electron-backscatter-diffraction-ebsd/

[31] “Introduction to Electron Backscatter Diffraction,” Institute of metallurgy and materials science - Polish academy of sciences.

[32] “Interpreting the Diffraction Pattern in EBSD,” *Oxford Instruments*. https://www.ebsd.com/ebsd-explained/interpreting-the-diffraction-pattern (accessed Jul. 28, 2022).

[33] A. J. Schwartz, M. Kumar, B. L. Adams, and D. P. Field, Eds., *Electron Backscatter Diffraction in Materials Science*. Boston, MA: Springer US, 2009. doi: 10.1007/978-0-387-88136-2.

[34] T. Baudin, “Principe et cartographies d’orientations,” p. 22.

[35] R. A. Schwarzer, “Automated crystal lattice orientation mapping using a computer-controlled SEM,” *Micron*, vol. 28, no. 3, pp. 249–265, Jun. 1997, doi: 10.1016/S0968-4328(97)00010-3.

[36] S. I. Wright, “Considerations for 3D EBSD,” EDAX-TSL, Draper, Utah.

[37] T. B. Britton *et al.*, “Tutorial: Crystal orientations and EBSD — Or which way is up?,” *Mater. Charact.*, vol. 117, pp. 113–126, Jul. 2016, doi: 10.1016/j.matchar.2016.04.008.

[38] “Edax insight volume 17 no2,” Jul. 2017. https://www.edax.com/-/media/ametekedax/files/news_events/insight_newsletter/edax-insight-vol-17-no2.pdf?la=en&revision=1c366a64-97ae-4a57-9d0f-855733719475

[39] S. I. Wright and B. L. Adams, “Automatic analysis of electron backscatter diffraction patterns,” *Metall. Trans. A*, vol. 23, no. 3, pp. 759–767, Mar. 1992, doi: 10.1007/BF02675553.

[40] S. I. Wright, “Fundamentals of Automated EBSD,” in *Electron Backscatter Diffraction in Materials Science*, A. J. Schwartz, M. Kumar, and B. L. Adams, Eds. Boston, MA: Springer US, 2000, pp. 51–64. doi: 10.1007/978-1-4757-3205-4_5.

[41] S. I. Wright and M. M. Nowell, “EBSD Image Quality Mapping,” *Microsc. Microanal.*, vol. 12, no. 01, pp. 72–84, Feb. 2006, doi: 10.1017/S1431927606060090.

[42] X. Tao and A. Eades, “Alternatives to Image Quality (IQ) Mapping in EBSD,” *Microsc. Microanal.*, vol. 8, no. S02, pp. 692–693, Aug. 2002, doi: 10.1017/S1431927602106465.

[43] R. de Kloe, “Electron BackScatter Diffraction - basics and applications -,” p. 40.

[44] “MTEX Toolbox | MTEX.” https://mtex-toolbox.github.io/ (accessed May 15, 2021).

[45] C. A. Volkert and E. T. Lilleodden, “Size effects in the deformation of sub-micron Au columns,” *Philos. Mag.*, vol. 86, no. 33–35, pp. 5567–5579, Nov. 2006, doi: 10.1080/14786430600567739.

[46] H. Zhang, B. E. Schuster, Q. Wei, and K. T. Ramesh, “The design of accurate micro-compression experiments,” *Scr. Mater.*, vol. 54, no. 2, pp. 181–186, Jan. 2006, doi: 10.1016/j.scriptamat.2005.06.043.

[47] I. N. Sneddon, “The relaxation between load and penetration in the axisymmetric boussinedq problem for a punch of arbitrary profile,” *Int. J. Engng Sci.*, vol. Vol. 3, pp. 47–57, 1965.

[48] “Properties: An Introduction to Iron,” *AZoM.com*. https://www.azom.com/properties.aspx?ArticleID=619 (accessed Aug. 31, 2022).

[49] “Modulus of Elasticity Young’s Modulus Strength for Metals - Iron and Steel.” https://www.engineersedge.com/manufacturing_spec/properties_of_metals_strength.htm (accessed Aug. 31, 2022).

[50] “Ferrous metals elastic modulus and Poisson ratio | Sonelastic®.” https://www.sonelastic.com/en/fundamentals/tables-of-materials-properties/ferrous-metals.html (accessed Aug. 31, 2022).

[51] admin, “Young’s modulus of several materials • pickedshares,” *pickedshares*, Jun. 02, 2021. https://pickedshares.com/en/youngs-modulus-of-several-materials/ (accessed Aug. 31, 2022).

[52] E. Borchi, M. Bruzzi, U. Biggeri, C. Furetta, and F. Lemeilleur, “ELASTIC MODULI OF POLYCRYSTALLINE DIAMOND,” p. 15.

[53] C. A. Klein and G. F. Cardinale, “Young’s modulus and Poisson’s ratio of CVD diamond,” p. 6.

[54] “Properties: Diamond (C) - Properties and Applications,” *AZoM.com*. https://www.azom.com/properties.aspx?ArticleID=262 (accessed Aug. 01, 2022).

[55] D. B. Williams and C. B. Carter, *Transmission electron microscopy: a textbook for materials science*, 2nd ed. New York: Springer, 2008.

[56] C. Hébert and D. Alexander, “Transmission electron microscopy for materials science,” *Coursera*. https://www.coursera.org/learn/microscopy (accessed Aug. 01, 2022).

[57] S. D. Findlay *et al.*, “Annular Bright-Field Scanning Transmission Electron Microscopy: Direct and Robust Atomic-Resolution Imaging of Light Elements in Crystalline Materials,” *Microsc. Today*, vol. 25, no. 6, pp. 36–41, Nov. 2017, doi: 10.1017/S1551929517001006.

[58] “Keywords ‘annular bright-field scanning transmission electron microscopy’ | Keywords | Glossary of TEM Terms | JEOL.” https://www.jeol.co.jp/en/words/emterms/search_result.html?keyword=annular%20bright-field%20scanning%20transmission%20electron%20microscopy (accessed Aug. 31, 2022).

[59] “4D STEM | Gatan, Inc.” https://www.gatan.com/techniques/4d-stem (accessed Jul. 29, 2022).

[60] S.-W. Kim, T.-Y. Ahn, and D.-J. Kim, “Analysis of dislocation density in strain-hardened alloy 690 using scanning transmission electron microscopy and its effect on the PWSCC growth behavior,” *Nucl. Eng. Technol.*, vol. 53, no. 7, pp. 2304–2311, Jul. 2021, doi: 10.1016/j.net.2021.01.008.

[61] Y. Meng, X. Ju, and X. Yang, “The measurement of the dislocation density using TEM,” *Mater. Charact.*, vol. 175, p. 111065, May 2021, doi: 10.1016/j.matchar.2021.111065.

[62] R. K. Ham, “The determination of dislocation densities in thin films,” *Philos. Mag.*, vol. 6, no. 69, pp. 1183–1184, Sep. 1961, doi: 10.1080/14786436108239679.

# Chapter 3: Microstructural study of the model alloys

## Introduction

This thesis chapter reviews the results of the APT experiments carried out to investigate the microstructure evolution of three model alloys.

Following neutron irradiation of RPV steels, nanometric clusters containing Mn, Ni and Si form and act as a barrier to dislocation motion, inducing hardening and embrittlement of the RPV steel. To study how each of the alloying solutes Mn and Ni, participate on cluster formation and the resulting irradiation hardening, as well as their combined effect, two binary alloys and a ternary alloy were studied in the non-irradiated (reference state) and neutron irradiated state.

Their microstructures before and after irradiation were studied by APT. Size, number density, volume fraction and chemical composition of the identified nanometric size clusters were calculated.

The cluster characteristics between the examined alloys are compared to evaluate the effect of Mn and Ni to the cluster formation.

However, comparing the effect of the irradiation on the evolved microstructure in the studied alloys is not trivial. Although the binary alloys were irradiated with the same conditions, the irradiation conditions of the ternary alloy were different, that is the ternary was irradiated at the dose of 0.1 dpa versus the 0.022 dpa dose of both the binary alloys. Nevertheless, the comparison of the measured microstructural characteristics between the three studied materials, offers some indications about the effect of each solute on the cluster formation, under irradiation.

Although the formation of Mn-Ni-Si solute clusters (MNSP) in either low Cu steels or non-containing Cu steels is not in question, there is a strong argument regarding the probable formation mechanism. Therefore, whether the MNSPs formation is driven by thermodynamic and thus are intermetallic phases or they are solute clusters induced by the kinetics of the high density of defects created under irradiation. This is a controversial topic in literature.

An isochronal post irradiation annealing (PIA) experiment at 400$^{o}$C, 500$^{o}$C and 600$^{o}$C, was designed to offer insight into this issue, by evaluating the MNSP cluster stability, specifically by measuring the dissolution or the coarsening of the identified clusters. If these clusters are intermetallic phases, they should be stable and coarsen, otherwise if the clusters result from radiation induced segregation, they should dissolve with the increasing annealing temperature.

# I. Microstructural study of the binary alloys

## 1. Microstructure of the Fe-Mn model alloy in the non-irradiated and neutron irradiated states

The unirradiated Fe-Mn alloy was analyzed by APT using the LEAP 5000 XR. Prior to this PhD study, B. Radiguet had also conducted APT experiments on this alloy using the then available, laser assisted atom probes, namely the LAWATAP (Laser Assisted Wide Angle Tomographic Atom Probe) and FLEXTAP (Flexible Tomographic Atom Probe) atom probes. The obtained raw results were now reconstructed using the GPM 3D Software and included in the microstructural analysis of this alloy, as well.

Since there were no significant variations in the Mn concentration detected in all analyzed samples, the average Mn content was calculated, and it is in good accordance with the target one (~ 0,85 at. % vs 1 at. %). Other elements, such as Ni, Si, P, C, N and O, were detected in lower concentrations and their weighted average concentration is tabulated in Table 3 along with two weighted standard deviations (Fe is balance).

The minor compositional differences that we observed between the results of the different APTs concerned only the P which was not detected only in the samples analyzed using the FLEXTAP, although the P content calculated using the other two atom probes was similar.

*Table 3:-Mean element content of the non-irradiated Fe-Mn model alloy as measured by APT (at. %) The uncertainty in the reported mean values is indicated using two standard error of the mean (Fe is balance).*

| **Element** | **Global content** (at. %) |
|---|---|
| **Mn** | 0.85 ± 0.05 |
| **Si** | 0.003 ± 0.002 |
| **P** | 0.003 ± 0.002 |
| **Cr** | 0.04 ± 0.01 |

A homogeneous solute distribution is observed in atom maps (Figure 104 - a). This was confirmed by the first nearest neighbors (1NN) distribution of Mn atoms, since it matches the random curve (Figure 104 - b) which is plotted using [30]:

$$F^r = 4\pi d_s^2 Q C_B e^{\left(-\frac{4}{3}\pi Q C_B d_s^3\right)} \quad (3.1)$$

where Q is detection efficiency (52% for the LEAP 5000 X HR), $C_B$ is the bulk solute concentration and $d_s$ is the sampling step.

Additionally, after applying the isoposition clustering algorithm no clusters were identified since the experimental concentration distribution was found almost identical to the random distribution plotted by the GPM 3D software (Figure 104 - c).

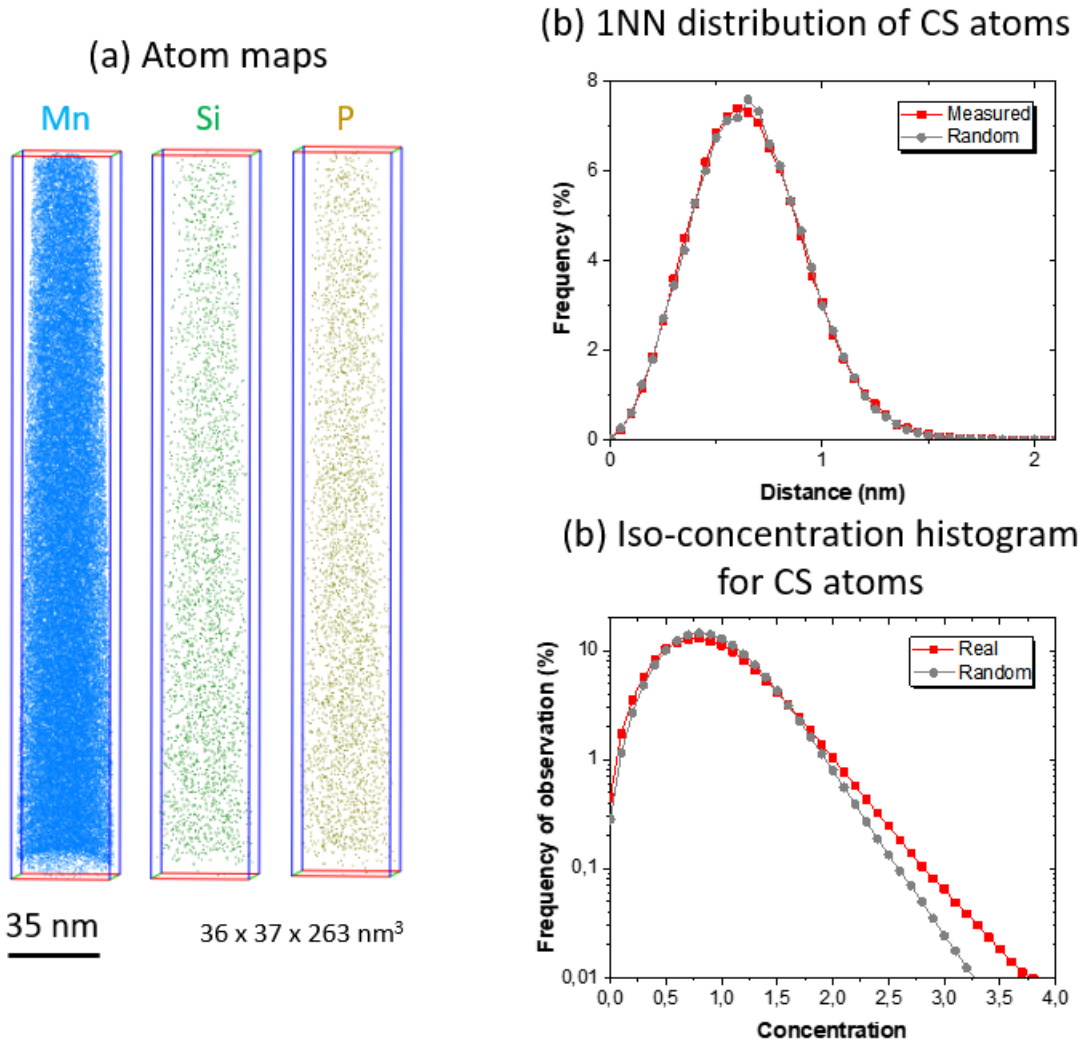


*Figure 104: Examples of (a) atom maps of Mn, Si and P (b) the first nearest neighbor distribution of Mn atoms compared to a random distribution and (c) iso-concentration histogram of Mn atoms, for the unirradiated Fe-Mn model alloy.*

After neutron irradiation at 0.022 dpa at approximately 300°C, APT analysis using the LEAP 5000 X HR measured an average global Mn content equal to 0.92 at. %, which is very similar as the global Mn content in the non-irradiated samples.

In Table 4, are reported the detected elements, their weighted average chemical concentration in at. %, along with the uncertainty of the measurement expressed as two times the standard error of the mean and Fe is the balance.

*Table 4: Average global, matrix and cluster content in at. % as measured by APT experiments of the neutron irradiated Fe-Mn model alloy (the balance is Fe). The uncertainty is expressed as two times the standard error of the mean.*

| Element | $X_{Global}$ (at. %) | $X_{matrix}$ (at. %) | $X_{clusters}$ (at. %) |
|---|---|---|---|
| **Mn** | 0.92 ± 0.03 | 0.87 ± 0.03 | 10.2 ± 0.7 |
| **Ni** | 0.042 ± 0.002 | 0.041 ± 0.002 | 0.26 ± 0.05 |
| **Si** | 0.016 ± 0.003 | 0.015 ± 0.004 | 0.04 ± 0.04 |
| **P** | 0.009 ± 0.002 | 0.008 ± 0.001 | 0.18 ± 0.07 |
| **C** | 0.141 ± 0.006 | 0.141 ± 0.006 | 0.21 ± 0.07 |
| **O** | 0.022 ± 0.006 | 0.023 ± 0.006 | 0.05 ± 0.03 |
| **N** | 0.003 ± 0.005 | 0.003 ± 0.006 | 0.02 ± 0,03 |
| **Cr** | 0.063 ± 0.004 | 0.063 ± 0.003 | 0.12± 0.04 |

About 100 clusters per tip were identified after applying the isoposition method (IPM) using as 'core solute element' (CS) the Mn. The used average minimum concentration threshold was $C_{Thr}^{CS} = 3.45\ at.\%$ and the minimum number of solute atoms $N_{Min}^{CS} = 7\ atoms$.

The solutes clusters can be observed in the atom maps of Figure 105 – a, where the radius of the atoms inside the clusters is magnified, to facilitate their visualization.

Figure 105 – b and c are the plots of the 1NN distribution and the iso-concentration histogram of Mn. Both experimental curves do not match the random one, indicating a non-homogeneous distribution of Mn.

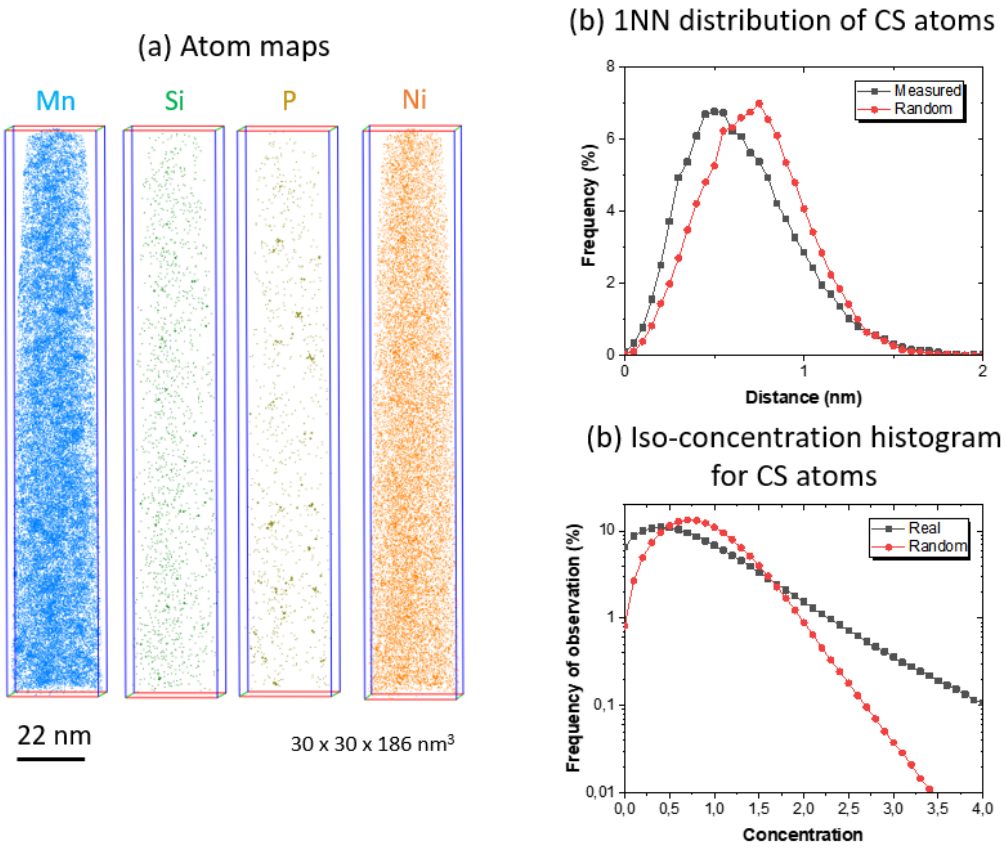


*Figure 105: Neutron irradiated Fe-Mn model alloy: (a) clusters are visible in the atom maps of Mn, Si and P. Their existence is verified by statistical tests: (b) the first nearest neighbor distribution of Mn atoms is different compared to a random distribution, as well as (c) the iso-concentration histogram of Mn atoms.*

By studying Table 4, that also summarizes the average cluster and matrix chemical composition, it can be observed that the matrix Mn content is slightly reduced, due to the presence of solutes clusters which are enriched in Mn reaching at about 10 at. %. Additionally, the clusters are slightly enriched in Ni, Si and P, without causing any measurable depletion of these elements from the ferritic matrix.

Concerning their size, the clusters present a mean Guinier and equivalent spherical radius of 1.1 ± 0.1 nm and 1.0 ± 0.1 nm respectively Their size distribution is illustrated in (Figure 106 – a) where it is evident that the peak frequency is between 0.7 nm and 0.8 nm.

The cluster morphology is examined by plotting their aspect ratio and oblateness after the first erosion, at the matrix – cluster interface. To study whether the cluster morphology changes with the cluster size, the clusters were divided into three class sizes using a step of 1nm (Figure 106 – b). Almost all clusters of the neutron irradiated Fe-Mn alloy lay on the center of the sphere quadrant and so, they are all considered to be spherical, suggesting that cluster morphology did not evolve with size.

Their mean number density was calculated at (14 ± 1) x$10^{23}$ $m^{-3}$ while their volume fraction at 0.98 ± 0.07 %.

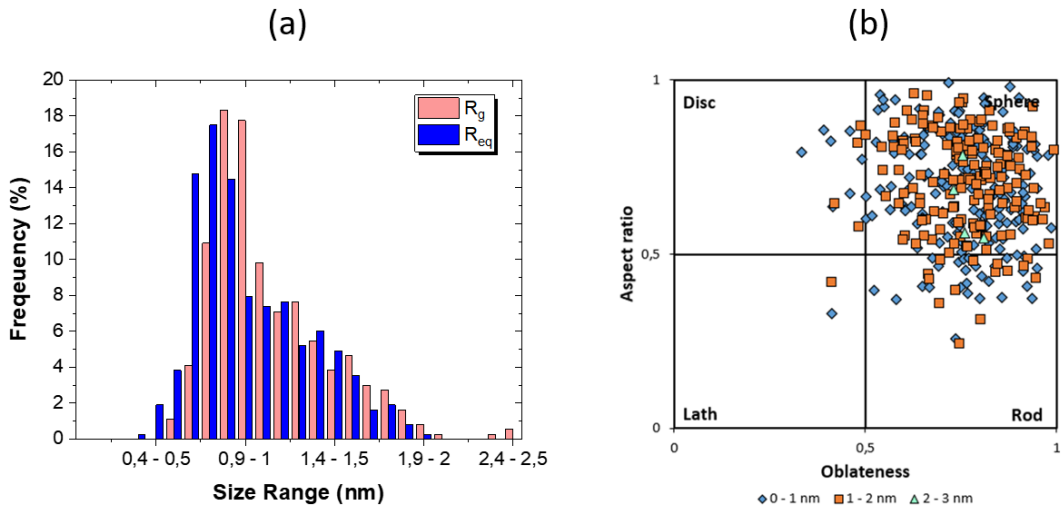


*Figure 106: (a) Guinier (red) and equivalent radius (blue) distribution and (b) Aspect ratio vs oblateness graph of the complete clusters identified in the neutron irradiated Fe-Mn analyses. The clusters in (b) are presented by three class sizes: blue diamond: 0 – 1 nm, orange square: 1 – 2 nm and blue triangle: 2 – 3 nm.*

In one of the analyzed volumes, clusters were identified on a dislocation line. (Figure 107 – a) shows the Fe matrix (in grey) of the analyzed tip along with all the identified clusters. The elements that constitute the clusters on the dislocation line are also displayed.

They exhibit a mean Guinier and equivalent spherical radius equal to 1.5 ± 0.3 nm and 1.4 ± 0.4 nm respectively. Their morphology mostly lies in the spherical quadrant as seen in (Figure 107 – b).

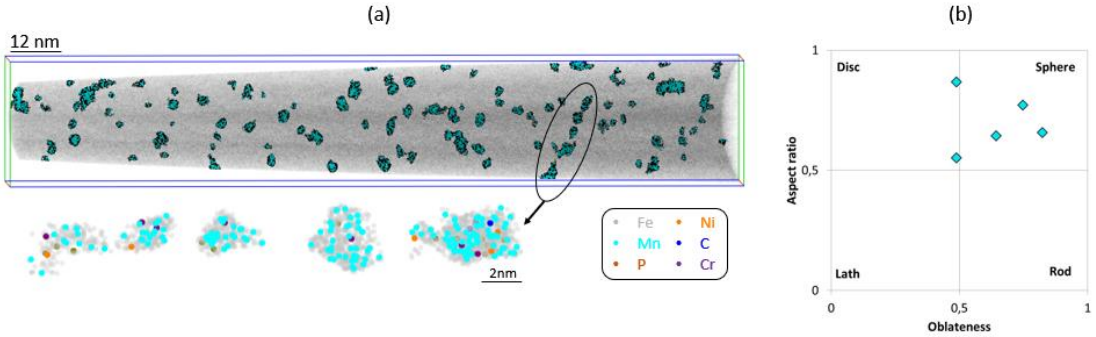


*Figure 107: Fe-Mn neutron irradiated sample: (a) Clusters detected on a dislocation line (b) Aspect ratio vs oblateness graph of these clusters.*

Assuming that the mean dislocation density for the model alloys is 5 x$10^{13}$ $m^{-2}$ [1], the mean number density of clusters decorating the dislocations is estimated to 1.0 x$10^{22}$ $m^{-3}$. These 5 clusters detected along a dislocation line segment, were the only ones in the 4 analyzed tips that is in a total volume of 3.2x$10^{-22}$ $m^3$. This calculates to a mean number density of 1.6x$10^{22}$ $m^{-3}$ for the clusters decorating the dislocations. And considering that, in the same volume, the detected length of the dislocation is 24.4 nm then the dislocation density can be estimated to 7.7 x$10^{13}$ $m^{-2}$, fairly similar to the assumed one for the model alloys.

## 2. Microstructure of the Fe-Ni model alloy in the non-irradiated and neutron irradiated states

The unirradiated Fe-Ni alloy was analyzed by APT using the LEAP 5000 XR. APT analysis detected higher Ni content than the target nominal one (~1.82 at. % vs 1 at. %). Other elements, such as Si, P, C, N and O, were identified in lower concentrations and their weighted average content is detailed in Table 5 along with two standard weighted deviations. The Fe content is calculated as the balance.

*Table 5: Mean content of the non-irradiated Fe-Ni model alloy as measured by APT (at. %) along with the uncertainty expressed by two times the standard error of the mean (the balance is Fe).*

| **Element** | **Global content** (at. %) |
|---|---|
| **Mn** | Not detected |
| **Ni** | 1.82 ± 0.10 |
| **Si** | 0.007 ± 0.008 |
| **P** | 0.002 ± 0.001 |
| **C** | 0.19 ± 0.12 |
| **O** | 0.02 ± 0.02 |
| **N** | 0.01 ± 0.02 |
| **Cr** | 0.005 ± 0.005 |

Atom maps of the elements identified in the unirradiated Fe-Ni alloy suggest a rather homogeneous solutes distribution (Figure 108 – a). This was confirmed as i.e., the experimental Ni 1NN distribution is almost identical to the random one (Figure 108 – b) and no clusters were identified after applying the IPM.

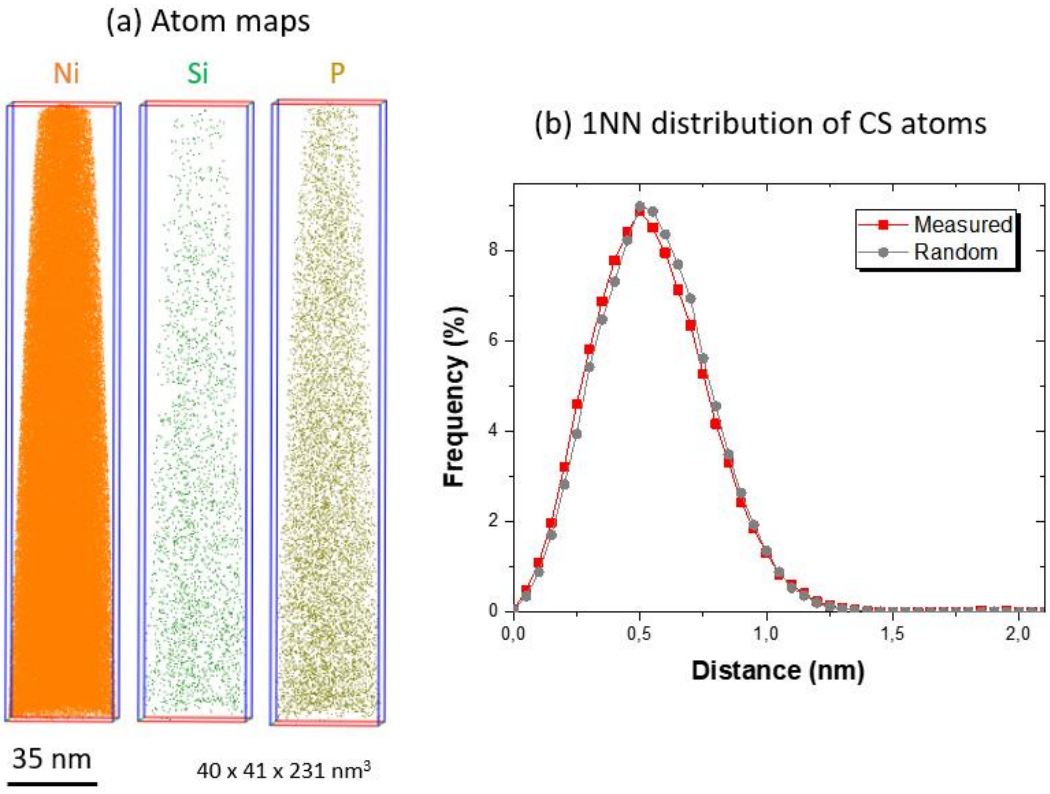


*Figure 108: Examples of (a) atom maps of Ni, Si and P (b) the first nearest neighbor distribution of Ni atoms compared to a random distribution, for the unirradiated Fe-Mn model alloy.*

APT experiments of the neutron irradiated Fe-Ni alloy confirmed the high Ni content, similar to the detected one in the non-irradiated samples. Indeed, the average global Ni concentration was calculated at 1.7 ± 0.1 at. %. Although Mn was not detected in the unirradiated Fe-Ni model alloy, very low concentrations of Mn were measured in the neutron irradiated samples.

The same lower concentration elements, that were identified in the unirradiated samples, were also present in the neutron irradiated ones, at concentrations reported in (Table 6), where the balance is Fe.

*Table 6: Average global, matrix and cluster content in at. % as measured by APT experiments of the neutron irradiated Fe-Ni model alloy (the balance is Fe). The uncertainty is expressed as two times the standard error of the mean.*

| Element | $X_{Global}$ (at. %) | $X_{matrix}$ (at. %) | $X_{clusters}$ (at. %) |
|---|---|---|---|
| **Mn** | 0.001 ± 0.002 | 0.001 ± 0.002 | Not detected |
| **Ni** | 1.71 ± 0.13 | 1.68 ± 0.16 | 17.21 ± 3.09 |
| **Si** | 0.03 ± 0.01 | 0.03 ± 0.01 | 0.36 ± 0.21 |
| **P** | 0.001 ± 0.001 | 0.001 ± 0.001 | Not detected |
| **C** | 0.24 ± 0.15 | 0.24 ± 0.15 | 0.29 ± 0.51 |
| **O** | 0.03 ± 0.02 | 0.03 ± 0.02 | 0.61 ± 0.41 |
| **N** | 0.03 ± 0.02 | 0.06 ± 0.02 | Not detected |
| **Cr** | 0.012 ± 0.006 | 0.012 ± 0.007 | 0.14 ± 0.13 |

The IPM clustering algorithm was applied using Ni as 'core solute element' (CS). The average minimum concentration threshold and number of solute atoms were $C_{Thr}^{CS} = 2.8\ at.\%$ and $N_{Min}^{CS} = 5.5\ atoms$ respectively.

In Figure 109, the solute clusters can be observed in the atom maps. To obtain a clear enough cluster visualization, the imaging radius of the atoms inside the identified clusters was augmented. Additionally, the 1NN distribution of the Ni atoms of this sample is observed to be slightly different from the random one.

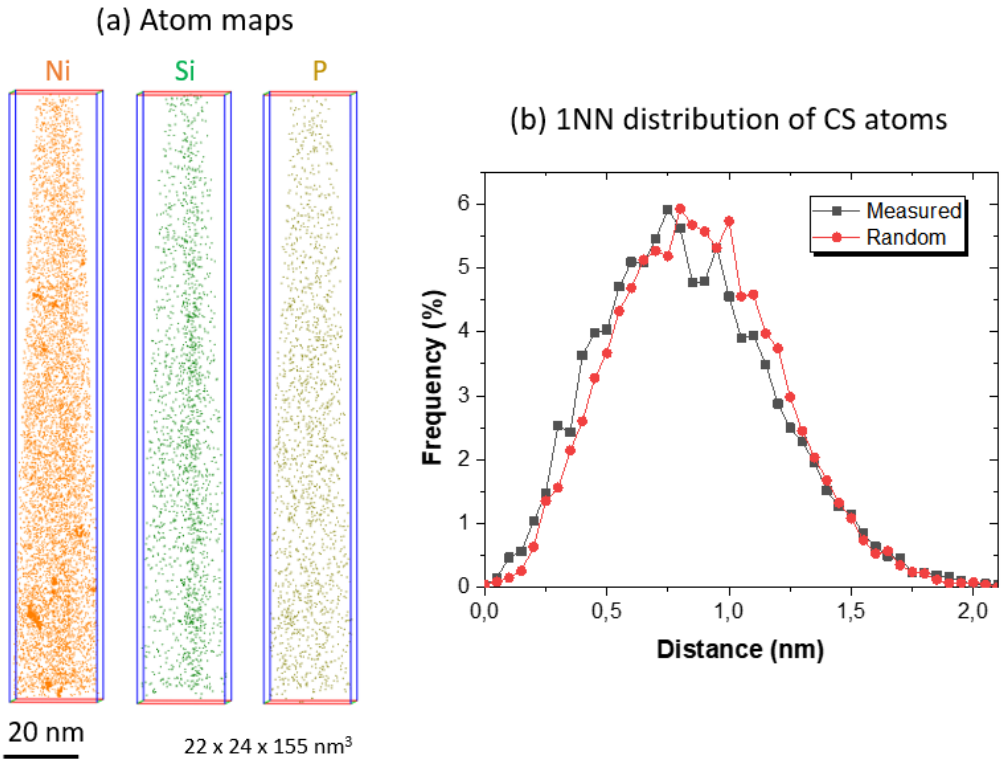


*Figure 109: Examples of (a) atom maps of Ni, Si and P (b) the first nearest neighbor distribution of Ni atoms compared to a random distribution, for the neutron irradiated Fe-Mn model alloy.*

Contrary to the neutron irradiated Fe-Mn alloy, only very few clusters were identified in the neutron irradiated Fe-Ni samples. More specifically, in average 9 clusters per tip were detected (including the ones located at the edge of the tips).

Table 6 also summarizes the average matrix and cluster chemical composition. The ferritic matrix content is slightly reduced in Ni, which is detected at a concentration of about 17 at. % inside the identified clusters. The clusters contain Si, C, O and Cr in low concentrations, but no P was identified.

The detected clusters have a slightly bigger size than the ones identified in the neutron irradiated Fe-Mn samples. More precisely, the clusters' mean Guinier and equivalent spherical radius are equal to 1.3 ± 0.2 nm and 1.2 ± 0.1nm respectively. Their size distribution plotted in Figure 110 – a, illustrates that the majority of the clusters are in the size range between 1 and 2 nm.

Their morphology lays on the spherical quadrant of the aspect ratio vs oblateness graph (Figure 110 – b). Cluster mean number density is (1.5 ± 0.4) x $10^{23}$ $m^{-3}$, while their volume fraction is 0.18 ± 0.04 %.

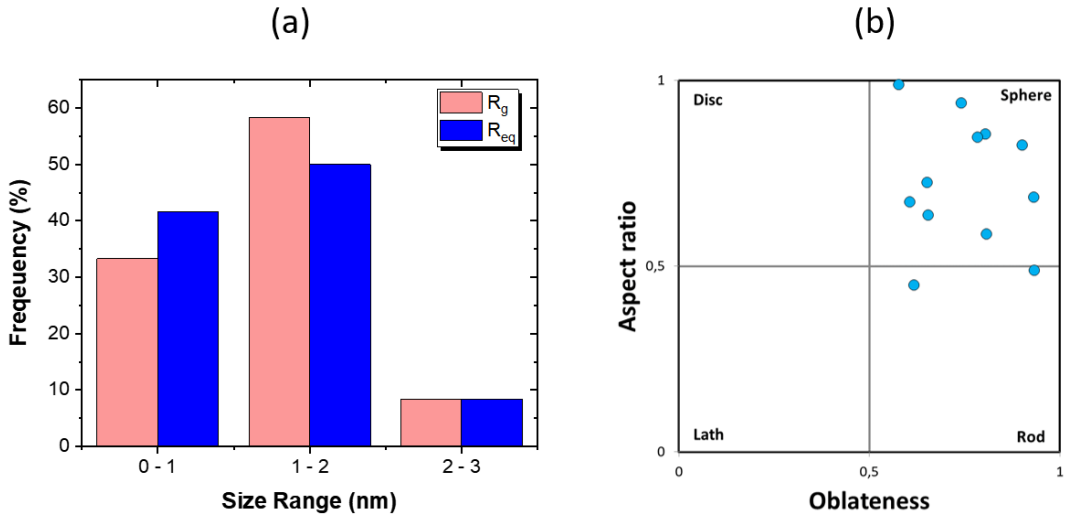


*Figure 110: (a) Guinier (red) and equivalent radius (blue) distribution and (b) aspect ratio vs oblateness graph of the complete clusters identified in the neutron irradiated Fe-Ni analyses.*

## 3. Cluster formation mechanism in the neutron irradiated binary alloys

According to the APT analysis, prior to irradiation, solute atoms distribution was homogeneous in both Fe-Mn and Fe-Ni model alloys. While after irradiation, APT analyses detected that small sized clusters have been generated in both alloys.

In the binary phase diagrams of the Fe-Mn [2] and Fe-Ni [3] (Figure 111), at the irradiation temperature of 300°C, the solubility limits of Mn and Ni are about equal to approximately 3 and 4.5 at. %, respectively. This clearly indicates that both the binary alloys are under-saturated, and therefore precipitation is not thermodynamically favored to any of them.

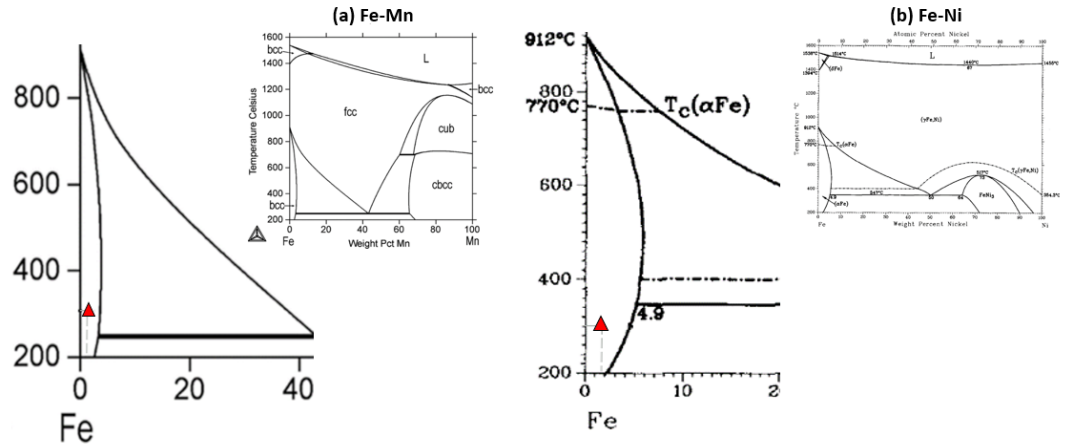


*Figure 111: (a) Fe-Mn [2] and (b) Fe-Ni [3] binary phase diagrams and zoomed section around 1 at. % Mn and 1.7 at. % Ni.*

Thus, the probable mechanism that created the observed clustering in such dilute alloys, is the radiation induced segregation. Point defects generated under irradiation may associate selectively with some solutes, forming stable enough point defect - solute complexes and thus the fluxes of the mobile defects and these solutes get coupled.

Having both PDs and solute fluxes oriented in the same direction (positive correlation), solutes are transported via the drag mechanism towards the local sinks, resulting in segregation at their vicinity which in turn may induce the nucleation and formation of the solute clusters.

The APT analysis of the detected solute clusters in the Fe-Mn and Fe-Ni binary alloys, indicated that they were enriched in Phosphorous and Silicon respectively, even though the model alloys contained these elements at a quite low bulk concentration. Specifically, the Mn-enriched clusters contained the relatively increased phosphorous amount of 0.18 at. % compared to 0.01 at. % of the bulk. Since both P and Mn are elements fast migrating preferentially by dumbbells [4], detecting both these two elements inside the clusters, implies the RIS as the acting solute transporting mechanism via SIA drag. Moreover, the Ni-enriched clusters contained Si in 0.36 at. % (vs 0.03 at. % of the bulk) and no phosphorous. According to Messina [4], at about 300$^{o}$C diffusivity by vacancies is much faster for Ni and slightly predominant for Si. Therefore, again RIS is indicated as the acting solute transporting mechanism, but in this case, via vacancy drag. Under neutron irradiation, as Castin suggests [5], heterogeneous nucleation of solute clusters is probable to occur on small, immobilized point-defect clusters. Hence, solute segregation is likely to happen mainly on small SIA loops acting as PDs sinks, since solute-vacancy clusters may dissolve in RPV operation temperatures.

In the neutron irradiated Fe-Mn alloy, Mn enriched clusters were formed at a high number density (14 ± 1) x$10^{23}$ $m^{-3}$ in the bulk and also on dislocations, but at a significant lower density, (about 1.0 x$10^{22}$ $m^{-3}$). Meslin et al. [6] had also studied a binary Fe–1 at. % Mn ferritic alloy, observed after irradiation with 10MeV Fe ions. Mn- enriched clusters, likely formed due to RIS, were observed on a planar feature that according to the authors, could be either a dislocation loop or a grain boundary. Williams et al. [7], studying an oxide-dispersion-strengthened (ODS) ferritic steel containing 0.45 at. % Mn, that was Fe ion-irradiated to about 2 dpa, observed segregation of Mn to dislocations.

Taking into consideration the above mentioned, it appears than under neutron irradiation Mn rich clusters form mainly in the matrix on PDs clusters, while in the case of ion irradiation Mn segregates preferably on network dislocations.

Solute segregation on locations that depend on the irradiation conditions (neutron vs ion irradiation) has also been reported in reactor pressure vessel steels by Odette et al. [8] for MNSPs formation. They observed that under neutron irradiation MNSPs mainly form in the matrix with a much larger volume fraction than on dislocations (about 1.4% vs 0.2% respectively), which is reversed in the case of ion irradiation.

# II. Microstructural study of the ternary model alloy

## 1. Microstructure of the ternary model alloy in the non-irradiated and neutron irradiated states

The global Mn and Ni content of the non-irradiated Fe-Mn-Ni alloy was calculated at (0.93 ± 0.01) at. % Mn and (0.74 ± 0.01) at. % Ni, which is very close to the target nominal content (1.1 at. % Mn and 0.7 at. % Ni). Other elements in lower concentrations were identified in all analyzed samples (Table 7).

*Table 7: Mean content of the non-irradiated Fe-Mn-Ni model alloy as measured by APT (at. %) along with along with two times the standard error of the mean (Fe is balance).*

| **Element** | **Global content** (at. %) |
|---|---|
| **Mn** | 0.93 ± 0.01 |
| **Ni** | 0.74 ± 0.01 |
| **Si** | 0.032 ± 0.003 |
| **P** | 0.003 ± 0.002 |
| **C** | 0.10 ± 0.08 |

Clustering was not observed on the atom maps (Figure 112 – a). The homogeneous distribution of the solute elements was confirmed by statistical tests (as in Figure 112 – b), that compared the experimental atom distributions against random ones, with Mn, Ni, Si and P as 'core solute element' (CS).

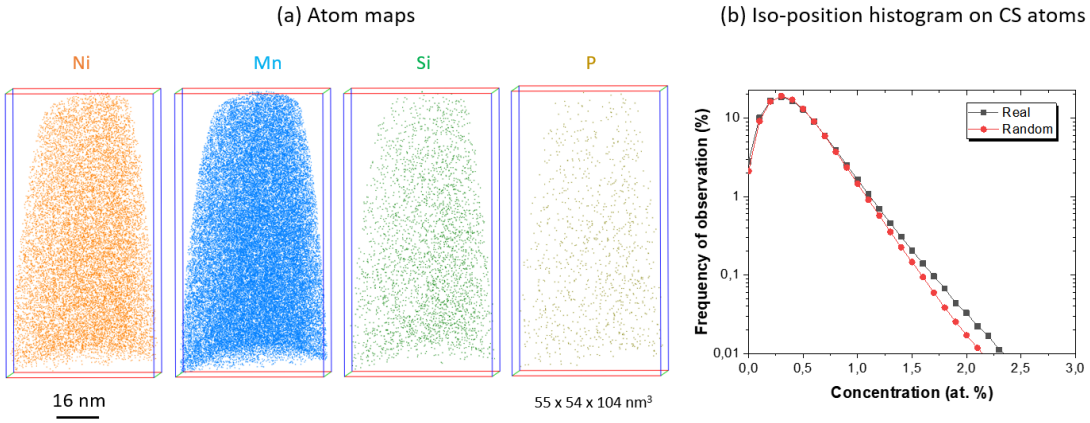


*Figure 112: (a) Atom maps of Mn, Si and P (b) iso-concentration histogram of CS atoms, of a sample of the neutron irradiated Fe-Mn model alloy.*

According to APT measurements of the neutron irradiated Fe-Mn-Ni alloy samples, they contain in average 1.29 ± 0.05 at. % Mn and 0.82 ± 0.04 at. % Ni. The detected slight difference in Mn bulk content between unirradiated and irradiated samples is attributed to the fact that they originated from 2 different casts that the manufacturer fabricated. Alike the unirradiated samples, solute elements in low concentrations were also identified (Table 8).

*Table 8: Mean global, matrix and cluster content in at. % as measured by APT experiments of the neutron irradiated Fe-Mn-Ni model alloy along with two times the standard error (Fe is balance).*

| Element | $X_{Global}$ (at. %) | $X_{matrix}$ (at. %) | $X_{clusters}$ (at. %) |
|---|---|---|---|
| **Mn** | 1.29 ± 0.05 | 1.17 ± 0.05 | 10.03 ± 0.69 |
| **Ni** | 0.82 ± 0.04 | 0.74 ± 0.03 | 7.95 ± 0.79 |
| **Si** | 0.043 ± 0.003 | 0.032 ± 0.004 | 0.9 ± 0.2 |
| **P** | 0.007 ± 0.001 | 0.003 ± 0.001 | 0.4 ± 0.2 |
| **C** | 0.017 ± 0.005 | 0.016 ± 0.004 | 0.06 ± 0.05 |
| **N** | 0.11 ± 0.02 | 0.10 ± 0.02 | 0.5 ± 0.1 |
| **Cr** | 0.009 ± 0.001 | 0.009 ± 0.001 | 0.027 ± 0.009 |

Solute clusters were identified and quantified in all analyzed volumes. The average minimum concentration threshold was $C_{Thr}^{CS} = 4.5\ at.\%$ and number of solute atoms were $N_{Min}^{CS} = 10\ atoms$

The chemical composition of the clusters along with the matrix and the global compositions are summarized in Table 8. Note that the matrix concentration of P significantly decreases along with a slight decrease in matrix Si concertation to counterbalance the significant increased Si and P content detected inside the clusters.

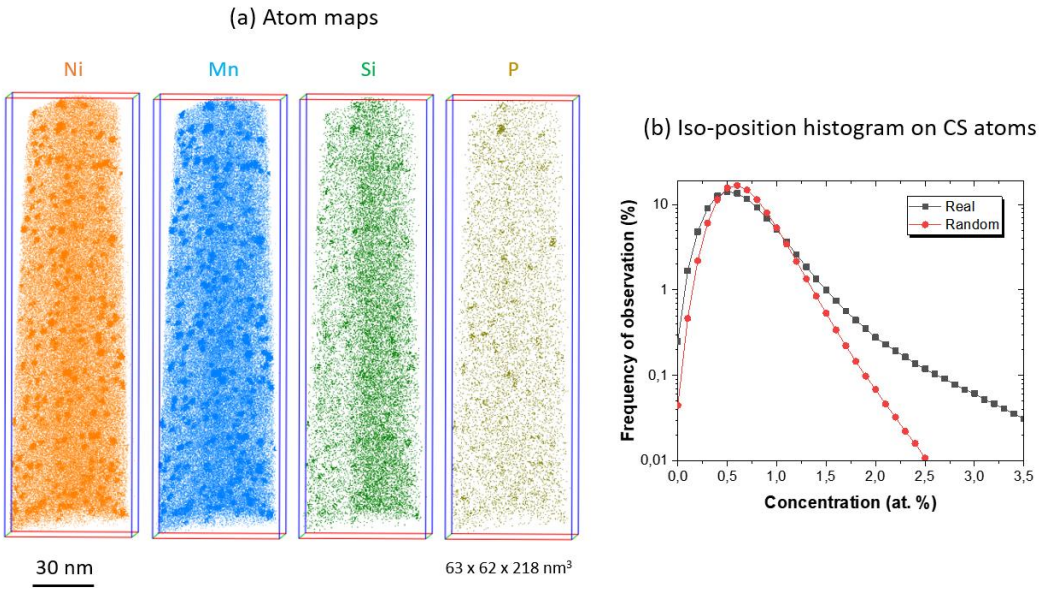


*Figure 113: (a) Atom maps of Ni, Mn, Si and P (b) iso-concentration histogram of Mn and Ni atoms, (c) iso-concentration histogram of CS atoms, of a sample of the neutron irradiated Fe-Mn model alloy.*

These clusters (Figure 114) had a slightly larger size, compared to the clusters of the binary materials. The calculated mean Guinier radius was (1.4 ± 0.1) nm and the equivalent spherical radius (1.4 ± 0.1) nm. The estimated mean number density was (6.2 ± 0.8) x$10^{23}$ $m^{-3}$ while their volume fraction was (1.35 ± 0.23) %.

The clusters morphology, judging from their aspect ratio vs oblateness graph is rather spherical, with no specific trend being apparent in Figure 114 – b, as the cluster size increases from 1 to 4 nm, with a step of 1 nm.

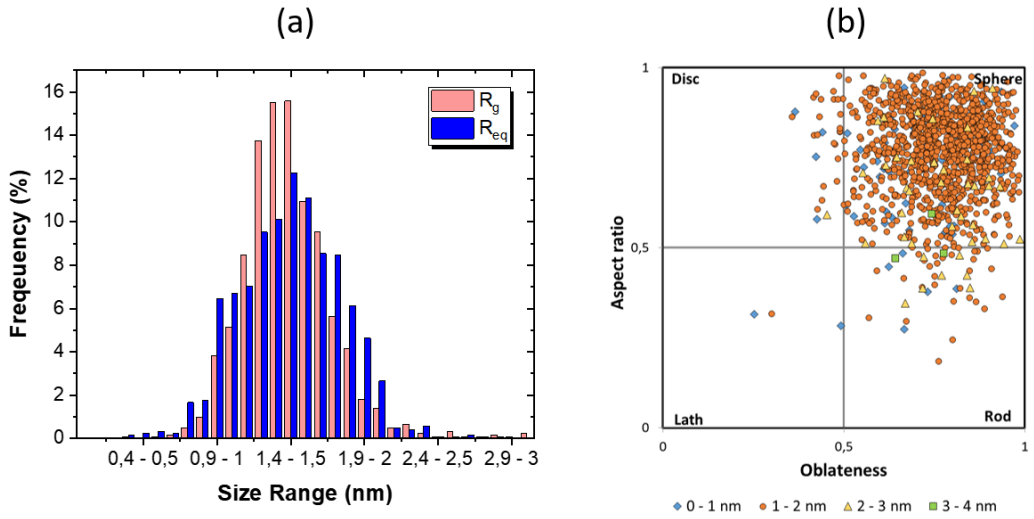


*Figure 114: (a) Frequency distribution of the Guinier (red) and equivalent radius (blue) and (b) Aspect ratio vs oblateness graph of the complete clusters identified in the neutron irradiated Fe-Mn-Ni analyses. The clusters in (b) are presented by 4 class sizes: grey diamond: 0 – 1 nm, orange square: 1 – 2 nm and blue triangle: 2 – 3 nm.*

Meslin et. al [9] previously studied the same ternary alloy, neutron irradiated at the same fluence (6.9 x$10^{19}$ n.$cm^{-2}$). Although, as APT analysis revealed, the bulk Mn and Ni content (1.12 ± 0.02 at. % Mn 0.73 ± 0.01 at. % Ni) was very similar to the ternary alloy studied in this work (1.26 ± 0.1 at. % Mn 0.75 ± 0.24 at. % Ni), the measured cluster characteristics are significantly different. While the average cluster content in Mn was similar, the Ni content was significantly lower than in this study (3.3 ± 0.5 at. % vs 7.99 ± 0.16 at. %) as well as the mean Guinier radius (0.7 ± 0.2 nm vs 1.4 ± 0.1 nm). The cluster number density was slightly lower in this study (7.7 ± 2.3 x$10^{23}$ $m^{-3}$ vs 6.2 ± 0.2 x$10^{23}$ $m^{-3}$ ).

We believe that these differences are mostly due to the different clustering algorithm available at that time, as well as the completely different approach used to define the cluster-matrix interface (erosion method). Also, it is important to note that in this work Mn and Ni, as well as Si and P were defined as the 'core solutes elements', in the cluster identification algorithm.

## 2. Microstructure of the post-irradiation annealed ternary alloy samples

Post-irradiation isochronal annealing (PIA) was performed for 30 minutes at 400 °C, 500 °C and 600°C at SCK.CEN, to evaluate the thermal stability of the MNSP clusters developed after neutron irradiation of the Fe-Mn-Ni alloy, at a dose of 0.1 dpa.

APT experiments were carried out analyzing samples of all PIA states to identify and quantify the existing clusters. Figure 115 illustrates APT volumes, one of each PIA states, where inside

the ferritic matrix (grey) the detected clusters can be easily observed (since the imaging radius of the atoms they include was augmented).

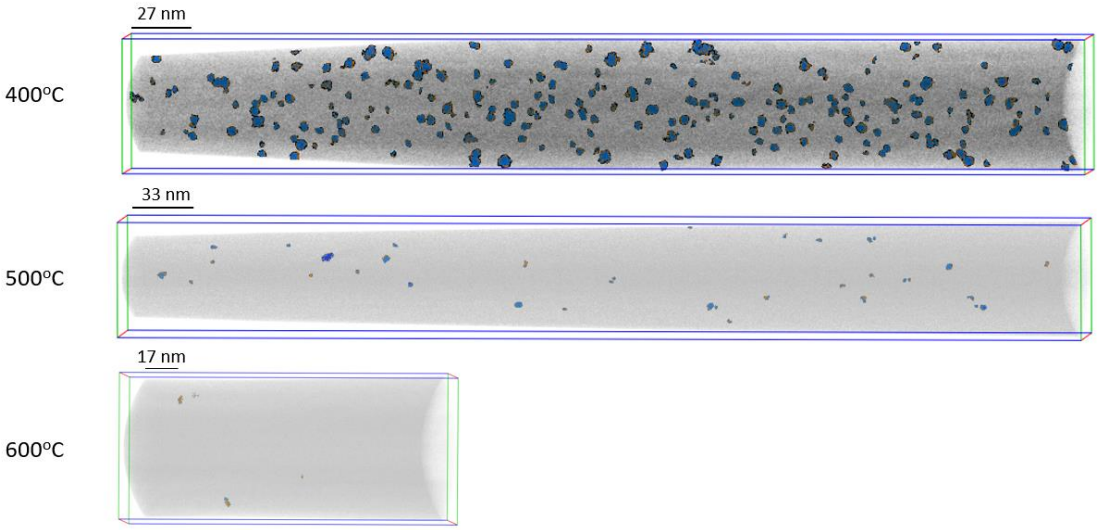


*Figure 115: APT volumes of post-irradiation annealed Fe-Mn-Ni samples at 400 °C, 500 °C and 600 °C. The ferritic matrix is represented in grey and the clusters by the Mn and Ni atoms they contain in blue and orange respectively.*

Table 9 summarizes the APT measured mean concentrations of Mn, Ni, Si and P at the three annealing states. Nominal and measured global Mn and Ni concentrations are in good agreement in all states. Concerning the detected clusters, an important decrease of their Mn and Ni content was observed with the increase of the annealing temperature.

*Table 9: The APT measured mean global, matrix and cluster solute content (in at. %) along with two times the standard error, of the neutron irradiated Fe-Mn-Ni model alloy after PIA at 400 °C, 500 °C and 600°C.*

| ***Annealing Temperature*** | | **Mn** (at. %) | **Ni** (at. %) | **Si** (at. %) | **P** (at. %) |
|---|---|---|---|---|---|
| ***at 400°C*** | **Global** | 1.19 ± 0.03 | 0.76 ± 0.01 | 0.038± 0.003 | 0.006± 0.001 |
| | **Matrix** | 1.14 ± 0.04 | 0.71 ± 0.02 | 0.031 ± 0.003 | 0.003±0.002 |
| | **Clusters** | 10.57 ± 0.98 | 9.39 ± 1.01 | 1.54 ± 0.30 | 0.80 ± 0.31 |
| ***at 500°C*** | **Global** | 1.23 ± 0.02 | 0.77 ± 0.01 | 0.042 ± 0.002 | 0.007 ± 0.001 |
| | **Matrix** | 1.22 ± 0.01 | 0.765 ± 0.005 | 0.041 ± 0.002 | 0.007 ± 0.001 |
| | **Clusters** | 7.49 ± 0.63 | 5.63 ± 0.43 | 0.46 ± 0.14 | 0.26 ± 0.11 |
| ***at 600°C*** | **Global** | 1.25 ± 0.02 | 0.78 ± 0.01 | 0.041 ± 0.004 | 0.006 ± 0.001 |
| | **Matrix** | 1.242 ± 0.004 | 0.78 ± 0.01 | 0.040 ± 0.005 | 0.006 ± 0.001 |
| | **Clusters** | 6.54 ± 0.36 | 2.72 ± 1.39 | 0.93 ± 0.50 | 2.45 ± 1.06 |

The calculated average Guinier and equivalent spherical radius along with the number density and volume fraction of the detected clusters in the three annealing states are detailed in Table 10. Note that for the 600°C annealed samples, in only two tips, a few clusters were detected.

*Table 10: Mean equivalent spherical radius, Guinier radius, number density and volume fraction of the post-irradiation annealed Fe-Mn-Ni samples.*

| ***Annealing Temperature*** | **<Req>** | **<Rg>** | **<ND>** | **<fv %>** |
|---|---|---|---|---|
| ***at 400°C*** | 1.5 ± 0.1 | 1.5 ± 0,1 | (2.6 ± 0.4)x$10^{23}$ | 0.69 ± 0.09 |
| ***at 500°C*** | 1.2 ± 0.2 | 1.5 ± 0.3 | (1.1 ± 0.8)x$10^{23}$ | 0.22 ± 0.19 |
| ***at 600°C*** | 1.5 ± 0.2 | 1.8 ± 0,3 | (5.80 ± 0.04)x$10^{21}$ | 0.010 ± 0.004 |

According to our APT study, as the annealing temperature increases (at 500 and 600 °C PIA temperatures) the $R_g$ is observed slightly larger than the equivalent spherical radius ($R_{eq}$) of the identified solute clusters, implying that the solute elements are positioned closer to the cluster's perimeter, probably due to the diffusion of elements away from the center of mass of the observed clusters (Figure 116).

Additionally, the number density (ND) of the SCs decreases significantly after annealing at 400°C (from (6.2 ± 0.8) x$10^{23}$ $m^{-3}$ of the as irradiated state to (2.6 ± 0.4) x$10^{23}$ $m^{-3}$ of the annealed at 400°C), which indicates that the SCs begin to dissolve. The number density keeps decreasing reaching (1.1 ± 0.8) x$10^{23}$ at 500°C and at 600°C SCs were not detected in half of the analyzed volumes while the other half had in average only 4 clusters in each analysis. Consequently, the volume fraction (VF) also decreases with annealing temperature.

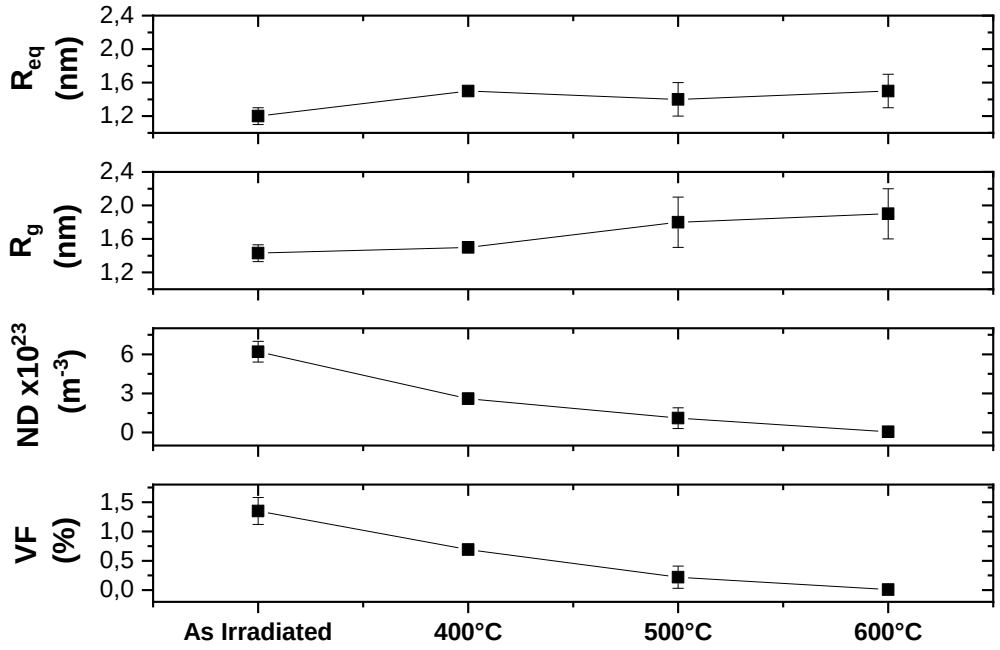


*Figure 116: Mean equivalent spherical and Guinier radius, number density and volume fraction of the neutron irradiated ternary alloy as irradiated and annealed at 400°C, 500°C and 600°C.*

The decrease of the volume fraction is evident in Figure 117 – a, where the contribution of Fe as well as of the solute elements is also illustrated. Concerning the clusters' average content (Figure 117 – b), it is apparent that annealing beyond 400°C decreases the Mn and Ni content.

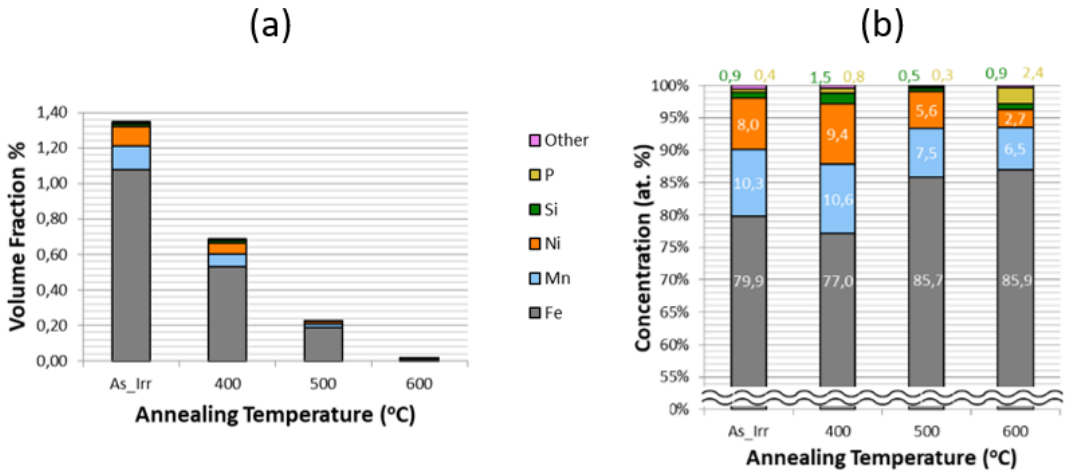


*Figure 117: (A) Cluster volume fraction evolution with the annealing time, detailing the contribution of Fe and solute elements (B) Composition of the clusters of the Fe-Mn-Ni alloy in the different annealing states.*

Therefore, the Mn-Ni-enriched clusters dissolve with increasing annealing temperature without coarsening and at 600 °C almost complete dissolution occurs.

To evaluate if these observations can be justified on the base of the theoretical diffusion distances, the following calculations were made.

The thermodynamic values of the diffusion pre-exponential factor ($D_0$) and activation energy (Q) for the Mn and Ni were retrieved from the literature [10], [11], and their values were derived by extrapolating the higher temperature experimental radioactive tracers diffusion values, in the ferromagnetic temperature range of the α-iron.

The diffusion coefficients (D) at 400°C, 500°C and 600°C were calculated using the exponential Arrhenius relation [12], [13]:

$$D = D_0 \, e^{\left(-\frac{Q}{RT}\right)} \tag{3.2}$$

where R is the gas constant, and T is the temperature in Kelvin.

Assuming that the studied material is an isotropic medium, the diffusion distances of Ni and Mn in α- Fe, at the annealing temperatures were estimated as:

$$< \bar{x} >= \sqrt{6Dt} \tag{3.3}$$

where t the annealing time.

The diffusion distance for the 30 minutes annealing time at 400°C, especially for the slower diffusing element (Ni), is not enough to cause complete clusters dissolution, justifying the existence of solute clusters at that temperature (Table 11). But for the annealing at 500°C and even more for the 600°C, the calculated diffusion distance is high enough suggesting that complete dissolution of the clusters should occur.

*Table 11: Diffusion distance of Mn and Ni calculated by the exponential Arrhenius equation using literature values for the pre-exponential diffusion factor ($D_0$) and the activation energy (Q) for Mn [10] and Ni [11].*

| Element | Parameters | | Diffusion distance (nm) | | |
|---|---|---|---|---|---|
| | $D_0$ ($cm^2/s$) | Q (J/mol) | 400 °C | 500 °C | 600 °C |
| **Mn** | 1.49 | 233600 | 1 | 16 | 130 |
| **Ni** | 1.4 | 245600 | 0.4 | 6 | 55 |

Considering another theoretical approximation, that is for systems that are relaxing to an equilibrium state approaching complete homogenization, the average concentration ($\bar{c}$) is estimated [14] by:

$$\bar{c}(t) = \int_0^h c(x,t)\,dt = \frac{8c_0}{\pi^2}\sum_{j=0}^{\infty}\frac{1}{(2j+1)}\exp\left(-\left[\frac{(2j+1)\pi}{h}\right]Dt\right) \tag{3.4}$$

where h the thickness of the diffusing slab

The solution of Eq.(3.4), for $\bar{c} < 0.8\ c_0$ can be very accurately approximated using:

$$\frac{\bar{c}}{c_0} = \frac{8}{\pi^2}e^{\left(-\frac{t}{\tau}\right)} \tag{3.5}$$

where $c_o$ the initial concentration and τ the relaxation time, which in the case of a sphere having diameter d, is calculated as:

$$\tau = \frac{d^2}{4\pi^2 D} \tag{3.6}$$

The relaxation time τ is a measure of how fast the system relaxes. At time t = τ, the concentration is relaxed to roughly two-thirds of its initial value.

Combining Eq (3.5) with Eq (3.6) and assigning to $c_o$ the as irradiated average concentration of Mn and Ni respectively and to d the average diameter of the clusters, the estimated concentrations after a time equal to the imposed annealing time, are given on Table 12.

*Table 12: Average theoretical Mn and Ni concentration for each post-irradiation annealing temperature, calculated using equation (1.3).*

| Element | Average concentration (at.%) | | |
|---|---|---|---|
| | 400 °C | 500 °C | 600 °C |
| Mn | 3 | 0 | 0 |
| Ni | 6.2 | 0 | 0 |

These values also suggest partial dissolution in the case of the samples annealed at 400°C and complete dissolution for those annealed at 500°C and 600°C. Therefore, both theoretical approximations are in an excellent agreement.

Indeed, in our APT experiments partial cluster dissolution was observed at the 400°C annealed samples, with a significant decrease in the number density of the clusters from (6.2 ± 0.8) $x10^{23}$ of the as irradiated state to (2.6 ± 0.4) $x10^{23}$ of the 400°C annealed. This is in agreement with Meslin at al. [9] who also reported partial cluster dissolution in the same ternary alloy (Fe-1.1Mn-0.7Ni) neutron irradiated at 0.2 dpa and annealed for 50 hours at 400°C.

Konstantinovic and Bonny [15] have studied the same ternary alloy (among two other alloys, namely the Fe - 0.3Cu and Fe - 0.1Cu - 1.08Mn - 0.75Ni) in the as irradiated and after 30 minutes isochronal annealing performed at the temperature range between 573 K and 973 K. They conducted positron annihilation spectroscopy (PAS) experiments performed with the coincidence doppler broadening spectrometer (CDB).

At about 680 K, they observed an important decrease of the S parameter, as "*a consequence of the dissolution of vacancy-solute complexes that do not contain Mn and Ni solute atoms together*" (denoted as A1 in Figure 118). This temperature corresponds well with the important decrease in cluster number density we detected using APT in our annealed samples at 400 °C.

Moreover, at about the 800 K (527 °C) annealing temperature, PAS revealed a small hump, present only in the alloys that contained Ni and Mn (denoted as A3 in Figure 118Figure 118) that was assigned to the next annealing stage A3. This stage is due to the dissolution of V–MnNi clusters that have significantly increased dissociation energy compared to the other V-solute clusters. The existence of this second stage at a higher temperature, according to the authors, indicates that "there is an additional thermal stability due to the presence of Mn and Ni solute atoms in the clusters" and the emission of vacancies from V–MnNi clusters could lead to the full cluster dissolution.

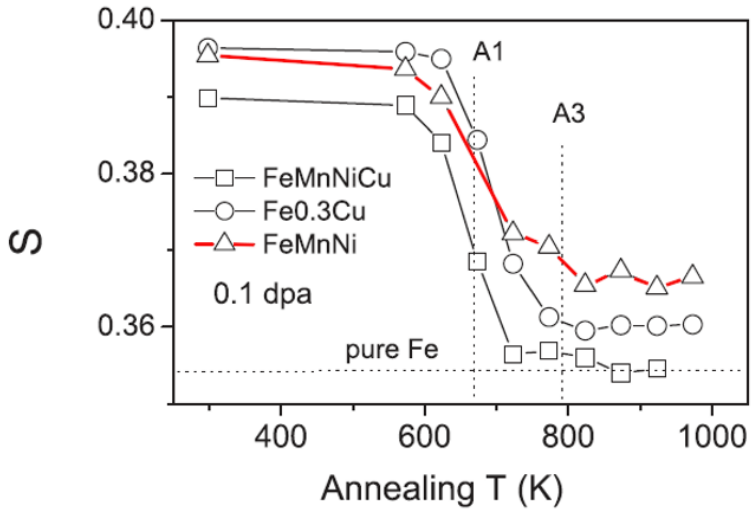


*Figure 118 : S parameter as a function of the annealing time for two Cu bearing alloys and a ternary Fe-Mn-Ni alloy, after neutron irradiation [15].*

This is maybe a possible explanation why some clusters still exist at the 500°C annealing temperature, although the previously presented theoretical diffusion calculations suggested complete dissolution.

Our APT experimental results are also in agreement with Kuramoto et al. [16]. They studied, using APT and PAS, a A533B steel containing 0.14 Cu, 1.31Mn and 0.64 Ni (at. %) neutron irradiated at a dose of 0.061 dpa. After irradiation, the steel was isochronally annealed (for 30 min) at temperatures from 250 to 600°C. They also observed that the annealing occurred at two stages: at the first annealing stage, up to about 450 °C, almost all vacancy-related defects recover and the majority (75%) of the solute clusters dissolve into the matrix in this first stage. At the next stage from 450 to 600 °C, they observed almost complete cluster dissolution.

Similar results, using small-angle neutron scattering (SANS), were reported by Bergner et al. [17]. They studied a Fe-1.2Mn-0.7Ni model alloy, neutron irradiated at 0.1 and 0.19 dpa and they observed that the Mn-Ni enriched clusters at 400$^{O}$C start dissolving and without any coarsening, they dissolved completely at 500$^{o}$C

## 3. Iron content in the neutron irradiated and post-irradiation annealed ternary alloy clusters

As stated in chapter 2, trajectory aberrations of the evaporating ions during an atom probe experiment, might bias the calculated chemical composition of the identified clusters, by the artificial introduction of Fe matrix atoms inside the solute clusters during reconstruction. Assuming that the detected clusters in the ternary alloy experiments were spherical, the CCC model was applied to quantify the correct Fe content.

Therefore, for each cluster the shape factor (S) was calculated from the dimensions, as derived from the cylindrical concentration profiles that were plotted through each particle along its three main directions. Such profiles were plotted for 16 and 15 of the bigger clusters of the as irradiated and PIA at 400$^{o}$C samples respectively, and only 5 for the PIA at 500 $^{o}$C since only one analysis had big enough clusters for the cylindrical profiles to fit in.

Figure 119 illustrates the core solutes (CS), solvent (Fe) and the total number of atoms along the z axis profile of a 3.6 nm in diameter neutron irradiated Fe-Mn-Ni cluster.

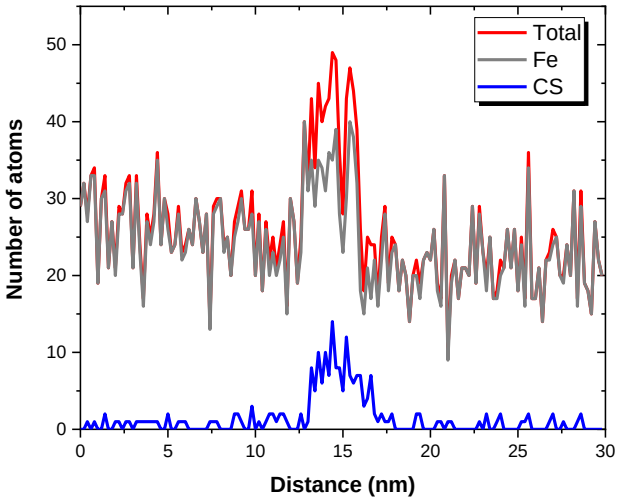


*Figure 119: Diagram of the core solutes (CS), solvent (Fe) and the total number of atoms derived from the concentration profile data, of a cluster in a Fe-Mn-Ni neutron irradiated sample. Atomic over-density is apparent at the clusters' area.*

Table 13 tabulates the average values of the size of the studied clusters, along with the shape factor (S), reduced density ($\rho_r$), the Fe content as calculated with the CCC model, and also the Fe content of the clusters calculated after deconvolution of the APT mass spectrum data.

CCC model suggests a lower Fe content (about 10% less) for the as irradiated and PIA at 400$^{o}$C clusters but no significant difference for the clusters PIA at 500$^{o}$C probably due the difficulty to find suitable ones. Therefore, we conclude that Fe is indeed the majority element, at a high concentration of about 70 at. %, of the clusters detected in the studied Fe-Mn-Ni samples in

the neutron irradiated but also after all the three PIA conditions and not just an artifact due to the ion trajectory aberrations.

*Table 13: Average Guinier radius (Rg), shape factor (S), reduced density ($\rho_r$), Fe content as calculated by the CCC model and as deconvoluted at the clusters core for the neutron irradiated and post-irradiation annealed samples of the Fe-Mn-Ni model alloy.*

| State | <Rg> (nm) | <S> | <$\rho_r$> | Fe content (at. %) | |
|---|---|---|---|---|---|
| | | | | Analysis average | CCC model average |
| **As irradiated** | 1.7 ± 0.3 | 0.7 ± 0.1 | 1.7 ± 0.4 | 79.9 ± 0.2 | 70 ± 12 |
| **400°C** | 1.9 ± 0.3 | 0.6 ± 0.1 | 2.2 ± 0.4 | 77.0 ± 0.5 | 69 ± 10 |
| **500°C** | 1.9 ± 0.9 | 0.5 ± 0.1 | 1.7 ± 0. 2 | 85.7 ± 0.5 | 85 ± 4.5 |

## 4. Study of the nature of the clusters observed in the ternary alloy samples

Some investigators consider that the MNPs could be crystalline intermetallic phases, as the G phases ($Mn_6Ni_{16}Si_7$) and/or Γ2 phases ($Mn_2Ni_3Si$). In a recent paper, Odette et al. [8] stated that "the very high displacement per atom (dpa) doses and radiation enhanced diffusion (RED) result in nearly full phase separation".

In order to better evaluate in which proportions solutes gathered inside the cores of the clusters, the ratio of Mn, Ni and Si concentrations were calculated and projected on the Gibbs triangle. By studying Figure 120, we notice that the dispersion of the Mn:Ni:Si ratio is rather random, not indicating a tendency towards a certain thermodynamically stable phase. In any of the studied states.

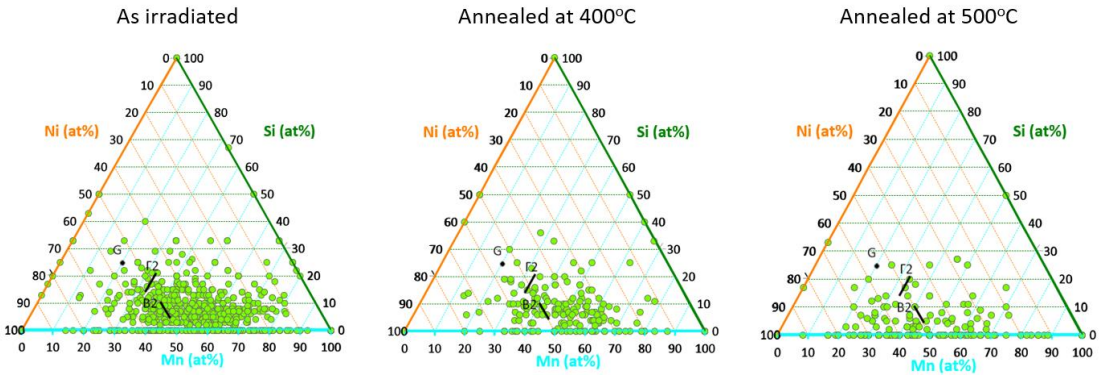


*Figure 120: The Mn:Ni:Si ratio of each cluster of the neutron irradiated and the post-irradiation annealed at 400°C and 500°C, ternary alloy, the projected on the Gibbs triangle. The G, Γ2 and B2 phases are indicated by the black dot and lines.*

But when we classified the detected clusters in four size ranges (that is having a radius, up to 1 nm, 1-1.5 nm, 1.5-2 nm and bigger than 2 nm) and with mean values of the Mn:Ni:Si ratios were plotted on the Gibbs triangle, they appeared to approach to the vicinity of the B2 BCC phase, as the annealing temperature increased (Figure 121).

This behavior seems to be controversial to the observed partial dissolution of the clusters and maybe is just the result of averaging the Mn:Ni:Si ratio. But keep in mind that it concerns only

a minority of the clusters generated under irradiation, that is only these that survived the annealing at 500 °C.

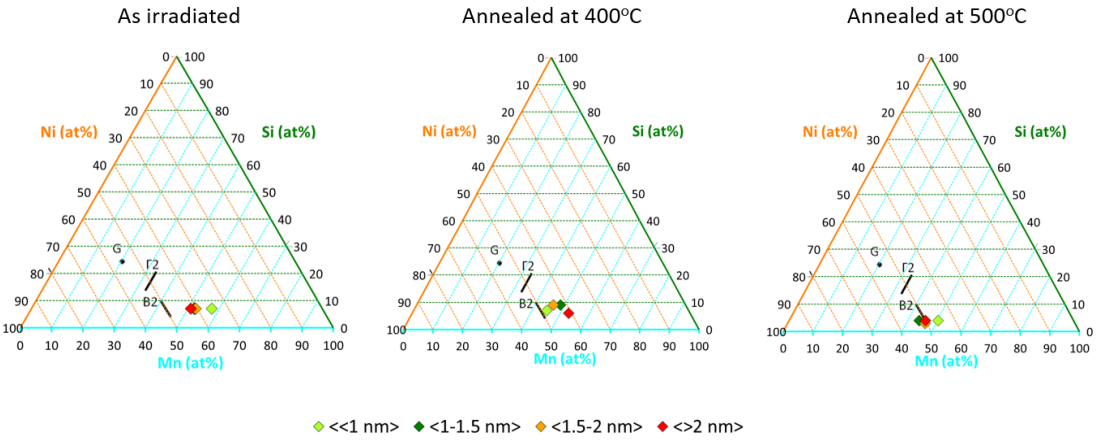


*Figure 121: The average Mn:Ni:Si ratio per cluster class size (from less than 1 nm/light green – to more than 2nm/red) projected on the Gibbs triangle, for the neutron irradiated and the post-irradiation annealed at 400°C and 500°C, ternary alloy. The G, Γ2 and B2 phases are indicated by the black dot and lines.*

Pascuet et al. [20] used a hybrid algorithm combination of Metropolis Monte Carlo (MMC) and molecular dynamics (MD) to study how the solutes accumulate near dislocation lines, focusing on the screw dislocation. They stated that the interaction of the dislocation strain field with the solute atoms reduces the strain energy and thus the heterogeneous nucleation of a cluster embryo decreases the solubility limit locally, hence catalyzing precipitation.

They observed that Mn is the element with the strongest an excess of Mn atoms tendency to segregate around dislocations. Ni atoms combine with Mn atoms and form the NiMn B2 structure among, especially if the bulk Mn concentration is higher than the Ni.

They concluded that the result of the solutes segregation was the formation of mixed phase precipitates, containing BCC B2 phase NiMn and BCC Mn, which they also observed experimentally. In Figure 122 – b are illustrated computer simulation views of solute segregation with B2 precipitates on a screw dislocation This looks very similar to the APT reconstruction (Figure 122 – a) of an irradiated low alloyed RPV steel (0.17 dpa at ≈290°C) [21].

In fact, recently Odette et al [8], reported that they observed in irradiated RPV steels using APT, chemically complex features similar to the complexions [22], [23], which are considered to be chemically, and maybe also structurally, discrete regions formed on microstructural features due to solute enrichment.

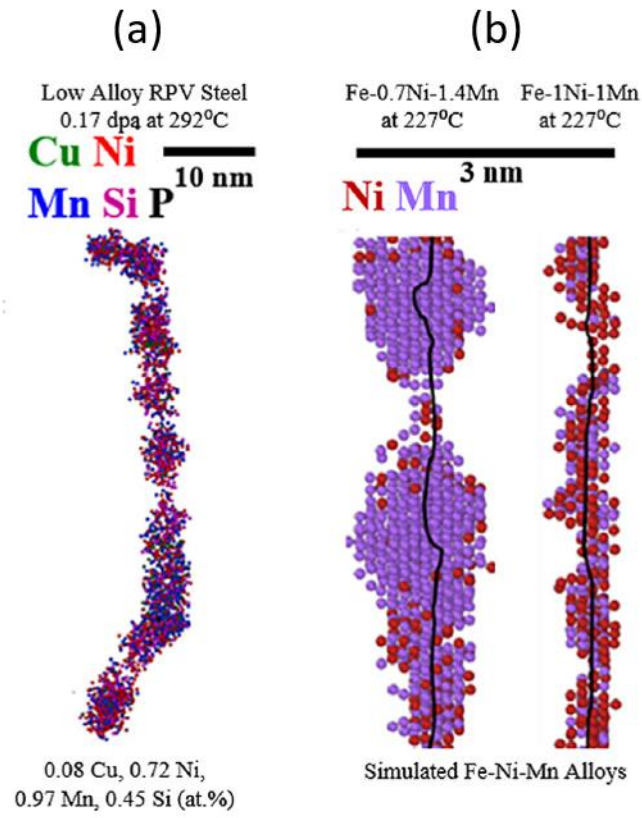


*Figure 122: Segregated dislocation with precipitates in (a) an APT reconstruction of a 0.08 Cu, 0.72 Ni, 0.97 Mn, 0.45 Si (at.%) RPV steel neutron irradiated at 292°C to ≈0.17 dpa and (d) 2 simulated thermal dislocation segregation and precipitation in a Fe-0.7% Ni-1.4% Mn and Fe-1 Ni-1 Mn alloy at 227°C. [8], [20], [21].*

Small MNSP clusters are considered as being B2 coherent transition phases, that is precursor phases of the more stable G phase [24–27] or the Γ2 phase [28], to which they might transform only if all the required conditions apply at the same time. For example, in the case of MNSP clusters, like the ones studied in this work, with Fe content exceeding 18 at. %, King et al [24] suggest that a structure of B2-type ordering is formed preferentially and B2 to G-phase transformation will not occur.

Additionally, for the nm-scale transition phases, deviations from stoichiometric compositions are the rule, not the exception, since for a wide range of precipitate compositions, free energy might decrease during precipitation [8].

Bonny et al. [29] using Monte Carlo simulations reported that in Fe-Mn-Ni alloy, when Mn concentration is higher than of Ni, they observed coexistence of three phases, namely a Fe-rich matrix, a single B2 NiMn precipitate and an additional Mn-rich precipitate. Also, they stated that the synergy of Ni and Mn might raise the solvus of the binary by up to 300 K, resulting in precipitation up to about 725 K, making NiMn precipitates thermodynamically stable at RPV's operating temperature.

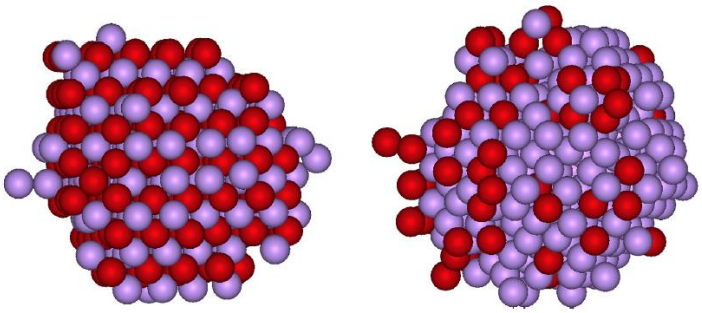

*Figure 123: Schematic of a B2 NiMn precipitate and Mn-rich precipitate. Ni atoms denoted in red and Mn atoms in purple [29].*

Taking into account the previously mentioned, we may assume that the few Fe-Mn-Ni clusters surviving the 30 minutes annealing at 500°C, are those that their composition, as a result of the RIS, is nearest to that of B2 phase, that is having the less excess in Mn. Since RIS leads to non-equilibrium solute segregation, these clusters are only a small minority, as evidenced by the sharp decrease, of the APT calculated, number density with the temperature. But of course, this is only a hypothesis made for explaining the few annealing persistent clusters and further research is needed to verify if it is valid.

Therefore, we can conclude that the mechanism that generated the detected clusters after neutron irradiation, even the very few that persisted the annealing, is radiation induced segregation. This is clearly indicated by the previously mentioned observations, namely:

- The Fe concentration of the clusters is high, even when the APT biases are compensated using the CCC model calculations.

- The ratio of the Mn:Ni:Si content of the clusters, when projected on the Gibbs triangle is randomly dispersed and thus not indicating a tendency towards a certain thermodynamically stable phase.

- And above all, that during the isochronal annealing clusters dissolution occurred at two stages. At about 400 °C we observed partial dissolution of the MNSP clusters while with increasing annealing temperature the clusters dissolve without coarsening and at 600 °C almost complete dissolution occurred.

## III. Effect of Mn and Ni to clustering

The clusters formed in the Fe-Mn alloy outnumbered those of the other two alloys, producing the highest number density ((1.4 ± 0.1) x$10^{24}$ $m^{-3}$) almost an order of magnitude higher that the density of the other binary alloy Fe-Ni ((1.5 ± 0.4) x$10^{23}$ $m^{-3}$). Because of this, the volume fraction of the clusters in Fe-Mn alloy was also significantly higher, although their radius was comparatively smaller than of the clusters in the Fe-Ni alloy (Figure 124).

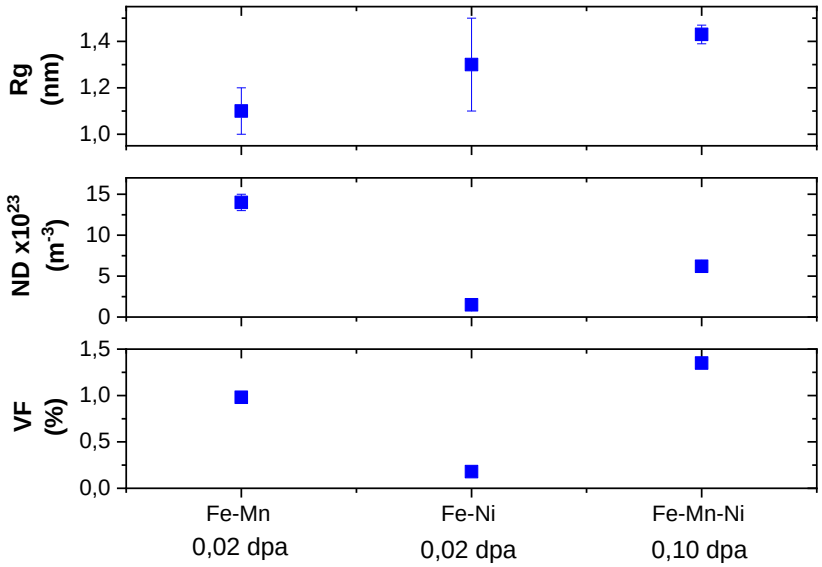


*Figure 124: Mean Guinier radius, number density and volume fraction of the clusters of the binary and ternary alloys.*

Figure 125 illustrates the average composition of the detected clusters in the three model alloys. Comparing between the binary alloys, the clusters in the Fe-Ni alloy were more solute enriched (about 17 at. % in Ni) in relation to the ones of the Fe-Mn (about 10 at. % in Mn).

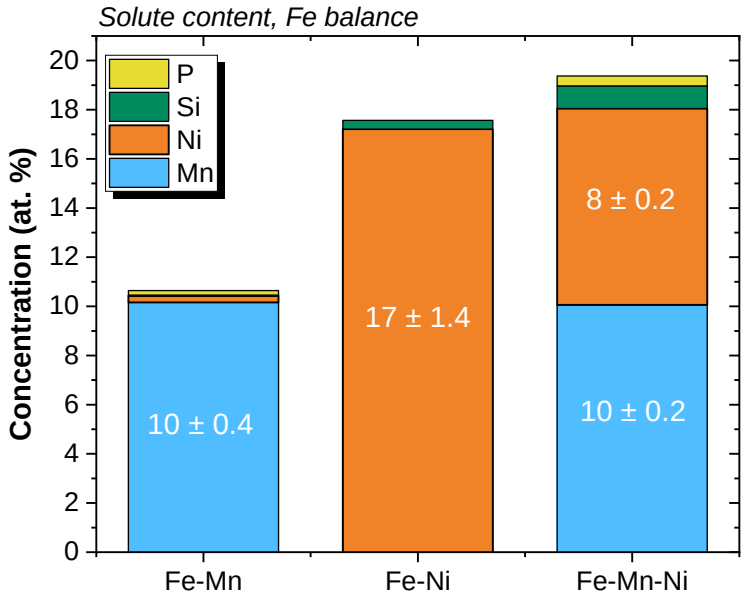


*Figure 125: Average cluster solute content of the neutron irradiated Fe-Mn, Fe-Ni and Fe-Mn-Ni model alloys.*

The clusters of the ternary alloy have about equal enrichment in Mn (10 at. %) and Ni (8 at. %) and contained both Si (0.9 at. %) and P (0.4 at. %), having the most increased average size (Rg = 1.4 nm). Their number density ((6.2 ± 0.2) $x10^{23}$ $m^{-3}$) was in between of those of the binary alloys, which in combination with the increased size, produced the irradiation induced microstructure with the highest volume fraction (1.35 ± 0.23 %) among all the alloys.

Considering the previously mentioned characteristics of the clusters, it appears that there is a synergistic effect between Mn and Ni. The Mn contributes by easily nucleating and thus producing solute clusters in high number density, while Ni increases their solute enrichment. Their combined effects lead to the significant increase of the volume fraction of the ternary alloy.

## Summary

Under neutron irradiation formation of nanosized solute clusters was observed using APT in all model alloys. The number density of the clusters identified in the Fe-Mn alloy was the highest, indicating that Mn is the element with the strongest tendency to nucleate solute clusters. In contrast, in the Fe-Ni alloy the calculated number density of the contained clusters was almost an order of magnitude lower, but the clusters were more solute enriched. Additionally, we observed that in the Fe-Mn alloy, the clusters formed at a high number density in the bulk and at a significant lower density on dislocations.

The Fe-Mn-Ni alloy had the higher volume fraction, due to the synergistic effect between Mn and Ni, that is the Mn contributed in producing an increased number density while the Ni facilitated the solute enrichment, increasing the size of the clusters.

The binary alloys Fe-Mn and Fe-Ni are both under-saturated as derived from their corresponding phase diagrams. Therefore, precipitation is not thermodynamically favored to any of them and the only possible mechanism that produced the observed clusters that formed under irradiation, is the irradiation induced segregation (RIS).

Studying the ternary Fe-Mn-Ni alloy, we observed that the detected clusters have high Fe content, even after excluding the APT biases by applying the CCC model. The Mn:Ni:Si content ratio of each cluster, when projected on the Gibbs triangle, presented a significant dispersion. Moreover, after isochronal post irradiation annealing, these clusters were not thermally stable, reaching complete dissolution at 600$^{o}$C without any coarsening. All these observations clearly indicate non equilibrium clustering of Mn and Ni and therefore we conclude that the formation mechanism of the clusters, was not irradiation enhanced but irradiation induced segregation (RIS).

Neutron irradiation altered the microstructure of the alloys generating solute clusters, with the described characteristics, which modified the mechanical behavior of the alloys as well, which will be studied and discussed in the next chapter.

# Bibliography


[1] G. Monnet, “Multiscale modeling of irradiation hardening: Application to important nuclear materials,” *J. Nucl. Mater.*, vol. 508, pp. 609–627, Sep. 2018, doi: 10.1016/j.jnucmat.2018.06.020.

[2] G. Vassilev, J. Miettinen, and K. Lilova, “Thermodynamic Description of Ternary Fe-B-X Systems. Part 3: Fe-B-Mn/ Opis Termodynamiczny Trójskładnikowych Układów Fe-B-X. Część 3: Fe-B-Mn,” *Arch. Metall. Mater. 2014 No 4 Dec.*, 2014, Accessed: Dec. 24, 2022. [Online]. Available: https://journals.pan.pl/dlibra/publication/103197/edition/89211

[3] L. J. Swartzendruber, “The Fe-Ni (iron-nickel) system,” vol. 12, no. 3, 1991.

[4] L. Messina, T. Schuler, M. Nastar, M.-C. Marinica, and P. Olsson, “Solute diffusion by self-interstitial defects and radiation-induced segregation in ferritic Fe–X (X=Cr, Cu, Mn, Ni, P, Si) dilute alloys,” *Acta Mater.*, vol. 191, pp. 166–185, Jun. 2020, doi: 10.1016/j.actamat.2020.03.038.

[5] N. Castin *et al.*, “The dominant mechanisms for the formation of solute-rich clusters in low-Cu steels under irradiation,” *Mater. Today Energy*, vol. 17, p. 100472, Sep. 2020, doi: 10.1016/j.mtener.2020.100472.

[6] E. Meslin, B. Radiguet, and M. Loyer-Prost, “Radiation-induced precipitation in a ferritic model alloy: An experimental and theoretical study,” *Acta Mater.*, vol. 61, no. 16, Art. no. 16, Sep. 2013, doi: 10.1016/j.actamat.2013.07.008.

[7] C. A. Williams, J. M. Hyde, G. D. W. Smith, and E. A. Marquis, “Effects of heavy-ion irradiation on solute segregation to dislocations in oxide-dispersion-strengthened Eurofer 97 steel,” *J. Nucl. Mater.*, vol. 412, no. 1, pp. 100–105, May 2011, doi: 10.1016/j.jnucmat.2011.02.029.

[8] G. R. Odette, N. Almirall, P. B. Wells, and T. Yamamoto, “Precipitation in reactor pressure vessel steels under ion and neutron irradiation: On the role of segregated network dislocations,” *Acta Mater.*, vol. 212, p. 116922, Jun. 2021, doi: 10.1016/j.actamat.2021.116922.

[9] E. Meslin, B. Radiguet, P. Pareige, and A. Barbu, “Kinetic of solute clustering in neutron irradiated ferritic model alloys and a French pressure vessel steel investigated by atom probe tomography,” *J. Nucl. Mater.*, vol. 399, no. 2–3, pp. 137–145, Apr. 2010, doi: 10.1016/j.jnucmat.2009.11.012.

[10] C. J. Smithells, W. F. Gale, and T. C. Totemeier, *Smithells metals reference book*, 8th ed. / edited by W.F. Gale, T.C. Totemeier. Amsterdam ; Boston: Elsevier Butterworth-Heinemann, 2004.

[11] K. Hirano, M. Cohen, and B. L. Averbach, “Diffusion of nickel into iron,” *Acta Metall.*, vol. 9, no. 5, Art. no. 5, May 1961, doi: 10.1016/0001-6160(61)90138-9.

[12] A. Paul and S. V. Divinski, Eds., *Handbook of solid state diffusion*. Amsterdam, Netherlands: Elsevier, 2017.

[13] D. A. Porter, K. Easterling, and M. Y. Sherif, *Phase transformations in metals and alloys*, 3rd ed.

[14] P. G. Shewmon, *Diffusion in solids*, 2.ed. Warrendale, Pa: Minerals, Metals & Materials Society, 1989.

[15] M. J. Konstantinovic and G. Bonny, “Thermal stability and the structure of vacancy–solute clusters in iron alloys”.

[16] A. Kuramoto *et al.*, “Post-irradiation annealing behavior of microstructure and hardening of a reactor pressure vessel steel studied by positron annihilation and atom probe tomography,” *J. Nucl. Mater.*, vol. 425, no. 1–3, Art. no. 1–3, Jun. 2012, doi: 10.1016/j.jnucmat.2011.10.019.

[17] F. Bergner, A. Ulbricht, P. Lindner, U. Keiderling, and L. Malerba, “Post-irradiation annealing behavior of neutron-irradiated FeCu, FeMnNi and FeMnNiCu model alloys investigated by means of small-angle neutron scattering,” *J. Nucl. Mater.*, vol. 454, no. 1–3, pp. 22–27, Nov. 2014, doi: 10.1016/j.jnucmat.2014.07.038.

[18] H. Ke *et al.*, “Thermodynamic and kinetic modeling of Mn-Ni-Si precipitates in low-Cu reactor pressure vessel steels,” *Acta Mater.*, vol. 138, pp. 10–26, Oct. 2017, doi: 10.1016/j.actamat.2017.07.021.

[19] M. Mamivand, P. Wells, H. Ke, S. Shu, G. R. Odette, and D. Morgan, “CuMnNiSi precipitate evolution in irradiated reactor pressure vessel steels: Integrated Cluster Dynamics and experiments,” *Acta Mater.*, vol. 180, pp. 199–217, Nov. 2019, doi: 10.1016/j.actamat.2019.09.016.

[20] M. I. Pascuet *et al.*, “Solute precipitation on a screw dislocation and its effects on dislocation mobility in bcc Fe,” *Journal of Nuclear Materials*, 2019.

[21] G. R. Odette, T. Yamamoto, T. J. Williams, R. K. Nanstad, and C. A. English, “On the history and status of reactor pressure vessel steel ductile to brittle transition temperature shift prediction models,” *J. Nucl. Mater.*, vol. 526, p. 151863, Dec. 2019, doi: 10.1016/j.jnucmat.2019.151863.

[22] S. J. Dillon, M. Tang, W. C. Carter, and M. P. Harmer, “Complexion: A new concept for kinetic engineering in materials science,” *Acta Mater.*, vol. 55, no. 18, pp. 6208–6218, Oct. 2007, doi: 10.1016/j.actamat.2007.07.029.

[23] M. Kuzmina, M. Herbig, D. Ponge, S. Sandlöbes, and D. Raabe, “Linear complexions: Confined chemical and structural states at dislocations,” *Science*, vol. 349, no. 6252, pp. 1080–1083, Sep. 2015, doi: 10.1126/science.aab2633.

[24] Y. Matsukawa *et al.*, “The two-step nucleation of G-phase in ferrite,” *Acta Mater.*, vol. 116, pp. 104–113, Sep. 2016, doi: 10.1016/j.actamat.2016.06.013.

[25] Y. Matsukawa, “Crystallography of Precipitates in Metals and Alloys: (1) Analysis of Crystallography,” in *Crystallography*, T. Akitsu, Ed. IntechOpen, 2019. doi: 10.5772/intechopen.82693.

[26] D. J. M. King, P. A. Burr, S. C. Middleburgh, T. M. Whiting, M. G. Burke, and M. R. Wenman, “The formation and structure of Fe-Mn-Ni-Si solute clusters and G-phase precipitates in steels,” *J. Nucl. Mater.*, vol. 505, pp. 1–6, Jul. 2018, doi: 10.1016/j.jnucmat.2018.03.050.

[27] D. J. M. King and M. R. Wenman, “Comment on “The two-step nucleation of G-phase in ferrite,” *J. Nucl. Mater.*, vol. 412, no. 1, pp. 100–105, 2018, doi: https://doi.org/10.1016/j.scriptamat.2018.11.053.

[28] T. M. Whiting, D. J. M. King, and M. R. Wenman, “On the formation and structure of Mn-Ni-Si Γ2 precipitates in steels,” *J. Nucl. Mater.*, vol. 542, p. 152429, Dec. 2020, doi: 10.1016/j.jnucmat.2020.152429.

[29] G. Bonny *et al.*, “On the thermal stability of late blooming phases in reactor pressure vessel steels: An atomistic study,” *J. Nucl. Mater.*, vol. 442, no. 1–3, pp. 282–291, Nov. 2013, doi: 10.1016/j.jnucmat.2013.08.018.

[30] B. Gomez-Ferrer, C. Heintze, and C. Pareige, On the role of Ni, Si and P on the nanostructural evolution of FeCr alloys under irradiation,J. Nucl. Mater., vol. 517, pp. 354, Apr. 2019, doi: 10.1016/j.jnucmat.2019.01.040.

# Chapter 4: Study of the mechanical properties and irradiation hardening of the ferritic model alloys

## Introduction

This chapter reviews the micro-compression experiments performed to investigate the mechanical properties of the model alloys, before and after neutron irradiation and to determine the irradiation hardening.

First, Electron Backscatter Diffraction (EBSD) analysis was carried out and Inverse Pole Figure (IPF) maps were constructed to select large enough grains with suitable lattice orientation inside which the pillars would be FIB-fabricated. Several important information was extracted from the EBSD data to calculate, for each grain, all the possible slip systems, estimating the primary and secondary ones, their Schmidt factor values and the angle between the slip plane and the surface plane of the pillar. After the grain selection, single-crystal micro-pillars, having diameter about 3 μm and aspect ratio of about 2.5, were FIB- fabricated. Then, in-situ micro-compression experiments were performed as detailed in chapter 2.

Having the compression data acquired from the indenter, engineering stress-strain curves were calculated and plotted. Additionally, in this chapter, the method of exploitation of these curves is explained and the derived mechanical properties of the alloys are detailed, along with the measured irradiation hardening.

The Sneddon's correction [1] was applied to accurately calculate the strain that the pillar is subjected to during compression. Indeed, since the applied stress is not confined only inside the material of the pillar but a part of it is distributed into the substrate bulk material and also on the tip of the indenter, causing a minimum of plastic deformation there as well, a correction is needed. The effect of the Sneddon correction to the stress-strain curve is studied and discussed in this chapter.

The existence of sample size effect is investigated and the observed load drops on the stress strain curves are also discussed.

## I. Exploitation of stress-strain curves

About 10 pillars for each model alloy, in each irradiation state, were fabricated and in-situ compressed with the methods described in Chapter 2.

Engineering stress-strain curves were calculated from the load-displacement data provided by the indenter, in combination with the pillars' geometry. Compression tests with possible experimental errors, such as pillar buckling or obvious indenter misalignment during the in-situ compression, were excluded from our results.

In general, the classical criterion of yield strength determination at 0.2% of strain, cannot be considered, since the shape of the compression curves of the micropillars is different from the well-known tensile test curve. Therefore, in the literature, the yield stress is approximated with stresses reported in a range of 1% to 5% plastic strains [1–5], since the errors due to early plasticity minimize while avoiding large strain hardening effects. In this study, the shape of the curves permitted the use of the stress at 2% strain (red dashed line in Figure 126), as a fair approximation of the yield strength, since it corresponds to a relatively small degree of plastic deformation at which significant work hardening is not expected.

However, due to the shape of the initial segments of certain curves of the neutron irradiated Fe-Mn samples, the stress at 2% strain is still in a linear segment. To ensure being clearly in the plastic domain, the stress at yield of 3% (green dashed line in Figure 126), was used for both the non-irradiated and neutron irradiated Fe-Mn samples.

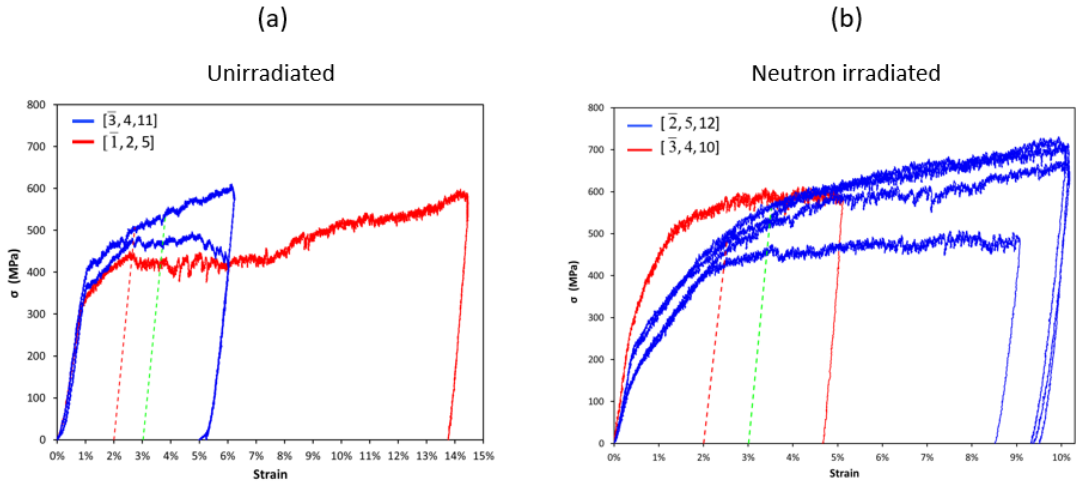


*Figure 126: Engineering stress-strain curves of (a) [3̄,4,11] and [1̄,2,5] oriented unirradiated Fe-Mn pillars and (b) [2̄,5,12] and [3̄,4,10] oriented neutron irradiated pillars. The stress at yield 2% and 3% are indicated with the red and green dashed lines respectively.*

To measure the stress at a specific strain, it is crucial to know the Young's Modulus. In polycrystal bulk materials, conventionally, the Young's modulus is measured using the slope of the initial linear segment of the stress-strain curve that corresponds to the elastic deformation of the material.

From the plotted engineering stress-strain curves, it is evident that the onset of the obtained curves usually had a non-linear shape, suggesting that plasticity occurs in the expected elastic domain and, as Lilleoden states [2], it is *"unclear whether such deformation can be considered*

*full yield or whether small-scale localized plasticity during contact development accounts for the residual deformation"*. Even the slight misalignment between the indenter and the axis of the pilar, that typically occurs in micro compression experiments, results in altering the shape of the elastic region. Thus, when contact is developed between the indenters' flat punch and the top surface of the pillar, plasticity is initiated prior to full yielding, therefore making the initial loading response inappropriate for measuring the elastic modulus. This is evidenced since the loading and unloading segments of the curve cannot be superimposed.

Hence, following the suggestion of A. Nomoto (CRIEPI) and according to the literature [2], [3], the unloading curve was used for the calculation of the elastic modulus.

To test the consistency and repeatability of the values obtained using the unloading curve, double loading experiments were performed on a test material (Fe-0.1Cu) used to establish experimental procedures for the in-situ micro-compression experiments (Figure 127).

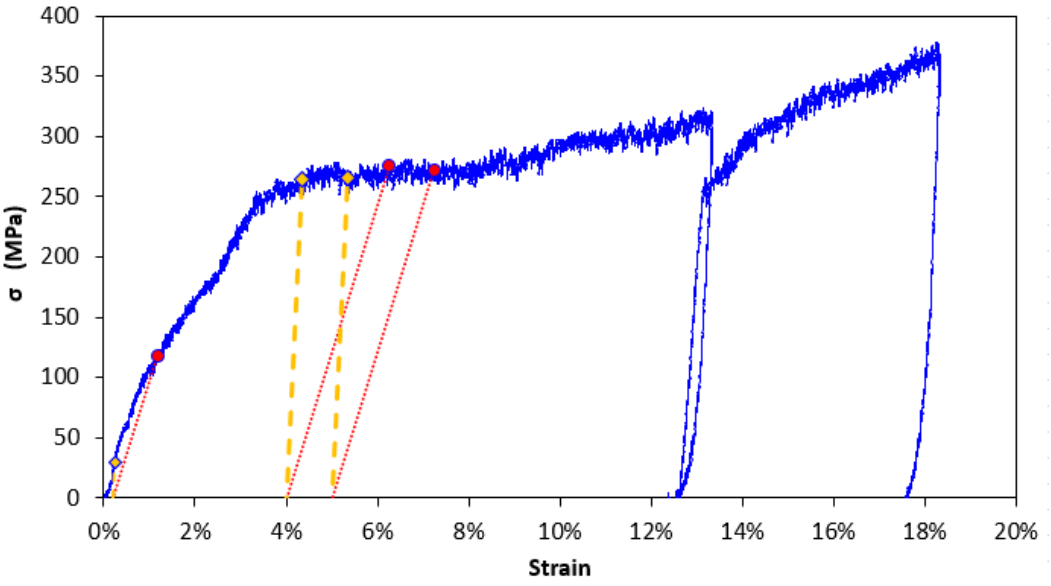


*Figure 127: Engineering stress-train curve of a double loading experiment on a Fe-0.1Cu alloy. The stress at yield of 0.2%, 4% and 5% using the loading curve are presented with the red dotted lines and using the unloading curve with the yellow dashed lines.*

In Figure 127, it is evident that the slopes of first unloading along with the second loading and second unloading linear segments of the stress-strain curve, are in very good agreement, thus providing almost similar Young's modulus values. Therefore, to calculate the stress needed to cause a certain degree of strain (i.e., at 0.2%, 4% etc), a line was plotted on the stress-strain diagram, passing from the strain value in question with slope equal to the slope of the unloading linear segment.

The stress at 4% and 5% calculated (Figure 3) using the slopes of the first and second unloading as well as the second loading segments were very similar but the values at 0.2% were very different. Note that the stress values at 4% and 5% strain are almost identical, due to a small load drop that occurred at about 5% strain.

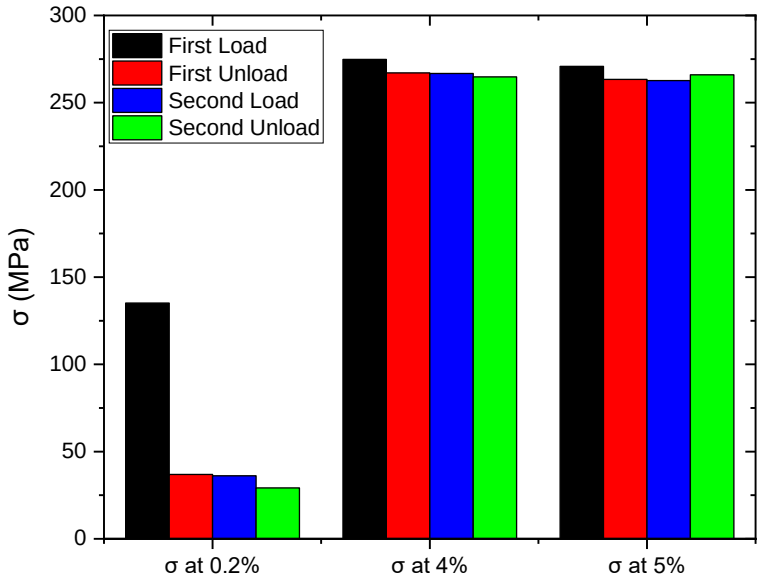


*Figure 128: Stress calculated at 0.2%, 4% and 5% of plastic deformation using the slope of the first and second loading (black and blue) as well as first and second unloading (red and green). The double loading experiment was performed on a testing material (Fe-0.1Cu).*

Nevertheless, when observing the curve in Figure 127, it is apparent that strain hardening rate is significantly reduced at the onset of plastic deformation. Single crystals when deformed, exhibit three-stage behavior [4–9] and the stress-strain curve has a similar shape as schematically illustrated in Figure 129.

In stage I, only the primary slip system is active. Dislocations glide easily without being hindered by other dislocations from different slip systems. This stage is often called 'easy glide' and the crystal may deform considerably at almost constant stress. The experimentally observed small work hardening is due to the accumulation of dislocation debris in the form of dipoles [10].This is a stage of low hardening which may be absent, or account for as much as 40 percent shear strain depending on the testing conditions.

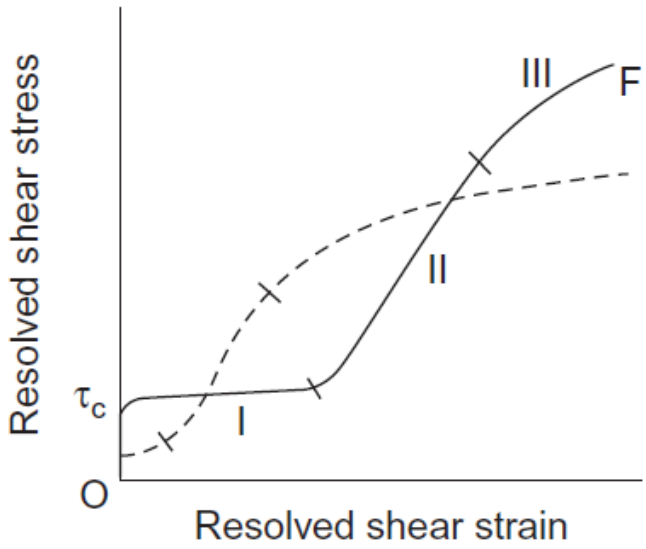


*Figure 129: Schematic of the Typical shear stress-shear strain curve of a single crystal. The curve has three parts corresponding to stages I, II and III. The extent of these stages depends on the material and crystal orientation of the load axis, as indicated by the solid and dashed line curve [4].*

Stage II initiates when the critical resolved shear stress is reached at the secondary system and thus it starts operating. Now dislocations moving on both slip systems may interact with each other, thus work-hardening of the crystal is taking place and hence increasing the slope of this linear segment of the curve.

Stage III corresponds, at high stresses, that the applied force becomes sufficient to overcome the obstacles and thus screw dislocations leave their original slip planes by cross slip. The curve becomes parabolic and thus its slope gets progressively less steep.

The extent of the 'easy glide' stage I, as well as of the other two stages, depends on the crystal orientation of the load axis and the material (solid and dashed curve). This three-stage behavior is well studied for the FCC metals and according to Bacon [4], BCC metals have similar behavior (but at higher stress) at intermediate temperatures.

To summarize, in this work, the stress values corresponding to a given strain were defined using the slope of the unloading curve, as calculated after applying the Sneddon correction.

## II. Mechanical properties of the model alloys

This section details the specificities of the micro-compression tests performed on the three model alloys at both unirradiated and neutron irradiated states. More specifically, the orientation of the selected grains inside which the pillars were fabricated is reported.

The orientation of these grains is also the orientation of the surface plane of the pillars. The pillar's surface plane is perpendicular to the loading axis which coincides with the pillar axis.

Due to high symmetry in the cubic crystal, each of the 24 stereographic triangles with <100>, <101>, and <111> at the corner of each triangle, are crystallographically equivalent [11]. Therefore, the orientation is usually represented on just one of the stereographic triangles, the [001]-[011]-[111] triangle, named Standard Stereographic Triangle (SST) and being the fundamental stereographic sector (FS) for the cubic crystal symmetry. Therefore, in this work we will use the equivalent orientation on the SST, while the EBSD acquired IPF orientation will be reported only on the relevant tables.

For each grain, the slip systems along with their Schmid factors and the angles between the plane of the slip systems and the surface plane (denoted as angle $\phi$) are derived from the EBSD data.

For each pillar, the recorded video of the SEM screen along with the load – displacement diagram was studied in order to identify which slip step was formed first on the pillar surface and at which strain. Then, slip trace analysis was carried out to identify the primary slip system activated during compression.

The engineering stress-strain curves of the pillars were plotted and following the procedure detailed in the previous section, the stress at 2% or 3% strain are derived. Using the Schmid factor of the identified activated slip system, the corresponding resolved shear stress is determined using equation (1.4).

## 1 - Mechanical properties of the Fe-Mn model alloy

EBSD data analysis of the non-irradiated Fe-Mn alloy revealed only two grains with favorable orientation which were selected for pillar fabrication. Figure 130 illustrates the selected grain orientations $[\bar{3}, 4,11]$ and $[\bar{1}, 2, 5]$ projected on the iso-Schmid maps of the {110} and {112} plane families, on the standard stereographic triangle. Two $[\bar{3}, 4,11]$ and five $[\bar{1}, 2, 5]$ oriented pillars were FIB-fabricated.

Unfortunately, in the case of the non-irradiated Fe-Mn material, after excluding the pillars that did not match the predefined dimensional (diameter, taper angle, aspect ratio) and the micro-compression system alignment criteria, as well as the pillars that trace analysis was inconclusive, only three out of the seven pillars were considered for the determination of the mechanical properties.

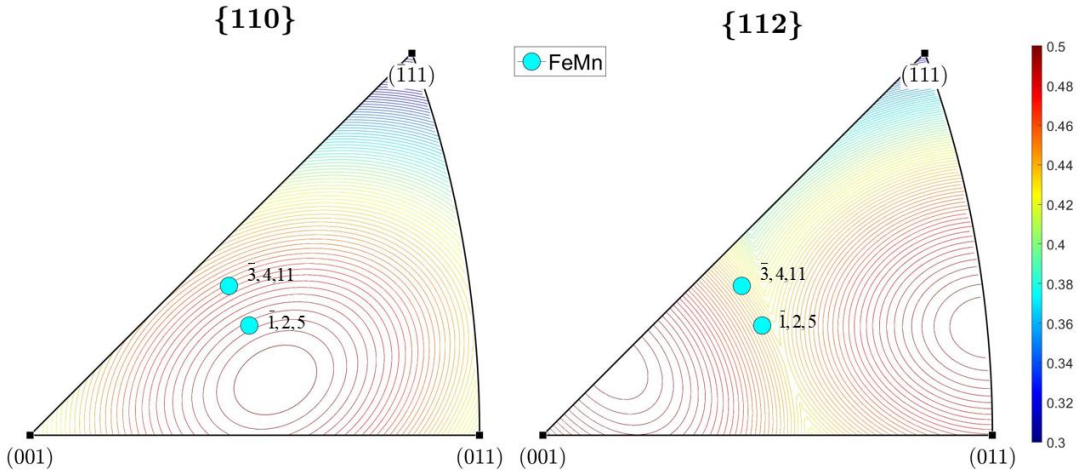


*Figure 130: The orientation of the surface of the pillars of the non-irradiated Fe-Mn, projected on iso-Schmid maps of the {110} and {112} slip plane families. The Schmid factors from 0.3 to 0.5 are illustrated via the color code from blue to red.*

The information derived from the EBSD acquired data for the orientations of the compressed pillars, is summarized in Table 14 and includes the possible slip systems with the two highest Schmid factors, and the calculated angle between the slip plane and the surface of the pillar, which is used for the slip trace analysis. Note that, by selecting grains with orientation where the angle χ is near zero, possible deviation from the Schmid's law minimizes (where χ is the angle that the MRSSP makes with the $(\bar{1}01)$ plane, as defined in chapter 1).

At the same time, the selection is made so that the Schmid factor of primary slip system has significant difference from that of the secondary, hence the slip systems do not operate simultaneously, facilitating the identification of the first activated one. Additionally, the angles between the planes of the primary and secondary slip system and the surface plane (denoted as angle ϕ) are different enough and are used for the determination of the activated slip system during slip trace analysis (detailed in chapter 2).

*Table 14: The orientation of the grains inside which the pillars of the unirradiated Fe-Mn alloy were fabricated, the equivalent orientation on the standard stereographic triangle (SST) and the first two theoretically activated slip systems along with their Schmid factors and the angles between the planes of the slip system and the surface plane (denoted as angle ϕ).*

| Orientation | Equivalent SST orientation | Slip system | Schmid factor | Angle ϕ (°) |
|---|---|---|---|---|
| [3, 4,11] | [ $\bar{3}$, 4,11] | (1, 1, 0) [-1, 1, 1] | 0.471 | 35 |
| | | ( 1, 1,-2) [-1,-1,-1] | 0.438 | 59 |
| [1, 5, 2] | [$\bar{1}$, 2, 5] | (1, 0, 1) [-1, 1, 1] | 0.489 | 39 |
| | | (-1, 2,-1) [ 1, 1, 1] | 0.439 | 58 |

During the study of the post compression SEM images, formation of either multiple or single slip steps on the surface of the pillar occurred mainly at the middle (Figure 6 – a) and upper region of the pillars (Figure 6 – b).

Slip trace analysis determined, for both orientations, that the slip plane of the first activated slip system was the {110} type plane, hence confirming the primary slip system as estimated by the EBSD data study.

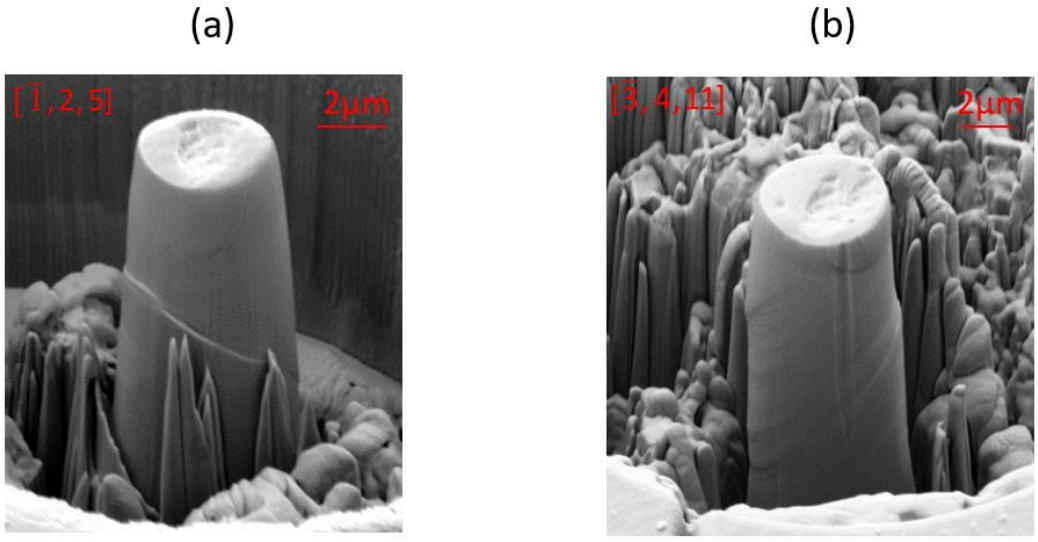


*Figure 131: SEM image of compressed unirradiated Fe-Mn pillars with localized slip planes fabricated in a (a) [$\bar{1}$, 2, 5] and (b) [$\bar{3}$, 4, 11] oriented grain.*

The engineering stress-strain curves of the [$\bar{3}$, 4,11] oriented pillars are plotted in blue in Figure 132, whereas the [ $\bar{1}$, 2, 5] pillars are in red. All curves are continuous and appear rather smooth, with a well-defined elastic domain.

From the stress-strain curve of each compressed pillar, the stress at 3% strain was determined and the corresponding resolved shear stress was calculated using the Schmid factor of the identified activated slip system in equation (1.4). The average resolved shear stress calculated at 3% strain was (230 ± 25) MPa (standard deviation denotes the uncertainty in stress calculations).

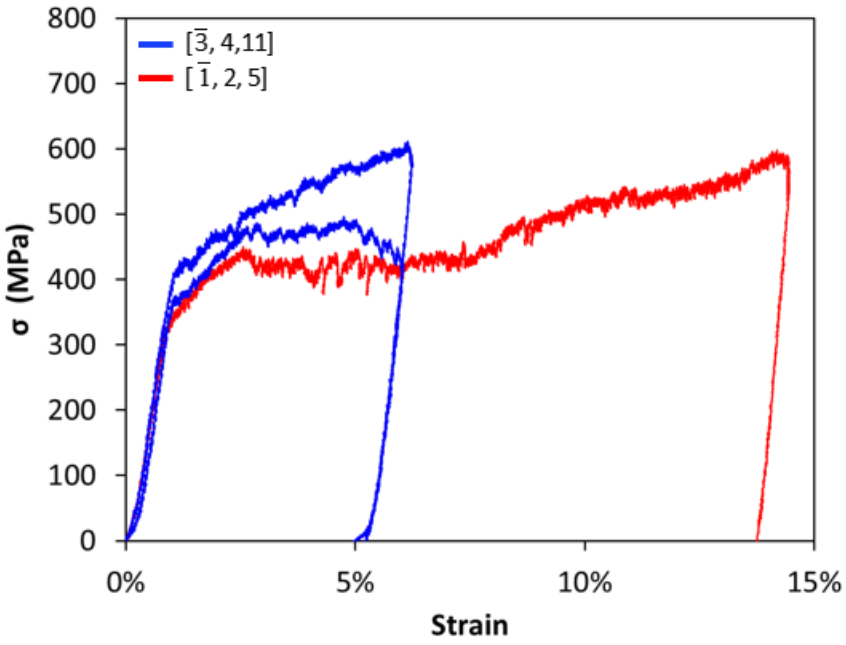


*Figure 132: Engineering stress-strain curves of the unirradiated Fe-Mn $[\bar{3}, 4, 11]$ and $[\bar{1}, 2, 5]$ oriented pillars, in blue and red respectively.*

In the neutron irradiated Fe-Mn sample, four pillars were fabricated in the $[\bar{3}, 4, 10]$ oriented grain and seven in the $[\bar{2}, 5, 12]$ oriented one. These selected orientations (red circles in Figure 133), projected on the iso-Schmid maps of the {110} and {112} plane families, are quite close with the orientations of the unirradiated Fe-Mn pillars (cyan circles in Figure 133).

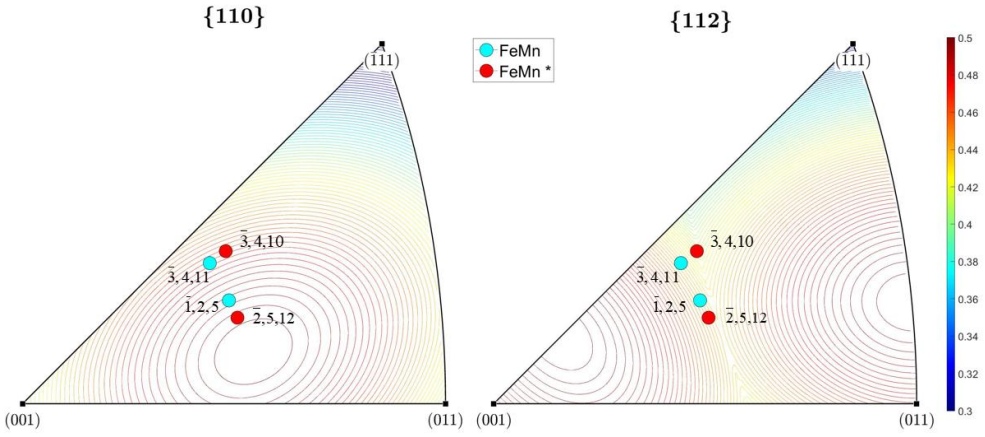


*Figure 133: The orientation of the surface of the unirradiated (cyan) and neutron irradiated (red) pillars of the Fe-Mn alloy, projected on iso-Schmid maps of the {110} and {112} slip plane families. The Schmid factors from 0.3 to 0.5 are illustrated via the color code from blue to red.*

The Schmid Factor and the angle ϕ from the EBSD study, are reported in Table 15, for the estimated primary and secondary slip systems of the two grains. As in the non-irradiated case, both the Schmid factors and the angles ϕ have a significant difference between these slip systems.

*Table 15: The orientation of the grains inside which the pillars of the neutron irradiated Fe-Mn alloy were fabricated, the equivalent orientation on the standard stereographic triangle (SST) and the first two theoretically activated slip systems along with their Schmid factors and the angles between the planes of the slip system and the surface plane (denoted as angle ϕ).*

| Orientation | Equivalent SST orientation | Slip system | Schmid factor | Angle ϕ (°) |
|---|---|---|---|---|
| [ $\bar{1}2$, 2, 5] | [ $\bar{2}$, 5, 12] | (-1, 1, 0) [-1,-1,-1] | 0.495 | 41 |
| | | ( 1, 1, 0) [ 1,-1, 1] | 0.450 | 57 |
| [ 4, 3, $\bar{1}0$] | [$\bar{3}$, 4,10] | ( 1, 1, 0) [ 1,-1,-1] | 0.473 | 35 |
| | | ( 2,-1, 1) [ 1, 1,-1] | 0.423 | 62 |

The post-compression SEM images study, indicated that the deformation of all pillars was localized on the upper part, forming multiple slip steps on their surface. The steps on the $[\bar{2}, 5, 12]$ oriented pillars seemed to be almost parallel to each other suggesting the activation of the same slip system, while on the $[\bar{3}, 4,10]$ oriented, slip steps in different directions indicate that more than one slip system was activated (Figure 134).

Analyzing the angles of the slip steps, we verified that the plane of the first activated slip system was a {110} type plane, in agreement with the EBSD analysis.

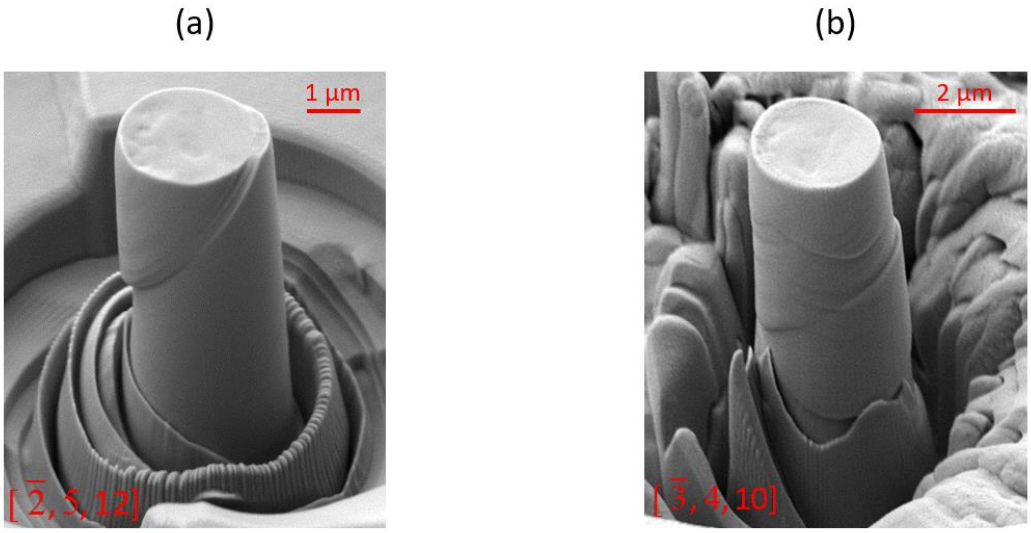


*Figure 134: Neutron irradiated Fe-Mn (a) $[\bar{2}, 5, 12]$ oriented compressed micro-pillar, presenting multiple parallel slip steps and (b) $[\bar{3}, 4, 10]$ oriented pillar slip steps are observed in different directions, indicating that more than one slip system was activated*

The stress-strain curves of the neutron irradiated Fe-Mn samples, had a rather continuous form exhibiting only a few and smaller load-drops than the unirradiated Fe-Mn curves (Figure 135).

The average resolved shear stress calculated at 3% strain was (265 $\pm$ 40) MPa. Thus, considering the calculated resolved shear stress of the unirradiated samples, the irradiation hardening is estimated at 35 MPa. The uncertainty of the irradiation hardening calculation is

the combination of the uncertainties of the irradiated and non-irradiated stress distributions, which is calculated using the quadrature sum as 47 MPa.

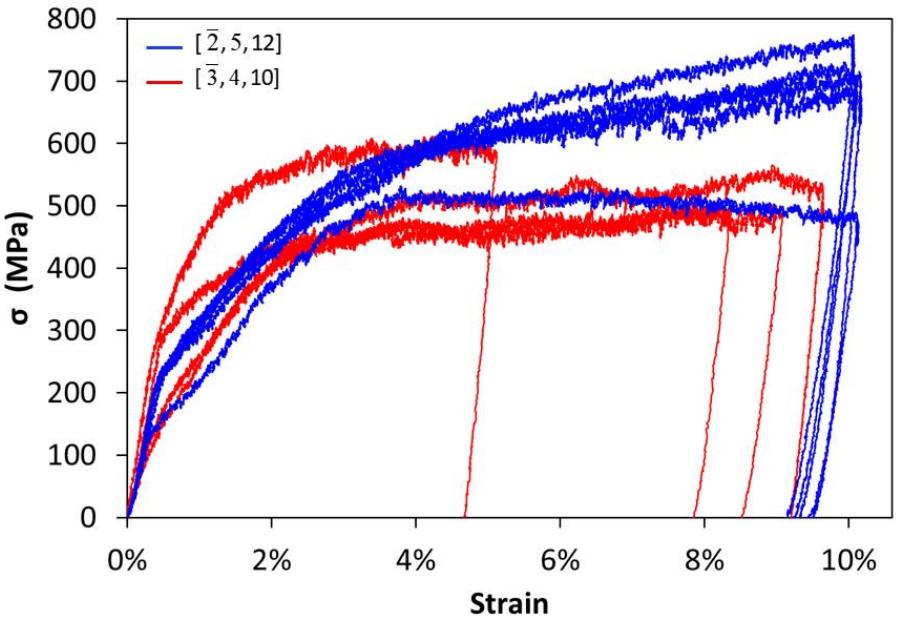


*Figure 135: Engineering stress - strain curves of Fe-Mn neutron irradiated [$\bar{2}$, 5, 12] and [$\bar{3}$, 4, 10] oriented pillars.*

## 2 - Mechanical properties of the Fe-Ni model alloy

Three grain orientations, namely the [$\bar{3}$, 4,11], [$\bar{1}$, 5,11] and [$\bar{2}$, 5,12] were selected for pillar fabrication of the unirradiated Fe-Ni pillars. In Figure 136, their projections are plotted on the iso-Schmid maps of the {110} and {112} slip plane families in the SST.

From the nine FIB-fabricated pillars, finally four were used to determine the mechanical properties of the Fe-Ni sample.

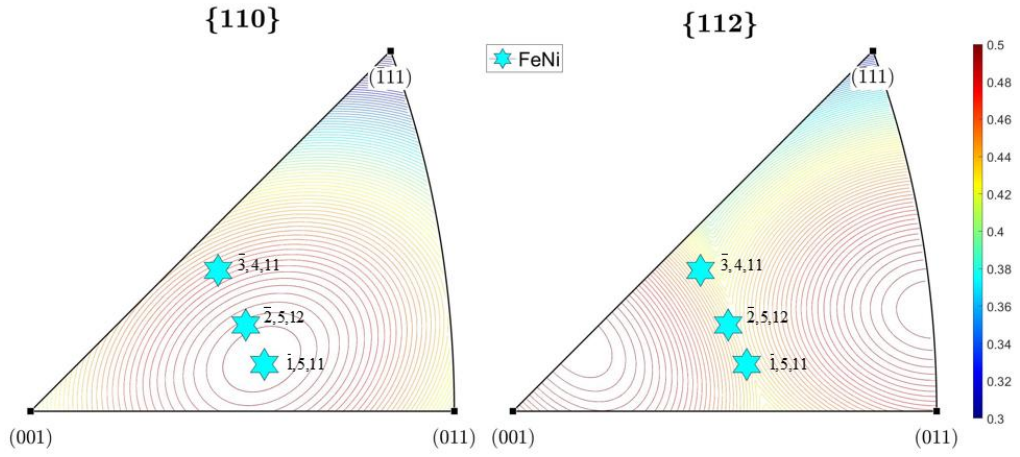


*Figure 136: The orientation of the surface of the pillars of the unirradiated Fe-Ni, projected on iso-Schmid maps of the {110} and {112} slip plane families. The Schmid factors from 0.3 to 0.5 are illustrated via the color code from blue to red.*

The EBSD estimated details of the primary and secondary slip systems are given in Table 16. For all three orientations, the difference in the values of the Schmid factors of the primary and secondary systems was significant. Also, the difference of the angle ϕ was high enough, especially for the $[\bar{3}, 4, 11]$ pillar orientation, simplifying the determination of the activated system.

*Table 16: The orientation of the grains inside which the pillars of the unirradiated Fe-Ni alloy were fabricated, the equivalent orientation on the standard stereographic triangle (SST) and the first two theoretically activated slip systems along with their Schmid factors and the angles between the planes of the slip system and the surface plane (denoted as angle ϕ).*

| Orientation | Equivalent SST orientation | Slip system | Schmid factor | Angle ϕ (°) |
|---|---|---|---|---|
| $[4, \bar{11}, 3]$ | $[\bar{3}, 4, 11]$ | ( 0,-1, 1) [ 1,-1,-1] | 0.472 | 35 |
| | | ( 1, 2, 1) [-1, 1,-1] | 0.428 | 60 |
| $[\bar{5}, 1, \bar{11}]$ | $[\bar{1}, 5, 11]$ | ( 0,-1, 1) [ 1, 1, 1] | 0.499 | 46 |
| | | ( 0, 1, 1) [ 1,-1, 1] | 0.468 | 54 |
| $[12, \bar{2}, \bar{5}]$ | $[\bar{2}, 5, 12]$ | (-1, 1, 0) [-1,-1, 1] | 0.497 | 41 |
| | | ( 1, 1, 0) [ 1,-1,-1] | 0.451 | 57 |

The study of the post-compression SEM images of the deformed pillars revealed that localized slip steps were present in all compressed pillars, mostly located in their center (Figure 137).

Slip trace analysis related the observed slip steps on the SEM micrographs with the theoretical estimated primary slip system, having a {110} type slip plane and the highest Schmid factor.

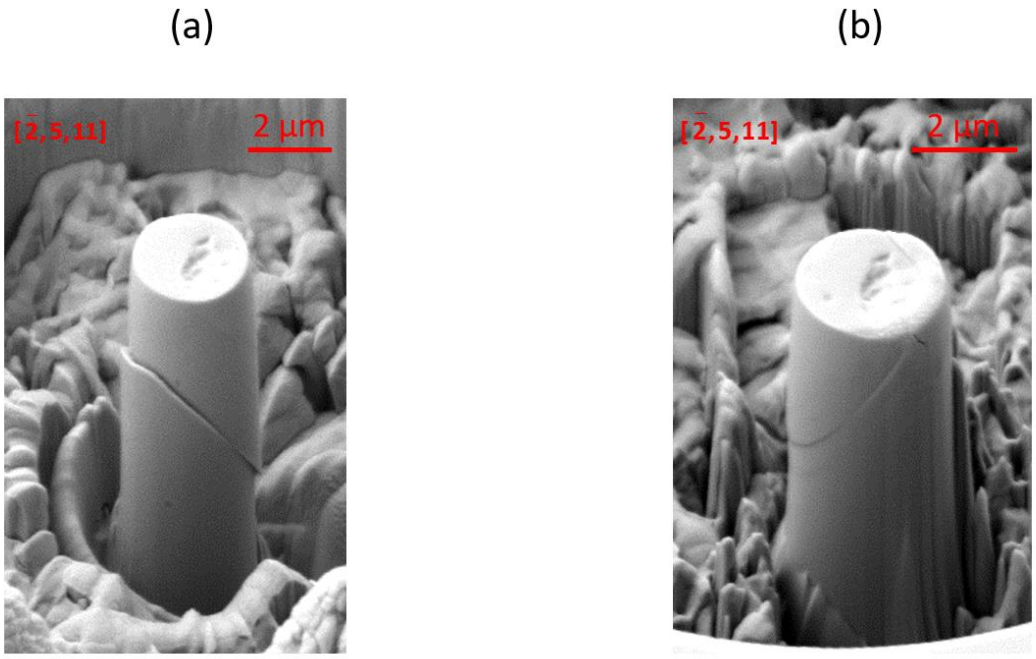


*Figure 137: Two compressed $[\bar{2}, 5, 12]$ oriented micro-pillars, presenting localized slip steps.*

The curves of all non-irradiated Fe-Ni samples presented a continuous stress-strain response with only small load drops (Figure 138).

The average measured resolved shear stress at 2% strain is (173 ± 42) MPa (uncertainty is estimated by standard deviation).

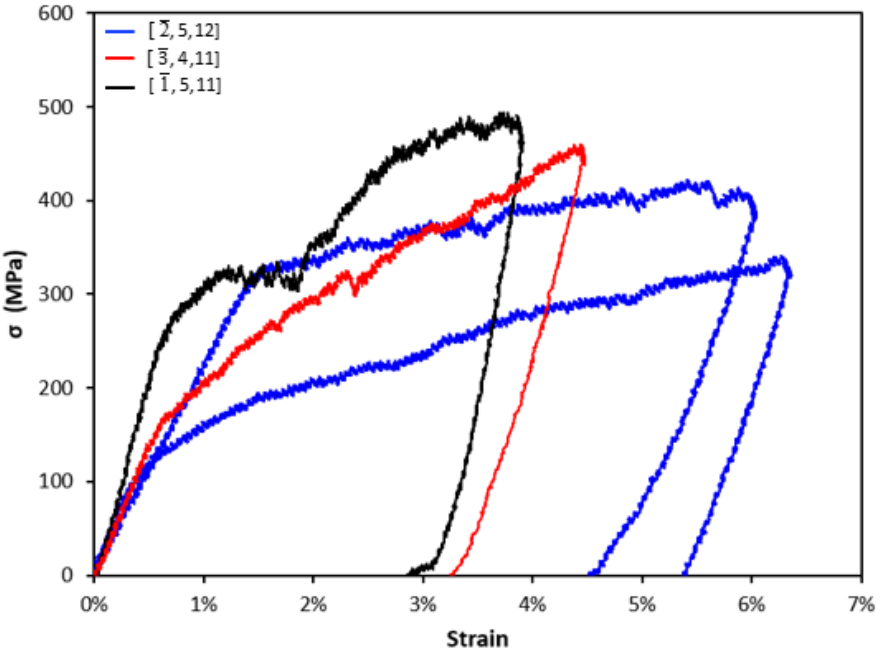


*Figure 138: Engineering stress – strain curves for [ 2̄,5,12], [ 3̄,4,11] and [ 1̄,5,11] oriented pillars of the Fe-Ni non-irradiated samples.*

Pillars in the neutron irradiated Fe-Ni sample, were fabricated inside [ 3̄, 5,12], [ 2̄, 5,11] and [ 1̄, 3, 7] oriented grains. Their projections to the standard stereographic triangle are close to those of the non-irradiated Fe-Ni pillars as seen in Figure 139.

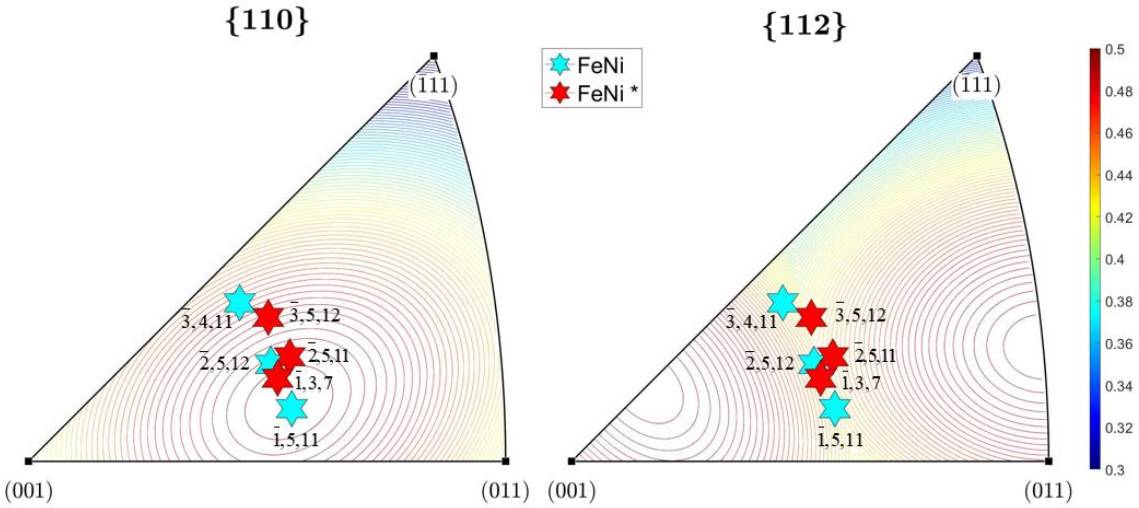


*Figure 139: The orientation of the surface of the unirradiated (cyan) and neutron irradiated (red) pillars of the Fe-Ni alloy, projected on iso-Schmid maps of the {110} and {112} slip plane families. The Schmid factors from 0.3 to 0.5 are illustrated via the color code from blue to red.*

Observing the results of the EBSD study reported on Table 17, one can notice that the angles ϕ of the estimated primary and secondary slip systems, are quite different for both the $[\bar{3},5,12]$ and $[\bar{1},3,7]$ oriented pillars but have a very small difference (of 7 degrees) for the $[\bar{2},5,11]$ oriented pillars, potentially complicating the identification of their activated slip system.

*Table 17: The orientation of the grains inside which the pillars of the neutron irradiated Fe-Ni alloy were fabricated, the equivalent orientation on the standard stereographic triangle (SST) and the first two theoretically activated slip systems along with their Schmid factors and the angles between the planes of the slip system and the surface plane (denoted as angle ϕ).*

| Orientation | Equivalent SST orientation | Slip system | Schmid factor | Angle ϕ (°) |
|---|---|---|---|---|
| $[\overline{12},\bar{3},\bar{5}]$ | $[\bar{3},5,12]$ | (-1, 1, 0) [-1,-1,-1] | 0.475 | 37 |
| | | ( 2, 1,-1) [ 1,-1, 1] | 0.422 | 60 |
| $[\bar{5},11,2]$ | $[\bar{2},5,11]$ | (0, 1, 1)[-1, 1,-1] | 0.493 | 41 |
| | | ( 1,-1,-2) [ 1,-1, 1] | 0.444 | 48 |
| [ 3, 1, 7] | $[\bar{1},3,7]$ | ( 0, 1, 1)[ 1,-1, 1] | 0.497 | 42 |
| | | ( 0,-1, 1) [ 1, 1, 1] | 0.452 | 56 |

Analysis of the post-compression SEM images of the deformed pillars revealed that multiple slip steps were present in almost all compressed pillars, whatever their orientation (Figure 140 – b to f). These steps were located at the middle and upper region of the pillars for the $[\bar{2},5,11]$ and $[\bar{1},3,7]$ orientations and all over the pillar height in the $[\bar{3},5,12]$ oriented pillars. Only one $[\bar{3},5,12]$ oriented pillar exhibited one single slip step (Figure 140 - a).

In the case of pillars presenting multiple slip events, the recorded SEM screen along with the load – displacement diagram was studied in order to identify which slip step was formed first on the pillar surface and at which strain.

Then, slip trace analysis was carried out and confirmed that the estimated primary slip system was the first activated, since the angle between the formed slip steps and the pillar surface matched with the corresponding angle ϕ. Particularly, for the $[\bar{2},5,11]$ oriented pillars the measured angles (42.4° and 43.3°) on the SEM images were in good agreement with the estimated angle ϕ (41.4 °), also confirming the estimated primary slip system.

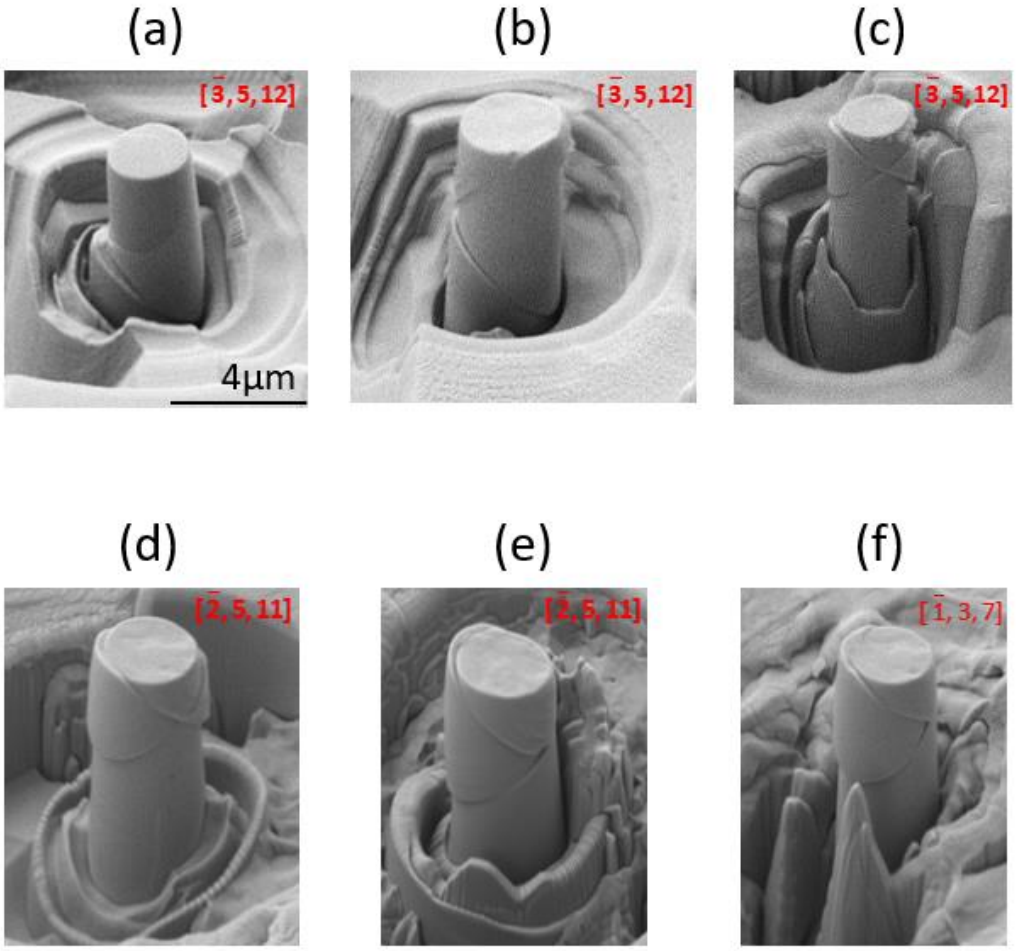


*Figure 140: Post-compression SEM images of $[\bar{3},5,12]$, $[\bar{2},5,11]$ and $[\bar{1},3,7]$ oriented pillars of the neutron irradiated Fe-Ni alloy. Pillar (a) shows single slip steps while (b – f) multiple.*

All the curves of the Fe-Ni neutron irradiated samples plotted in a rather continuous form, presenting only a few small load drops (Figure 141).

The average measured resolved shear stress at 2% strain is (240 $\pm$ 40) MPa.

Considering the average value of the resolved shear stress at 2% strain of the non-irradiated Fe-Ni samples, the irradiation hardening is calculated at (67 ± 57) MPa (the reported uncertainty is the quadrature sum of the uncertainties of the irradiated and non-irradiated stress distributions).

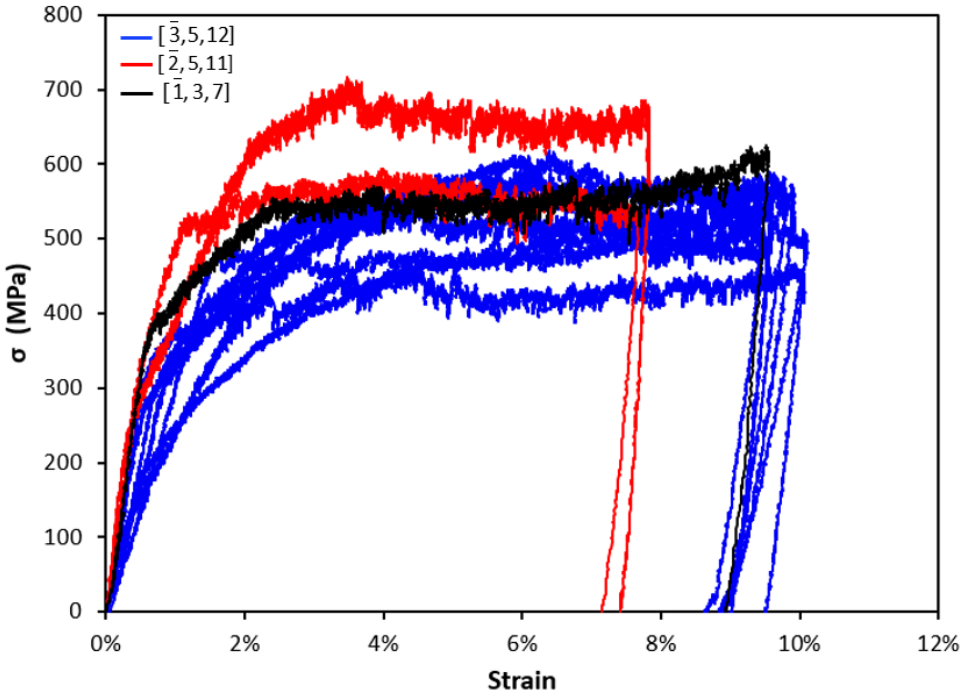


*Figure 141: Engineering stress - strain curves of neutron irradiated Fe-Ni [ $\bar{3}$,5,12] , [ $\bar{2}$,5,11] and [ $\bar{1}$,3,7] oriented pillars.*

## 3 - Mechanical properties of the Fe-Mn-Ni model alloy

In the non-irradiated Fe-Mn-Ni alloy, pillars were FIB-fabricated inside grains having [ $\bar{2}$, 5, 12] , [ $\bar{1}$, 4, 9] and [ 0, 1, 2] orientations. Figure 142 illustrates these orientations on the standard stereographic triangle.

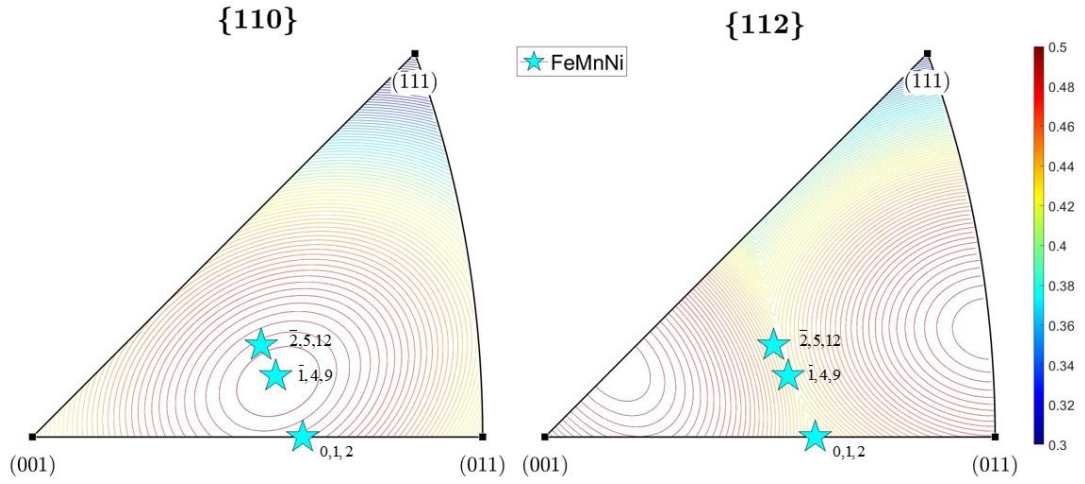


*Figure 142: The orientation of the surface of the pillars of the neutron irradiated Fe-Mn-Ni, projected on iso-Schmid maps of the {110} and {112} slip plane families. The Schmid factors from 0.3 to 0.5 are illustrated via the color code from blue to red.*

It must be noted that the [0,1,2] orientation is onto the circumference of the SST and due to the symmetry, we expect the activation of two slip systems at the same time, that cannot be distinguished from one another [8].

In Table 18, the details of the estimated primary and secondary slip systems from the EBSD study are reported.

*Table 18: The orientation of the grains inside which the pillars of the unirradiated Fe-Mn-Ni alloy were fabricated, the equivalent orientation on the standard stereographic triangle (SST) and the first two theoretically activated slip systems along with their Schmid factors and the angles between the planes of the slip system and the surface plane (denoted as angle ϕ).*

| Orientation | Equivalent SST orientation | Slip system | Schmid factor | Angle ϕ (°) |
|---|---|---|---|---|
| [ $\bar{5}$, 12, $\bar{2}$] | [ $\bar{2}$, 5, 12] | ( 0,-1, 1) [ 1,-1,-1] | 0.493 | 41 |
| | | ( 0, 1, 1) [-1, 1,-1] | 0.447 | 57 |
| [ 9, 1, $\bar{4}$] | [ $\bar{1}$, 4, 9] | ( 1, 1, 0) [ 1,-1,-1] | 0.499 | 44 |
| | | (-1, 1, 0) [-1,-1, 1] | 0.469 | 55 |
| [ 0, 2, 1] | [ 0, 1, 2] | (-1, 1, 0) [ 1, 1,-1]<br>( 1, 1, 0) [-1, 1,-1] | 0.489 | 51 |
| | | ( 1, 2, 1) [-1, 1,-1] | 0.424 | 57 |

Analysis of the post-compression SEM images of the deformed pillars revealed that multiple slip steps, almost parallel to each other, were present in the majority of the compressed pillars mainly located in their middle region, illustrated in Figure 143.

Slip trace analysis verified that the first activated slip system was indeed the theoretical estimated primary one.

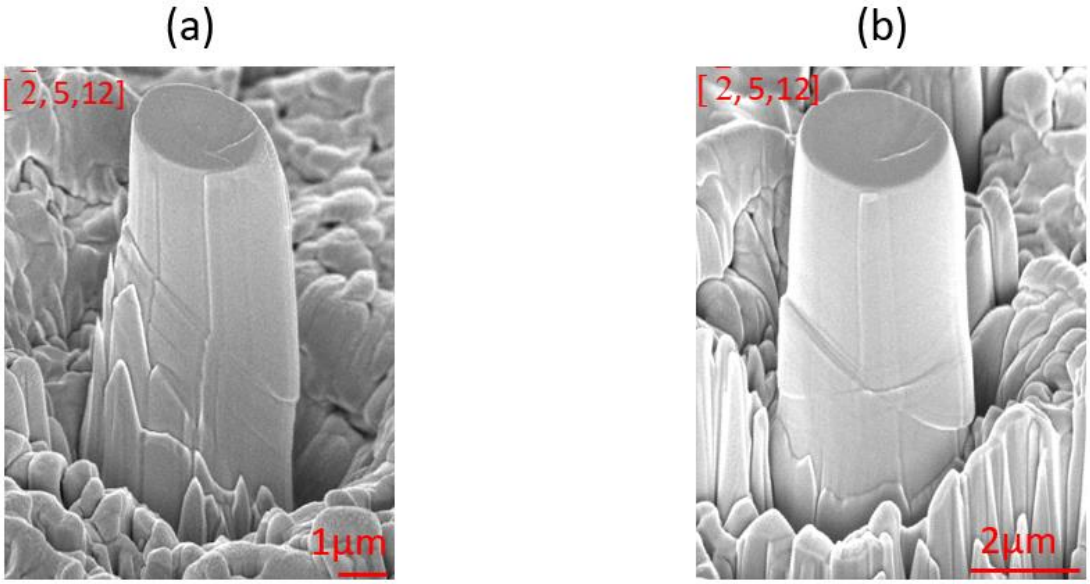


*Figure 143: Post-compression SEM images of [ $\bar{2}$, 5, 12] oriented pillars presenting multiple slip steps.*

The engineering stress-strain curves of the unirradiated Fe-Mn-Ni alloy had not a smooth shape and exhibit more and larger load drops than the other non-irradiated materials (Figure 144).

From the study of the stress-strain curves, the average resolved shear stress at 2% strain was calculated to be (191 ± 15) MPa (standard deviation expresses the uncertainty).

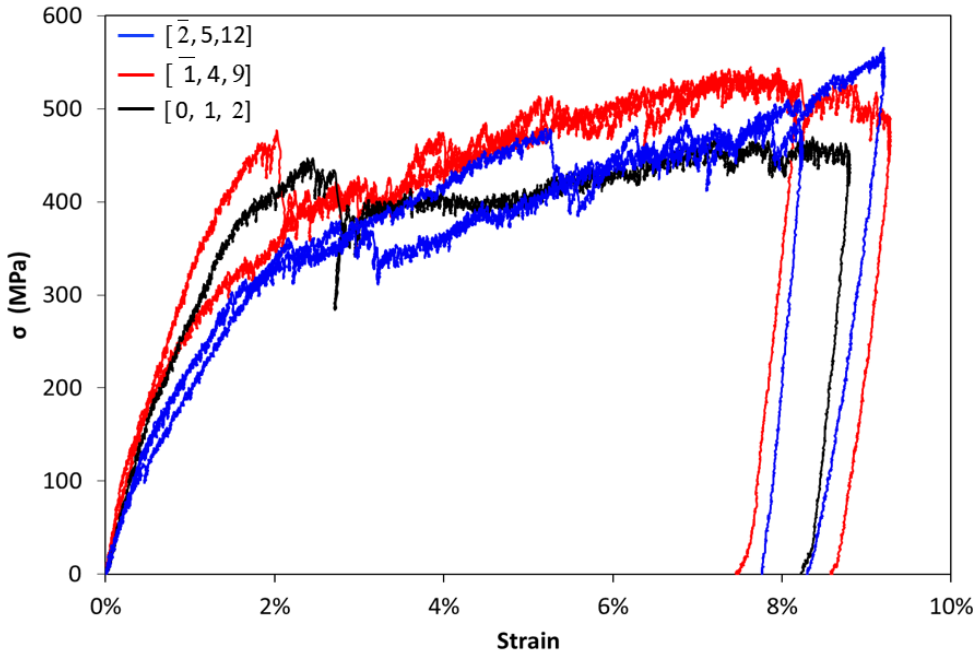


*Figure 144: Engineering stress - strain curves of unirradiated Fe-Mn-Ni [2̄,5,12], [1̄, 4, 9] and [0, 1, 2] oriented pillars.*

Pillars were FIB-fabricated in the neutron irradiated ternary alloy, at the favorable orientation [2̄,3,8] and since there was no other favorable grain available on the sample, the one with [2̄,7,10] orientation was selected since the grain was big enough allowing fabrication of many pillars (Figure 145).

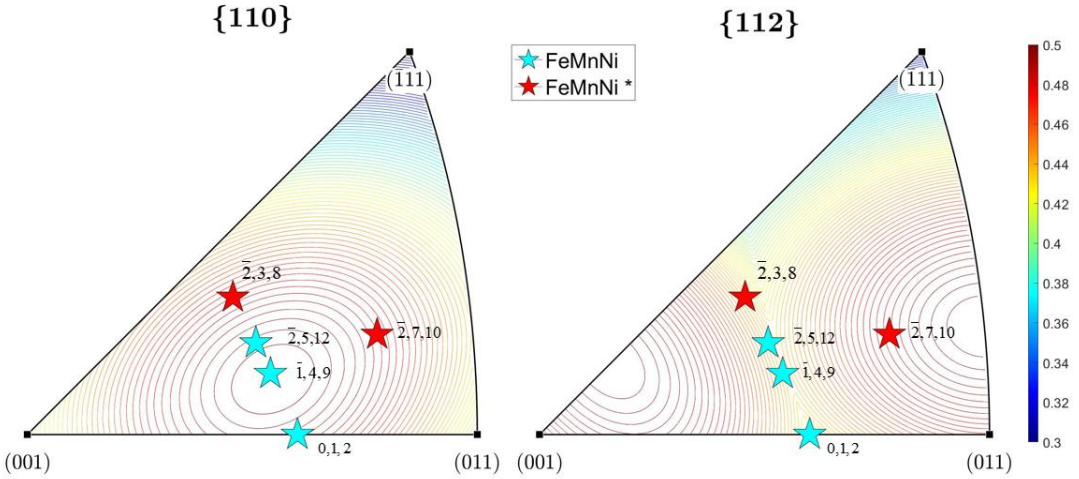


*Figure 145: The orientation of the surface of the unirradiated (cyan) and neutron irradiated (red) pillars of the Fe-Mn-Ni alloy, projected on iso-Schmid maps of the {110} and {112} slip plane families. The Schmid factors from 0.3 to 0.5 are illustrated via the color code from blue to red.*

The primary and the secondary slip system of the [2̄,7,10] oriented pillars, have very similar values of Schmid factor (as detailed in Table 19), being different only by 3‰ and therefore if the primary slip system was not correctly identified, the error in the calculation of the resolved shear stress, would be very small.

*Table 19: The orientation of the grains inside which the pillars of the neutron irradiated Fe-Mn-Ni alloy were fabricated, the equivalent orientation on the standard stereographic triangle (SST) and the first two theoretically activated slip systems along with their Schmid factors and the angles between the planes of the slip system and the surface plane (denoted as angle ϕ).*

| Orientation | Equivalent SST orientation | Slip system | Schmid factor | Angle ϕ (°) |
|---|---|---|---|---|
| [ 7, $\bar{2}$, 10] | [ $\bar{2}$, 7,10] | (-1, 2,-1) [-1,-1,-1] | 0.484 | 45 |
| | | ( 0,-1, 1) [ 1, 1, 1] | 0.481 | 40 |
| [ 3, $\bar{2}$, 8] | [ $\bar{2}$, 3, 8] | (-1, 1, 0) [ 1, 1, 1] | 0.473 | 36 |
| | | ( 1, 2,-1) [-1, 1, 1] | 0.434 | 59 |

Analysis of the post-compression SEM images of the deformed pillars revealed that multiple slip steps, almost parallel to each other, were present in the majority of the pillars, located mainly in their upper region.

The theoretical angle ϕ and that of the slip steps on the $[\bar{2}, 3, 8]$ oriented pillars matched during slip trace analysis, verifying the activation of the estimated primary slip system.

For the $[\bar{2}, 7,10]$ oriented pillars, it was quite difficult to identify the slip system activated during compression, since the Schmidt factor values as well as angles ϕ were very similar for the primary and secondary slip systems (Figure 146). Therefore, probably both these systems were activated, and the calculations of the resolved shear stress was made, assuming that the activated system was the theoretically estimated primary one.

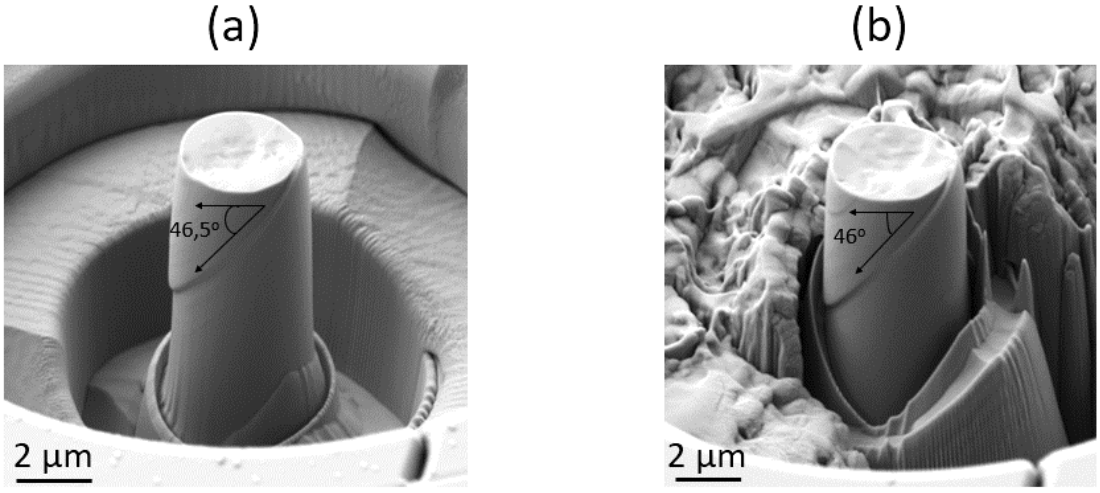


*Figure 146: Two compressed pillars of the $[\bar{2}, 7, 10]$ orientation, exhibiting slip steps parallel to each other. The angle of the slip step is illustrated in each case.*

The compression curves of the $[\bar{2}, 3, 8]$ oriented pillars, were smoother than those of the $[\bar{2}, 7,10]$ oriented ones, that exhibited some small load drops which are pointed out with arrows on Figure 147.

The calculated average resolved shear stress at 2% strain was (371 ± 69) MPa, which in combination with the calculated average resolved shear stress of the unirradiated samples results to an irradiation hardening of 180 MPa, with uncertainty calculated as the quadrature

sum of the standard deviations of the irradiated and non-irradiated distributions giving a value of 71 MPa.

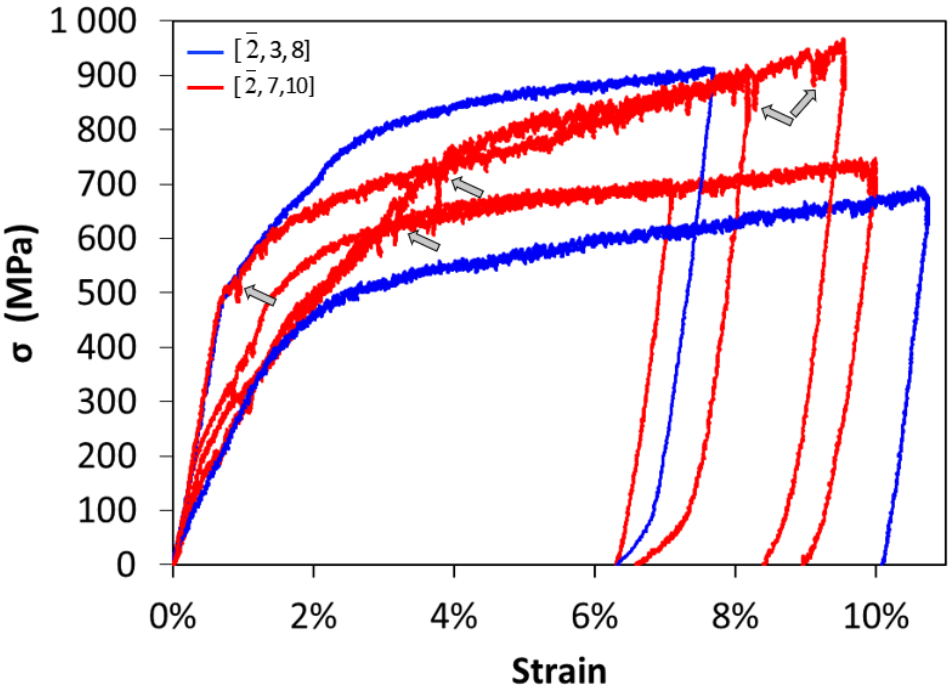


*Figure 147: Engineering stress - strain curves of Fe-Mn-Ni neutron irradiated [ $\bar{2}$, 3, 8] and [ $\bar{2}$, 7, 10] oriented pillars. The grey arrows point to load-drops observed on the stress-strain curves of the [ $\bar{2}$, 7, 10] oriented pillars.*

Moreover, pillars were FIB-fabricated in the post-irradiation annealed at 400°C during 30', Fe-Mn-Ni samples and in-situ compression experiments were performed to examine the annealing effect on the mechanical properties.

The pillars were fabricated in grains having the favorable orientations of [ $\bar{1}$, 6, 13] and [ $\bar{2}$, 2, 5], as well to the [ 0, 1, 3] and [$\bar{2}$,0,11] oriented grains that allowed multiple pillar fabrication (Figure 148).

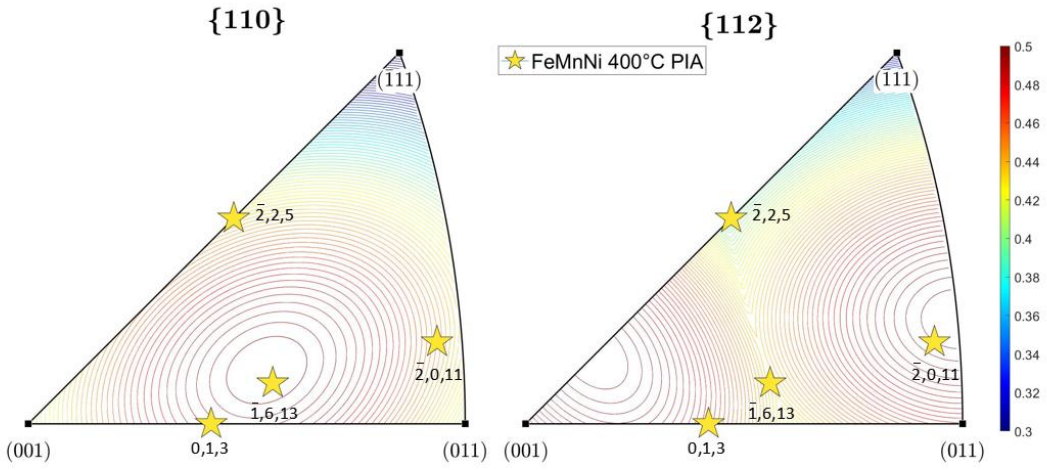


*Figure 148: The orientation of the surface of the pillars of the neutron irradiated, post-irradiation annealed (30' at 400°C) Fe-Mn-Ni, projected on iso-Schmid maps of the {110} and {112} slip plane families. The Schmid factors from 0.3 to 0.5 are illustrated via the color code from blue to red.*

In any case, for all orientations the EBSD estimated primary slip system had significantly increased Schmid factor value compared to that of the secondary, thus facilitating the identification of the first activated one (Table 20).

Particularly, the [0,1,3] and $[\bar{2},2,5]$ orientations are located onto the circumference of the SST therefore two indistinguishable slip systems are expected to be active simultaneously due to the symmetry.

*Table 20: The orientation of the grains inside which the pillars of the neutron irradiated Fe-Mn-N annealed at 400°C were fabricated, the equivalent orientation on the standard stereographic triangle (SST) and the first two theoretically activated slip systems along with their Schmid factors and the angles between the planes of the slip system and the surface plane (denoted as angle ϕ).*

| Orientation | Equivalent SST orientation | Slip system | Schmid factor | Angle ϕ (°) |
|---|---|---|---|---|
| [2, 2, 5] | $[\bar{2},2,5]$ | ( 0, 1, 1)[ 1, $\bar{1}$, 1]<br>( 1, 0, 1) [$\bar{1}$, 1, 1] | 0.433 | 30 |
| | | ( 1, 2, 1) [ 1, $\bar{1}$, 1] | 0.393 | 38 |
| [6, 1, 13] | $[\bar{1},6,13]$ | ( 0, 1, 1)[ 1, $\bar{1}$, 1] | 0.499 | 46 |
| | | ( 0, $\bar{1}$, 1) [ 1, 1, 1] | 0.476 | 54 |
| [1, 0, 3] | [0,1,3] | ( 0, $\bar{1}$, 1)[ 1, 1, 1]<br>( 0, 1, 1) [ 1, $\bar{1}$, 1] | 0.490 | 48 |
| | | ($\bar{1}$, $\bar{1}$, 2) [ 1, 1, 1] | 0.471 | 50 |
| [10, 2, 11] | $[\bar{2},0,11]$ | ( 1, 2, 1)[ 1, $\bar{1}$, 1] | 0.498 | 47 |
| | | ( 0, 1, 1) [ 1, $\bar{1}$, 1] | 0.448 | 52 |

Multiple slip traces, mostly parallel to each other, were present in the majority of the pillars along with few slip steps. In Figure 149 – a, multiple slip traces are easily observed (white arrows) all over the surface of a $[\bar{2}, 2, 5]$ oriented pillar (along with two slip steps) and also, in the upper part of a $[\bar{2}, 0,11]$ oriented pillar, above the apparent slip step in Figure 149 – b.

Slip trace analysis matched the angle between the formed slip steps and the pillar surface, with the angle ϕ of the $[\bar{1}, 6,13]$ oriented pillar, confirming the EBSD estimated primary slip system. For the other orientations, the angles ϕ also matched the EBSD estimated angle, but it was not conclusive, since there was only a small difference between the angles of the primary and secondary systems (Table 20). Therefore, considering the significant difference in the values of the Schmid factors, we accepted the theoretically estimated primary slip systems.

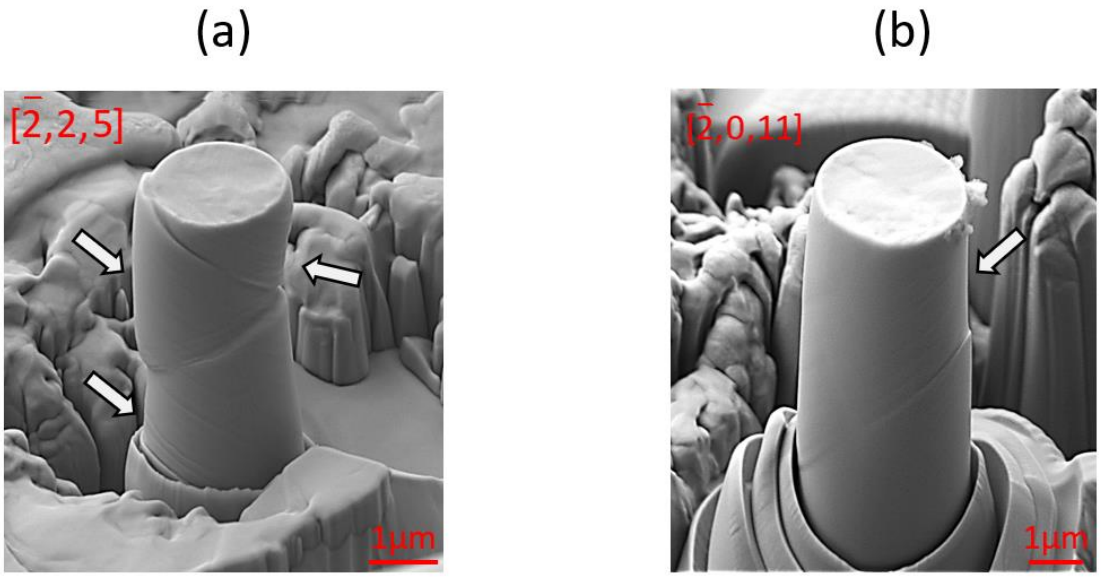


*Figure 149: Multiple slip traces, parallel to each other, are observed on the surface of (a) [ 2̄, 2, 5] and (b) [ 2̄, 0, 11] orientation pillars of the post-irradiation annealed at 400°C Fe-Mn-Ni. The white arrows are pointing to the multiple slip traces to facilitate their visualization.*

The Fe-Mn-Ni PIA, 30' at 400°C samples, presented smooth engineering stress-strain curves, some of which exhibited small load drops.

After studying the obtained engineering stress strain curves (Figure 150), the average resolved shear stress at 2% strain was calculated as (351 ± 86) MPa.

Comparing this value with the measured average critical resolved shear stress (at 2% strain) of the Fe-Mn-Ni unirradiated samples, we calculate the residual irradiation hardening after PIA as (159 ± 87) MPa.

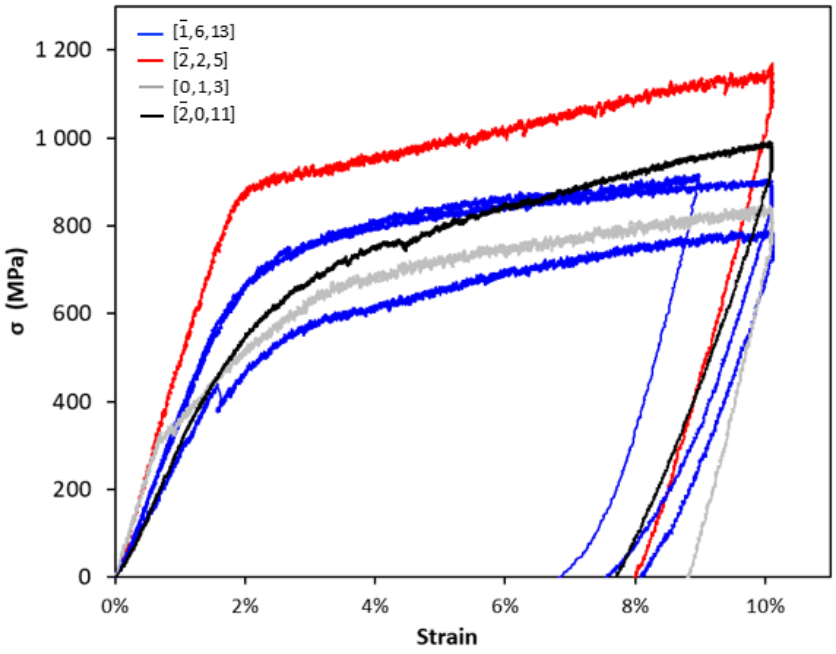


*Figure 150: Engineering stress - strain curves of post-irradiation annealed at 400°C Fe-Mn-Ni [ 1̄, 6, 13] , [ 2̄, 2, 5] , [ 0, 1, 3] and [ 2̄, 0, 11] oriented pillars.*

In summary, after in-situ micro-compression, slip events were apparent on the surface of both the non-irradiated and neutron irradiated pillars. Multiple slip traces were also observed particularly in the neutron irradiated pillars.

The engineering stress-strain curves were plotted and the stress at yield of 2% for the Fe-Ni and Fe-Mn-Ni samples and at 3% for the Fe-Mn was calculated. The Schmid factor of the activated slip system for each pillar was used to calculate the average resolved shear.

Irradiation hardening was determined as the difference of the average resolved shear stress of the irradiated and unirradiated state, for each material, is reported along with irradiation hardening (expressed also as the percentage increase) in Table 21.

*Table 21: Mean resolved shear stress of the Fe-Ni, Fe-Mn and Fe-Mn-Ni samples (including the post-irradiation annealed (30' at 400°C) Fe-Mn-Ni), calculated from the engineering stress-strain curves (at 2% of strain for the Fe-Ni and Fe-Mn-NI samples and at 3% for the Fe-Mn samples, incertitude is expressed by the standard deviation) and irradiation hardening values, also expressed as the percentage increase.*

| **Model alloy** | **$\langle\tau\rangle_{unirradiated}$ (MPa)** | **$\langle\tau\rangle_{irradiated}$ (MPa)** | **$\Delta\langle\tau\rangle$ (MPa)** | **Increase in τ (%)** |
|---|---|---|---|---|
| Fe-Mn | 230 ± 25 | 265 ± 40 | 35 ± 47 | 15% |
| Fe-Ni | 173 ± 42 | 243 ± 40 | 67 ± 57 | 39 % |
| Fe-Mn-Ni | 191 ± 15 | 371 ± 69 | 180 ± 71 | 104 % |
| Fe-Mn-Ni PIA 400°C | | 351 ± 86 | 159 ± 87 | 84 % |

## III. On the measured irradiation hardening

Dislocations in order to propagate inside the single crystal of the pillars, need to overcome the resistance of the lattice friction (Peierls – Nabarro stress), solid solution, dislocation forest (network) and other obstacles, as the solute clusters, if present.

Since all non-irradiated studied alloys did not contain any solute clusters and assuming that the density of the dislocations in all the samples was roughly the same, it was expected that the alloy containing the highest amount of solutes, that is the ternary Fe – Mn – Ni alloy (containing about 1.29 at. % Mn and 0.82 at. % Ni), consequently would exhibit the highest resistance (solid solution resistance) to dislocation motion.

However, the Fe – Mn (containing about 0.9 at. % Mn) alloy was the one which needed the highest average resolved shear stress for the same degree of plastic deformation.

Figure 151 illustrates two representative engineering stress-strain curves of each of the non-irradiated materials, where it is apparent that the Fe-Mn pillars needed higher stress for yielding. This also becomes evident, when comparing the measured mean resolved shear stress values for the three model alloys (Table 21).

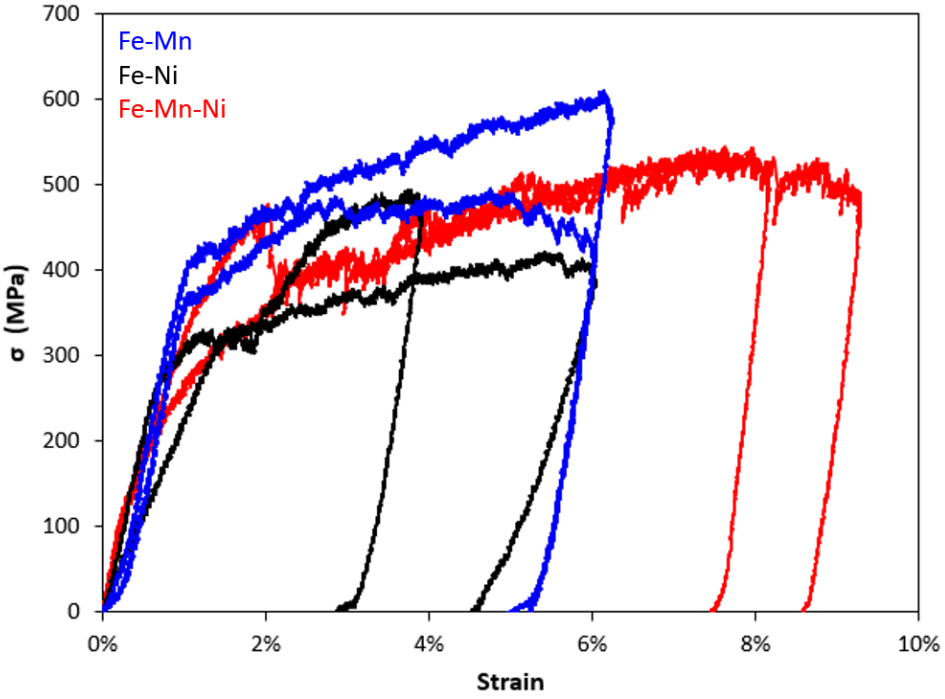


*Figure 151: Two engineering stress-strain curves of each unirradiated alloy; Fe-Mn-Ni in red, Fe-Ni in black and Fe-Mn in blue.*

The increase in the needed stress for yielding the Fe-Mn alloy, can be justified if, compared to the other two alloys, it contained a significantly higher dislocation density. Therefore, we assumed that the model alloys did not contain the same dislocation density, which was increased in the case of the Fe-Mn samples.

After neutron irradiation, solute clusters were present in all the studied model alloys, as evidenced by APT analysis.

Although their nanometric size, these clusters act as barrier to dislocation movement, elevating the stress needed to cause plastic deformation. This is evidenced by comparing the mechanical data of the irradiated with the non-irradiated model alloys. To suppress the crystal lattice orientation effect, the Schmid factor of the activated slip system of each pillar was used to calculate the resolved shear stress, which was plotted as a function of strain in Figure 152.

The highest percent increase (104%) in the resolved shear stress, after irradiation, was exhibited by the ternary alloy, which was irradiated at a higher dose (0.1 dpa) than the binary alloys. Between the binary alloys, both irradiated at 0.02 dpa, the resolved shear stress increased by 41% in the case of the Fe-Ni alloy, while only by 15% for the Fe-Mn which exhibited higher stress values.

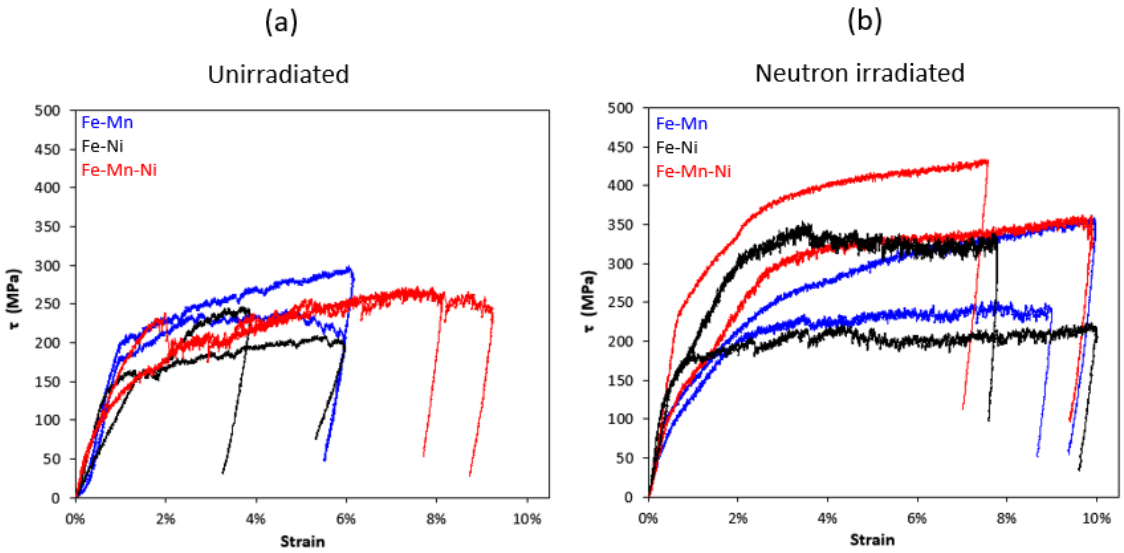


*Figure 152: Resolved shear stress as a function of strain of two compressed pillars of each (a) unirradiated and (b) neutron irradiated alloy; Fe-Mn-Ni in red, Fe-Ni in black and Fe-Mn in blue.*

The bulk mechanical properties of the binary alloys (Fe-Ni and Fe-Mn) in the non-irradiated and neutron irradiated states (at the same irradiation conditions as those of this study) were studied a decade ago by Kočík et al. [12] in the context of the PERFORM 60 project.

For the Fe-Ni alloy, the reported average micro-hardness (MHV0.1) results were 153.5 for the irradiated and 110.8 for the non-irradiated, giving a hardness change (ΔHv) of 42.7.

By applying the equation (1.21), which according to Busby et al [13] correlates the change in yield stress ($\sigma_Y$) and the change in hardness, the irradiation hardening is estimated to 131 MPa.

In the micro-compression experiments, the average stress (σ) measured values were 496 MPa and 352 MPa respectively, and thus the hardening due to irradiation is calculated at 144 MPa. Therefore, the results of the two methods, having a difference of about 9%, are in good agreement.

On the contrary, for the Fe-Mn alloy the reported micro-hardness change of ΔHv 71.8 corresponds to 200 MPa which is very different from the measured 117 MPa at the micro-compression tests. To our interpretation, the significant difference, for only the Fe-Mn, supports our hypothesis that particularly in the studied samples of this alloy, an increased dislocation density was present affecting the mechanical properties. Dislocation density definition using TEM, can be conclusive about this issue but such a study is not available yet.

## IV. On the effect of Sneddon correction

To accurately calculate the stress and the strain that the pillar subjected during compression, as mentioned in chapter 2, the correction proposed by Sneddon [1]was applied using equation (2.46).

$$\Delta L_{Pillar} = \Delta L_{Mes} - \Delta_{Sub} - \Delta L_{Tip} = \Delta L_{Mes} - \frac{\left(1-v_{Sub}^2\right)}{E_{Sub}} \cdot \frac{F_{mes}}{D_{Base}} - \frac{\left(1-v_{Tip}^2\right)}{E_{Tip}} \cdot \frac{F_{mes}}{D}$$

where $F_{mes}$ the measured force and $\Delta L_{Mes}$ the difference of the measured displacement by the instrument, $D$ and $D_{Base}$ the diameter of the pillar at top and at its base, respectively. $E_{Sub}$, $v_{Sub}$ represent the Young's modulus and Poisson's ratio of model alloy assumed to be 200 GPa and 0.3 respectively [14–17]. Also, $E_{Tip}$, $v_{Tip}$ represent the Young's modulus and Poisson's ratio of the diamond indenter's tip, considered to be 1050 GPa and 0.1 respectively [36–38].

The applied stress is not confined only inside the material of the pillar but a part of it, is distributed into the substrate bulk material, being at the region below the base of the pillar, causing a minimum of plastic deformation there as well. A lessen deformation also occurs to the indenter although the diamond flat punch has much higher strength. In literature several authors have applied this correction either considering only the displacement in the base of the pillar or in both base and indenter [21–24]. In this study, the Sneddon correction was applied for both the indenter and the base of the pillar.

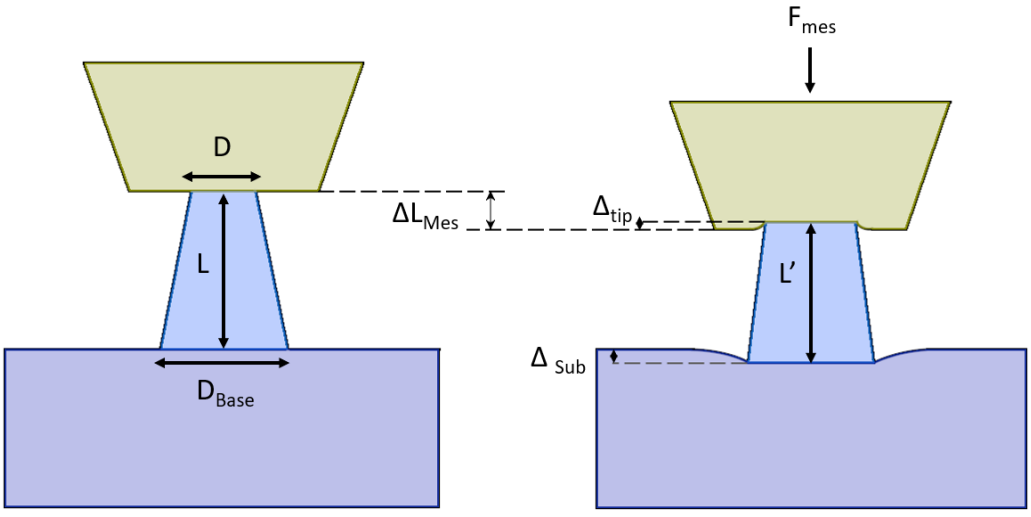


*Figure 153: Schematics of a pillar before and during uniaxial compression, illustrating the deformation at the indenter's tip ($\Delta_{Tip}$), substrate ($\Delta_{Sub}$) and the pillar ($\Delta L_{pillar}$ = L- L'). $F_{Mes}$ is the measured applied load. The indenter is illustrated in green, the pillar in blue and the substrate material in purple.*

When plastic deformation of the specimen occurs in a continuous and uniform manner, applying the equations for the true stress $\sigma_T$ and true strain $\varepsilon_T$, is appropriate for stress–strain

curve calculations. The engineering stress–strain values obtained from Equations (2.48) and (2.49) are related to the true stress–strain values by:

$$\sigma_T = \sigma(1+\varepsilon) \quad (4.1)$$

$$\varepsilon_T = \ln(1+\varepsilon) \quad (4.2)$$

However, in the performed in-situ micro-compression experiments, deformation often occurred inhomogeneously with slip steps that appeared early enough, causing major geometrical changes on the shape of the pillars, making these formulas inapplicable. As a consequence, we decided to use the engineering stress–strain values instead. In these calculations, the cross section of the pillar was estimated using the top diameter of the pillar, not only because it is easily obtained on the SEM images, and thus minimizing measurement errors, but also because deformation was localized, usually confined to the upper part of the pillar, therefore we considered more accurate to calculate the stress where deformation occur.

Nevertheless, the values of the measured stress at various strains in the plastic regime, with or without applying the Sneddon correction were almost identical, for all the studied samples either they were neutron irradiated or not. For example, the highest difference produced in the stress at 2% strain, was observed at a pillar of the Fe-Mn-Ni PIA at 400$^{o}$C material and it was only 2 MPa (743 MPa and 741 MPa before and after the Sneddon correction) while the second highest difference was 1 MPa, observed at a Fe-Mn irradiated pillar (481 MPa vs 482 MPa respectively).

While it appears that applying Sneddon's correction is not beneficial for stress-strain values, it is essential for calculating the elastic modulus. The measured Young's modulus was in average calculated decreased by 8% for the unirradiated and 13% for the irradiated alloys without considering the Sneddon's correction. This observation is in good agreement with Volkert and Lilleodden [22], who also reported negligible effect on the stress–strain curves but 30% decrease of the measured Young's modulus without Sneddon correction, while compressing Au FIB fabricated micropillars.

Having verified that in the plastic regime, the obtained values for the stress strain value pairs are merely insignificantly affected by applying the Sneddon correction, we did not attempt to more accurately define the Young's modulus of each of the studied materials. This is beyond of the scope of this study and would need additional experiments especially designed for this measurement since it can be affected of many parameters. For example, even the slight misalignment of micro-compression system, can significantly underestimate the calculated elastic modulus [21] , therefore experiments using multiple loading/unloading cycles, as suggested by Greer [23], are needed to ensure that the unloading data are indeed elastic. Using a similar procedure, Choi et al. performed six loading/unloading cycles and averaged the modulus values measured between the third to the sixth cycle and determined the stiffness performing a linear fit to the first 20% values of the unloading curve [25].

Additionally, the calculation of the elastic modulus is affected by factors as the taper angle [26], aspect ratio [25] of the pillars and the pillar orientation.

Moreover, in cubic single crystals, because they are not isotropic, lattice orientation affects significantly the theoretical Young's modulus, calculated using equation (4.3) [8].

$$\frac{1}{E_{hkl}} = S_{11} - 2\left[(S_{11} - S_{12}) - \frac{1}{2}S_{44}\right]\left(\alpha^2\beta^2 + \alpha^2\gamma^2 + \beta^2\gamma^2\right) \quad (4.3)$$

where $S_{ij}$ are components of the compliance tensor and α, β, and γ are the direction cosines of the [hkl] direction and the [100], [010], and [001] directions, respectively.

or using the equivalent equation [27], [28]:

$$\frac{1}{E_{hkl}} = S_{11} - 2\left[(S_{11} - S_{12}) - \frac{1}{2}S_{44}\right]\left[\frac{h^2k^2 + k^2l^2 + l^2h^2}{(h^2 + k^2 + l^2)^2}\right] \quad (4.4)$$

As for most cubic materials, in the case of α-Fe, the elasticity modulus measured along the <111> direction $E_{<111>}$ is larger than the $E_{<100>}$ (276 GPa vs 129 GPa respectively), representing the extreme values of the modulus [8].

Providing further details concerning how the Sneddon correction affected the measurements of the studied materials, we observed that the Young's modulus calculated, for example in a $[\bar{2}, 5, 12]$ Fe-Mn neutron irradiated pillar, using the unloading curve, was at about 125 GPa without Sneddon correction and with it at 137 GPa. Thus, giving a Young's modulus value increased by about 10% for that pillar. By averaging the differences of all the compressed pillars of this material the average difference becomes about 13%. Table 22 summarizes the resulting percent difference in the Young's modulus of each material after the calculation of the Sneddon correction.

*Table 22: The calculated percent difference in the Young's modulus of each model alloy after applying of the Sneddon correction in the non-Irradiated and irradiate state*

| Material | ΔE$_Y$ (%) Non-Irradiated | ΔE$_Y$ (%) Irradiated |
|---|---|---|
| **Fe-Ni** | 4.4 | 11.5 |
| **Fe-Mn** | 11.1 | 13.1 |
| **Fe-Mn-Ni** | 9.3 | 13.7 |

## V. On the observed load-drops

Stress strain curves of the non-irradiated samples of the studied ferritic model alloys in general presented small load drops.

We operated the intender at displacement-controlled mode at a constant strain rate (0.001 $s^{-1}$), but the indenter is intrinsically load-controlled. When a slip step is formed on the pillar surface, the deformation of the pillar is detected by the piezo loading/capacitive sensing system and the feedback loop properly adapts the force that the indenter applies on the pillar top. If the slip event evolves too rapidly, the feedback loop fails to compensate the strain rate and a load drop appears on the curve.

The stress strain curves of the studied α-Fe alloys, have a noticeably different shape than those observed when compressing austenitic-Fe [29], having fewer and less steep load drops (Figure 154).

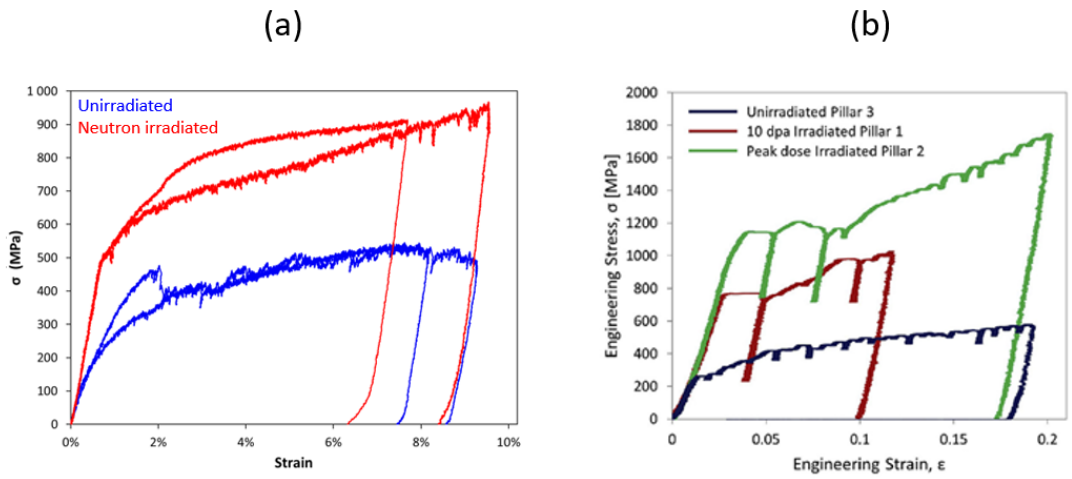


*Figure 154: Engineering stress strain curves of (a) unirradiated (in blue) and neutron irradiated (in red) pillars of the ternary alloy of this study and (b) unirradiated and ion irradiated austenitic pillars of [17]. The austenitic pillars present steep load drops compared to the BCC pillars.*

Contrary to the FCC metals, having dislocation motion restricted on a defined slip plane due to their planar core, the screw components of the BCC dislocations core extents to multiple planes. Thus, they can move on variable slip systems by cross-slip on any possible slip plane when gliding. The non-planar core of the BCC screw dislocations causes a significant increased lattice friction and subsequently the mobility of the BCC screw dislocations is slower and hence they stay longer inside the pillars before annihilating when reaching the pillar's surface. Therefore, the possibility of dislocation interaction considerably increases, which subsequently increases the formation of dislocation junctions that might operate as new dislocation sources. Consequently giving to the stress-strain curve a serrated shape resembling to work hardening with only few moderate load drops [30–32].

The neutron irradiated samples of this study produced curves with almost no load-drops. The nanometric irradiation induced clusters act as obstacles, impeding dislocation motion and inducing hardening. Due to the considerably increased stress needed for dislocation gliding while overcoming the obstacles, the shape of the curve becomes smoother without load drops.

Concerning the way that plastic deformation occurred in the studied model alloys, the following observation was made; the slip steps when are formed on the surface of the pillars, become gradually larger as the strain increases. Figure 155 shows sequential SEM images of a neutron irradiated Fe-Mn $[\bar{2}, 5, 12]$ oriented compressed pillar, correlated with the pillar's stress – strain curve. The slip step starts appearing at about 4 % of strain and it is clearly visible at the third frame corresponding to 6.8% strain, while multiple almost parallel slip traces are forming on the surface as well.

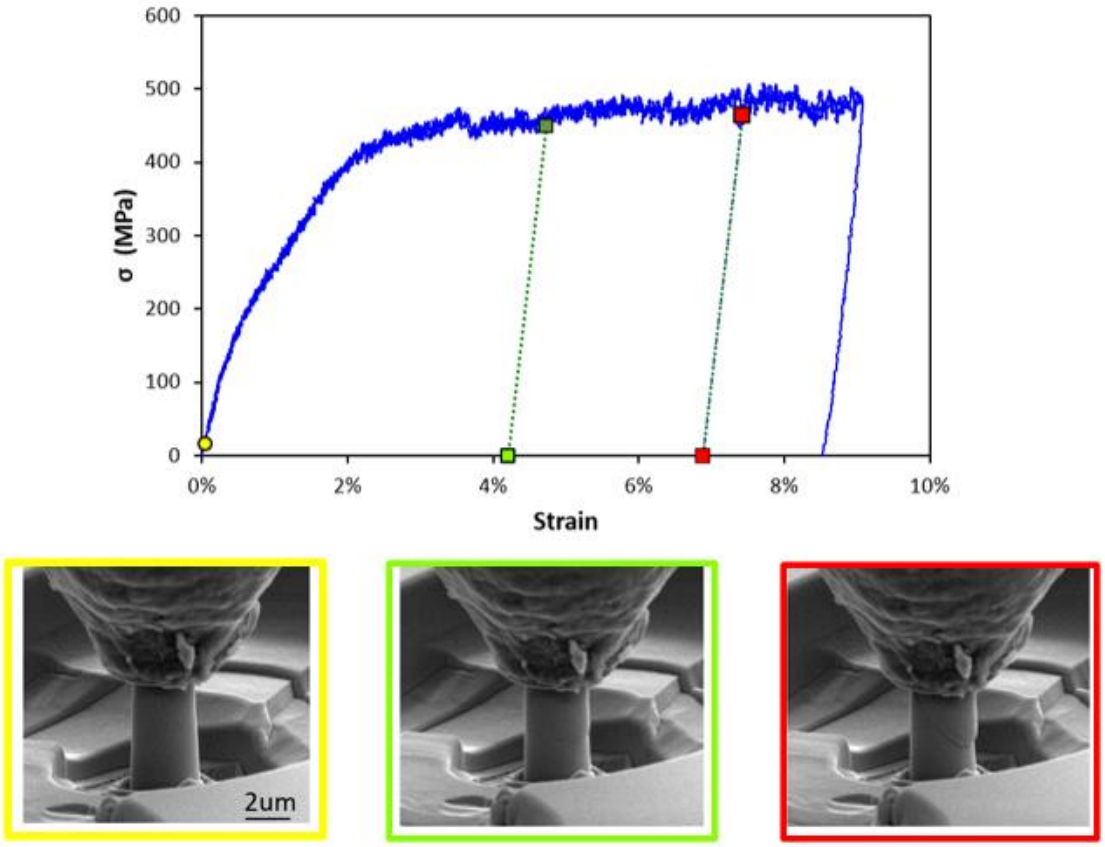


*Figure 155: Sequential SEM images of the compression of a neutron irradiated Fe-Mn pillar. A slip step starts appearing at about 4%, it is clearly visible at the third frame corresponding to 6.8% strain.*

Instead, in FCC metals [3], [29] large slip steps are formed suddenly, and steep load drops appear on the stress – strain curve. This implies that dislocations manage to eliminate the irradiation defects along a specific path, thus forming defect-free channels where additional dislocations can easily glide.

This behavior wasn't observed to any of the alloys of our study, suggesting that no dislocation channeling occurred while compressing these ferritic alloys.

## VI. Investigation of sample size effect

In metals, dislocation density ($\rho_d$) typically varies from $10^{12}$ $m^{-2}$ for the well annealed up to about $10^{15}$ $m^{-2}$ for the heavy cold rolled ones. The average distance between neighboring dislocations is $l_d = 1/\sqrt{\rho_d}$ [4], which becomes of the order of 1 μm, at the lowest dislocation density. Pillars with diameter of about 1 μm or less, might contain only a very limited number of small segments of the initial dislocation structure, meaning that higher stress is necessary for deformation to occur, thus significant size effect will be present.

For the assumed dislocation density for the model alloys ($5x10^{13}$ $m^{-2}$) the average dislocations distance becomes smaller (about 0.14 μm), therefore it was estimated that in combination with the increased nominal diameter of the fabricated pillars (3 μm), enough dislocations will be present, and deformation will occur in the bulk like regime, avoiding extensive size effects.

Nevertheless, the average yield stress of the commercial pure iron is about 200 MPa [33] which is around the half of the average measured stress values for the non-irradiated samples, that specifically are 474 MPa for the Fe-Mn, 352 MPa for the Fe-Ni and 386 MPa for the Fe-Mn-Ni. This implies the existence of sample size effect, phenomenon that increased the stress needed for yielding.

To verify the existence and observe the size effect, in the irradiated Fe-Mn sample, a smaller pillar with about half the diameter of our pillars, that is 1.5 μm, was FIB-fabricated and compressed. In Figure 156 – a the stress strain curve is plotted along with the curves of three pillars with the standard diameter, having the same crystal orientation $[\bar{3}, 4, 10]$ as the smaller pillar and in Figure 156 – b with a pillar with the different orientation $[\bar{12}, 2, \bar{5}]$. Obviously, the size effect was significantly increased with the decrease in the dimensions of the pillar, almost doubling the needed stress.

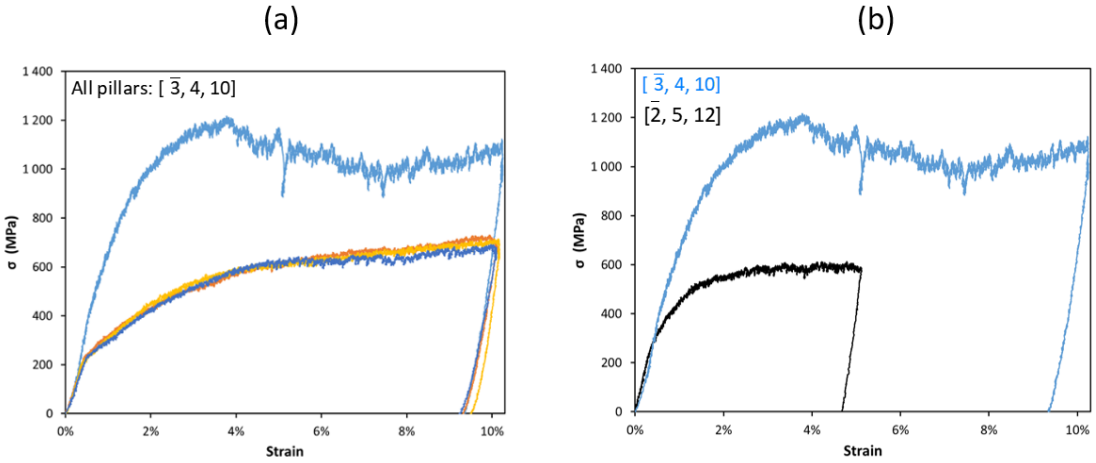


*Figure 156: Engineering stress-strain curves of Fe-Mn pillars of (a) only $[\bar{3}, 4, 10]$ orientation and (b) $[\bar{3}, 4, 10]$ and $[\bar{2}, 5, 12]$ orientation, where the light blue stress-strain curve corresponds to a pillar of smaller dimensions.*

From the available bibliographic and experimental data, we cannot conclude if the size effect has the same extent, in both the non-irradiated and irradiated state pillars, that is depending only on the experimentally controllable variables such as the size and crystal orientation of the pillars. On the contrary, judging from the dispersion (as expressed by the standard deviation values) between the calculated resolved shear stress values, the magnitude of the acting size effect appears to be rather stochastic, as expected if additional factors affect it, such as for example, the initial local dislocation density inside the pillar volume and maybe the Ga ion irradiation damage on the surface of the pillar.

## Summary

In-situ micro-compression experiments, on FIB-fabricated single crystal pillars, having diameter about 3 μm, were performed to study the mechanical properties of the three model alloys, at the unirradiated and neutron irradiated states. Additional experiments were performed on the Fe-Mn-Ni alloy after isochronal (30') post-irradiation annealing at 400 $^{o}$C.

Instead of using the classical criterion of yield strength determination at 0.2% of strain, it was approximated at a higher strain (2% and 3% in this study) due to early plasticity, inevitable in micro-compression testing. Furthermore, we explained the necessity of using the slope of the unloading curve for determining the Young Modulus, instead of the typically used, initial linear elastic segment of the curve.

Details were provided concerning, the selected grain orientations for pillar fabrication, the identification of the activated primary slip system, the slip steps observed on the pillars surface after compression and the measured average resolved shear stress for Fe-Mn-Ni and Fe-Ni alloys (at 2% strain) and for Fe-Mn (at 3% strain). The average irradiation hardening was estimated for the Fe-Mn alloy as (35 ± 47) MPa, for the Fe-Ni (70 ± 57) MPa and for the Fe-Mn-Ni (180 ± 110) MPa which was reduced to (159 ± 87) MPa after post-irradiation annealing at 400$^{o}$C.

Further, it was discussed that the application of the Sneddon's correction had negligible effect on the stress–strain values of the plastic regime but affected the calculation of the Young's modulus.

Studying the stress-strain curves, although the diameter of the pillars was more than one-micron, elevated stress was needed for yielding which evidenced the presence of sample size effect.

Additionally, only few small load drops were observed on the stress-strain curves, which in combination with the progressive formation of the slip steps on the surface of the pillars, rule out dislocation channeling, that is reported to occur to the FCC iron alloys.

In the next chapter, the measured change in the mechanical properties and the observed irradiation induced microstructure are correlated, using two theoretical models evaluating the ability of the solute clusters to hinder the motion of the dislocations during the plastic deformation of the model alloys.

# Bibliography


[1] I. N. Sneddon, “The relaxation between load and penetration in the axisymmetric boussinedq problem for a punch of arbitrary profile,” *Int. J. Engng Sci.*, vol. Vol. 3, pp. 47–57, 1965.

[2] E. Lilleodden, “Microcompression study of Mg (0001) single crystal,” *Scr. Mater.*, vol. 62, no. 8, pp. 532–535, Apr. 2010, doi: 10.1016/j.scriptamat.2009.12.048.

[3] H. Yilmaz, “Mechanical Properties of BCC Nanopillars,” University of Manchester, 2018.

[4] D. Hull and D. J. Bacon, *Introduction to dislocations*, 5. ed. Amsterdam Heidelberg: Butterworth Heinemann, Elsevier, 2011.

[5] S. I. Rao *et al.*, “Large-scale dislocation dynamics simulations of strain hardening of Ni microcrystals under tensile loading,” *Acta Mater.*, vol. 164, pp. 171–183, Feb. 2019, doi: 10.1016/j.actamat.2018.10.047.

[6] Z.-W. Zhang, Z. Li, Y. Liu, and J.-T. Wang, “Path Dependency of Plastic Deformation in Crystals: Work Hardening, Crystallographic Rotation and Dislocation Structure Evolution,” *Crystals*, vol. 12, no. 7, p. 999, Jul. 2022, doi: 10.3390/cryst12070999.

[7] A. S. Argon, “MECHANICAL PROPERTIES OF SINGLE-PHASE CRYSTALLINE MEDIA: DEFORMATION AT LOW TEMPERATURES,” in *Physical Metallurgy*, Elsevier, 1996, pp. 1877–1955. doi: 10.1016/B978-044489875-3/50026-0.

[8] T. H. Courtney, *Mechanical behavior of materials*, 2. ed. Long Grove, Illinois: Waveland Press, 2005.

[9] T. W. Clyne and J. E. Campbell, *Testing of the Plastic Deformation of Metals*, 1st ed. Cambridge University Press, 2021. doi: 10.1017/9781108943369.

[10] “Deformation of a single crystal.” https://www.doitpoms.ac.uk/tlplib/work_harden/single_crystal.php (accessed Jan. 25, 2023).

[11] H. K. D. H. Bhadeshia, *Geometry of Crystals, Polycrystals, and Phase Transformations*, 1st ed. CRC Press, 2017. doi: 10.1201/9781315114910.

[12] “Prediction of the effects of Radiation for reactor pressure vessel and in-core components using multi-scale modelling - 60 years’ foreseen plant lifetime,” PERFORM 60 FP7 project, Jun. 2012.

[13] J. T. Busby, M. C. Hash, and G. S. Was, “The relationship between hardness and yield stress in irradiated austenitic and ferritic steels,” *J. Nucl. Mater.*, vol. 336, no. 2–3, pp. 267–278, Feb. 2005, doi: 10.1016/j.jnucmat.2004.09.024.

[14] “Properties: An Introduction to Iron,” *AZoM.com*. https://www.azom.com/properties.aspx?ArticleID=619 (accessed Aug. 31, 2022).

[15] “Modulus of Elasticity Young’s Modulus Strength for Metals - Iron and Steel.” https://www.engineersedge.com/manufacturing_spec/properties_of_metals_strength.htm (accessed Aug. 31, 2022).

[16] “Ferrous metals elastic modulus and Poisson ratio | Sonelastic®.” https://www.sonelastic.com/en/fundamentals/tables-of-materials-properties/ferrous-metals.html (accessed Aug. 31, 2022).

[17] admin, “Young’s modulus of several materials • pickedshares,” *pickedshares*, Jun. 02, 2021. https://pickedshares.com/en/youngs-modulus-of-several-materials/ (accessed Aug. 31, 2022).

[18] E. Borchi, M. Bruzzi, U. Biggeri, C. Furetta, and F. Lemeilleur, “ELASTIC MODULI OF POLYCRYSTALLINE DIAMOND,” p. 15.

[19] C. A. Klein and G. F. Cardinale, “Young’s modulus and Poisson’s ratio of CVD diamond,” p. 6.

[20] “Properties: Diamond (C) - Properties and Applications,” *AZoM.com*. https://www.azom.com/properties.aspx?ArticleID=262 (accessed Aug. 01, 2022).

[21] H. Zhang, B. E. Schuster, Q. Wei, and K. T. Ramesh, “The design of accurate micro-compression experiments,” *Scr. Mater.*, vol. 54, no. 2, Art. no. 2, Jan. 2006, doi: 10.1016/j.scriptamat.2005.06.043.

[22] C. A. Volkert and E. T. Lilleodden, “Size effects in the deformation of sub-micron Au columns,” *Philos. Mag.*, vol. 86, no. 33–35, Art. no. 33–35, Nov. 2006, doi: 10.1080/14786430600567739.

[23] J. R. Greer, W. C. Oliver, and W. D. Nix, “Size dependence of mechanical properties of gold at the micron scale in the absence of strain gradients,” *Acta Mater.*, vol. 53, no. 6, Art. no. 6, Apr. 2005, doi: 10.1016/j.actamat.2004.12.031.

[24] C. P. Frick, B. G. Clark, S. Orso, A. S. Schneider, and E. Arzt, “Size effect on strength and strain hardening of small-scale [111] nickel compression pillars,” *Mater. Sci. Eng. A*, vol. 489, no. 1–2, pp. 319–329, Aug. 2008, doi: 10.1016/j.msea.2007.12.038.

[25] I. Choi, Y. Gan, D. Kaufmann, O. Kraft, and R. Schwaiger, “Measurement of Young’s modulus of anisotropic materials using microcompression testing,” *J. Mater. Res.*, vol. 27, no. 21, pp. 2752–2759, Nov. 2012, doi: 10.1557/jmr.2012.18.

[26] L. Zábranský *et al.*, “The Effect of a Taper Angle on Micro-Compression Testing of Mo-B-C Coatings,” *Materials*, vol. 13, no. 14, Art. no. 14, Jul. 2020, doi: 10.3390/ma13143054.

[27] M. Rabiei *et al.*, “Measurement Modulus of Elasticity Related to the Atomic Density of Planes in Unit Cell of Crystal Lattices,” *Materials*, vol. 13, no. 19, p. 4380, Oct. 2020, doi: 10.3390/ma13194380.

[28] J.-M. Zhang, Y. Zhang, K.-W. Xu, and V. Ji, “Young’s modulus surface and Poisson’s ratio curve for cubic metals,” *J. Phys. Chem. Solids*, vol. 68, no. 4, pp. 503–510, Apr. 2007, doi: 10.1016/j.jpcs.2007.01.025.

[29] A. Reichardt *et al.*, “Nanoindentation and in situ microcompression in different dose regimes of proton beam irradiated 304 SS,” *J. Nucl. Mater.*, vol. 486, pp. 323–331, Apr. 2017, doi: 10.1016/j.jnucmat.2017.01.036.

[30] J. P. Hirth and J. Lothe, *Theory of dislocations*, 2nd ed. Malabar, FL: Krieger Pub. Co, 1992.

[31] J.-Y. Kim, D. Jang, and J. R. Greer, “Tensile and compressive behavior of tungsten, molybdenum, tantalum and niobium at the nanoscale,” *Acta Mater.*, vol. 58, no. 7, Art. no. 7, Apr. 2010, doi: 10.1016/j.actamat.2009.12.022.

[32] R. Gröger, A. G. Bailey, and V. Vitek, “Multiscale modeling of plastic deformation of molybdenum and tungsten- I. Atomistic st,” *Mater. Sci. Forum*, vol. 482.

[33] E. Lucon, K. Abiko, M. Lambrecht, and B. Rehmer, “Tensile Properties of Commercially Pure, High Purity and Ultra High Purity Iron: Results of an International Round-Robin,” National Institute of Standards and Technology, NIST TN 1879, Apr. 2015. doi: 10.6028/NIST.TN.1879.

# Chapter 5: Microstructure and mechanical properties correlation

## Introduction

APT experiments detailed in chapter 3, revealed that nanosized clusters were generated during neutron irradiation, in the three studied model alloys. This microstructural change is manifested in the change of their mechanical properties, studied in chapter 4. This final chapter aims to correlate the measured irradiation hardening with the observed microstructure.

Theoretical models predicting the mechanical response based on the microstructural data, obtained using atom probe tomography analysis, are widely used in material science especially when studying alloys for nuclear applications. In this study, the obstacle strength of the irradiation induced clusters detected in the ferritic model alloys, is fitted so that the measured irradiation hardening matches the predicted, by such models.

Further, from the engineering stress-strain curves of the non-irradiated and neutron irradiated state, the increase in the energy dissipated during the micro-compression tests is derived and the average contribution of each cluster is calculated. Eventually, the resistance of the clusters to dislocation motion, expressed by the obstacle strength suggested from the theoretical models, is discussed in conjunction with the calculated energy needed to overcome each cluster.

Additionally in this chapter, the microstructure of the model alloys before and after deformation is investigated to estimate changes due to the imposed compression. Non-compressed and in-situ compressed micro-pillars were lifted out, shaped into TEM lamellas and APT tips and analyzed to evaluate the way of deformation of the 3 μm ferritic micro-pillars, estimate the dislocation density and quantify the characteristics of irradiation induced clusters, after compression at about 10% strain.

## I. Estimation of the obstacle strength of the clusters identified in the three ferritic model alloys

All the three studied model alloys experienced irradiation-induced changes to their microstructures, with the APT observed solute clustering been the most prominent. The microstructural alterations were manifested by the measured changes in the mechanical properties of the model alloys, during the in-situ micro-compression tests. To correlate the characteristics of the developed solute clusters (as the chemical nature, number density and size) with the measured irradiation hardening, estimating the ability of each cluster to hinder the motion of dislocations, the obstacle strength was determined using two relatively recent published theoretical models.

Namely, the Bacon-Kocks-Scattergood (BKS) model [1] as modified and published in 2018 by Monnet [2], [3] and a microstructure-based strength calculation model published in 2017 by Chauhan et al. [4]. In both models, the APT quantified characteristics of the detected solute clusters are used. The former predicts the irradiation hardening, calculating the increase in the critical resolved shear stress and estimates the ability of the obstacles to hinder dislocation movement using the specific resistance stress of the obstacles ($\Omega_{obs}$), acting as a friction stress only inside the precipitate. The latter model predicts the theoretical yield stress ($\sigma_Y$), estimating the obstacle strength ($\alpha_p$) of the clusters.

### 1. Estimation of the obstacle strength of the three model alloys using the Bacon-Kocks-Scattergood model

For the RPV steels, according to Monnet [2] the irradiation hardening can be estimated using equation (5.1), assuming that the matrix damage contribution is negligible compared to that of the solute clusters, for the not elevated fluences that the samples of this study were irradiated.

$$\Delta\sigma = \mathrm{M}\left(\sqrt{\tau^2_{forest} + \tau^2_{SC} + \tau^2_{carbide}} - \sqrt{\tau^2_{forest} + \tau^2_{carbide}}\right) \tag{5.1}$$

where M is the Taylor factor, that accounts for averaging of the grain orientations over all grains in polycrystal samples, and $\tau_{forest}$, $\tau_{sc}$ and $\tau_{carbide}$ the contributions to the shear stress of the dislocation forest, solute clusters and carbides respectively.

The micro-compression testing was performed on single crystal pillars, fabricated in model alloys that did not contain any carbides and thus the previous equation can be simplified to express the increase of the critical resolved shear stress as:

$$\Delta\tau = \sqrt{\tau^2_{forest} + \tau^2_{SC}} - \tau_{forest} \tag{5.2}$$

To estimate the contribution of the dislocation forest ($\tau_{forest}$) the Taylor equation was used (Eq (1.10))

$$\tau = \alpha_{forest} G b \sqrt{\rho_d} \tag{1.10}$$

with Taylor coefficient ($\alpha_{forest}$) equal with 0.27 [5] and ($\rho_d$) the suggested in the literature [6, 7] for the model alloys, dislocation density of around 5 x$10^{13}$ $m^{-2}$.

The same value of dislocation density was used for all the model alloys except for the Fe-Mn. For the Fe-Mn samples, it was assumed that the unexpectedly higher stress values needed for yielding, were due to a higher content of forest dislocations (chapter 4) and thus, a dislocation density of $10^{14}$ $m^{-2}$ was arbitrarily attributed only for the Fe-Mn alloy.

The contribution of the solute clusters was calculated according to the Bacon-Kocks-Scattergood (BKS) model, as modified by Monnet [2], using the number density and diameter of the clusters as obtained from APT analysis.

The specific resistance stress of the obstacles ($\Omega_{obs}$) was derived from equation (1.16), by adjusting its value, so that the calculated resolved shear stress fits in good agreement with that of the measured at the micro compression tests.

$$\tau_{obs} = \left( \frac{\Omega_{obs}}{\Omega_{\infty}} \frac{\ln(2\bar{D}/b)}{\ln(l/b)} \right)^{3/2} \frac{\ln(l/b)}{2\pi} Gb\sqrt{N_D D} \qquad (1.16)$$

The results are illustrated in the Figure 157 and suggest that although the Fe-Mn alloy developed the highest number density of clusters (14 ± 1) x$10^{23}$ $m^{-3}$, dislocations can pass relatively easily through these obstacles, since the specific stress resistance ($\Omega_{obs}$), indicated from the BKS model, was equal to 1.45, that is the lowest among the model alloys. On the other hand, for the clusters in Fe-Ni and Fe-Mn-Ni alloys, the indicated $\Omega_{obs}$ value was 3.40 significantly elevated compared to the $\Omega_{obs}$ of the Fe-Mn.

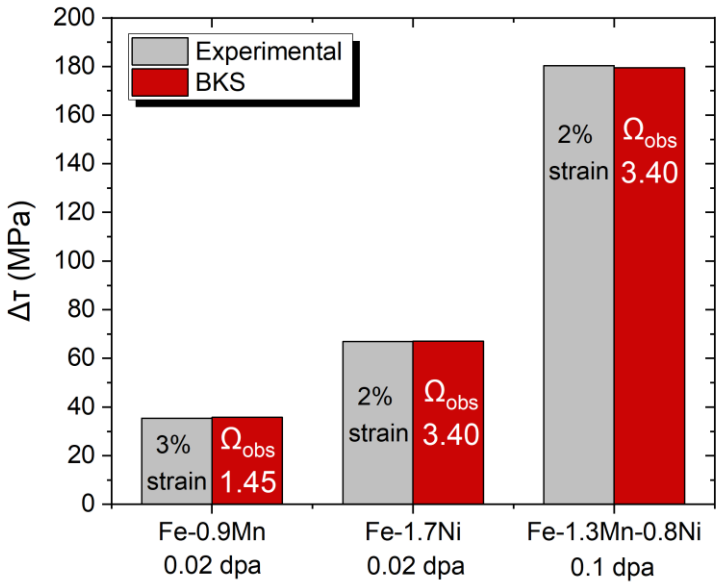


*Figure 157: The experimentally calculated irradiation hardening for each model alloy (in grey) is fitted in good agreement with the irradiation hardening predicted by the modified BKS model (in red). The fitted obstacle resistance is indicated on the graph, for each model alloy.*

It is important to specify that, the calculated $\Omega_{obs}$ values from the BKS model are not considered to be the exact values finally defining the stress resistance of the irradiation induced clusters at the 3μm scale, due to the two made assumptions. Namely, that the matrix damage contribution was considered as negligible, and also, the exact dislocation density in each alloy is unknown and hence the value used was the one retrieved from literature. Additionally, the irradiation hardening is not directly comparable between the alloys, since as mentioned, they were not exposed to the same neutron irradiation dose and thus the obtained values do not correspond to the same irradiation conditions.

Nevertheless, we consider that the $\Omega_{obs}$ values are representative of the resistance of the clusters, thus suitable to make accurate comparisons between the alloys.

Therefore, to our interpretation, the obtained specific resistance values, suggest that the presence of Ni in the solute clusters leads to an enhanced resistance to dislocation motion, while the Mn produces clusters, that cannot effectively hinder the motion of the dislocations which pass through them relatively easily and hence the Mn enriched clusters, mainly contribute to irradiation hardening due to their highly increased number density.

## 2. Estimation of the obstacle strength of the three model alloys using a microstructure-based strength calculation model

A microstructure-based strength calculation model published by Chauhan et al. [4] was also used to estimate the obstacle strength ($\alpha_p$) of the observed clusters, by fitting its value so that the calculated theoretical yield stress ($\sigma_Y$) to be in good agreement with the experimentally measured stress values.

This model considers the strengthening contributions of the lattice friction or Peierls-Nabarro stress ($\sigma_0$), the solid solution strengthening ($\sigma_s$), the dislocation forest strengthening ($\sigma_d$) and the particle strengthening ($\sigma_p$), while in our case the Hall-Petch strengthening ($\sigma_g$) was omitted since the pillars of this study were single crystals.

In more details, the model considers the lattice friction or Peierls-Nabarro stress ($\sigma_0$) required to move a dislocation through the perfect lattice of the iron as 53.9 MPa.

The solid solution strengthening ($\sigma_s$) is calculated using the suggested by Lacy and Gensamer [4] equation :

$$\sigma_s = 0.00689\, k\, X^n \tag{5.3}$$

where X is the atomic percent concentration of substitutional elements, n = 0.75 for all elements, and k is a strengthening coefficient of the elements, also provided by Lacy and Gensamer.

The dislocation forest strengthening ($\sigma_d$) is calculated by the Bailey-Hirsch relationship as:

$$\sigma_d = \alpha_d M G b \sqrt{\rho_d} \tag{5.4}$$

where $\alpha_d$ is a coefficient for the interaction with forest dislocations (used as equal to 0.33 according to the authors), M is the Taylor factor equal to 3.06 for polycrystalline BCC metals and $\rho_d$ is the dislocation density.

For the particle strengthening ($\sigma_p$), the authors use the equation based on dispersed barrier hardening (discussed in chapter 1) after the original formulation of Seeger as:

$$\sigma_p = \alpha_p M G b \sqrt{N_p d_p} \quad (5.5)$$

where $\alpha_p$ is the obstacle strength, $N_p$ is the number density of solute clusters and $d_p$ is their average diameter.

For the studied alloys, to calculate the theoretical yield stress ($\sigma_Y$) the mentioned strengthening contributions are combined in the equation:

$$\sigma_Y = \sigma_0 + \sigma_s + \sqrt{\sigma_d^2 + \sigma_p^2} \quad (5.6)$$

The data derived from APT analysis of each tip of the neutron irradiated model alloys were used for the calculations of this model. Specifically, the atomic percent content in Si, Mn, Ni and Cr and the number density and diameter of the solute clusters, were used.

The dislocation density used was the same as in the modified BKS model, that is 5 x$10^{13}$ $m^{-2}$ for the Fe-Ni and Fe-Mn-Ni alloys and the elevated density of $10^{14}$ $m^{-2}$ for the Fe-Mn alloy.

The obtained values for the obstacle strength of the irradiated alloys are $\alpha_{p\text{-}Mn}$ = 0.15 for the Fe-Mn, $\alpha_{p\text{-}Ni}$= 0.25 for the Fe-Mn-Ni and $\alpha_{p\text{-}Mn\text{-}Ni}$= 0.3 for Fe-Ni alloy.

Therefore, this model (in agreement with the BKS model) also suggests that the 'softer' clusters were those formed in the Fe-Mn alloy while when Ni was contained, the clusters became significantly 'harder', as the model suggested for the Fe-Mn-Ni and Fe-Ni model alloys.

## II. Estimation of the dissipated energy during pillar deformation

After establishing that the clusters developed in each model alloy, presented a different resistance to dislocation motion depending on their composition (that is their Ni and/or Mn content), the energy dissipated by the dislocations for overcoming the resistance of the solute clusters during the plastic deformation of the micropillars, was studied.

The energy transferred from the indenter to the pillar up to a certain degree of strain (that is the same strain used for defining the hardening, either 2% for Fe-Ni and Fe-Mn-Ni or 3% for Fe-Mn) was calculated as the integrated area under the stress-strain curve (as marked in Figure 158) multiplied with the pillar volume [8], since this integrated area is the energy needed for plastic deformation of the material per unit of volume.

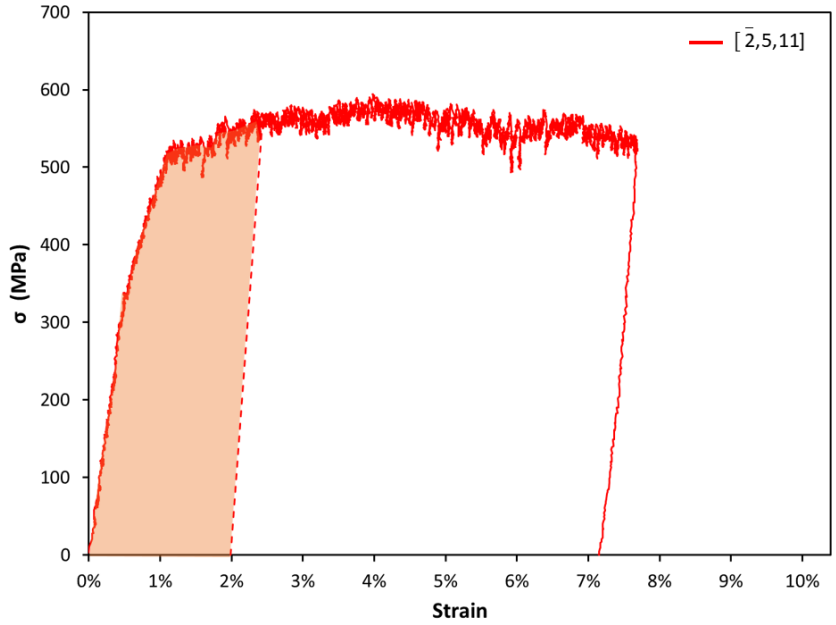


*Figure 158: Engineering stress-strain curve of a $[\bar{2},5,11]$ oriented pillar of the neutron irradiated Fe-Ni alloy, where the highlighted area under the curve up to 2% strain was used for the calculations of the dissipated energy.*

The Table 23 summarizes, the average values calculated for each material in the non-irradiated and neutron irradiated states. Specifically, the volume of the pillars was calculated taking into account the taper as well, and the error for the average energy needed, is expressed by the standard deviation.

*Table 23: Average values of the pillar volume, the area under the curve (up to 2% strain for Fe-Ni and Fe-Mn-Ni alloys and up to 3% strain for the Fe-Mn alloy), and the calculated dissipated energy per cubic meter to cause an 1% increase in strain (from 2% to 3% strain for Fe-Ni and Fe-Mn-Ni, and from 3% to 4% strain for Fe-Mn), in the unirradiated and neutron irradiated states.*

| Material | State | <Pillar Volume> ($\mu m^3$) | <Area under Curve> (MPa) | <Energy per $m^3$> for 1% Δ (strain) (MPa) |
|---|---|---|---|---|
| **Fe-Mn** | Non-Irradiated | 146 ± 2 | 11.8 ± 0.9 | 4.8 ± 0.5 |
| | Irradiated | 145 ± 32 | 12.1 ± 1.8 | 5.7 ± 0.9 |
| **Fe-Ni** | Non-Irradiated | 143 ± 12 | 5.2 ± 1.1 | 3.4 ± 0.7 |
| | Irradiated | 92 ± 39 | 7.5 ± 1.2 | 5.1 ± 0.7 |
| **Fe-Mn-Ni** | Non-Irradiated | 153 ± 17 | 5.9 ± 0.8 | 3.9 ± 0.2 |
| | Irradiated | 195 ± 90 | 10.4 ± 1.8 | 7.9 ± 1.4 |

Considering that the shape of the initial part of the stress-strain curve is not usually linear, due to the probable misalignment of the compression system, it does not represent exactly the elastic deformation and therefore is inducing an error in calculating the energy dissipated for the elastic deformation of the material.

To avoid this error, the energy per cubic meter, corresponding to 1% of deformation was calculated as the area beneath the curve from 2% to 3% strain for Fe-Ni and Fe-Mn-Ni, and from 3% to 4% strain for Fe-Mn (Figure 159).

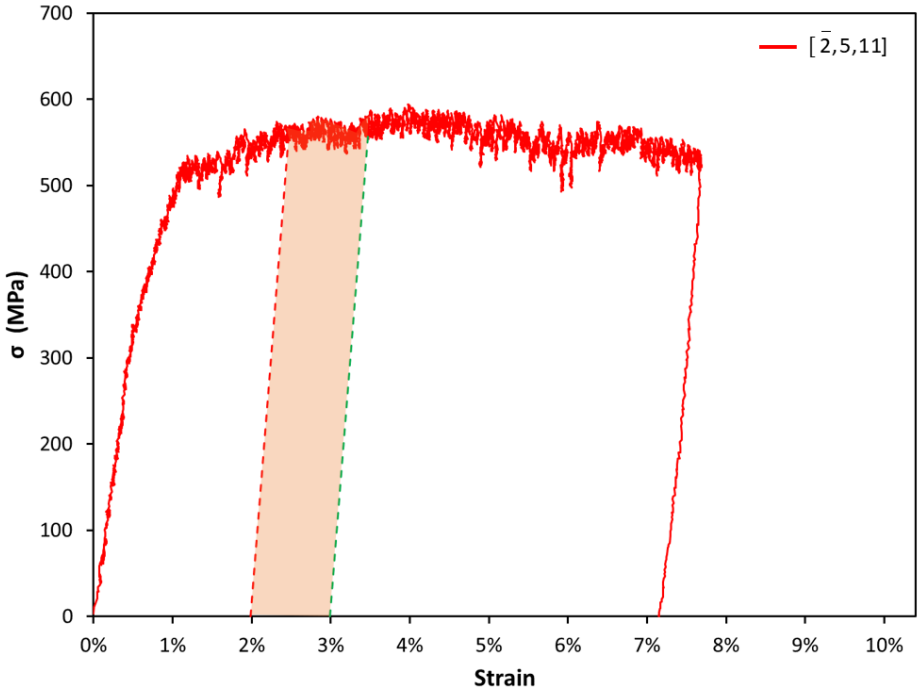


*Figure 159: Engineering stress-strain curve of a [2̄,5,11] oriented pillar of the neutron irradiated Fe-Ni alloy, where the highlighted area under the curve corresponds to the dissipated energy for an 1% increase in strain (from 2% to 3% strain).*

Assuming that the increase in the needed energy after neutron irradiation is mainly dissipated by dislocations to overcome the formed clusters, then the average dissipated energy per cluster for each material was estimated.

Table 24 reports the increase in needed energy per cubic meter to cause an additional 1% strain (from the strain that the irradiation hardening was calculated) as well as the average increase in the dissipated energy per cluster for each material, after neutron irradiation.

The uncertainty for the increase in the energy was calculated as the quadrature sum of the uncertainties of the irradiated and non-irradiated energy distributions, while the uncertainty for the per cluster increase in energy, was calculated using the quadrature sum of the uncertainties of the increase in the energy and of the number density.

*Table 24: Number density of the irradiation induced clusters and the calculated increase in the energy dissipated after neutron irradiation per cubic meter and per cluster, to cause an additional 1% strain (from 2% to 3% strain for Fe-Ni and Fe-Mn-Ni, and from 3% to 4% strain for Fe-Mn).*

| Model alloy | ND ($m^{-3}$) | For 1% increase of the strain | |
|---|---|---|---|
| | | Δ <Energy> /$m^3$ (J) | ΔE/cluster (J) |
| **Fe-Mn** | $1.4 \times 10^{24} \pm 1.0 \times 10^{23}$ | $0.9 \times 10^{6} \pm 1.1 \times 10^{6}$ | $6.7 \times 10^{-19} \pm 7.7 \times 10^{-19}$ |
| **Fe-Ni** | $1.5 \times 10^{23} \pm 4.0 \times 10^{22}$ | $1.7 \times 10^{6} \pm 1.0 \times 10^{6}$ | $1.1 \times 10^{-17} \pm 0.7 \times 10^{-17}$ |
| **Fe-Mn-Ni** | $6.2 \times 10^{23} \pm 8.0 \times 10^{22}$ | $4.0 \times 10^{6} \pm 1.4 \times 10^{6}$ | $6.5 \times 10^{-18} \pm 2.5 \times 10^{-18}$ |

By studying the reported values in Table 24 it is evident that, at the scale of 3 μm, dislocations need the highest amount of energy to overcome the resistance of each cluster in the Fe-Ni alloy, while about half of this energy (58%) is needed for overcoming each cluster of Fe-Mn-Ni alloy and only 6% of it for the Fe-Mn alloy.

Therefore, there is a good agreement between the 'strength' of the clusters as suggested by the theoretical models and the calculations of the energy that dislocations need to overcome them. The clusters formed in Fe-Mn are the weakest since their obstacle strength is the lowest as suggested by the theoretical models and indeed, dislocations need the smallest amount of energy to overcome each cluster. On the contrary the obstacle strength of the Ni enriched clusters is significantly higher and accordingly, higher is the dissipated energy.

## III. APT and TEM investigation of the microstructure of micro-pillars after plastic deformation

To study the effect of the deformation on the microstructure, APT tips and TEM lamellas were milled from lifted-out pillars.

TEM lamellas were fabricated to evaluate the initial dislocation density in a non-compressed pillar of the non-irradiated Fe-Mn-Ni model alloy and the dislocation density after compression at about 6% strain of a neutron irradiated pillar of the same alloy.

To investigate if the deformation caused any APT observable changes in the microstructure and to the solute distribution, APT tips from two compressed non-irradiated Fe-Mn-Ni pillars and two compressed pillars of the neutron irradiated Fe-Mn alloy, were fabricated and analyzed. The characteristics of the irradiation induced solute clusters, in the bulk material and in the compressed pillars, are compared and discussed.

### 1. Dislocation density estimation in micro-pillars of the Fe-Mn-Ni model alloy

A non-compressed pillar was lifted out from the non-irradiated Fe-Mn-Ni sample and thinned to a TEM lamella in CRIEPI, where it was TEM studied using a JEOL ARM operating at 300kV.

The lamella just after its Ga ion FIB fabrication is illustrated in Figure 160 – a, where the damage due to the ion milling is apparent. To decontaminate the lamella's surface from the Ga ions' damage and at the same time, to additionally reduce the width of the lamella, Argon ion polishing was applied using a precision ion polishing system (PIPS II, Gatan), which effectively reduced the surface artifacts (Figure 160 – b), providing a clear view of the existing dislocation network. However, two square shaped areas consisting of amorphous material were observed after PIPS polishing.

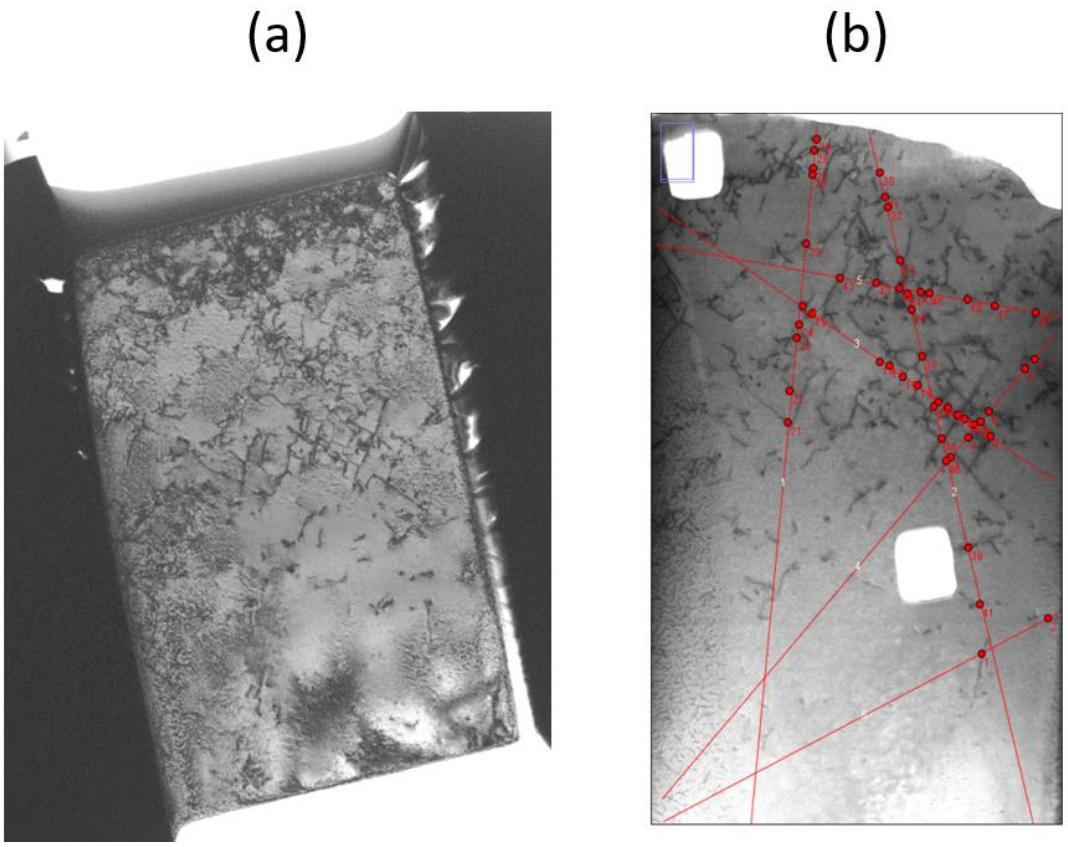


*Figure 160: TEM lamella of a non-compressed pillar of the unirradiated Fe-Mn-Ni model alloy (a) after FIB preparation as observed by TEM and (b) after PIPS milling as observed by STEM, at the Central Research Institute of Electric Power Industry (CRIEPI).*

The thickness of the lamella was estimated about 75 nm after applying the Energy-Filtered TEM (EFTEM) technique. The dislocation density measurement was carried out using the line intercept method with the help of the ImageJ software (Figure 160), as detailed in chapter 2. It was calculated as (6.9 ± 0.2) $x10^{13}$ $m^{-2}$ (the uncertainty is expressed by the standard deviation), being slightly higher than the literature retrieved dislocation density for such model alloys ($5x10^{13}$ $m^{-2}$).

Additionally, the dislocation density was measured for the Fe-0.1Cu testing material. A compressed pillar was lifted out, welded on a Mo TEM grid, and send to CRIEPI where it was thinned to a TEM lamella and studied. On the TEM micrographs (Figure 161), we observe that the pillar extends on two grains, having different diffraction patterns.

The top grain was deformed due to compression up to 9 % strain, with the lower grain appearing intact. Therefore, the dislocation density of the lower grain was estimated as (4.6 ± 0.5) $x10^{13}$ $m^{-2}$ and is matching very well the suggested in literature.

Consequently, for both the Fe-Mn-Ni and the Fe-0.1Cu model alloys, the dislocation density was calculated to be in good agreement with the theoretical value of $5x10^{13}$ $m^{-2}$, justifying its use as the average dislocation density in the prediction models for the estimating the obstacle strength.

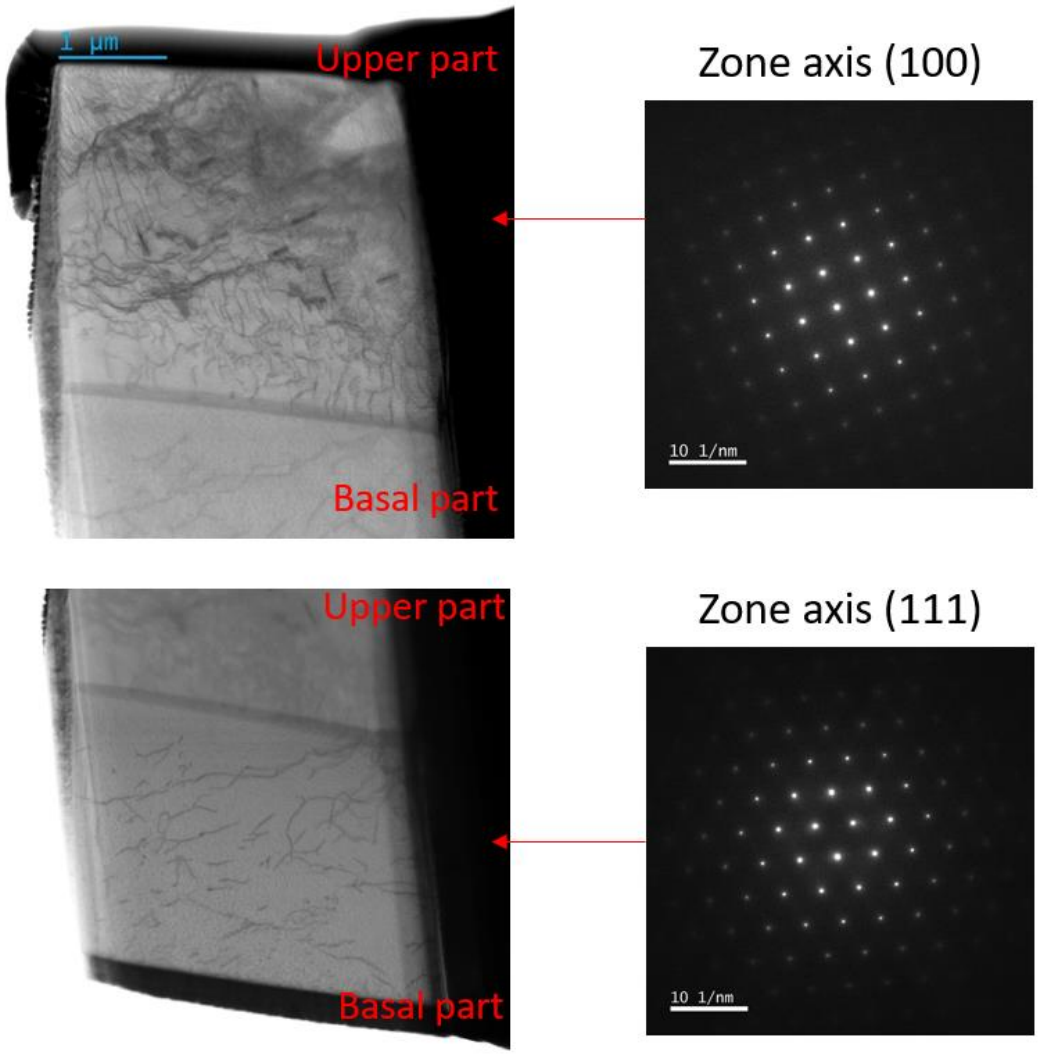


*Figure 161: STEM micrographs of a TEM lamella fabricated from a compressed unirradiated Fe-0.1Cu pillar. Two different grains are identified along the pillar and their corresponding diffractions patterns (at zone axis (100) for the upper grain and at zone axis (111) for the lower grain) are detailed.*

A compressed, at about 6% strain, $[\bar{2},7,10]$ oriented pillar of the neutron irradiated Fe-Mn-Ni alloy, was lifted-out and milled to a TEM lamella. Figure 162 - a illustrates the pillar during deposition of a protective Pt layer, prior to lift out, and Figure 162 - b during the FIB thinning process to become a TEM lamella, which extended approximately 4 µm from the top surface of the pillar. The thinned lamella was additionally polished using PIPS II to reduce the surface artifacts.

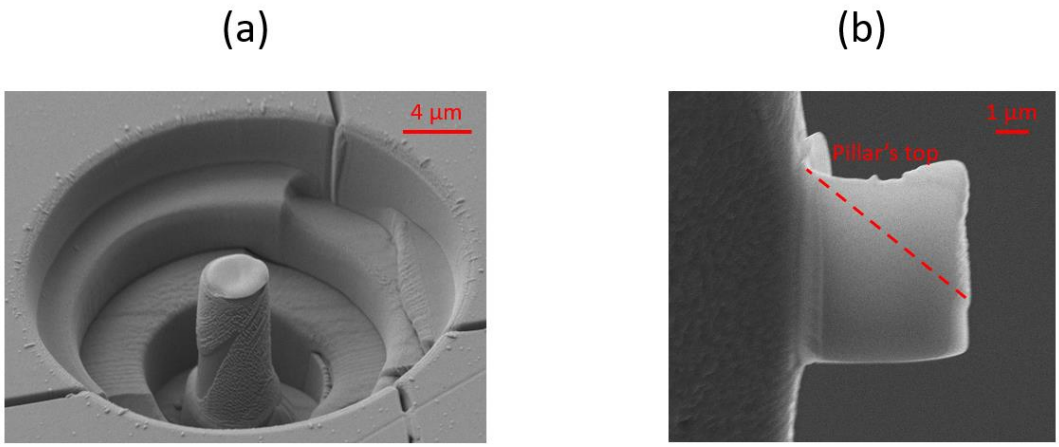


*Figure 162: A compressed pillar of the neutron irradiated Fe-Mn-Ni alloy (a) during deposition of a protective Pt layer, prior to lift out and (b) during thinning to a lamella. The location of the observed slip step (dashed line) and the top of the pillar are indicated.*

EF-TEM measurements were performed at the two selected regions of interest around the slip trace and the lamella thickness was estimated about 100 nm.

Using the GENESIS JEOL ARM operating at 200kV, STEM micrographs were obtained from these regions, with the help of A. Etienne, for dislocation density measurements (Figure 163).

The average dislocation density was calculated as (40.5 ± 4.2) x $10^{13}$ $m^{-2}$, which is almost 6 times larger than the one estimated for the non-compressed and unirradiated Fe-Mn-Ni pillar.

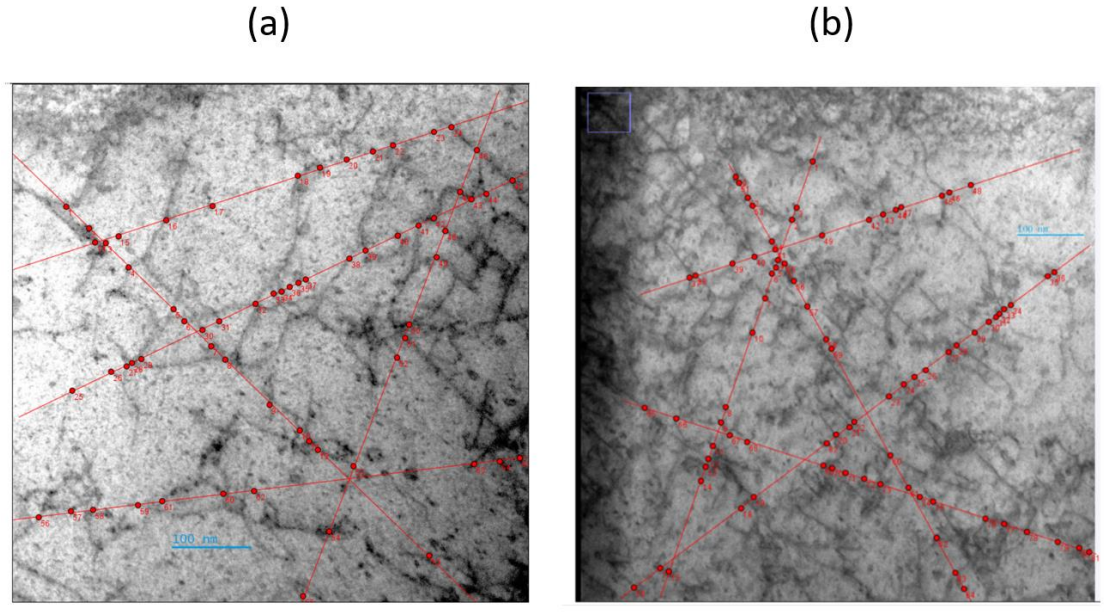


*Figure 163: STEM micrographs of two regions of the lamella fabricated from a compressed pillar of the neutron irradiated Fe-Mn-Ni model alloy where The line intercept method was applied.*

The study of the STEM micrographs did not reveal formation of dislocation channels, that is the formation of rather narrow defect-free paths where dislocations have clear out the irradiation defects, creating an easy pathway for additional dislocations to follow, and hence strain is localized in these paths. The absence of dislocation channels suggests that deformation occurs rather delocalized.

Additionally, features resembling to 'black dots' were observed. Considering the thickness of the lamella, the dimensions of the examined area, and by counting the observed 'black dots' (Figure 164), their number density was estimated around 8.5 x$10^{22}$ $m^{-3}$ which is relatively close to the density of the solute clusters observed using APT (6.2 ± 0.2) x$10^{23}$ $m^{-3}$. However, such a comparison cannot be conclusive, mainly because the size of the clusters detected using APT is at, or below, the TEM's resolution limit and additionally, a lot of factors inducing uncertainties should be also considered.

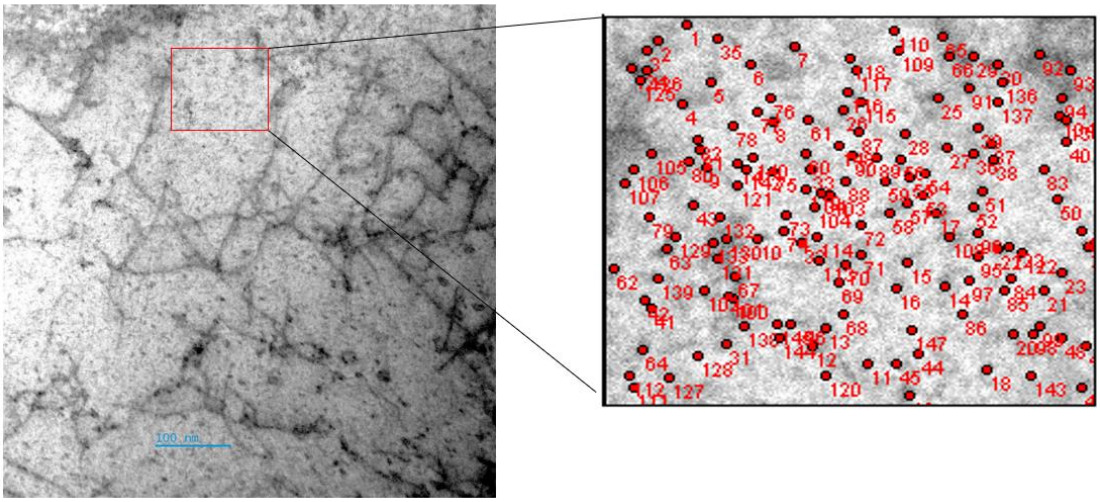

*Figure 164: STEM micrograph of a region of the lamella fabricated from a compressed pillar of the neutron irradiated Fe-Mn-Ni model alloy, presenting features resembling black dots, which in the insert, are marked with red circles for their density measurement.*

## 2. APT study of the microstructure of the deformed Fe-Mn-Ni and Fe-Mn pillars

- Study of deformed pillars of the non-irradiated Fe-Mn-Ni alloy

To investigate if plastic deformation produced any APT observable changes in the microstructure of the compressed non-irradiated pillars, two compressed at about 8% strain $[\bar{2}, 5, 12]$ oriented pillars, fabricated in the Fe-Mn-Ni alloy, were lifted out, milled into APT tips and analyzed using the LEAP 4000 X HR.

Their average global Mn and Ni content was calculated at (0.89 ± 0.05) at. % Mn and (0.71 ± 0.02) at. % Ni, which is in very good agreement with the measured bulk content (0.93 ± 0.01) at. % Mn and (0.74 ± 0.01) at. % Ni). Other elements identified in lower concentrations are also reported in Table 25.

*Table 25: Comparison between the APT measured mean content (at. %) of the compressed pillars and of the bulk sample of the non-irradiated Fe-Mn-Ni model alloy (Fe is balance and the uncertainty is expressed as two times the standard error of the mean).*

| Element | Pillar content (at. %) | Bulk content (at. %) |
|---|---|---|
| **Mn** | 0.89 ± 0.05 | 0.93 ± 0.01 |
| **Ni** | 0.71 ± 0.02 | 0.74 ± 0.01 |
| **Si** | 0.027 ± 0.001 | 0.032 ± 0.003 |
| **P** | 0.005 ± 0.003 | 0.003 ± 0.002 |
| **C** | 0.27 ± 0.21 | 0.10 ± 0.08 |
| **N** | 0.007 ± 0.002 | 0.003 ± 0.004 |
| **Cr** | 0.007 ± 0.001 | 0.009 ± 0.013 |

Clustering was not observed on the atom maps, nor solute segregation on network dislocations (Figure 165 – a). The homogeneous distribution of the solute elements was confirmed by statistical tests, as in Figure 165 – b, that compared the experimental atom distributions against random ones, with Mn, Ni, Si and P as the 'core solute element' (CS).

Therefore, the analyses of the non-irradiated bulk samples and compressed pillars, were very similar, with no observable differences in the APT studied microstructure.

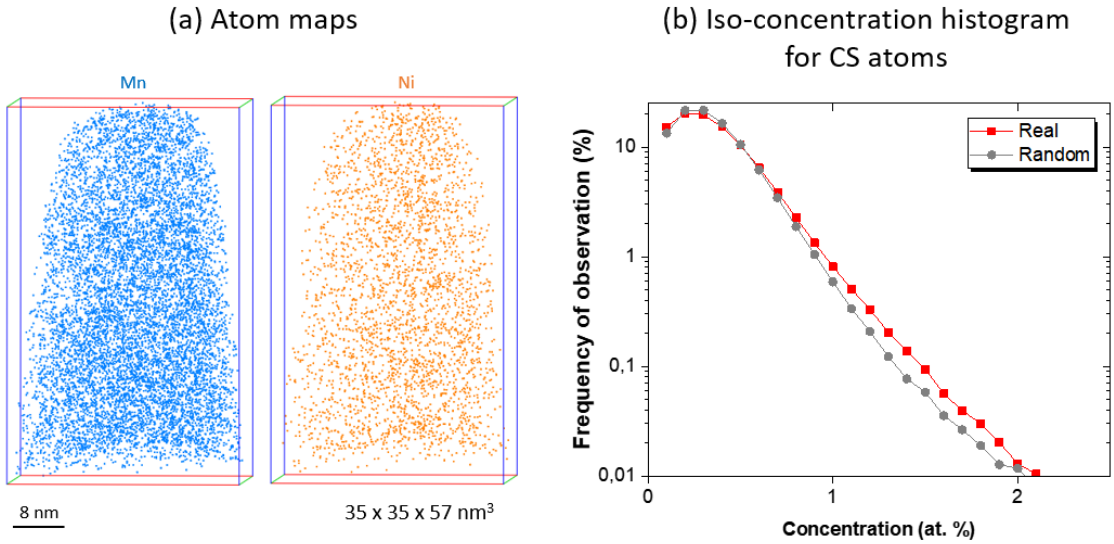


*Figure 165: (a) Atom maps of Mn and Ni and (b) iso-concentration histogram of CS atoms, of a tip fabricated from a compressed pillar of the neutron irradiated Fe-Mn-Ni model alloy.*

- <u>Study of deformed pillars of the neutron irradiated Fe-Mn alloy</u>

Two compressed, at about 9% strain, $[\bar{3}, 4, 10]$ oriented pillars of the neutron irradiated Fe-Mn alloy, were lifted out and milled into APT tips which were studied using the LEAP 5000 XR.

Since there were no significant variations in the concentration of the detected elements between the two analyzed tips, the measured average chemical concentration in at. % was calculated and tabulated in Table 26, along with the uncertainty expressed as two times the standard error of the mean (Fe is the balance).

The average global content of the compressed pillars of the neutron irradiated Fe-Mn alloy is in agreement with the global content of the bulk Fe-Mn samples (presented in chapter 3).

*Table 26: Average global, matrix and cluster content in at. % as measured by APT experiments of the compressed pillars of the neutron irradiated Fe-Mn model alloy (Fe is balance and the uncertainty is expressed as two times the standard error of the mean).*

| Element | $X_{Global}$ (at. %) | $X_{matrix}$ (at. %) | $X_{clusters}$ (at. %) |
|---|---|---|---|
| **Mn** | 0.96 ± 0.05 | 0.83 ± 0.08 | 11 ± 2 |
| **Ni** | 0.054 ± 0.010 | 0.05 ± 0.02 | 0.07 ± 0.05 |
| **Si** | 0.015 ± 0.001 | 0.015 ± 0.001 | 0.02 ± 0.04 |
| **P** | 0.011 ± 0.003 | 0.008 ± 0.004 | 0.1 ± 0.1 |
| **C** | 0.47 ± 0.01 | 0.47 ± 0.01 | 0.3 ± 0.2 |
| **N** | 0.003 ± 0.005 | 0.003 ± 0.005 | 0.05 ± 0.05 |
| **Cr** | 0.066 ± 0.003 | 0.065 ± 0.001 | 0.1 ± 0.1 |

About 40 clusters per tip were identified after applying the isoposition method (IPM) using as 'core solute element' (CS) the Mn. The used average minimum concentration threshold was $C_{Thr}^{CS} = 3.81\ at.\%$ and the minimum number of solute atoms $N_{Min}^{CS} = 5\ atoms$.

The irradiation induced solute clusters can be observed in the atom maps of Figure 166 – a, where the radius of the atoms inside the clusters is magnified, to facilitate their visualization. Figure 166 – b and c, are the plots of the 1NN distribution and the iso-concentration histogram of Mn. Both experimental curves do not match the random one, indicating a non-homogeneous distribution of Mn.

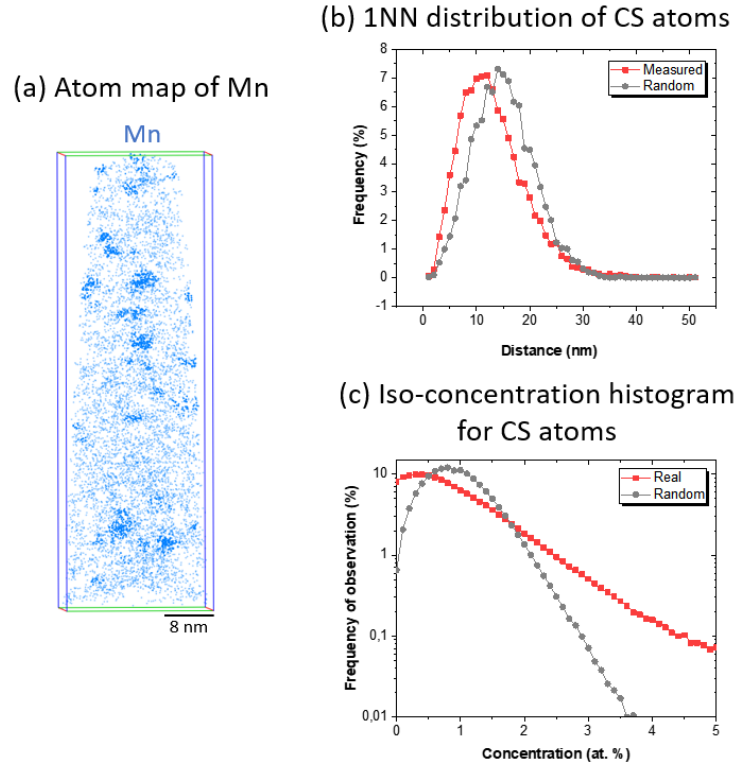


*Figure 166: APT tips fabricated from compressed pillars of the neutron irradiated Fe-Mn model alloy: (a) clusters are visible in the atom maps of Mn. Their existence is verified by statistical tests: (b) the first nearest neighbor distribution of Mn atoms is different compared to a random distribution, as well as (c) the iso-concentration histogram of Mn atoms.*

The matrix Mn content is observed slightly reduced, due to the presence of solutes clusters which are enriched in Mn, reaching about 11 at. % (Table 26). The above-mentioned clusters have very similar composition to those detected in the bulk neutron irradiated Fe-Mn samples (Chapter 3).

The cluster morphology was examined, after erosion at the matrix – cluster interface, by plotting their aspect ratio and oblateness. The clusters lay on the center of the sphere quadrant (Figure 167) and so, they were assumed to be spherical.

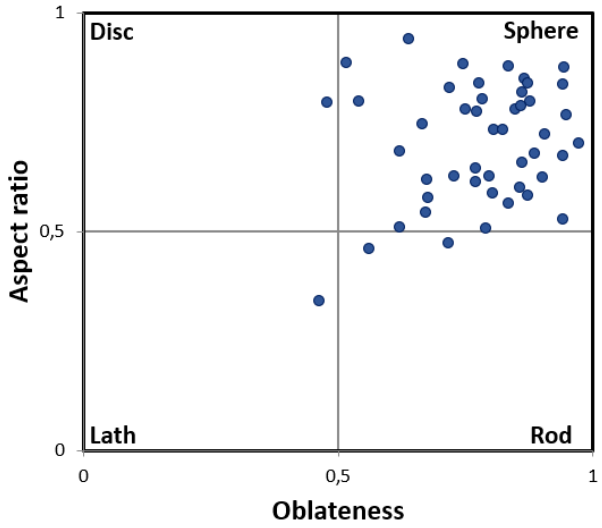


*Figure 167: Aspect ratio vs oblateness graph of the complete clusters identified in the tips made of compressed pillars of the neutron irradiated Fe-Mn alloy.*

Their mean number density was calculated at (17 ± 2) x$10^{23}$ $m^{-3}$ while their volume fraction at (1.8 ± 0.3) %.

Concerning their size, the clusters present a mean Guinier and equivalent spherical radius of (1.2 ± 0.1) nm and (1.1 ± 0.1) nm respectively. Their size distribution illustrated in Figure 168 – a appears to be bimodal (whether taking account the Guinier or equivalent sphere radius), unlike the case of the bulk Fe-Mn sample which presents a clearly monomodal distribution (Figure 168 – b).

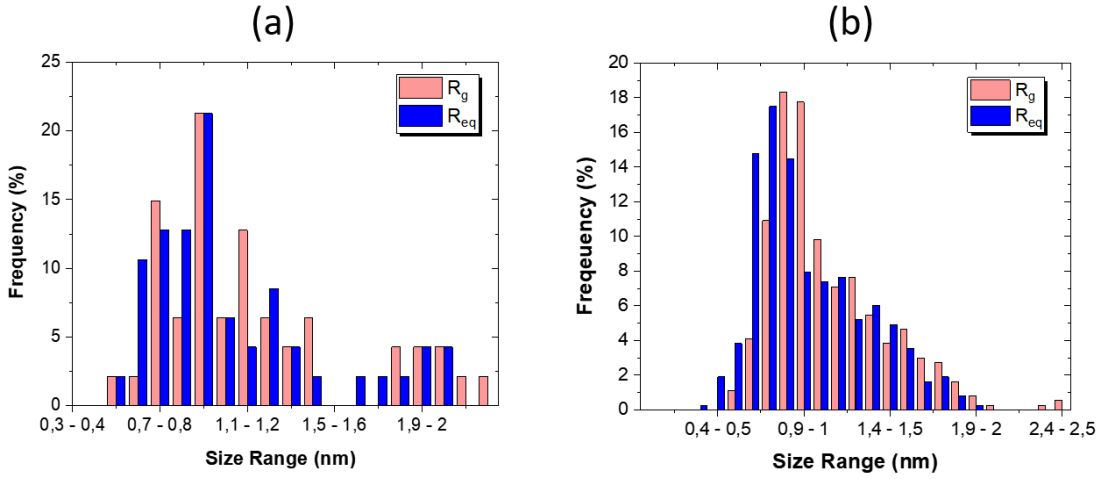


*Figure 168: Guinier (red) and equivalent sphere (blue) radius distribution of clusters identified in the tips (a) made of compressed pillars and (b) of the bulk, of the neutron irradiated Fe-Mn alloy.*

Additionally, observing the histogram of the number of atoms contained in the complete clusters in the pillars' tips, the clusters appear as belonging to two different families regarding their size. The 'small' cluster family consisting of clusters having up to 1000 atoms and the 'large' cluster family consisting of clusters having 1200 atoms or more (Figure 169 – a). Comparing with the same histogram of the bulk material, the 'large' family is almost absent (Figure 169 – b).

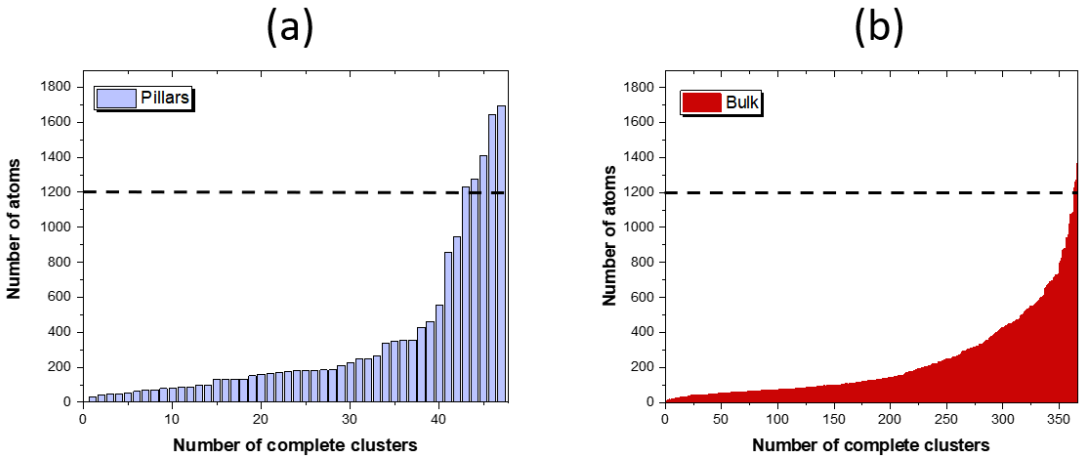


*Figure 169: Histogram of number of atoms inside the complete clusters of the (a) two tips made from compressed pillars and (b) four tips fabricated from the bulk, neutron irradiated Fe-Mn model alloy.*

The total analyzed volume of all the bulk samples was considerably larger than that of the compressed pillars. Thus, to avoid misinterpretation due to statistical difference, the clusters contained in each tip of the bulk Fe-Mn were compared separately with those of the pillars.

Almost no 'large' clusters were observed in the histograms of each bulk tip (two of which are illustrated in Figure 170) and hence, reinforced our initial assumption that a family of 'large' clusters was present only in the compressed pillars.

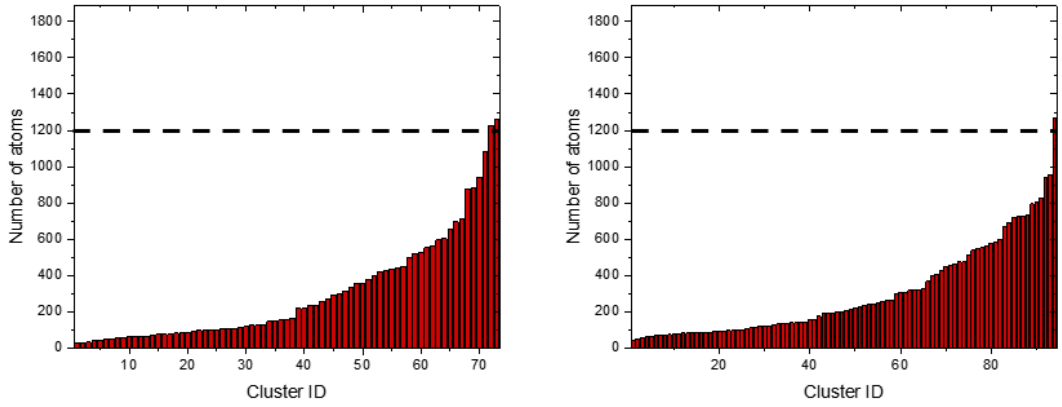


*Figure 170: Histogram of the number of atoms contained in the complete clusters of two bulk neutron irradiated Fe-Mn tips.*

The number density of the 'large family' clusters in the compressed pillars was calculated as $(14 \pm 4)\ x10^{22}\ m^{-3}$ which is considerably more elevated than that of the 'large family' in the bulk, measured as $(1.3 \pm 3.8)\ x10^{22}\ m^{-3}$ (the uncertainty is expressed by the standard error).

The noticeable high uncertainty value, for the bulk 'large family', casts doubt on the very existence of this family, suggesting that the detected large clusters are just a random size fluctuation in the case of the bulk samples.

Nevertheless, as illustrated in Figure 171, the difference between the two number densities is clearly statistically significant, suggesting that a mechanism was active during compression leading to the formation of a number of bigger clusters in the deformed pillars.

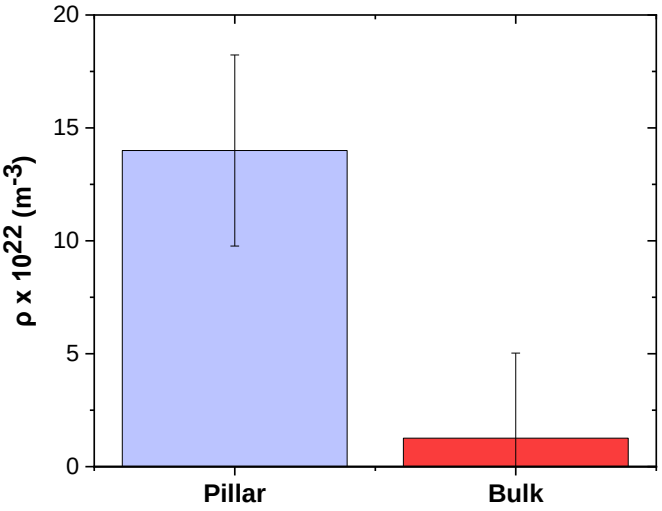


*Figure 171: Number density of the complete clusters having more than 1200 atoms, identified in the analyzed tips of the bulk (in red) and of the compressed pillars (in purple) of the neutron irradiated Fe-Mn model alloy.*

- Pressure effect on solutes diffusion

Compression of the pillars involves elevated pressure values, therefore the effect of pressure on the solute diffusion is briefly discussed.

Diffusion coefficients in solids are determined by thermodynamic factors such as temperature and pressure. While the effect of temperature is pronounced, the pressure has an almost negligible effect on the diffusivity of solutes at ambient pressures, thus activation enthalpy and energy almost coincide (ΔH ≈ Q) and only at high pressures can become significant.

Considering the expression of the activation enthalpy as a function of activation energy (Q) ΔH = Q + p ΔV, the diffusion coefficient (D) is expressed by:

$$D = D_o \, e^{\left(-\frac{\Delta H}{RT}\right)} = D_o \, e^{\left(-\frac{Q+p\Delta V}{RT}\right)} \tag{5.7}$$

where p the hydrostatic pressure, and ΔV the so-called activation volume of diffusion, which is the isothermal change of volume of the material associated with a diffusion jump and is defined as the pressure derivative of the Gibbs energy at constant temperature:

$$\Delta V = \left(\frac{\partial \Delta G}{\partial p}\right)_T \tag{5.8}$$

Activation volume increases with increasing temperature (Figure 172 - a) and for the transition element diffusers as Mn (as well as for Fe, Cr, Co) are fairly high [9].

According to Eq. (5.7), diffusion coefficient increases with the temperature increase but decreases with the increase of pressure (Figure 172 - b).

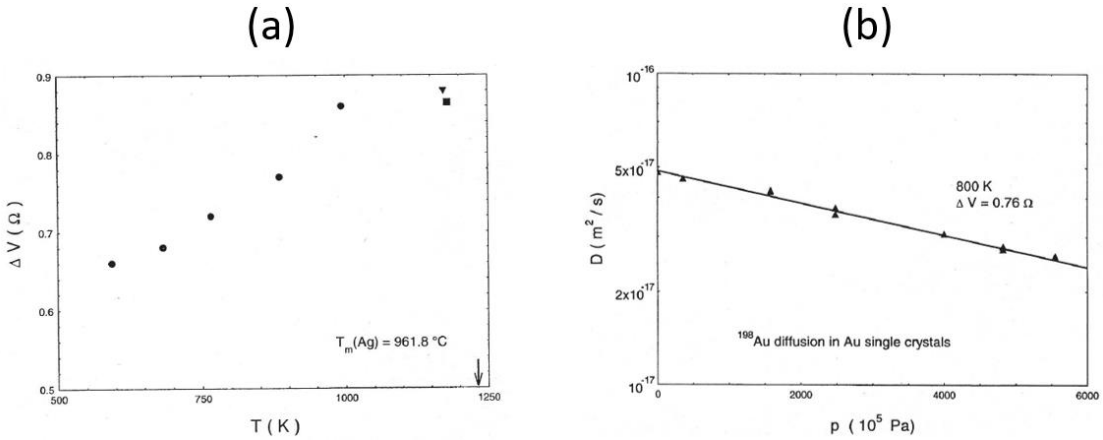


*Figure 172: (a) Activation volume of silver self-diffusion for various temperatures (b) Pressure dependence of self-diffusion in gold at 800 K [9]*

Considering that the performed micro-compression tests imposed to the pillars a pressure that peaked between 400 and 800 MPa and that the tests were carried out at ambient temperature, lasting only a few minutes, the diffusion distance during compression is expected to be negligible.

Additionally, the Mn concentration in the 'large' clusters (Figure 173), was measured to be very similar between the pillars (11 ± 2 at. %) and the bulk (10 ± 1 at. %).

Therefore, due to the previous theoretical consideration and the measured Mn content of the 'large' clusters, the possibility that diffusion was the possible mechanism the clusters' enlargement, was eliminated.

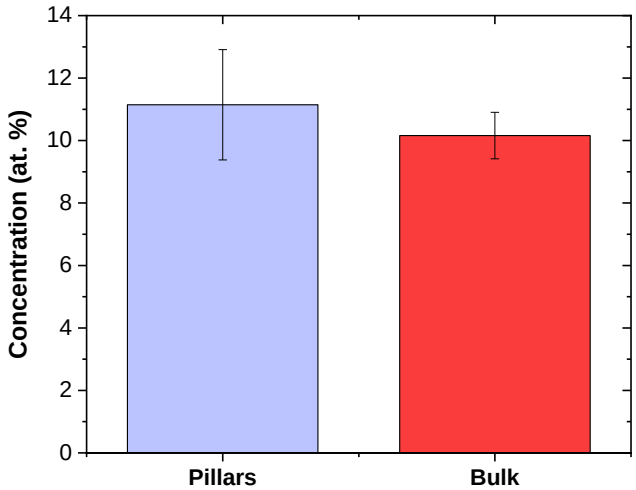


*Figure 173: Average Mn content (at. %) of the clusters containing more than 1200 atoms, in the tips made from compressed pillars (purple) and from the bulk material (red) of the Fe-Mn neutron irradiated sample.*

- Possible way of formation of the ‘large’ clusters

A possible explanation of the existence of the observed ‘large’ clusters is the following. As the dislocations move and encounter shearable clusters, they cut through them, displacing the part of the cluster above the slip plane in relation to the part below it. Following dislocations might increase the displacement of the parts of the cluster, but without completely separating them. When this process occurs, it results in altering the spherical shape of the cluster. During APT analysis, when reconstructing, it is probable that the clustering algorithm applied the best fit ellipsoid so that to include both parts of a cluster and consequently while forming the ellipsoid shape, assigned some matrix atoms as well, to the cluster (Figure 174).

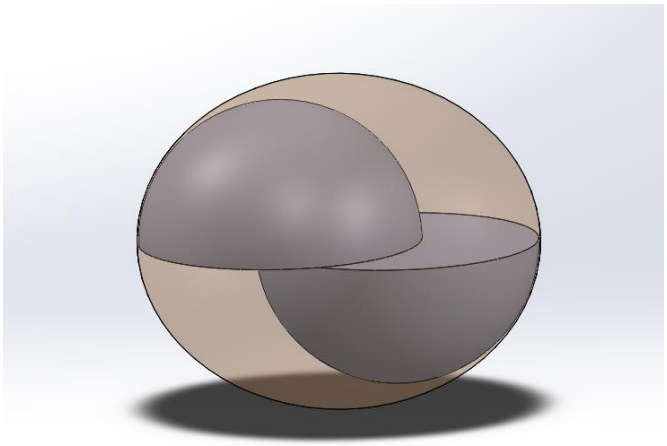

*Figure 174: Schematic of a partially sheared cluster surrounded by an ellipsoid shape.*

Therefore, more atoms were assigned to the cluster, increasing its radius and eventually resulting in the bimodal size distribution (Figure 168) observed only for the clusters of the compressed pillars.

The clusters laying on the glide plane of a dislocation are random in size, so prior to compression their average $R_g$ should have been equal to the average $R_g$ value of the clusters in the bulk, that is (1.1 ± 0.1) nm.

The measured Guinier radius of the ‘large’ cluster family is (2.1 ± 0.8) nm. It is almost increased by 1 nm than average cluster size in un-deformed samples. Considering that the Burgers vector in the α-Fe lattice is 0.248 nm, subsequently, about 4 dislocations are needed to pass through an average sized cluster and cause the observed increase in the cluster’s radius, reshaping it into a ‘large cluster’.

The assumption that, the clusters of the ‘large family’ are the partially sheared clusters from the gliding dislocations, will be evaluated by studying such Mn-enriched clusters in a simulated volume. However, this needs additional development of the GPM 3D software, that will be implemented by the software engineers.

In summary, TEM experiments on non-compressed pillars of the unirradiated Fe-Mn-Ni model alloy estimated the dislocation density to be in good agreement with the one derived from literature and used in the theoretical models.

In the case of deformed neutron irradiated pillars, STEM revealed significantly elevated dislocation density, no formation of dislocation channels and numerous features resembling to “black dots”.

APT analysis of the compressed non-irradiated Fe-Mn-Ni pillars, did not reveal any differences in the microstructure or in the solute distribution, as well as in the neutron irradiated Fe-Mn compressed pillars, with the exception that bigger sized clusters were present in considerably increased number density, which were assumed as clusters that dislocations have partially sheared.

## Summary

The Bacon-Kocks-Scattergood (BKS) model as modified and published by Monnet and a microstructure-based strength calculation model published by Chauhan et al, were used to estimate the obstacle strength of the neutron irradiation induced solute clusters, in the studied ferritic model alloys. Additionally, from the stress-strain curves plotted from the in situ micro-compression data, the energy dissipated for deforming the pillars was calculated. The increase in the needed energy for the irradiated pillars was attributed to the presence of the solute clusters and the amount of energy to overcome each cluster was deduced.

Both models suggested that the clusters formed in the Fe-Mn alloy are the weakest ones, having the lowest obstacle strength and hence hindering less the dislocations motion, as confirmed by the small dissipated energy amount to overcome the resistance of each cluster during deformation. When they contain Ni, the clusters became significantly harder, as the models suggested for the Fe-Ni and Fe-Mn-Ni alloys and consequently significant higher was the estimated needed energy per cluster for deforming.

Additionally, APT tips and TEM lamellas were fabricated from lifted-out pillars and the microstructure of the model alloys before and after deformation was investigated.

The TEM calculated dislocation density of a non-compressed pillar of the non-irradiated Fe-Mn-Ni model alloy, was similar to the literature suggested of $5x10^{13}$ $m^{-2}$. The measured dislocation density of a compressed neutron irradiated pillar of the same alloy, was about 6 times increased and dislocation channeling was not observed.

APT analysis of the compressed irradiated Fe-Mn pillars indicated that the characteristics of the clusters were similar with those of the bulk ones, with the exception that an increased number density of ‘large’ clusters was detected, that is clusters consisting of 1200 atoms or more, which were assumed to be clusters partially sheared by a small number of dislocations that passed through them.

## Bibliography

[1] D. J. Bacon, U. F. Kocks, and R. O. Scattergood, “The effect of dislocation self-interaction on the orowan stress,” *Philos. Mag.*, vol. 28, no. 6, Art. no. 6, Dec. 1973, doi: 10.1080/14786437308227997.

[2] G. Monnet, “Multiscale modeling of irradiation hardening: Application to important nuclear materials,” *J. Nucl. Mater.*, vol. 508, pp. 609–627, Sep. 2018, doi: 10.1016/j.jnucmat.2018.06.020.

[3] G. Monnet, L. Vincent, and L. Gélébart, “Multiscale modeling of crystal plasticity in Reactor Pressure Vessel steels: Prediction of irradiation hardening,” *J. Nucl. Mater.*, vol. 514, pp. 128–138, Feb. 2019, doi: 10.1016/j.jnucmat.2018.11.028.

[4] A. Chauhan *et al.*, “Microstructure characterization and strengthening mechanisms of oxide dispersion strengthened (ODS) Fe-9%Cr and Fe-14%Cr extruded bars,” *J. Nucl. Mater.*, vol. 495, pp. 6–19, Nov. 2017, doi: 10.1016/j.jnucmat.2017.07.060.

[5] A. Arsenlis, M. Rhee, G. Hommes, R. Cook, and J. Marian, “A dislocation dynamics study of the transition from homogeneous to heterogeneous deformation in irradiated body-centered cubic iron,” *Acta Mater.*, vol. 60, no. 9, pp. 3748–3757, May 2012, doi: 10.1016/j.actamat.2012.03.041.

[6] N. Castin *et al.*, “The dominant mechanisms for the formation of solute-rich clusters in low-Cu steels under irradiation,” *Mater. Today Energy*, vol. 17, p. 100472, Sep. 2020, doi: 10.1016/j.mtener.2020.100472.

[7] E. Meslin *et al.*, “Characterization of neutron-irradiated ferritic model alloys and a RPV steel from combined APT, SANS, TEM and PAS analyses,” *J. Nucl. Mater.*, vol. 406, no. 1, pp. 73–83, Nov. 2010, doi: 10.1016/j.jnucmat.2009.12.021.

[8] A. Reichardt *et al.*, “Nanoindentation and in situ microcompression in different dose regimes of proton beam irradiated 304 SS,” *J. Nucl. Mater.*, vol. 486, pp. 323–331, Apr. 2017, doi: 10.1016/j.jnucmat.2017.01.036.

[9] H. Mehrer, “Diffusion in Solids under Pressure,” *Defect Diffus. Forum*, vol. 309–310, pp. 91–112, Mar. 2011, doi: 10.4028/www.scientific.net/DDF.309-310.91.

# General summary and conclusions

The Reactor Pressure Vessel is probably the most important component of a Nuclear Power Plant, housing the reactor core, and since it is irreplaceable, determines as well the lifetime of the NPP.

During NPP operation, neutrons generated from the nuclear reactions taking place inside the core, alter the microstructure within the BCC crystal lattice of the RPV steel. Irradiation creates a high concentration of point defects (PDs) that migrate towards the sinks. Since the movement of the solute atoms is mediated by the PDs, the PDs supersaturation can enhance the thermodynamically possible precipitation (REP) or, if a solute element preferentially associates with the PDs, coupling between the fluxes of the PDs and the solute occurs, which may lead in the formation of nanosized solute clusters, even if it is not thermodynamically favorable (so called Radiation Induced Segregation phenomena).

Therefore nano-sized solute clusters, containing mainly Cu, Mn, Ni and Si, are developed during the neutron irradiation. They act as barrier to dislocation motion resulting in hardening and embrittlement. To predict and prevent such phenomenon, extensive studies were carried out during the last decades investigating the mechanisms involved in the solute clustering, which were mainly focused on the effect of Cu.

The objectives of this PhD work were to investigate the role of the Mn and Ni in the clustering process, in the absence of the well-studied Cu impurity and also the impact on the materials' mechanical properties. This was possible while studying two ferritic binary model alloys (Fe-Mn, Fe-Ni) and a ternary model alloy (Fe-Mn-Ni) in the non-irradiated and neutron irradiated states, using mainly atom probe tomography (APT) and in-situ SEM micro-compression.

The APT microstructural study of the three model alloys revealed the formation of nano-sized clusters under neutron irradiation. The clusters formed in the Fe-Mn alloy outnumbered those of the other two alloys, producing the highest number density, almost an order of magnitude higher that the number density of the other binary alloy (Fe-Ni), the clusters of which were more solute enriched. Therefore, it appears that there is a synergistic effect between Mn and Ni. The Mn contributes by producing solute clusters in high number density and while Ni increases their solute enrichment, which combined together led to the significant increased volume fraction of the clusters developed in the Fe-Mn-Ni alloy.

According to the binary phase diagrams of the Fe-Mn and Fe-Ni, both studied binary alloys are initially under-saturated. Therefore, precipitation is not thermodynamically favored and the only possible mechanism that produced the observed clusters that formed under irradiation, is the radiation induced segregation.

Concerning the clusters detected in the ternary alloy, their thermal stability was evaluated with the post-irradiation isochronal annealing (PIA) experiments, performed for 30 minutes at 400 °C, 500 °C and 600°C at SCK.CEN. As observed by APT analysis, these clusters partially dissolved at 400 °C and reached almost complete dissolution at 600°C. Additionally, the Fe concentration of the ternary alloy's clusters was high, even when the APT biases were compensated by applying the Chemical Composition Correction model's calculations. Moreover, the ratio of the Mn:Ni:Si content of the clusters did not indicate a tendency towards a certain thermodynamically stable phase. Therefore, it is concluded that the

mechanism that generated the detected clusters in the ternary alloy was the radiation induced segregation, as well.

The mechanical properties of the three alloys before and after irradiation were assessed by in-situ SEM micro-compression of FIB fabricated single crystal micro-pillars, inside grains having favorable crystal orientation, selected after EBSD study.

The micro-mechanical tests were performed at ambient temperature, with the picoindenter operating in displacement-controlled mode. From the acquired load-displacement data, in combination with the pillar geometry, the engineering stress-strain curves were plotted and studied. Instead of using the classical criterion of yield strength determination at 0.2% of strain, it was approximated in this study at a higher strain (2% and 3%) due to early plasticity, inevitable in micro-compression testing. Additionally, the application of the Sneddon's correction was evaluated to have negligible effect on the stress–strain values of the plastic regime.

The irradiation hardening was calculated higher in the ternary alloy, which was irradiated at 0.1 dpa. Between the binary alloys, both irradiated at a lower dose of 0.022 dpa, the Fe-Ni presented higher hardening than the Fe-Mn. The Fe-Mn alloy in the unirradiated state, unexpectedly, needed the highest average resolved shear stress for the same degree of plastic deformation and therefore it was assumed that Fe-Mn samples contained higher dislocation density.

The ability of the irradiation induced clusters to hinder the motion of the dislocations, was evaluated using the obstacle strength, provided from two, relatively recent published, theoretical models. The APT-calculated characteristics of the solute clusters (as the chemical nature, number density and size) were correlated with the mechanical response at the micro-compression tests, by fitting the obstacle strength so that the measured irradiation hardening to match the predicted by the models.

The obtained specific resistance and obstacle strength values, suggest that the presence of Ni in the solute clusters leads to an enhanced resistance to dislocation motion, while the Mn produces clusters, that cannot effectively hinder the dislocations which pass through them relatively easily and hence the Mn-enriched clusters, mainly contribute to irradiation hardening due to their highly increased number density.

The study of the energy dissipated by the dislocations for overcoming the solute clusters during the plastic deformation of the micropillars, indicated that dislocations need the highest amount of energy to overcome the resistance of each cluster in the Fe-Ni alloy, while about half of this energy was needed for overcoming each cluster of Fe-Mn-Ni alloy and only 6% of it of the Fe-Mn alloy. Therefore, there is a good agreement between the 'strength' of the clusters as suggested by the theoretical models and the calculations of the energy that dislocations need to overcome them.

To study the effect of the deformation on the microstructure, APT tips and TEM lamellas were fabricated from lifted out pillars. The TEM calculated dislocation density of a non-compressed pillar of the non-irradiated Fe-Mn-Ni model alloy, verified the literature suggested for the model alloys (that is $5x10^{13}$ $m^{-2}$).

APT analysis of the compressed neutron irradiated Fe-Mn pillars, indicated that the characteristics of the clusters were similar with those of the bulk ones, with the exception that

an increased number density of ‘large’ clusters was detected. These ‘large’ clusters were assumed to be clusters partially sheared from the dislocations that passed through them. To our knowledge and up to date, this work is the first one of its kind.

This study has provided further insights on the effect of the solute elements Mn and Ni on the microstructure evolution after neutron irradiation, as well as their effect on the mechanical behavior of 3 μm in diameter BCC pillars. However, further investigations are needed to provide verification on the universality of the reported observations.

Therefore, more APT and micro-compression experiments following the established methodology, using binary and ternary model alloys having different than the studied solute content and being neutron irradiated at the same irradiation conditions, should provide further evidence concerning the role of Mn and Ni alloying elements and the impact of the clusters that these elements form, on the mechanical properties of the alloys.

Additionally, bulk polycrystal testing in combination with micro-compression of pillars having different diameters, would contribute to evaluate the extent of the influence of the sample size effect on the mechanical results.

To further investigate the mechanical properties of the ferric alloys, the combination of APT microstructure analysis with in-situ TEM tensile or compression experiments, would be most beneficial, providing in-depth and detailed understanding of the deformation mechanisms involved during micro-mechanical testing.

Finally, the coupling of atomic scale analyses using APT and the micromechanical testing such as in-situ compression or in-situ tensile testing is very attractive and promising, especially when having the possibility to work on radioactive materials in a unique platform as the GENESIS, gathering in one lab all the needed facilities.

# Appendices

# Appendix 1: The Genesis platform

The Group Physique des Matériaux (GPM) is a joint research unit (Unité Mixte de Recherche 6634) between the University of Rouen Normandy, INSA Rouen Normandy and the CNRS, with a history of more than fifty years in scientific instrumentation and is a world-famous pioneer in the design and development of the tomographic atomic probe.

In 2016, within the GPM laboratory an instrumental platform for material characterization at a very fine scale was established in a 500 $m^2$ building. The principal objective of the GENESIS (Groupe d'Etudes et de Nanoanalyses des Effets d'Irradiations) platform is the research, in the atomic scale, for materials intended for nuclear power plants applications analyzing and evaluating the irradiation damage that neutron irradiation causes.


*Figure 175: The GENESIS platform building at GPM.*

From 2019, GENESIS platform is authorized to handle radioactive samples and the building is divided in two zones depending on the possibility of contamination risk. Areas for sample preparation or storage and waste storage include risk of contamination whereas the zones where APT and TEM experiments take place can only encounter an irradiation risk, coming from the radioactive sample to be analyzed.

Safety regulations are strictly followed. Passive and operational dosimeters are mandatory to monitor the dose received by the user and to estimate its impact on their health. In addition, the ALARA (As Low As Reasonably Possible) principle is applied and as much as possible, the activity of the source as well as the time of exposure of the user are limited. This is achieved by preparing experiments in advance, using tweezers and glove boxes to handle active specimens and by using lead boxes and shields for sample transport and manipulations respectively.

It is worth mentioning that all the thesis experiments were performed in the GENESIS platform, that not only provided a safe and hospitable working environment, but also all the necessary cutting-edge equipment for the manipulations and the nanoscale analyses of the neutron irradiated materials, as well as the mechanical testing.

Figure 176 – a illustrates the ZEISS XB540 SEM/FIB used for sample preparation having a modified airlock for safe introduction and housing of radioactive specimens.

The glove box used for the introduction of the Hysitron PI87R picoindenter inside the SEM chamber for the in-situ micro-compression experiments is depicted in Figure 176 – b.

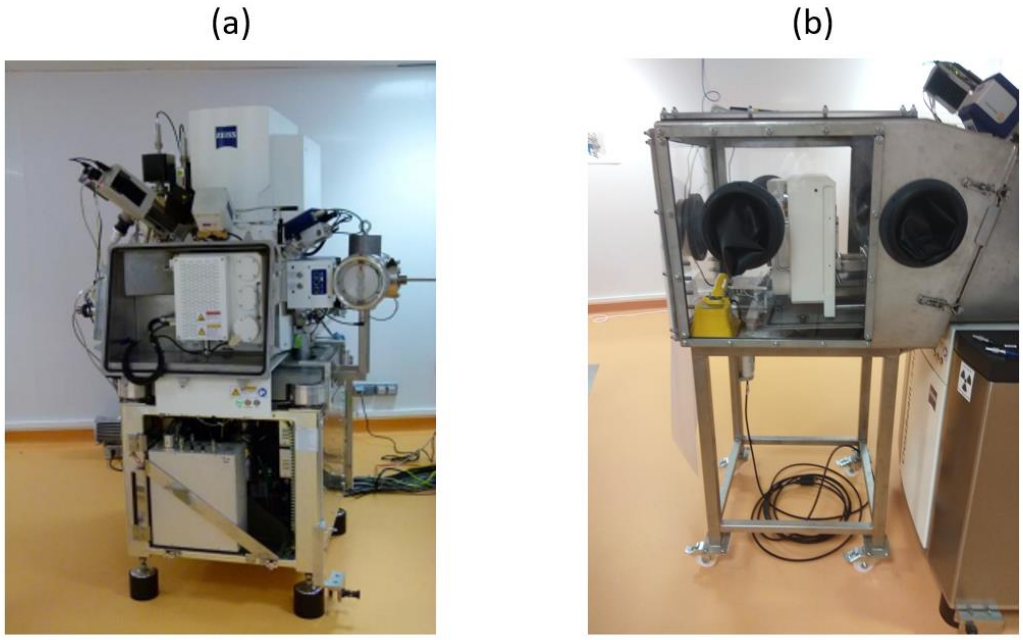


*Figure 176: Some of the GENESIS platform instrumentation used in this thesis: (a) The ZEISS XB540 SEM/FIB having a modified airlock for safe introduction and housing of radioactive specimens and (b) The glove box used for the introduction of the Hysitron PI87R picoindenter inside the SEM chamber.*

## Appendix 2: Custom Specimen holder for the Struers Tegramin polisher

For polishing neutron irradiated samples, the use of an automatic polisher is mandatory for safety reasons in the GENESIS platform which is equipped with the Struers Tegramin polisher. (Figure 177). Unfortunately, the specimen holders were fabricated for specimens that were oversized for the stub of Hysitron Picoindenter PI 87R. Therefore, it was necessary to design and fabricate a custom specimen holder that should fit in both the indenters stub and the specimen mover plate of the polisher.

(A) (B)

*Figure 177: (A) The Struers Tegramin Polisher and (B) the polisher inside the glovebox at the GENESIS platform.*

Our custom designed holder was designed, having in mind that it should be easy to use, minimizing the necessary time for clamping the radioactive specimen and hence only one M3 screw was used. The drawings of the holder are published in the following figures and it was fabricated by C. Vaudolon in the Uninversity of Rouen (Figure 178).

*Figure 178:The custom designed and made specimen holder.*

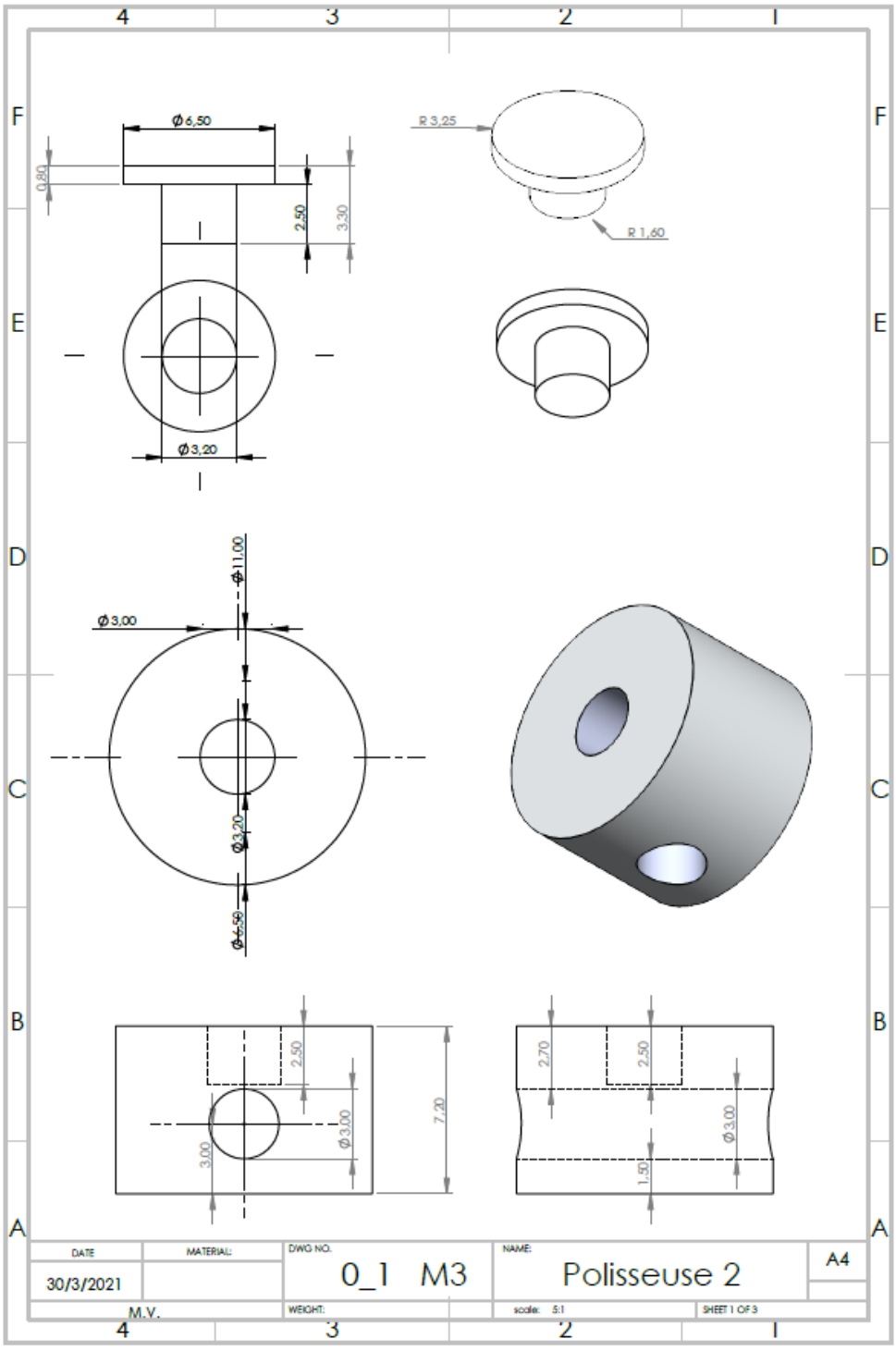


*Figure 179:Drawing with dimensions of the custom designed specimen holder (1/3)*

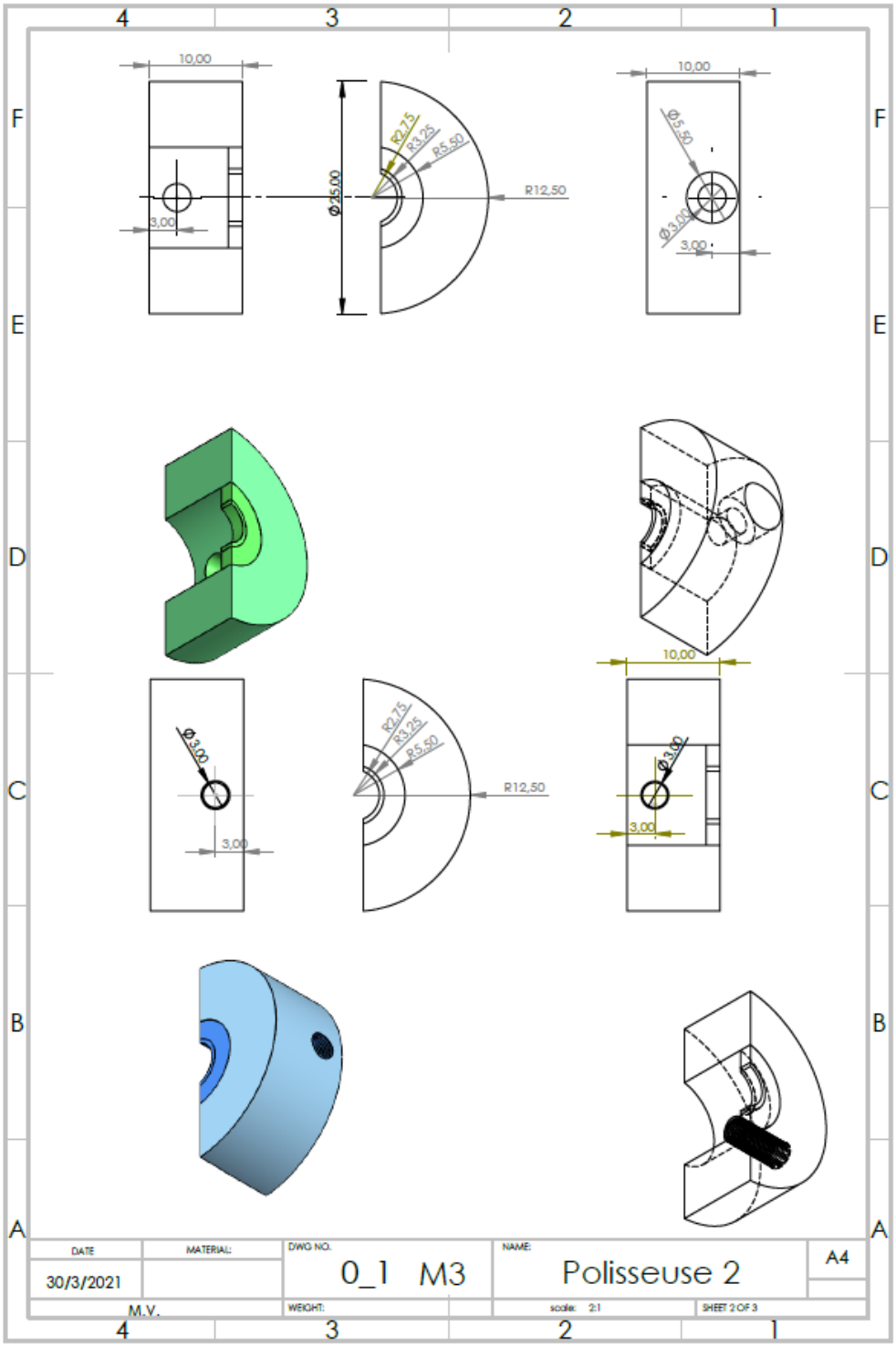


*Figure 180: Drawing with dimensions of the custom designed specimen holder (2/3)*

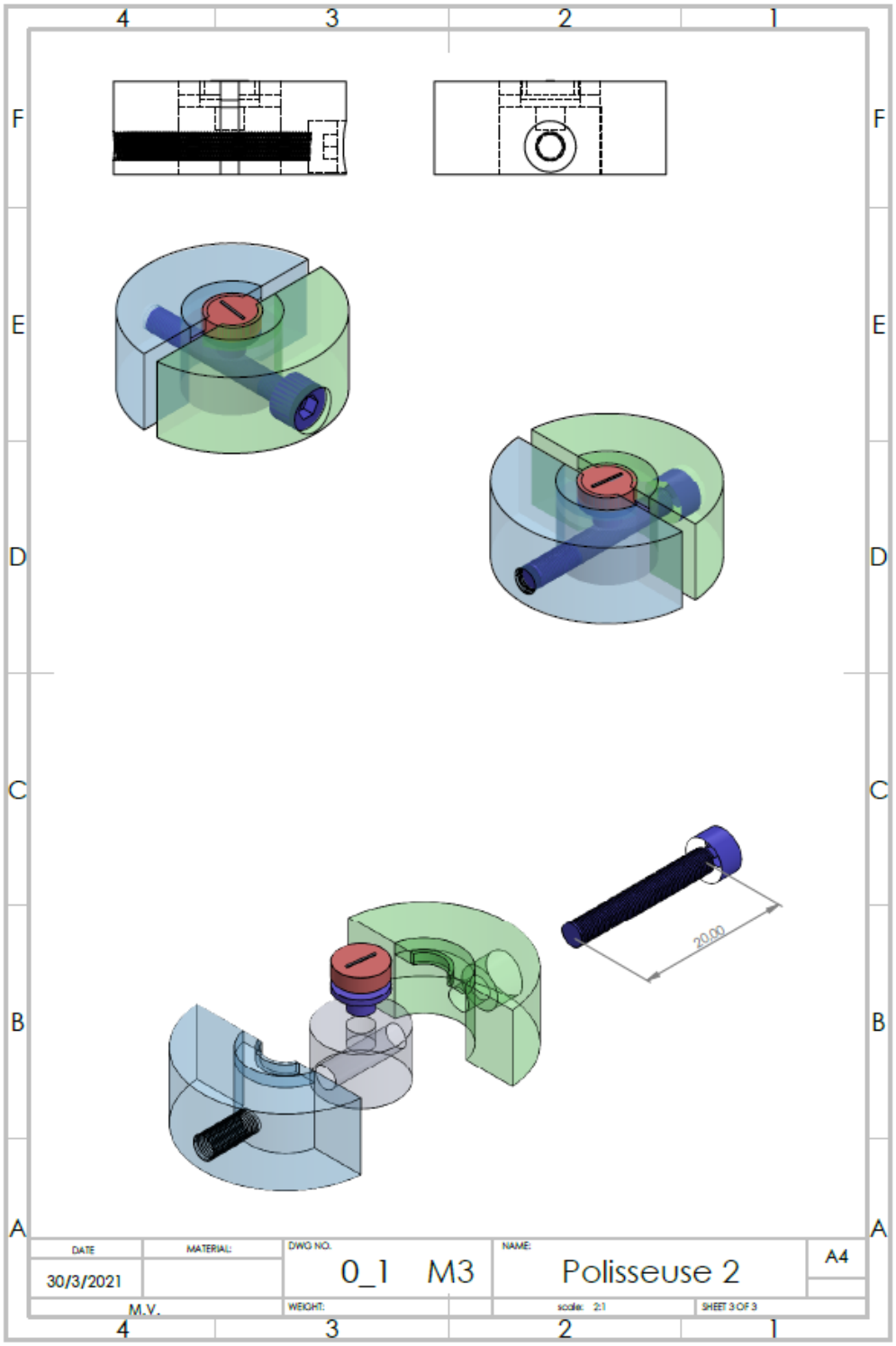


*Figure 181: 3D views of the custom designed specimen holder (3/3)*

# Appendix 3: Effect of peak at 29 amu on clustering and on the estimated hardening

In the APT community, it is commonly known that when dealing with steels that have alloying elements of Ni and Si, the peak at 29 atomic mass units (amu) on the mass-to-charge-state spectrum can cause some level of ambiguity in determining the composition. Consequently, peak deconvolution based on the relative natural abundance of each element can provide accurate measurement of the Fe, Ni, and Si content present at this peak.

The evaporation field required for the first ionic charge state of Si (45 V/n) is much higher compared to the evaporation fields required for $Fe^{2+}$ and $Ni^{2+}$ (33 and 36 V/nm, respectively). Therefore, it is unlikely for the $Si^{+}$ ions to contribute significantly to the mass-to-charge-state spectrum and the contribution of $^{29}Si^{+}$ is assumed to be negligible.

Thus, in this study, the number of the events detected at this peak was deconvoluted between the majority isotope of nickel ($^{58}Ni^{2+}$) and a minority isotope of iron ($^{58}Fe^{2+}$). Indeed, for the as-irradiated Fe-Mn-Ni alloy, after deconvolution the detected ions were attributed by about 67% as $^{58}Ni^{2+}$ and 33% as $^{58}Fe^{2+}$.

Clusters are identified based on the local concentration of solute elements of interest as e.g., the Ni for the MNSP clusters. At the cluster identification stage, deconvolution has not been yet performed and the user must assign each peak to a single element. Therefore, depending on the peak 29 characterization, local concentration variation may occur which in turn may produce different results in the detection and quantification of the clusters (size, number density etc), and consequently affect the predicted hardening calculated from the theoretical models.

In literature the vast majority of the authors, assign the peak at 29 amu as $^{58}Ni^{2+}$, while others choose not to include this peak in cluster identification process[1]. In this study we also identified all the events at this peak as $^{58}Ni^{2+}$, ignoring the possibility of the co- exitance of $^{58}Fe^{2+}$. We decided to evaluate the extent that treating peak 29 either as Fe or as Ni affects the clusters characteristics and consequently the predicted hardening by theoretical models, as the modified BKS model. Therefore, the APT data of the Fe-Mn-Ni samples at the as-irradiated and PIA 400, 500 and 600 states, were treated twice, the first-time considering peak 29 as $^{58}Ni^{2+}$ and the second as $^{58}Fe^{2+}$.

Treating this peak as Ni, produced clusters with mildly increased size compared to the size obtained when treating it as Fe. Additionally, a significant larger number of clusters was detected inside the analyzed volumes which led in turn in increased number density. The calculated values are summarized in Table 27 for the four studied irradiation states (as-irradiated, isochronally annealed at 400°C, 500°C, 600°C) as well as the observed percentage decrease, when treating peak 29 as corresponding to Fe instead of Ni.

[1] K. Lindgren, M. Boåsen, K. Stiller, P. Efsing, M. Thuvander, Evolution of precipitation in reactor pressure vessel steel welds under neutron irradiation, J. Nucl. Mater. 488 (2017) 222–230. https://doi.org/10.1016/j.jnucmat.2017.03.019

*Table 27: Number density ($N_D$), Guinier radius (Rg) and the predicted by the modified BKS irradiation hardening (Δτ), for the Fe-Mn-Ni model alloy in the as-irradiated and annealed at 400, 500, 600 degrees, when treating the peak at 29 amu as Fe and as Ni.*

| | $N_D$ x$10^{22}$ ($m^{-3}$) | | | Rg (nm) | | | Δτ (MPa) | | |
|---|---|---|---|---|---|---|---|---|---|
| | **p29-Fe** | **p29-Ni** | **Decrease** | **p29-Fe** | **p29-Ni** | **Decrease** | **p29-Fe** | **p29-Ni** | **Decrease** |
| **As irr** | 40 | 62 | 35,48% | 1,19 | 1,43 | 16,78% | 109,37 | 182,93 | 40,21% |
| **400** | 17 | 26 | 34,62% | 1,21 | 1,47 | 17,69% | 61,14 | 107,04 | 42,89% |
| **500** | 5,7 | 11 | 48,18% | 1,4 | 1,76 | 20,45% | 32,42 | 74,39 | 56,41% |
| **600** | 0,2 | 0,58 | 65,52% | 1,66 | 1,85 | 10,27% | 1,77 | 6,45 | 72,58% |

The upper and lower boundaries between which lie the actual values of Rg and number density of the clusters, are illustrated in Figure 182.

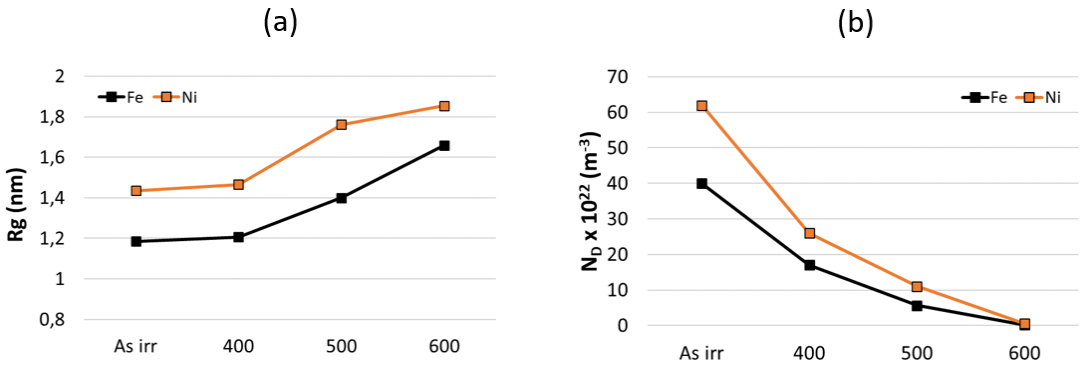


*Figure 182: (a) Guinier Radius and (b) Number density of the clusters identified in the Fe-Mn-Ni alloy in the as-irradiated and the at 400°C, 500°C and 600°C PIA samples, considering the events at peak 29 amu either as Fe (in black) or as Ni (in orange).*

Using these data in the equation (4.1) the predicted hardening is plotted in the Figure 183 below, calculated according to the modified BKS model, using the estimated value of specific resistance stress, $\Omega_{obs}$=3.40.

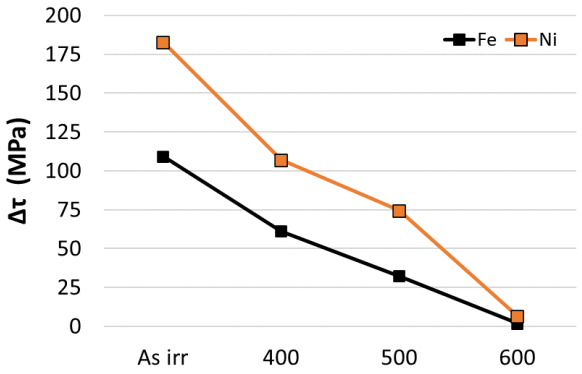


*Figure 183: Irradiation hardening estimated by the modified BKS model, using the APT data of the identified clusters in the as-irradiated and the at 400°C, 500°C and 600°C PIA samples, considering the events at peak 29 amu either as Fe (in black) or as Ni (in orange).*

Therefore, it is obvious that both the available options (that is treating the events of the peak at 29 amu either as Ni or Fe) introduce a calculation error. Considering that deconvolution of the events of this peak, attributed about the 67% to Ni and only about 33% to Fe, hence we assumed that the clustering calculations become more accurate by attributing the peak at 29 amu to $^{58}Ni^{2+}$.

Moreover, the distribution of the events at 29 amu was inhomogeneous within the reconstructed data. Inside the clusters the percentage of the peak 29 events to the total events was significantly increased compared to the matrix. In more details, for the as-irradiated samples the percentage of the events at 29 amu in the clusters was 4.4 times higher than that in the matrix and was rather similar (4.8 times higher) for the PIA at 400°C and (4 times) for the PIA at 500°C, while for the two of the four analyzed PIA at 600°C samples, which contained clusters, was only 2.1 times higher than the matrix. This observation was considered to further support, the attribution of peak 29 to $^{58}Ni^{2+}$

# Appendix 4: Details of the APT experiments results

## 1. APT analysis results of the Fe-Mn alloy

*Table 28: Number of atoms (Nat) and global composition of each analyzed tip of the non-irradiated Fe-Mn alloy.*

| | | Concentration (at. %) | | | | | | |
|---|---|---|---|---|---|---|---|---|
| **Sample ID** | **Nat (x10$^6$)** | **Fe** | **Mn** | **Ni** | **Cr** | **Si** | **P** | **C** |
| 120504-a | 1.49 | 99.18 | 0.68 | 0 | 0.03 | 0.01 | 0 | 0.02 |
| 120504-b | 0.56 | 98.99 | 0.88 | 0 | 0.05 | 0 | 0 | 0 |
| 120504-c | 2.49 | 99.10 | 0.85 | 0 | 0.00 | 0 | 0 | 0 |
| Fe-Mn-t21 | 2.22 | 96.92 | 0.86 | 0.20 | 0.07 | 0.01 | 0.01 | 0.74 |
| Fe-Mn-t24 | 8.67 | 98.76 | 0.96 | 0 | 0.03 | 0.00 | 0.00 | 0.20 |
| Fe-Mn-t23 | 1.96 | 98.21 | 0.95 | 0.06 | 0.04 | 0.00 | 0.01 | 0.57 |
| lawa-1 | 9.86 | 99.02 | 0.75 | 0 | 0.04 | 0.00 | 0.00 | 0.01 |
| **Total** | **27.25** | **98.73** | **0.85** | **0.02** | **0.04** | **0.00** | **0.00** | **0.17** |

*Table 29: Number of atoms (Nat) and global composition of each analyzed tip of the neutron irradiated Fe-Mn alloy.*

| | | Concentration (at. %) | | | | | | |
|---|---|---|---|---|---|---|---|---|
| **Sample ID** | **Nat (x10$^6$)** | **Fe** | **Mn** | **Ni** | **Cr** | **Si** | **P** | **C** |
| FeMn-t15 | 2.64 | 98.68 | 0.96 | 0.04 | 0.06 | 0.01 | 0.01 | 0.13 |
| FeMn-t14 | 3.49 | 98.73 | 0.91 | 0.04 | 0.06 | 0.02 | 0.01 | 0.14 |
| FeMn-t16 | 3.64 | 98.67 | 0.94 | 0.04 | 0.07 | 0.02 | 0.01 | 0.15 |
| FeMn-t13 | 4.32 | 98.73 | 0.90 | 0.04 | 0.06 | 0.01 | 0.01 | 0.14 |
| **Total** | **14.08** | **98.70** | **0.92** | **0.04** | **0.06** | **0.02** | **0.01** | **0.14** |

*Table 30: Number of atoms (Nat) and solute clusters' composition of each analyzed tip of the neutron irradiated Fe-Mn alloy.*

| | | Concentration (at. %) | | | | | | |
|---|---|---|---|---|---|---|---|---|
| **Sample ID** | **Nat** | **Fe** | **Mn** | **Ni** | **Cr** | **Si** | **P** | **C** |
| FeMn-t15 | 3 890 | 87.65 | 11.34 | 0.33 | 0.13 | 0.00 | 0.17 | 0.15 |
| FeMn-t14 | 4 165 | 88.15 | 11.02 | 0.18 | 0.20 | 0.05 | 0.19 | 0.05 |
| FeMn-t16 | 9 675 | 88.51 | 10.33 | 0.28 | 0.12 | 0.08 | 0.23 | 0.32 |
| FeMn-t13 | 9 125 | 89.96 | 9.08 | 0.24 | 0.08 | 0.02 | 0.14 | 0.20 |
| **Total** | **26 855** | **88.82** | **10.16** | **0.26** | **0.12** | **0.04** | **0.18** | **0.21** |

*Table 31: Number of atoms (Nat) and solute clusters composition, classified by size range of the detected clusters in the neutron irradiated Fe-Mn alloy.*

| | | Concentration (at. %) | | | | | | |
|---|---|---|---|---|---|---|---|---|
| **Size Range (Rg)** | **Nat** | **Fe** | **Mn** | **Ni** | **Cr** | **Si** | **P** | **C** |
| 0-1 | 11 223 | 89.42 | 9.65 | 0.23 | 0.12 | 0.04 | 0.11 | 0.19 |
| 1-2 | 13 686 | 88.02 | 10.90 | 0.29 | 0.13 | 0.06 | 0.21 | 0.23 |
| 2-3 | 1 946 | 91.02 | 7.86 | 0.19 | 0.00 | 0.00 | 0.41 | 0.21 |
| **Total** | **26 855** | **88.82** | **10.16** | **0.26** | **0.12** | **0.04** | **0.18** | **0.21** |

*Table 32: Number of atoms, number of particles, number density, equivalent spherical radius (Req), Guinier radius (Rg) and volume fraction (fv) of each analyzed tip of the neutron irradiated Fe-Mn alloy.*

| | | **Number of Particles** | | | | **Number Density x$10^{23}$($m^{-3}$)** | | | | | | |
|---|---|---|---|---|---|---|---|---|---|---|---|---|
| | | By Size Range (Rg) | | | **Total Pcls** | By Size Range (Rg) | | | **Total** | | | |
| **Sample ID** | **Nat ($x10^6$)** | 0 - 1 | 1 - 2 | 2 - 3 | | **0 - 1** | **1 - 2** | **2 - 3** | | **<Req>** | **<Rg>** | **fv %** |
| FeMn-t16 | 3.6 | 35.8 | 72.7 | 0.0 | **108.5** | 4.37 | 8.89 | 0.00 | **13.26** | 1.09 | 1.20 | 1.05 |
| FeMn-t15 | 2.6 | 56.6 | 30.9 | 0.0 | **87.5** | 9.54 | 5.20 | 0.00 | **14.75** | 0.88 | 0.98 | 0.80 |
| FeMn-t14 | 3.5 | 41.3 | 59.2 | 0.0 | **100.5** | 5.27 | 7.55 | 0.00 | **12.81** | 1.06 | 1.17 | 1.11 |
| FeMn-t13 | 4.3 | 103.1 | 49.1 | 4.8 | **157.0** | 10.61 | 5.06 | 0.00 | **16.17** | 0.89 | 1.03 | 0.92 |
| **Total** | **14.1** | **236.8** | **211.9** | **4.8** | **453.5** | **7.48** | **6.69** | **0.15** | **14.32** | **0.97** | **1.09** | **0.98** |

*Table 33: Number of atoms (Nat) and global composition of each analyzed tip fabricated from compressed pillars of the non-irradiated Fe-Mn alloy.*

| | | Concentration (at. %) | | | | | | |
|---|---|---|---|---|---|---|---|---|
| **Sample ID** | **Nat ($x10^6$)** | **Fe** | **Mn** | **Ni** | **Cr** | **Si** | **P** | **C** |
| FeMn -tip10 | 0.82 | 98.17 | 0.99 | 0.06 | 0.06 | 0.02 | 0.01 | 0.48 |
| FeMn -tip11 | 0.76 | 98.22 | 0.94 | 0.05 | 0.07 | 0.02 | 0.01 | 0.47 |
| **Total** | **1.57** | **98.20** | **0.96** | **0.05** | **0.07** | **0.02** | **0.01** | **0.47** |

*Table 34: Number of atoms (Nat) and global composition of each analyzed tip fabricated from compressed pillars of the neutron irradiated Fe-Mn alloy.*

| | | Concentration (at. %) | | | | | | |
|---|---|---|---|---|---|---|---|---|
| **Sample ID** | **Nat** | **Fe** | **Mn** | **Ni** | **Cr** | **Si** | **P** | **C** |
| FeMn-tip10 | 2 980 | 88.13 | 10.87 | 0.09 | 0.14 | 0.03 | 0.07 | 0.37 |
| FeMn-tip11 | 815 | 87.11 | 12.15 | 0.00 | 0.13 | 0.00 | 0.37 | 0.12 |
| **Total** | **3 795** | **87.91** | **11.15** | **0.07** | **0.14** | **0.03** | **0.13** | **0.32** |

*Table 35: Number of atoms (Nat) and solute clusters' composition of each analyzed tip fabricated from compressed pillars of the neutron irradiated Fe-Mn alloy.*

| | | Concentration (at. %) | | | | | | |
|---|---|---|---|---|---|---|---|---|
| **Size Range (Rg)** | **Nat** | **Fe** | **Mn** | **Ni** | **Cr** | **Si** | **P** | **C** |
| **0-1** | 906 | 88.07 | 11.59 | 0.00 | 0.23 | 0.00 | 0.11 | 0.00 |
| **1-2** | 1 061 | 85.22 | 13.20 | 0.26 | 0.29 | 0.09 | 0.09 | 0.47 |
| **2-3** | 1 828 | 89.39 | 9.74 | 0.00 | 0.00 | 0.00 | 0.16 | 0.38 |
| **Total** | **3 795** | **87.91** | **11.15** | **0.07** | **0.14** | **0.03** | **0.13** | **0.00** |

*Table 36: Number of atoms, number of particles, number density, equivalent spherical radius (Req), Guinier radius (Rg) and volume fraction (fv) of each analyzed tip fabricated from compressed pillars of the neutron irradiated Fe-Mn alloy.*

| | | **Number of Particles** | | | | **Number Density ($m^{-3}$) x$10^{23}$** | | | | | | |
|---|---|---|---|---|---|---|---|---|---|---|---|---|
| | | By Size Range (Rg) | | | **Total Pcls** | By Size Range (Rg) | | | **Total** | | | |
| **Sample ID** | **Nat (x$10^6$)** | 0 - 1 | 1 - 2 | 2 - 3 | | 0 - 1 | 1 - 2 | 2 - 3 | | **<Req>** | **<Rg>** | **fv %** |
| FeMn-tip10 | 0.82 | 16.5 | 8.9 | 2.5 | 28.0 | 8.98 | 4.83 | 1.38 | 15.20 | 1.06 | 1.12 | 1.54 |
| FeMn-tip11 | 0.76 | 12.1 | 18.8 | 2.7 | 33.5 | 7.10 | 11.04 | 1.58 | 19.71 | 1.10 | 1.26 | 2.11 |
| **Total** | **1.57** | **28.6** | **27.7** | **5.2** | **61.5** | **8.08** | **7.81** | **1.48** | **17.36** | **1.08** | **1.19** | **1.82** |

## 2. APT analysis results of the Fe-Ni alloy

*Table 37: Number of atoms (Nat) and global composition of each analyzed tip of the non-irradiated Fe-Ni alloy.*

| | | Concentration (at. %) | | | | | | |
|---|---|---|---|---|---|---|---|---|
| **Sample ID** | **Nat (x$10^6$)** | **Fe** | **Mn** | **Ni** | **Cr** | **Si** | **P** | **C** |
| FeNi-tip1 | 2.14 | 97.54 | 0 | 1.83 | 0.007 | 0.007 | 0.001 | 0.40 |
| FeNi-tip2 | 7.80 | 98.09 | 0 | 1.74 | 0.001 | 0.002 | 0.002 | 0.10 |
| FeNi-tip7 | 2.08 | 97.69 | 0 | 1.87 | 0.005 | 0.006 | 0.002 | 0.26 |
| FeNi-tip8 | 3.14 | 97.57 | 0 | 1.97 | 0.012 | 0.021 | 0.002 | 0.21 |
| **Total** | **15.16** | **97.85** | **0** | **1.82** | **0.005** | **0.007** | **0.002** | **0.19** |

*Table 38: Number of atoms (Nat) and global composition of each analyzed tip of the neutron irradiated Fe-Ni alloy.*

| | | Concentration (at. %) | | | | | | |
|---|---|---|---|---|---|---|---|---|
| **Sample ID** | **Nat (x$10^6$)** | **Fe** | **Mn** | **Ni** | **Cr** | **Si** | **P** | **C** |
| FeNi-tip7 | 2.35 | 97.91 | 0.004 | 1.62 | 0.01 | 0.02 | 0.001 | 0.22 |
| FeNi-tip8 | 1.76 | 97.82 | 0 | 1.65 | 0.01 | 0.03 | 0.000 | 0.28 |
| FeNi-tip9 | 1.01 | 97.27 | 0 | 1.95 | 0.02 | 0.03 | 0.001 | 0.50 |
| FeNi-tip8re | 1.77 | 98.05 | 0 | 1.73 | 0.01 | 0.05 | 0 | 0.07 |
| **Total** | **6.89** | **97.83** | **0.001** | **1.71** | **0.01** | **0.03** | **0.001** | **0.24** |

*Table 39: Number of atoms (Nat) and solute clusters' composition of each analyzed tip of the neutron irradiated Fe-Ni alloy.*

| | | Concentration (at. %) | | | | | | |
|---|---|---|---|---|---|---|---|---|
| **Sample ID** | **Nat** | **Fe** | **Mn** | **Ni** | **Cr** | **Si** | **P** | **C** |
| FeNi-tip7 | 186 | 69.45 | 0 | 27.19 | 0 | 0 | 0 | 2.15 |
| FeNi-tip8 | 640 | 83.41 | 0 | 16.28 | 0 | 0 | 0 | 0.16 |
| FeNi-tip9 | 1 272 | 82.91 | 0 | 14.84 | 0.31 | 0.55 | 0 | 0.16 |
| FeNi-tip8re | 710 | 79.57 | 0 | 19.68 | 0 | 0.42 | 0 | 0.14 |
| **Total** | **2 808** | **81.29** | **0** | **17.21** | **0.14** | **0.36** | **0** | **0.28** |

*Table 40: Number of atoms (Nat) and solute clusters composition, classified by size range of the detected clusters in the neutron irradiated Fe-Ni alloy.*

| | | Concentration (at. %) | | | | | | |
|---|---|---|---|---|---|---|---|---|
| **Size Range (Rg)** | **Nat** | **Fe** | **Mn** | **Ni** | **Cr** | **Si** | **P** | **C** |
| 0-1 | 198 | 84.39 | 0 | 14.30 | 0 | 0 | 0 | 0 |
| 1-2 | 1 405 | 79.63 | 0 | 19.45 | 0 | 0.21 | 0 | 0.43 |
| 2-3 | 1 205 | 82.71 | 0 | 15.08 | 0.33 | 0.58 | 0 | 0.17 |
| **Total** | **2 808** | **81.29** | **0** | **17.21** | **0.14** | **0.36** | **0** | **0** |

*Table 41: Number of atoms, number of particles, number density, equivalent spherical radius (Req), Guinier radius (Rg) and volume fraction (fv) of each analyzed tip of the neutron irradiated Fe-Ni alloy.*

| | | **Number of Particles** | | | | **Number Density ($m^{-3}$) x$10^{23}$** | | | | | | |
|---|---|---|---|---|---|---|---|---|---|---|---|---|
| | | By Size Range (Rg) | | | **Total Pcls** | By Size Range (Rg) | | | **Total** | | | |
| **Sample ID** | **Nat (x$10^6$)** | 0 - 1 | 1 - 2 | 2 - 3 | | **0 - 1** | **1 - 2** | **2 - 3** | | **<Req>** | **<Rg>** | **fv %** |
| Ni-tip7 | 2.35 | 4.33 | 2.17 | 0 | **6.5** | 0.82 | 0.41 | 0 | 1.23 | 1.03 | 0.98 | 0.16 |
| Ni-tip8 | 1.76 | 0 | 6.00 | 0 | **6.0** | 0 | 1.52 | 0 | 1.52 | 1.02 | 1.24 | 0.09 |
| Ni-tip9 | 1.01 | 3.50 | 0 | 3.50 | **7.0** | 1.53 | 0 | 1.53 | 3.07 | 1.37 | 1.50 | 0.41 |
| Ni-tip8re | 1.77 | 1.13 | 3.38 | 0 | **4.5** | 0.28 | 0.85 | 0 | 1.13 | 1.39 | 1.48 | 0.14 |
| **Total** | **6.89** | **9.0** | **11.5** | **3.5** | **24.0** | **0.58** | **0.74** | **0.23** | **1.55** | **1.20** | **1.30** | **0.18** |

## 3. APT analysis results of the Fe-Mn-Ni alloy

*Table 42: Number of atoms (Nat) and global composition of each analyzed tip of the non-irradiated Fe-Mn-Ni alloy.*

| | | Concentration (at. %) | | | | | | |
|---|---|---|---|---|---|---|---|---|
| **Sample ID** | **Nat (x106)** | **Fe** | **Mn** | **Ni** | **Cr** | **Si** | **P** | **C** |
| N085A-1 | 4.74 | 98.10 | 0.93 | 0.75 | 0.01 | 0.03 | 0.005 | 0.12 |
| N085A-3 | 0.85 | 94.45 | 0.92 | 0.71 | 0.01 | 0.04 | 0 | 0.28 |
| N085A-4 | 3.43 | 98.20 | 0.94 | 0.74 | 0.01 | 0.03 | 0.002 | 0.03 |
| N085A-5 | 0.56 | 98.00 | 0.96 | 0.75 | 0.01 | 0.03 | 0 | 0.13 |
| **Total** | **9.59** | **97.81** | **0.93** | **0.74** | **0.01** | **0.03** | **0.003** | **0.10** |

*Table 43: Number of atoms (Nat) and global composition of each analyzed tip of the neutron irradiated Fe-Mn-Ni alloy.*

| | | Concentration (at. %) | | | | | | |
|---|---|---|---|---|---|---|---|---|
| **Sample ID** | **Nat ($x10^6$)** | **Fe** | **Mn** | **Ni** | **Cr** | **Si** | **P** | **C** |
| As Irr-01882 | 25.05 | 97.57 | 1.35 | 0.87 | 0.01 | 0.04 | 0.007 | 0.01 |
| As Irr-01878 | 1.03 | 97.77 | 1.24 | 0.81 | 0.01 | 0.04 | 0.007 | 0.01 |
| As Irr-01884 | 10.47 | 97.77 | 1.27 | 0.80 | 0.01 | 0.04 | 0.007 | 0.03 |
| As Irr-01879 | 25.66 | 97.70 | 1.27 | 0.82 | 0.01 | 0.04 | 0.006 | 0.02 |
| As Irr-01877 | 14.90 | 97.85 | 1.20 | 0.77 | 0.01 | 0.05 | 0.006 | 0.01 |
| **Total** | **77.10** | **97.70** | **1.29** | **0.82** | **0.01** | **0.04** | **0.007** | **0.02** |

*Table 44: Number of atoms (Nat) and solute clusters' composition of each analyzed tip of the neutron irradiated Fe-Mn-Ni alloy.*

| | | Concentration (at. %) | | | | | | |
|---|---|---|---|---|---|---|---|---|
| **Sample ID** | **Nat** | **Fe** | **Mn** | **Ni** | **Cr** | **Si** | **P** | **C** |
| As Irr-01882 | 33324 | 78.30 | 11.06 | 8.39 | 0.02 | 0.97 | 0.49 | 0.04 |
| As Irr-01878 | 1964 | 85.50 | 6.82 | 6.23 | 0 | 0.97 | 0.37 | 0 |
| As Irr-01884 | 8452 | 72.14 | 12.04 | 11.70 | 0.04 | 2.10 | 1.17 | 0.13 |
| As Irr-01879 | 17451 | 77.23 | 10.87 | 9.48 | 0.02 | 0.88 | 0.42 | 0.10 |
| As Irr-01877 | 55116 | 82.80 | 8.94 | 6.68 | 0.04 | 0.68 | 0.22 | 0.05 |
| **Total** | **116307** | **79.94** | **10.03** | **7.95** | **0.03** | **0.90** | **0.40** | **0.06** |

*Table 45: Number of atoms (Nat) and solute clusters composition, classified by size range of the detected clusters in the neutron irradiated Fe-Mn-Ni alloy.*

| | | Concentration (at. %) | | | | | | |
|---|---|---|---|---|---|---|---|---|
| **Size Range (Rg)** | **Nat** | **Fe** | **Mn** | **Ni** | **Cr** | **Si** | **P** | **C** |
| 0-0.5 | 165 | 90.53 | 3.64 | 4.01 | 0 | 1.82 | 0 | 0 |
| 0.5-1 | 6113 | 84.62 | 8.65 | 5.26 | 0.05 | 0.83 | 0.17 | 0.10 |
| 1-1.5 | 50503 | 80.42 | 9.95 | 7.76 | 0.02 | 0.78 | 0.29 | 0.06 |
| 1.5-2 | 48973 | 79.12 | 10.37 | 8.31 | 0.03 | 0.93 | 0.44 | 0.04 |
| 2-2.5 | 5281 | 77.13 | 10.76 | 9.33 | 0.04 | 1.38 | 0.72 | 0.04 |
| 2.5-3 | 2811 | 78.06 | 9.04 | 9.23 | 0 | 1.60 | 1.34 | 0.28 |
| 3-3.5 | 2461 | 82.53 | 8.09 | 7.05 | 0 | 1.23 | 0.62 | 0 |
| **Total** | **116307** | **79.94** | **10.03** | **7.95** | **0.03** | **0.90** | **0.40** | **0.05** |

*Table 46: Number of atoms (Nat) and global composition of each analyzed tip of the neutron irradiated Fe-Mn-Ni alloy, post-irradiation annealed at 400°C.*

| | | Concentration (at. %) | | | | | | |
|---|---|---|---|---|---|---|---|---|
| **Sample ID** | **Nat (x10$^6$)** | **Fe** | **Mn** | **Ni** | **Cr** | **Si** | **P** | **C** |
| 400-02477 | 7.02 | 97.89 | 1.18 | 0.77 | 0.008 | 0.04 | 0.007 | 0.09 |
| 400-02472 | 5.72 | 98.04 | 1.14 | 0.73 | 0.005 | 0.04 | 0.006 | 0.01 |
| 400-02476 | 27.16 | 97.93 | 1.20 | 0.76 | 0.007 | 0.04 | 0.005 | 0.02 |
| **Total** | **39.90** | **97.94** | **1.19** | **0.76** | **0.007** | **0.04** | **0.006** | **0.03** |

*Table 47: Number of atoms (Nat) and solute clusters composition, classified by size range of the detected clusters in the neutron irradiated Fe-Mn-Ni alloy, post-irradiation annealed at 400°C.*

| | | Concentration (at. %) | | | | | | |
|---|---|---|---|---|---|---|---|---|
| **Sample ID** | **Nat** | **Fe** | **Mn** | **Ni** | **Cr** | **Si** | **P** | **C** |
| 400-02477 | 6036 | 77.29 | 10.09 | 8.21 | 0.03 | 1.61 | 0.64 | 0.30 |
| 400-02472 | 5630 | 77.92 | 10.80 | 8.53 | 0.04 | 1.14 | 0.27 | 0.02 |
| 400-02476 | 13660 | 76.53 | 10.70 | 8.07 | 0.02 | 1.68 | 1.09 | 0.11 |
| **Total** | **25326** | **77.02** | **10.57** | **9.39** | **0.03** | **1.54** | **0.80** | **0.13** |

*Table 48: Number of atoms (Nat) and solute clusters composition, classified by size range of the detected clusters in the neutron irradiated Fe-Mn-Ni alloy, post-irradiation annealed at 400°C.*

| | | Concentration (at. %) | | | | | | |
|---|---|---|---|---|---|---|---|---|
| **Size Range (Rg)** | **Nat** | **Fe** | **Mn** | **Ni** | **Cr** | **Si** | **P** | **C** |
| 0.5-1 | 1503 | 88.54 | 5.99 | 4.64 | 0.07 | 0.60 | 0.16 | 0 |
| 1-1.5 | 3765 | 79.55 | 9.03 | 8.99 | 0 | 2.02 | 0.36 | 0.03 |
| 1.5-2 | 15178 | 75.46 | 11.37 | 10.15 | 0.03 | 1.63 | 0.78 | 0.11 |
| 2-2.5 | 2883 | 75.03 | 11.86 | 10.03 | 0.04 | 1.32 | 1.18 | 0.07 |
| 2.5-3 | 1997 | 78.32 | 9.06 | 7.01 | 0.05 | 1.05 | 1.68 | 0.75 |
| **Total** | **25326** | **77.02** | **10.57** | **9.39** | **0.03** | **1.54** | **0.80** | **0.08** |

*Table 49: Number of atoms (Nat) and global composition of each analyzed tip of the neutron irradiated Fe-Mn-Ni alloy, post-irradiation annealed at 500°C.*

| | | Concentration (at. %) | | | | | | |
|---|---|---|---|---|---|---|---|---|
| **Sample ID** | **Nat (x10$^6$)** | **Fe** | **Mn** | **Ni** | **Cr** | **Si** | **P** | **C** |
| 500-02318 | 36.38 | 97.87 | 1.22 | 0.76 | 0.008 | 0.04 | 0.007 | 0.03 |
| 500-02317 | 6.15 | 97.71 | 1.26 | 0.78 | 0.014 | 0.05 | 0.008 | 0.06 |
| 500-02326 | 24.82 | 97.77 | 1.26 | 0.79 | 0.010 | 0.04 | 0.006 | 0.02 |
| 500-02284 | 21.90 | 97.84 | 1.22 | 0.77 | 0.011 | 0.04 | 0.007 | 0.02 |
| **Total** | **89.25** | **97.82** | **1.23** | **0.77** | **0.010** | **0.04** | **0.007** | **0.03** |

*Table 50: Number of atoms (Nat) and solute clusters composition, classified by size range of the detected clusters in the neutron irradiated Fe-Mn-Ni alloy, post-irradiation annealed at 500°C.*

| | | Concentration (at. %) | | | | | | |
|---|---|---|---|---|---|---|---|---|
| **Sample ID** | **Nat** | **Fe** | **Mn** | **Ni** | **Cr** | **Si** | **P** | **C** |
| 500-R73_02318 | 3554 | 16.01 | 7.46 | 5.37 | 0.09 | 0.42 | 0.30 | 0.06 |
| 500-R73_02317 | 546 | 12.87 | 5.86 | 6.69 | 0.00 | 0.92 | 0.10 | 0.00 |
| 500-R73_02326 | 20514 | 15.16 | 7.31 | 5.67 | 0.02 | 0.43 | 0.22 | 0.09 |
| 500-R73_02284 | 1229 | 15.58 | 11.23 | 5.11 | 0.33 | 0.81 | 0.91 | 1.30 |

*Table 51: Number of atoms, number of particles, number density, equivalent spherical radius (Req), Guinier radius (Rg) and volume fraction (fv) of each analyzed tip of the neutron irradiated Fe-Mn-Ni alloy.*

| | | Number of Particles | | | | | | | | Number Density ($m^{-3}$) x$10^{23}$ | | | | | | | | | | |
|---|---|---|---|---|---|---|---|---|---|---|---|---|---|---|---|---|---|---|---|---|
| | | By Size Range (Rg) | | | | | | | Total Pcls | By Size Range (Rg) | | | | | | | Total | | | |
| **Sample ID** | **Nat (x$10^6$)** | **0 - 0.5** | **0.5 - 1** | **1 - 1.5** | **1.5 - 2** | **2 - 2.5** | **2.5 - 3** | **3 - 3.5** | | **0 - 0.5** | **0.5 - 1** | **1 - 1.5** | **1.5 - 2** | **2 - 2.5** | **2.5 - 3** | **3 - 3.5** | | **<Req>** | **<Rg>** | **fv %** |
| **As Irr-01882** | 25.05 | 0 | 18.5 | 282.3 | 222.1 | 23.1 | 4.6 | 2.3 | **553.0** | 0 | 0.23 | 3.47 | 2.73 | 0.28 | 0.06 | 0.03 | **6.79** | 1.5 | 1.5 | 1.49 |
| **As Irr-01878** | 1.03 | 0 | 5.9 | 7.8 | 7.8 | 0 | 0 | 0 | **21.5** | 0 | 1.76 | 2.34 | 2.34 | 0 | 0 | 0 | **6.44** | 1.2 | 1.3 | 1.76 |
| **As Irr-01884** | 10.47 | 0 | 7.6 | 73.0 | 28.9 | 1.3 | 1.3 | 0 | **112.0** | 0 | 0.22 | 2.15 | 0.85 | 0.04 | 0.04 | 0 | **3.29** | 1.5 | 1.4 | 0.81 |
| **As Irr-01877** | 8.66 | 0 | 15.6 | 95.9 | 148.6 | 8.4 | 0 | 0 | **268.5** | 0 | 0.55 | 3.41 | 5.28 | 0.30 | 0 | 0 | **9.54** | 1.5 | 1.5 | 2.38 |
| **As Irr-01879** | 25.66 | 1.2 | 34.4 | 378.9 | 52.3 | 8.3 | 4.8 | 1.2 | **481.0** | 0.01 | 0.41 | 4.54 | 0.63 | 0.10 | 0.06 | 0.01 | **5.77** | 1.4 | 1.3 | 1.06 |
| **Total** | **70.86** | **1.2** | **81.9** | **837.8** | **459.8** | **41.1** | **10.6** | **3.5** | **1436.0** | **0.01** | **0.36** | **3.64** | **2.00** | **0.18** | **0.05** | **0.02** | **6.24** | **1.4** | **1.4** | **1.35** |

*Table 52: Number of atoms, number of particles, number density, equivalent spherical radius (Req), Guinier radius (Rg) and volume fraction (fv) of each analyzed tip of the neutron irradiated Fe-Mn-Ni alloy, post-irradiation annealed at 400°C.*

| | | Number of Particles | | | | | | | | Number Density ($m^{-3}$) x$10^{23}$ | | | | | | | | | | |
|---|---|---|---|---|---|---|---|---|---|---|---|---|---|---|---|---|---|---|---|---|
| | | By Size Range (Rg) | | | | | | | Total Pcls | By Size Range (Rg) | | | | | | | Total | | | |
| **Sample ID** | **Nat (x$10^6$)** | **0 - 0.5** | **0.5 - 1** | **1 - 1.5** | **1.5 - 2** | **2 - 2.5** | **2.5 - 3** | **3 - 3.5** | | **0 - 0.5** | **0.5 - 1** | **1 - 1.5** | **1.5 - 2** | **2 - 2.5** | **2.5 - 3** | **3 - 3.5** | | **<Req>** | **<Rg>** | **fv %** |
| **400-02472** | 5.72 | 0.0 | 2.6 | 39.4 | 26.3 | 2.6 | 0.0 | 0.0 | 71.0 | 0 | 0.14 | 2.12 | 1.41 | 0.14 | 0 | 0 | 3.82 | 1.5 | 1.5 | 0.98 |
| **400-02477** | 7.02 | 0.0 | 2.5 | 20.9 | 24.6 | 1.2 | 1.2 | 0.0 | 50.5 | 0 | 0.11 | 0.92 | 1.08 | 0.05 | 0.05 | 0 | 2.21 | 1.5 | 1.5 | 0.53 |
| **400-02476** | 27.16 | 0.0 | 13.2 | 116.0 | 75.4 | 8.4 | 2.4 | 1.2 | 216.5 | 0 | 0.15 | 1.31 | 0.85 | 0.09 | 0.03 | 0.01 | 2.45 | 1.5 | 1.5 | 0.66 |
| **Total** | **39.90** | **0.0** | **18.3** | **176.4** | **126.3** | **12.2** | **3.6** | **1.2** | **338.0** | **0** | **0.14** | **1.36** | **0.97** | **0.09** | **0.03** | **0.01** | **2.61** | **1.5** | **1.5** | **0.69** |

*Table 53: Number of atoms, number of particles, number density, equivalent spherical radius (Req), Guinier radius (Rg) and volume fraction (fv) of each analyzed tip of the neutron irradiated Fe-Mn-Ni alloy, post-irradiation annealed at 500°C.*

| | | **Number of Particles** | | | | | | | | | **Number Density ($m^{-3}$) x$10^{23}$** | | | | | | | | | | | |
|---|---|---|---|---|---|---|---|---|---|---|---|---|---|---|---|---|---|---|---|---|---|---|
| | | By Size Range (Rg) | | | | | | | | **Total Pcls** | By Size Range (Rg) | | | | | | | | **Total** | | | |
| **Sample ID** | **Nat (x$10^6$)** | **0 - 0.5** | **0.5 - 1** | **1 - 1.5** | **1.5 - 2** | **2 - 2.5** | **2.5 - 3** | **3 - 3.5** | **3.5 - 4** | | **0 - 0.5** | **0.5 - 1** | **1 - 1.5** | **1.5 - 2** | **2 - 2.5** | **2.5 - 3** | **3 - 3.5** | **3.5 -4** | | **<Req>** | **<Rg>** | **fv %** |
| **500-02318** | 36.38 | 0 | 11.9 | 10.8 | 8.7 | 0 | 1.1 | 0 | 0 | **32.5** | 0 | 0.10 | 0.09 | 0.07 | 0 | 0.01 | 0.01 | 0 | **0.27** | 1.1 | 1.3 | 0.03 |
| **500-02317** | 6.15 | 0 | 3.3 | 2.2 | 0 | 1.1 | 0 | 0 | 0 | **6.5** | 0 | 0.16 | 0.11 | 0 | 0.05 | 0 | 0 | 0 | **0.33** | 0.9 | 1.2 | 0.01 |
| **500-02326** | 24.82 | 0 | 16.8 | 62.1 | 66.0 | 72.5 | 29.8 | 5.2 | 2.6 | **255.0** | 0 | 0.21 | 0.77 | 0.82 | 0.90 | 0.37 | 0.06 | 0.03 | **3.16** | 1.5 | 1.9 | 0.74 |
| **500-02284** | 21.90 | 0 | 2.2 | 5.5 | 2.2 | 1.1 | 0 | 0 | 0 | **11.0** | 0 | 0.03 | 0.08 | 0.03 | 0.02 | 0 | 0 | 0 | **0.15** | 1.1 | 1.4 | 0.01 |
| **Total** | **89.25** | **0** | **34.2** | **80.6** | **76.9** | **74.7** | **30.9** | **5.2** | **2.6** | **305.0** | **0** | **0.12** | **0.28** | **0.27** | **0.26** | **0.11** | **0.02** | **0.01** | **1.05** | **1.4** | **1.8** | **0.22** |

*Table 54: Number of atoms, number of particles, number density, equivalent spherical radius (Req), Guinier radius (Rg) and volume fraction (fv) of each analyzed tip of the neutron irradiated Fe-Mn-Ni alloy, post-irradiation annealed at 600°C.*

| | | **Number of Particles** | | | | **Number Density ($m^{-3}$) x$10^{21}$** | | | | | | |
|---|---|---|---|---|---|---|---|---|---|---|---|---|
| | | By Size Range (Rg) | | | **Total Pcls** | By Size Range (Rg) | | | **Total** | | | |
| **Sample ID** | **Nat (x$10^6$)** | 0 - 1 | 1 - 2 | 2 - 3 | | **0 - 1** | **1 - 2** | **2 - 3** | | **<Req>** | **<Rg>** | **fv %** |
| **600-01949** | 2.92 | 0 | 0 | 0 | 0 | 0 | 0 | 0 | 0 | 0 | 0 | 0 |
| **600-01943** | 12.90 | 0 | 0 | 0 | 0 | 0 | 0 | 0 | 0 | 0 | 0 | 0 |
| **600-01952** | 18.69 | 1.2 | 1.2 | 1.2 | 3.5 | 1.92 | 1.92 | 1.92 | 5.76 | 1.7 | 1.7 | 0.01 |
| **600-01951** | 26.39 | 0 | 3.0 | 2.0 | 5.0 | 0 | 3.50 | 2.33 | 5.83 | 1.4 | 2.0 | 0.01 |
| **Total** | **60.91** | **1.2** | **4.2** | **3.2** | **8.5** | **0.59** | **2.11** | **1.60** | **4.30** | **1.5** | **1.9** | **0.01** |

Appendix 5: Details of the measured dissipated energy for 1% increase in strain

| | Pillar ID | Energy per $m^3$ for 3%→4% strain [MPa] |
|---|---|---|
| **Fe-Mn Non-Irradiated** | T9-34.7 | 4,72 |
| | T9-34.2 | 4,15 |
| | T9-34.6 | 5,44 |
| **Fe-Mn Irradiated** | T12-1.4 | 5,00 |
| | T12-1.12 | 5,13 |
| | T12-1.11 | 5,95 |
| | T12-1.10 | 5,85 |
| | T12-1.9 | 5,51 |
| | T12-1.8 | 5,76 |
| | T12-1.6 | 8,22 |
| | T12-1.5 | 6,08 |
| | T12-1.3 | 4,69 |
| | T12-1.2 | 4,64 |
| | T12-1.1 | 5,93 |

| | Pillar ID | Energy per $m^3$ for 2%→3% strain [MPa] |
|---|---|---|
| **Fe-Ni Non-Irradiated** | T8-1.1 | 3,84 |
| | T8-1.2 | 2,43 |
| | T8-1.9 | 3,92 |
| **Fe-Ni Irradiated** | T14-1.1 | 5,23 |
| | T14-1.2 | 4,09 |
| | T14-1.3 | 4,66 |
| | T14-1.4 | 4,96 |
| | T14-1.5 | 5,25 |
| | T14-1.6 | 4,84 |
| | T14-1.7 | 4,19 |
| | T14-1.10 | 6,67 |
| | T14-1.11 | 5,62 |
| | T14-1.12 | 5,40 |

| | Pillar ID | Energy per $m^3$ for 2%→3% strain [MPa] |
|---|---|---|
| **Fe-Mn-Ni Non- Irradiated** | T5-1.1 | 3,75 |
| | T5-1.3 | 3,55 |
| | T5-1.7 | 3,96 |
| | T5-1.9 | 4,05 |
| | T5-1.10 | 4,00 |
| **Fe-Mn-Ni Irradiated** | T11-1.1 | 6,21 |
| | T11-1.2 | 8,90 |
| | T11-1.3 | 8,57 |
| | T11-1.5 | 7,13 |
| | T11-1.6 | 6,16 |
| | T11-1.7 | 10,37 |
| | T11-1.9 | 8,19 |